Planets in Binary Star Systems and in Transitional Disks

Dissertation

der Mathematisch-Naturwissenschaftlichen Fakultät

der Eberhard Karls Universität Tübingen

zur Erlangung des Grades eines

Doktors der Naturwissenschaften

(Dr. rer. nat.)

vorgelegt von

Tobias Wolfgang Andreas Müller

aus Böblingen

Tübingen

2013

Tag der mündlichen Qualifikation:	28.01.2014
Dekan:	Prof. Dr. Wolfgang Rosenstiel
1. Berichterstatter:	Prof. Dr. Wilhelm Kley
2. Berichterstatter:	Prof. Dr. Klaus Werner
3. Berichterstatter:	Prof. Dr. Francesco Marzari

Zusammenfassung

Die Entdeckung von exosolaren Planeten in Binärsternen und insbesondere die in engen ($< 20\,\mathrm{AU}$) Systemen wie z. B. γ Cephei (Campbell et al., 1988; Hatzes et al., 2003) oder α Centauri (Dumusque et al., 2012) hat besondere Ansprüche an die Planetenentstehungstheorien gestellt. Die Gezeitenkräfte, welche auf die proto-planetare Scheibe aufgrund des Binärsterns wirken, verändern deren Struktur drastisch, indem sie massive Spiralarme entstehen und die Scheiben exzentrisch werden lassen. In Müller and Kley (2012) untersuchen wir dies in zwei-dimensionalen Modellen, welche die Aufheizung der Scheibe durch viskose Heizung und $p\,dV$-Arbeit sowie die Abkühlung der Scheibe durch radiative Abstrahlung mit berücksichtigen. Dabei zeigen wir, dass die Scheiben weniger exzentrisch werden als in isothermen Modellen, was die Entstehung von Planeten vereinfacht.

Diese Modellrechnungen berücksichtigen bisher nicht die Eigengravitation der Scheiben. Um diese korrekt zu behandeln, ist es nötig, die endliche Ausdehnung der Scheibe in vertikaler Richtung zu berücksichtigen. Da dies in zwei-dimensionalen Berechnungen nicht direkt möglich ist, wird das Gravitationspotential mit einem Smoothing-Parameter ϵ so ausgeschmiert, dass die Ergebnisse näherungsweise dieselben sind. Ein ähnliches Problem tritt auf, wenn man die Gravitationskräfte der Scheibe auf einen in der Scheibe eingebetteten Planeten untersucht. In Müller et al. (2012) analysieren wir dieses Problem. Wir vergleichen die realen Kräfte zwischen verschiedenen Punkten in der Scheibe bzw. von der Scheibe auf den Planeten mit den genäherten Kräften, welche durch ein ausgeschmiertes Potenzial entstehen. Wir ermitteln Werte für ϵ in Abhängigkeit des Abstandes zwischen Punkten in der Scheibe bzw. des Abstandes zum Planeten, welche die bestmögliche Approximation geben.

Bisher wurden keine Planeten in ihrer Entstehungsphase beobachtet. Transitional Disks sind proto-planetare Scheiben mit einem Loch in der Mitte, welches durch einen Planeten entstanden sein könnte. Daher sind die in letzter Zeit häufig beobachteten Transitional Disks ein heißer Kandidat für Beobachtungen von entstehenden Planeten. Obwohl diese Transitional Disks ein Loch in der Mitte haben, zeigen sie trotzdem Akkretion auf den Stern. Eine Möglichkeit, Material durch das Loch auf den Stern zu bekommen, ist mit Hilfe eines Planeten. Außerdem wird die Scheibe bei schwereren ($> 3\,M_{\mathrm{jup}}$) Planeten exzentrisch und somit kann einfacher Material durch das Loch hindurch gelangen. In Müller and Kley (2013) untersuchen wir die Akkretion durch die Scheibe auf den Stern mit isothermen und radiativen Modellen.

Alle bisher erwähnten Simulationen wurden mit dem `FARGO` Code erstellt, welcher den FARGO Algorithmus (Masset, 2000) zur Beschleunigung der Rechnungen verwendet. Die Anwendbarkeit des Algorithmus auf unsere Problemstellungen ist von Dong et al. (2011) bezweifelt worden. Die Autoren behaupten, dass sehr große Auflösungen und zusätzliche Zeitschrittkriterien notwendig wäre, um korrekte Ergebnisse zu erzielen. In Kley et al. (2012) untersuchen wir diese Bedenken und zeigen mit Hilfe von Vergleichen von fünf verschiedenen Codes, dass diese Bedenken gegenstandslos sind.

Für Planeten in Binärsternen stellt sich natürlich auch die Frage nach Habitabilität. In Müller and Haghighipour (2014) erweitern wir Arbeiten von Kaltenegger and Haghighipour (2013) und Haghighipour and Kaltenegger (2013) zur Habitabilität in Binärsternen auf Mehrsternsysteme. Wir zeigen, dass die Idee von einem inneren und äußeren Radius bei Mehrsternsystemen keinen Sinn macht und zeigen eine alternative Definition auf. Außerdem präsentieren wir eine interaktive Website zur Berechnung der habitablen Zone in Mehrsternsystemen.

Contents

1. Introduction

1.1. Solar System

The Solar System is our home and therefore the first planetary system to be known. It played an important role in the research of planet formation theories as it was the only planetary system known until about twenty years ago.

1.1.1. History

In ancient times only the inner planets Mercury and Venus and the outer planets Mars, Jupiter and Saturn have been known. They attracted attention as they were the only lights which could be seen with the naked eye that were moving on the sky in relation to all the other stars. Therefore ancient Greeks called them πλάνητες ἀστέρες (planetes asteres, "wandering stars") from which today's name planets came from. They played an important role in mythology and many of the Roman and Greek gods were named after them. In the 2nd millennium BC they were identified and studied by Babylonian astronomers (Sachs, 1974), which e.g. recorded the rise times of Venus in the *Venus tablet of Ammisaduqa* from the 7th century BC. In the 6th and 5th centuries BC the Pythagoreans in Greece developed a planetary theory in which the Earth, the Moon, the Sun and the other to date known planets are rotating around a central fire at the center of the Universe. This model was improved by Aristarchus of Samos (310 BC – ca. 230 BC) when he identified the Sun as the central fire and based on his theory invented the first heliocentric model.

By the 1st century BC the Greeks started to develop their own mathematical schemes to predict the positions of the planets. In the 2nd century CE Claudius Ptolemy (ca. 90 CE – ca. 168 CE) published the Μαθηματικὴ Σύνταξις (syntaxis mathematica) also known as the *Almagest* where he describes the motions of the stars and planets and presents his geocentric model which later has been known as the Ptolemaic system. In this geocentric model the Earth sits at the center and is orbited by the seven planets: the Moon, Mercury, Venus, the Sun, Mars, Jupiter and Saturn. The planets move on epicyclic orbits around the Earth which means that they are assumed to move in a small circle called an epicycle around a point which moves along larger circle called a deferent. As this model could explain the sometimes retrograde motion of the planets it became the dominant astronomical conception of the Universe for over 13 centuries. Figure 1.1 illustrates the model as seen in the 16th century.

During the scientific revolution which started in the 16th century Nicolaus Copernicus (1473 – 1543) revived the heliocentric model in his *De revolutionibus orbium coelestium* (On the Revolutions of the Heavenly Spheres) as the Copernican system. In his model the universe consisted of eight spheres (see Figure 1.2). In the center was the Sun followed by the planets

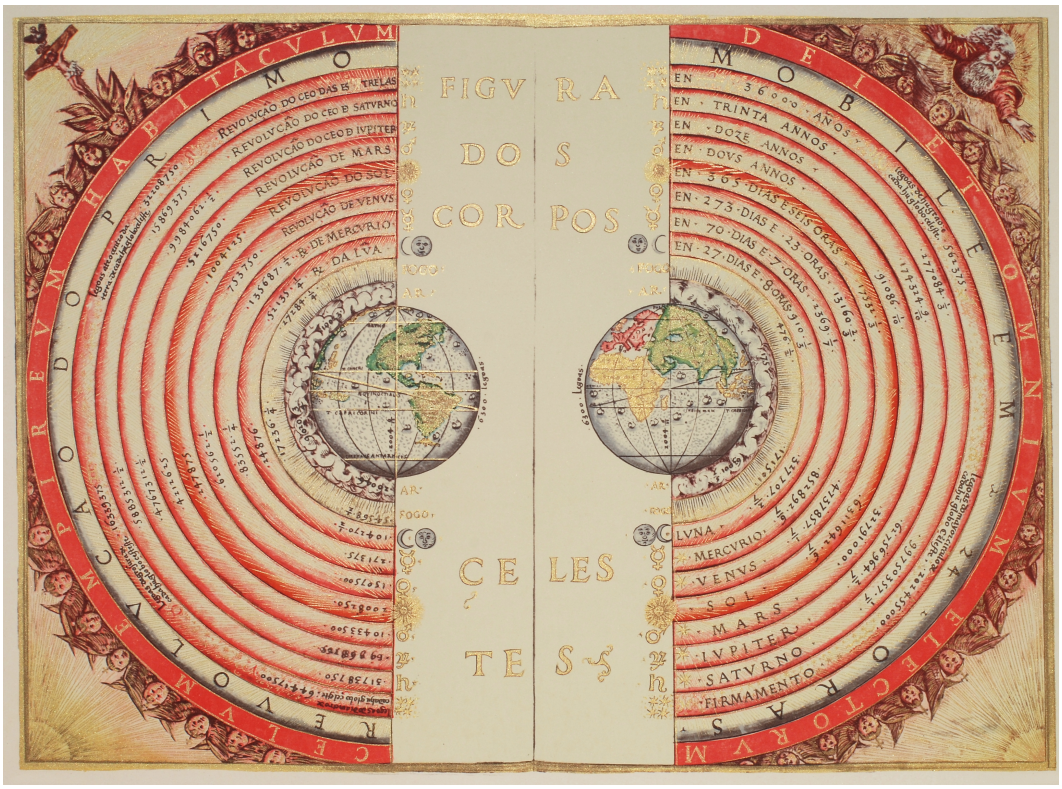

Figure 1.1.: *Figura dos corpos celestes* (Figure of the heavenly bodies) – Illuminated illustration of the Ptolemaic geocentric conception of the Universe by Portuguese cosmographer and cartographer Bartolomeu Velho (?-1568). From his work *Cosmographia*, 1568 (Bibilotèque nationale de France, Paris). Notice that the Moon and the Sun are also listed as planets which move around the Earth.

Figure 1.2.: Page 9 verso of *De revolutionibus orbium coelestium* (On the Revolutions of the Heavenly Spheres) from Nicolaus Copernicus illustrating his heliocentric system.

which were in order Mercury, Venus, Earth, Mars, Jupiter and Saturn. The Sun and the Moon are no longer planets, whereas the Earth has become one. The outermost sphere consisted of the fixed stars. The Moon has its own sphere around the Earth. As Copernicus believed that the planets are god-made their orbits must be perfect circles and therefore he still needed Ptolemy's epicircles to describe the motion of the planets. Tycho Brahe (1546 – 1601) disagreed with the idea of a moving Earth for religious and physical reasons and developed a geo-heliocentric system. In the Tychonic system, the five planets (Mercury, Venus, Mars, Jupiter and Saturn) orbit the sun, while the Sun and the Moon orbit around the Earth.

In 1609 Johannes Kepler (1571 – 1630) published his book *Astronomia nova* (A New Astronomy) were he presented his two laws of planetary motion. The first law states that the orbit of every planet is an ellipse with the Sun at one of the two foci. The second law states that a line joining a planet and the Sun sweeps out equal areas during equal intervals of time. He derived them from analysis of Mars' orbit which had been documented by Tycho Brahe. With the invention of the telescope, Galileo Galilei (1564 – 1642) discovered in 1610 the four Galilean moons of Jupiter. As they were moving very fast on a straight line very close to Jupiter and disappeared from time to time, he concluded that they were behind Jupiter and orbited him. Later that year he discovered a full set of phases of Venus which were predicted by the heliocentric system and could not be explained with the geocentric system which therefore became indefensible.

Giordano Bruno (1548 – 1600) went one step further and suggested that all the stars on the sky were suns like your own which also habit other planets. He saw the Solar System as a prototype which existed infinitely many times in the universe. He agreed with Copernicus that the Earth and the outer planets were moving around the Sun, but the Sun itself was not the center of the universe for him and the motion of the stars over the sky was an illusion created by the rotation of the Earth around its axis. Over two hundred years later in 1838 Friedrich Bessel (1784 – 1846) measured the parallax of the star 61 Cygni to be 0.314 arcseconds. This was a prove that the Earth itself must be moving and therefore the geocentric models cannot be true. The fact that the Sun itself is a star among many others became more and more obvious in the following decades.

With better optical instruments additional planets and moons were discovered in the Solar System. In 1781 William Herschel (1738 – 1822) discovered Uranus and in 1846 Neptune was discovered by Johann Galle (1812 – 1910) by looking at positions predicted by Urbain Le Verrier (1811 – 1877). Finally in 1930 Pluto was discovered by Clyde Tombaugh (1906 – 1997). In 2005 Eris was discovered and with a mass slightly larger than Pluto it would have been the tenth planet of the Solar System. This led to a discussion of the planetary status of Pluto and in 2006 Pluto was demoted to be a dwarf planet by the International Astronomical Union (IAU).

1.1.2. Present status

In 2006 the IAU released a definition of the term planet as (International Astronomical Union, 2006):

> "A 'planet' is defined as a celestial body that (a) is in orbit around the Sun, (b) has sufficient mass for its self-gravity to overcome rigid body forces so that it

Table 1.1.: Properties and orbital parameters of the planets in the Solar System.

Quantity	Mass	Radius	Semi-major axis	Eccentricity	Inclination
Unit	M_{jup}	r_{jup}	AU		°
Mercury	0.000174	0.0349	0.387	0.206	7.0
Venus	0.00256	0.0866	0.723	0.00676	3.4
Earth	0.00315	0.0911	1.00	0.0167	0.00054
Mars	0.000339	0.0485	1.53	0.0933	1.9
Jupiter	1.00	1.00	5.20	0.0485	1.3
Saturn	0.299	0.832	9.54	0.0555	2.5
Uranus	0.0457	0.362	19.2	0.0469	0.77
Neptune	0.0540	0.352	30.1	0.00895	1.8

assumes a hydrostatic equilibrium (nearly round) shape, and (c) has cleared the neighborhood around its orbit."

By this definition the Solar System consists of the Sun and eight planets. These are, in order from the innermost to the outermost: Mercury, Venus, Earth, Mars, Jupiter, Saturn, Uranus and Neptune. The four inner planets are primarily composed of rock and metal and are called *terrestrial planets*. The four outer planets are substantially more massive (see Table 1.1). Being primarily composed of Hydrogen and Helium Jupiter and Saturn are therefore called *gas giants*. Uranus and Neptune however are composed of gases with higher melting points called ices and are therefore being called *ice giants*.

All eight planets are more or less coplanar but there is a small misalignment of about 7 ° between the mean orbital plane of the planets and the Sun's equator. The planets have rather low eccentricities with the exception of Mercury having the largest one of about 0.2 (see Table 1.1). Their semi-major axis ranges from 0.38 AU for Mercury being the inner most planet up to 30.1 AU for Neptune being the outermost planet. Only Earth lies within the habitable zone which ranges from 0.97 – 1.67 AU (Kopparapu, 2013) and is defined by property that a rocky planet with a $CO_2/H_2O/N_2$ atmosphere within the habitable zone could maintain liquid water. The mass of all the planets is only about 0.13 % of the total Solar System and therefore most of the mass is concentrated in the Sun. The angular momentum of the Solar System is, in contrast to the mass, mainly in the orbital angular momentum of the planets.

Besides the eight planets there are several dwarf planets like Ceres, Eris, Haumea and Makemake. Except for Ceres all dwarf planets are trans-Neptunian objects meaning that they have larger orbits than Neptune. Ceres orbits the Sun on an orbit between Mars and Jupiter within the asteroid belt.

1.2. Extrasolar planets

The planets of the Solar System have been the only known planets for centuries. In 1992 the first extrasolar planet was discovered around the millisecond pulsar PSR B1257+12 (Wol-

szczan and Frail, 1992). Only three years later, "a Jupiter-mass companion to a solar-type star" (Mayor and Queloz, 1995) was found and triggered a gold rush for the discovery of more extrasolar planets. Since then, more than 973 extrasolar planets have been discovered by ground-based observation and by two planet-hunter missions COROT and Kepler from space. So planets around stars are nothing special anymore for the Solar System as already predicted by Giordano Bruno.

With hundreds of discoveries of extrasolar planets the International Astronomical Union convened a Working Group on Extrasolar planets. In 2001 it released a working definition of an extrasolar planet and refined it in 2003. The current working definition defines extrasolar planets as (Working Group on Extrasolar Planets, 2003):

> "1) Objects with true masses below the limiting mass for thermonuclear fusion of deuterium (currently calculated to be 13 Jupiter masses for objects of solar metallicity) that orbit stars or stellar remnants are 'planets' (no matter how they formed). The minimum mass/size required for an extrasolar object to be considered a planet should be the same as that used in our Solar System.
>
> 2) Substellar objects with true masses above the limiting mass for thermonuclear fusion of deuterium are 'brown dwarfs', no matter how they formed nor where they are located.
>
> 3) Free-floating objects in young star clusters with masses below the limiting mass for thermonuclear fusion of deuterium are not 'planets', but are 'sub-brown dwarfs' (or whatever name is most appropriate)."

1.2.1. Observational methods

Most of the extrasolar planets discovered so far cannot be directly seen through an optical telescope. The have been discovered by different indirect methods.

Radial velocity

The vast majority of the extrasolar planets discovered have been detected by the radial velocity method. When a star is orbited by one or multiple planets all objects move around the center of mass of the system. If the orbits are not in a plane perpendicular to the line of sight to the star, the star wobbles a little bit forward and backward with respect to the observer. This results in periodic shifts of the spectral lines in the spectrum of the star due to the Doppler effect, and dynamic models can be applied to the data to calculate the parameters of potential planets. As the inclination of the orbital plane is usually not known, only a lower limit of the planets masses can be calculated.

The velocities to be measured are very small. Jupiter forces the Sun to change the velocity by about $12.4\,\mathrm{m\,s^{-1}}$ over a period of 12 years and the Earth only by about $9\,\mathrm{cm\,s^{-1}}$ over a period of 1 year. Therefore long-term observations with very high spectral resolution are needed. As the Doppler spectroscopy requires high signal-to-noise ratios to achieve the high precisions needed, it is only used for nearby stars within a few hundred light years from Earth. It favors

massive planets which are close to low-mass stars as these systems have the highest radial velocities.

The first extrasolar planet discovered around a solar-type star was a massive planet ($M \sin i = 0.47\,M_{\mathrm{jup}}$) with an orbital period of 4.23 days. For this discovery the ELODIE spectrograph from the Haute-Provence Observatory in France was used, which had an precision of $13\,\mathrm{m\,s^{-1}}$. The latest instrument installed for the HARPS (the High Accuracy Radial velocity Planet Searcher) at the ESO La Sille telescope in Chile has an precision of $2.5\,\mathrm{cm\,s^{-1}}$ (Wilken et al., 2012). With this precision it now should be possible to detect Earth-like planets around solar-type stars.

Transits and transit timing variations

Transit detections build upon the effect that a planet transiting in front of a star dims the light received by an observer. This can be also seen for Mercury or Venus transiting the Sun. Stars with one or more transiting planets show periodic dips in their light curve (light intensity as a function of time). From the shape, length and periodicity of the dips in the light curve the planet's radius and orbital period can be calculated. In combination with spectroscopy even the atmosphere of the planet can be analyzed. The problem with this method is that it can only be used if the planet's orbital plane is aligned with the observer's vantage point. The probability for this is the ratio of the radius of the star to the radius of the orbit. For example a planet at a distance of 1 AU orbiting around a sun-sized star has a probability of only 0.46 %. With this method it is possible to detect planets around stars that are located thousand light years away, but as the false-detection is rather high, follow-up confirmation is needed which is usually only possible for nearer objects. This method favors large planets close to the star as they have the largest intensity decrease and can be observed more easily for multiple orbits.

If a planetary system has more than one planet, but not all of them are transiting, they still might be detectable due to transit timing variations. If a planetary system hosts more than one planet then transits are not periodic within one orbit, but change a little bit for each orbit due to the gravitational effect of the other planets. This can be also measured and used for dynamical models to calculate the parameters of additional unseen planets.

The COROT and Kepler space missions and many ground-bases projects have detected hundreds of planets using the transit and transit timing variation method.

Imaging

As planets are usually extremely faint light sources it is difficult to see them directly. It is only possible for planets that have a large separation to their host star and works best if they are hot enough to emit infrared radiation. To see the planets, the star itself has to be blocked using a coronagraph. This method works for all orientation of the planetary orbits in respect to the observer's vantage point. The orbital parameters of planets can be obtained easily with multiple observations, but statements about their size or mass are not possible and require additional observation through other methods. As the planets are spatially resolved they can be observed with spectroscopy as well to investigate the planet's atmosphere.

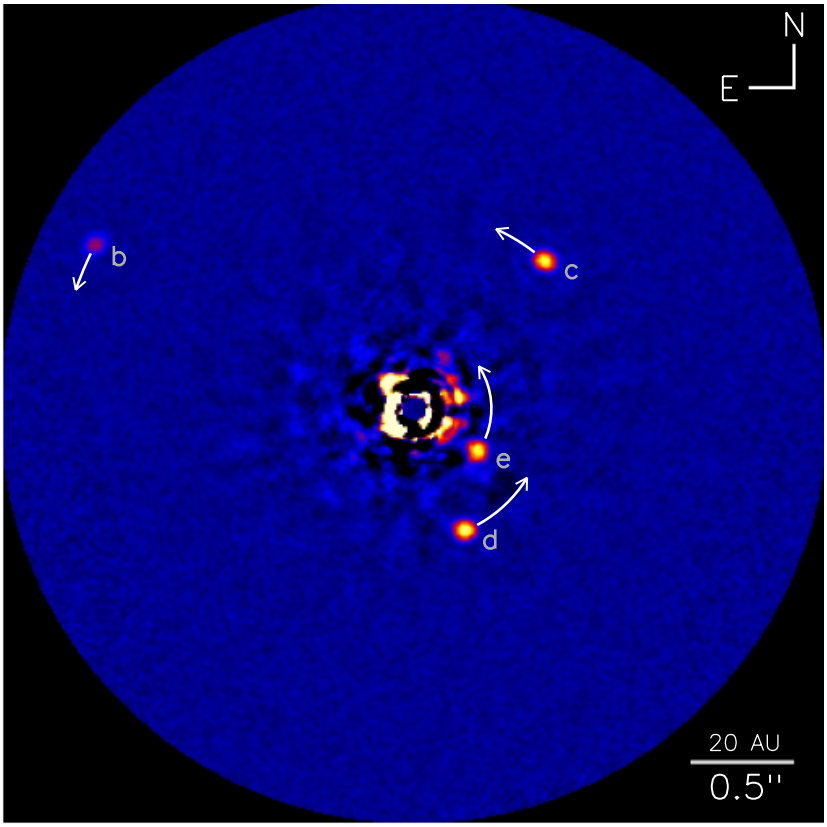

Figure 1.3.: Image of HR 8799 and its four planets in L' band at 3.776 µm. The planets are located at 68, 38, 24 and 14.5 AU. Image with permission from Ben Zuckerman.

The most impressive image of extrasolar planets (see Figure 1.3) is that of HR 8799, a star which is 39.4 parsec away and located in the Pegasus constellation. Marois et al. (2008) found three planets orbiting HR 8799 with semi-major axes of 68, 38 and 24 AU. Two years later a fourth planet at 14.5 AU was discovered (Marois et al., 2010).

Gravitational microlensing

Gravitational microlensing is an effect of general relativity. If two stars are almost exactly aligned along the line of sight, the gravitational field of the nearer star acts like a lens, magnifying the light of the distant background star. Usually these magnifications occur as short events lasting only for a few days or weeks, when Earth and the two stars are in the perfect position. If the nearer star has a planet, its gravitational field disturbs the signal like a scratch in an optical lens. This effect can be measured to detect the planet. Gravitational microlensing events have been observed over a thousand times during the last decade and over twenty planets have been detected so far. The disadvantage of this method is that the stars have to be observed for very long times until they might get into right constellation and that the detections are not reproducible as the same constellation will never appear again. And as the planets are usually kiloparsecs away it is impossible to confirm the planets using the other methods. Only the mass of the planet and its current separation to the host star can

be calculated.

Pulsar timing

A pulsar is a highly magnetized, rotating neutron star. It emits radio waves which can be only seen if the beam of emission is pointing towards Earth. As it rotates extremely regularly the light beam can be seen as a periodic light curve. If a pulsar has one or more planets it orbits around the center of mass of the planetary system. This results in a small timing variation of the periodicity of the light curve. This method can detect planets of masses down to a tenth of an Earth mass and also planets that are very far away from the pulsar. The first extrasolar planet detected was around the pulsar PSR 1257+12 (Wolszczan and Frail, 1992).

1.2.2. Diversity

One of the first questions that arose when the first extrasolar planets were discovered was how the other planetary systems compare to our own Solar System. Although there is still an observational bias in the planet discoveries due to the detection methods, it became very clear that the Solar System is not a prototype for all extrasolar planetary systems.

Figure 1.4 shows all the to date discovered extrasolar planets by their mass and semi-major axis in comparison to the planets of the Solar System. The very massive planets with masses up to tens of Jupiter masses very nearby the star at separation less than 0.1 AU, the so-called *Hot Jupiters*, are completely absent in the Solar System, but can be found very often. This is due to observational bias and correcting for it they account for about 1 % of all planets. We also find many lower mass planets with masses between one to several Earth masses, the so-called *Super Earths*, with very small orbits. It is not surprising to find many planets with small orbits as due to their short orbital period it is easier to detect them. But nevertheless it stands out that we do not have planets with this small separation within the Solar System.

Earth-mass planets at distance around 1 AU seem to be lacking in other planetary systems, but this can also be due to observational bias as it is difficult to detect low-mass planets.

There are also planets with much larger separations (up to thousands of AU) than in the Solar System.

The planets in the solar systems have, except for Mercury, more or less circular orbits with eccentricities of less than 0.09 (see Table 1.1). Figure 1.5 shows the eccentricity distribution of the extrasolar planets. It is clearly visible that eccentric orbits are a common phenomenon. As eccentric orbits occur for planets within single star systems as well, the binary companion cannot be the sole cause for the eccentricity of the orbits.

The fact that many planets are part of a multistellar, typically a binary, system is also highlighted in Figure 1.4. The planets in binary systems occur as two types. They either have so-known s-type orbits, which means that they orbit a single star (circumprimary or circumsecondary) or they have p-type orbits, which means that they orbit around both stars around their center of mass (circumbinary). Most of the planets in binaries were found in rather close binaries with separations of less than 20 AU such as γ Cephei and α Centauri or with separations of more than 100 AU.

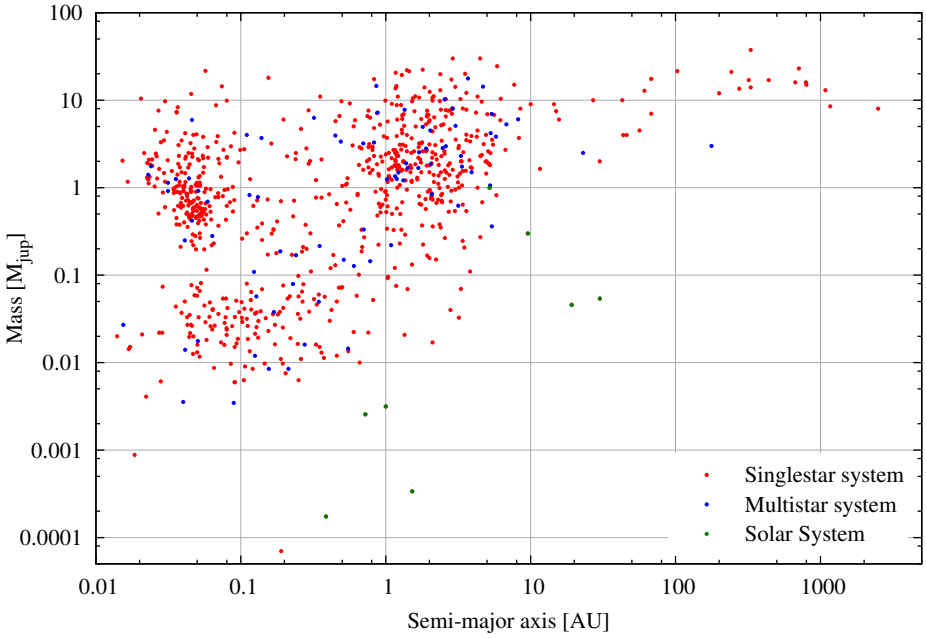

Figure 1.4.: Mass vs. semi-major axis of all to date known extrasolar planets and the planets of the Solar System. Data taken from the Open Exoplanet Catalogue (Rein, 2012).

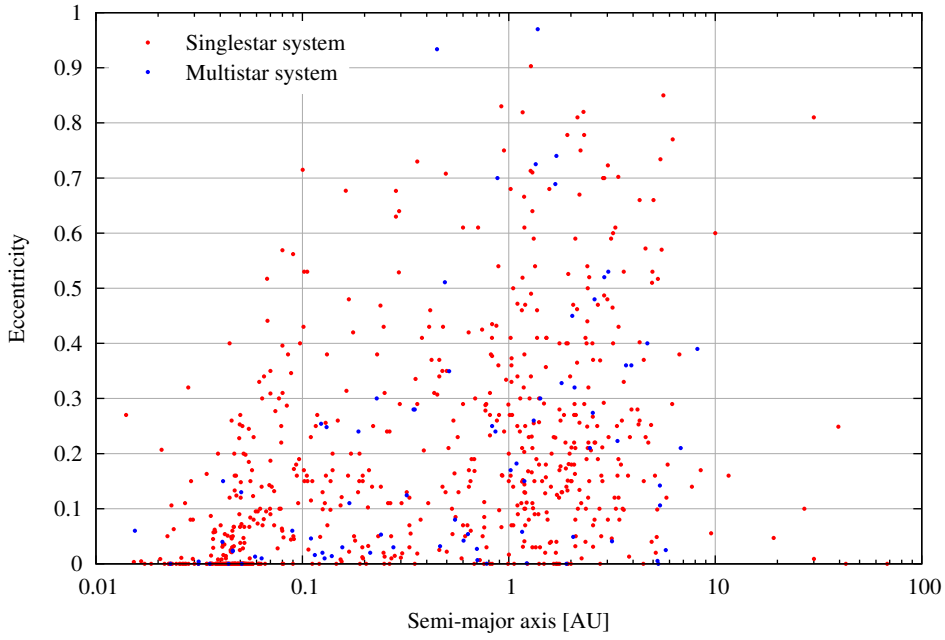

Figure 1.5.: Eccentricity vs. semi-major axis of all to date known planets for which the eccentricity is known. Data taken from the Open Exoplanet Catalogue (Rein, 2012).

1.3. Formation of planets

The first theories of planetary formation emerged in the 18th century in the context of cosmogony theories. Emmanuel Swedenborg (1688 – 1772) published his book *Opera Philosophica et Mineralia* (Philosophical and Mineralogical Works) in 1734 where he proposed the nebular hypothesis. It was further developed by Immanuel Kant (1724 – 1804) in his book *Allgemeine Naturgeschichte und Theorie des Himmels* (Universal Natural History and Theory of Heaven) from 1755. Pierre-Simon Laplace (1749 – 1827) independently proposed his version of the nebular hypothesis in the last book of his series *Exposition du systeme du monde* (The System of the World) in 1796. Both versions of the theory were combined by Arthur Schopenhauer (1788–1860) to the Kant-Laplace theory.

The idea of the nebular hypothesis is, that stars from in gaseous, massive, dense clouds mainly composed of hydrogen. They are gravitationally unstable and therefore collapse to smaller denser clumps which will become the stars. Due to conservation of angular momentum not all matter can collapse into the central object and therefore a flat disc of material, the protoplanetary or accretion disc, is left over. Within this disc the planets form due to different mechanisms. These protoplanetary disks can be observed around young stars for the first few million years of their evolution.

1.3.1. Core Accretion

The core accretion model (Mizuno, 1980; Pollack et al., 1996) is a bottom-up method for making planets and the most commonly accepted theory of planet formation. Small microscopic dust grains within the protoplanetary disk, settle to the midplane of the disk and start to collide and coagulate to larger grains due to electrostatic forces. The evolution of the particles within the disk is dominated by the gravitational field of the star and the drag forces from the surrounding gas which is assumed to be turbulent. The gravitational interaction of the particles itself is very weak and does not play an important role until the objects have grown up to km-sized objects, known as planetesimals.

When the objects reach km-size their self-gravity starts to play an important role and they start to become more roundish. With increasing size they also get less coupled to the gas and their motion is governed by mutual gravitational interaction and gravitational interaction with the star. Colliding planetesimals usually merge to a more massive planetesimal and some small fragments, resulting in net-growth. This results in a run-away growth which ends with a few massive planet cores as a left over. They have accumulated almost all planetesimals during this growth phase as they changed their orbital parameters frequently due to close encounters with other planetesimal.

Whereas in the inner regions these cores grow to terrestrial planets, they can accumulate much more mass in the colder, outer regions of the disk, where the temperature is cold enough to condense ices. When a core grows to several Earth masses it starts slowly to accrete the surrounding gas. As it gets more massive more and more gas is accreted resulting again in a run-away growth. This process is stopped when the disk has dissipated or the planet has opened a large gap within in the disk.

However there are a number of problems with this scenario. First of all small protoplanets

may undergo a rapid inward migration due to gas drag and therefore move into the central star before they reach a certain size. Also the dust grains and larger particles need to have the correct collision velocities to allow net-growth within the collisions. Last but not least the core accretion model requires a few million years to form gas giants (Alibert et al., 2004) which might be longer than the actual lifetimes of the protoplanetary disk.

1.3.2. Gravitational Instability

In contrast to the Core Accretion model in the Gravitational Instability scenario (Kuiper, 1951; Cameron, 1978; Boss, 1997) planets are formed top-down directly from the gaseous disk. It builds on the fact that a gaseous disk can become unstable if it is massive and cool enough (Toomre, 1964). In the unstable regime a gravitational instability can create local and global spiral waves with mass and angular momentum transport, and can even lead the disks to fragmentation into dense clumps. These dense clumps can become self-gravitational precursors to gas giants.

As the disk heats up during the fragmentation it must be able to cool fast enough to allow fragmentation (Gammie, 2001). This usually is true for the outer parts of the disk beyond about 50 AU where the gas is optically thin and therefore can cool on timescales less then the local period. In the inner parts the gas is optically thick and allows only inefficient cooling thus preventing fragmentation.

Thus, the problem with this scenario is the presupposition of a massive enough disk and the constraint of only forming planets in the outer disk, but these planets could migrate inwards after their formation due to the interaction with the rest of the disk. In addition the planets do not have a solid core by necessity.

1.3.3. Binary stars

Many of the stars known are actually binary or even multiple star systems. Mizar and Alcor, the first known binary star system, was already discovered in the 17^{th} century, and as of today it is actually a six star system. Stars in binary star systems can of course also host planets. Two types of configuration are distinguished:

Planets in so-called *S-type* orbits encircle only one component of a binary system. They are also known as circumprimary or circumsecondary planets. In most cases the binary system has a wide separation and the planet formation scenarios work the same way as in a single star system. However there are a few system where the binary separation is rather small (< 25 AU) like for example γ Cephei. γ Cephei is a binary system consisting of a $1.4\,M_{\odot}$ subgiant star and a $0.4\,M_{\odot}$ red dwarf with a separation of 20 AU at an eccentricity of 0.4. The system hosts an $1.6\,M_{\text{jup}}$ planet at 2 AU around the subgiant star. Planet formation is somewhat more difficult in these kind of systems (Nelson, 2000) because the companion star disturbs the protoplanetary disk and induces strong spiral arms due to its tidal forces. These spiral arms heat up the disk and make gravitational collapse unlikely (Johnson and Gammie, 2003). In addition the orbits of small particles within the protoplanetary disk are disturbed, which results in higher relative velocities between particles and thus collisions between particles are more likely disruptive (Paardekooper et al., 2008).

Planets in so-called *P-type* orbits encircle both components of a binary star system. They are also known as circumbinary planets. The stars in these systems usually have a small separation and the protoplanetary disk embraces both stars. The motion of the two stars only effects the very inner parts of the disk and thus planet formation scenarios can still work for this case.

For the writing of this introduction the *Astrophysics of Planet Formation* book by Philip J. Armitage and the English and German *Wikipedia*, especially the articles about planets, extrasolar planets and the time line of discovery of Solar System planets and their moons, have been used.

2. Overview of work

2.1. S-type planets in binaries

As of today, planets have been found in over 60 multi-star systems. The multi-star systems with planets range from binaries over triple star system such as Gliese 667 with 7 planets, which of 3 are in the habitable zone (Anglada-Escudé et al., 2012; Delfosse et al., 2013), up to even quadruple systems like KIC 4862625 (Schwamb et al., 2013).

Most of these systems are either widely separated with separations over 100 AU and have s-type planets around a single star or have a very small separation with p-type planets around two stars. There is evidence from observation for fewer planets in close binary systems which separations less than 100 AU (Eggenberger et al., 2007). This is in agreement with theory which expects that planet formation is much more challenging in close binary systems. Nevertheless, there are several systems with a close binary separation such as γ Cephei (Campbell et al., 1988; Hatzes et al., 2003), α Centauri (Dumusque et al., 2012), Gliese 86 (Queloz et al., 2000; Els et al., 2001), HD 41004 (Zucker et al., 2004) and HD 196885 (Correia et al., 2008). Planet formation theories should also provide a scenario for those systems and therefore the study of those systems is of particular importance.

Several effects change the planet formation process in these close binary star systems. The most influential may be the truncation of the disk due to the tidal torques of the companion star (Artymowicz and Lubow, 1994). The disk can only extend up to the truncation radius which depends on the mass ratio of the stars, the eccentricity of the binary system and the viscosity within the disk. The much smaller than usual disk results in several problems. The total disk mass is smaller providing less material for planet formation and the timescales within the disks are much smaller so that planet formation has much less time.

Additionally, the tidal forces excite eccentric modes in the disk (Whitehurst, 1988; Lubow, 1991; Kley et al., 2008). This effect has been recently studied in the case of planet formation by Paardekooper et al. (2008); Kley and Nelson (2008), who showed that despite the high eccentricity of a γ Cephei-type binary the disk became eccentric with an average eccentricity of about $e_{\rm disk} \approx 0.12$ and a coherent disk precession (Kley and Nelson, 2008). The disk eccentricity increases the relative encounter velocities between planetesimals (Paardekooper et al., 2008) making collisions more disruptive. This decreases the efficiency of planet formation through planetesimal collisions.

The tidal forces also induce spiral arms within the protoplanetary disk. These are strong shocks which can heat up the disk significantly. Previous simulations typically model the disk isothermally, which means that they used a fixed (in time and space) radial temperature distribution throughout the whole simulation. In Müller and Kley (2012) we extended the simulations with an energy equation. We accounted for heating through viscous dissipation and $p\,dV$ work and a local radiative cooling approach. The simulations were made for the

γ Cephei system which is known for over 25 years to host a protoplanet (Campbell et al., 1988; Hatzes et al., 2003), and the α Centauri system which is our closest neighbor in the milky way. We show that for protoplanetary disks with low viscosities ($\alpha \lesssim 0.01$) the eccentricities are much smaller ($e_{\text{disk}} \approx 0.04 - 0.06$) than in the isothermal case, resulting in better conditions for planet formation. Picogna and Marzari (2013) confirmed these smaller eccentricities in their 3D simulations.

Another effect which most simulations to-date neglect is the self-gravity of the disk. This has been analyzed by Marzari et al. (2009), who concluded that the inclusion of self-gravity leads to disks with lower eccentricity on average. However many of the simulations done are made in 2D and especially the inclusion of self-gravity is tricky as it also depends on the disk's vertical structure. To account for this, usually a Plummer form of the gravitational potential is used, which runs as $\propto (r^2+\epsilon^2)^{-1/2}$, where ϵ is called the smoothing parameter. This is also the case for the `FARGO` code (Masset, 2000) that we used with a self-gravity implementation of Baruteau (2008) which expects an $\epsilon = \epsilon(r)$. One needs to find a value or function for ϵ which produces the correct results. In Müller et al. (2012) we extend work done by Huré and Pierens (2009) for finding correct values of ϵ for self-gravitating disks and also cover the case of an embedded planet which is somewhat similar. We find that an ϵ of $1.2\,H$ is needed for best agreement with 3D simulations. This is a much higher value than most of the simulations have used and therefore previous simulations with self-gravity overestimate the effect of self-gravity.

2.2. Transitional disks

While many extrasolar planets have been detected to date, none have been observed during their formation phase. As the early stages of planet formation take place in protoplanetary disk around young stars one would expect that a forming planet shapes the structure of these disks. Thus even a not directly detectable protoplanet could be revealed by its surrounding disk structure. The most promising candidate for such findings are so-called transitional disks which show an extended inner hole in the disk which can be seen directly or by a deficiency in the IR excess in the spectral energy distribution (SED) of the star. Many of these transitional disks have been discovered in the last years, e.g. by surveys of the Spitzer Space Telescope (Muzerolle et al., 2010; Kim et al., 2013). Recent observations presented by Mayama et al. (2012) show a kind of spiral arm connecting the outer disk through the cleared area with the star. The authors claim that this indicates the probable existence of an unseen planet in the inner region.

Transitional disks show nevertheless mass accretion onto the star even though the gap or the inner hole may reduce this. The accretion rates $\dot{M}$ through the disks are, however, by an order of magnitude smaller than that of a continuous disk (Kim et al., 2013). For smaller mass planets ($< M_{\text{jup}}$) the mass accretion rate across a gap has been analyzed by Lubow and D'Angelo (2006). For larger mass planets ($> 3\,M_{\text{jup}}$) the disk become eccentric (Kley and Dirksen, 2006) which makes it easier to push material through the gap. Both studies used locally isothermal simulations. In Müller and Kley (2013) we analyzed the mass accretion in transitional disks using more realistic radiative models with stellar irradiation for a range of different planet masses. We found that for the radiative models the disk is less eccentric than in the isothermal cases and thus have lower mass accretion rates through the gap.

For the simulations in Müller and Kley (2013) we used the `FARGO` code which uses the FARGO algorithm (Masset, 2000) to speed up calculations. The applicability of this algorithm for this kind of problems has been questioned recently by Dong et al. (2011). Dong et al. claimed that a very high spatial resolution of about 256 grid cells per scale height of the disk is needed. In addition they suggest to include some gravity related timestep criterion which would result in very small time steps. This would make the use of the FARGO algorithm almost useless. We addressed those concerns in Kley et al. (2012). We adapted the setup by Dong et al. (2011) and simulated it with five different codes. Comparing different resolutions with and without the use of the FARGO algorithm we rebutted the statements by Dong et al. (2011). We also showed that an additional timestep limitation is not needed.

2.3. Habitable zones in binary stars

The question of existence of extraterrestrial life occupied humanity for centuries. One prerequisite for extraterrestrial life is the existence of a planet-like object that can host life. The definition of prerequisites for a planet to be able to host life is difficult as we could imagine life that is different to the life forms known on earth. Nevertheless astronomers stick usually to the definition that a planet is habitable if it is a rocky Earth-like planet that can maintain liquid water on its surface. The holy grail of the planet searchers is to find an Earth-mass planet around a Sun-like star in its habitable zone.

The extent of the habitable zone around a star depends on many factors. The two most important are the stellar parameters of the star, such as luminosity, temperature and spectral energy distribution, and the atmosphere of the planet. To calculate the extent of the habitable zone usually a $CO_2/H_2O/N_2$ atmosphere similar to Earth is assumed (Kasting et al., 1993). Kasting et al. used one-dimensional climate models for the planet atmosphere and calculated the size of the annulus shaped habitable zone around the Sun from 0.95 to 1.37 AU. In these models the inner edge of the habitable zone was determined by the loss of water and the outer edge by the maximum greenhouse provided by a CO_2 atmosphere. Kopparapu et al. (2013a,b) improved the model and used more accurate line data and recalculated the size of habitable zone around the Sun to range from 0.97 to 1.67 AU where the Earth lies at the inner edge of the habitable zone and Mars with its semi-major axis of 1.524 AU still lies within the habitable zone.

As planets have been found around binary and multiple stars, the question for habitability applies there as well. The calculation of the habitable zones in binary systems has been addressed recently by Kaltenegger and Haghighipour (2013) for planets on s-type orbits and Haghighipour and Kaltenegger (2013) for planets on p-type orbits. The authors adapted the one-dimensional climate models from Kopparapu et al. (2013a,b) and accounted for the stellar flux from both stars to the planet to calculate the inner and outer radii of the habitable zone. As both stars may have different spectral energy distributions they introduced a spectral weight factor for each star to account for this. As both stars move with time the habitable zone also changes with time. To illustrate this I rendered movies of the habitable zones changing over time which are presented as snapshots in the paper by Haghighipour and Kaltenegger (2013) or can be watched online at `http://astro.twam.info/hz-ptype`.

In Müller and Haghighipour (2014) we extended this approach to multiple star systems with

more than two stars. In binary systems with planets on arbitrary orbits or in multiple star systems the habitable zone is not necessarily annulus shaped and therefore the definition of an inner and outer radius of the habitable zone is obsolete. We presented an alternative way to calculate the extent of the habitable zone in multiple star systems which also works in single stars or binary systems as a special case. To simplify calculations of the habitable zone we presented an interactive website at http://astro.twam.info/hz which calculates the habitable zone of a given binary or multiple star system automatically.

3. Publications

In this chapter the publications written during my thesis are presented. They are in the order of publication date:

Müller and Kley (2012):
T. W. A. Müller, W. Kley
Circumstellar disks in binary star systems. Models for γ Cephei and α Centauri
Published in *Astronomy & Astrophysics* Volume 539, March 2012, Article A18

Müller et al. (2012):
T. W. A. Müller, W. Kley, F. Meru
Treating gravity in thin disk simulations
Published in *Astronomy & Astrophysics* Volume 541, May 2012, Article A123

Kley et al. (2012):
W. Kley, T. W. A. Müller, S. M. Kolb, P. Benitez-Llambay, F. Masset
Low-mass planets in nearly inviscid disks: Numerical treatment
Published in *Astronomy & Astrophysics* Volume 546, October 2012, Article A99

Müller and Kley (2013):
T. W. A. Müller, W. Kley
Modelling accretion in transitional disks
Published in *Astronomy & Astrophysics* Volume 560, December 2013, Article A40

Müller and Haghighipour (2014):
T. W. A. Müller, N. Haghighipour
Calculating the Habitable Zone of Multiple Star Systems
Published in *The Astrophysical Journal* Volume 782, February 2014, Article 26

A&A 539, A18 (2012)
DOI: 10.1051/0004-6361/201118202

Astronomy & Astrophysics

Circumstellar disks in binary star systems

Models for γ Cephei and α Centauri

T. W. A. Müller and W. Kley

Institut für Astronomie & Astrophysik, Universität Tübingen, Auf der Morgenstelle 10, 72076 Tübingen, Germany
e-mail: Tobias_Mueller@twam.info

Received 4 October 2011 / Accepted 2 December 2011

ABSTRACT

Context. As of today, over 50 planetary systems have been discovered in binary star systems, some of which have binary separations that are smaller than 20 AU. In these systems the gravitational forces from the binary have a strong influence on the evolution of the protoplanetary disk and hence the planet formation process.
Aims. We study the evolution of viscous and radiative circumstellar disks under the influence of a companion star. We focus on the eccentric γ Cephei and α Centauri system as examples and compare disk quantities such as disk eccentricity and precession rate to previous isothermal simulations.
Methods. We performed two-dimensional hydrodynamical simulations of the binary star systems under the assumption of coplanarity of the disk, host star and binary companion. We used the grid-based, staggered mesh code FARGO with an additional energy equation to which we added radiative cooling based on opacity tables.
Results. The eccentric binary companion perturbs the disk around the primary star periodically. Upon passing periastron, spirals arms are induced that wind from the outer disk towards the star. In isothermal simulations this results in disk eccentricities up to $e_{\rm disk} \approx 0.2$, but in more realistic radiative models we obtain much smaller eccentricities of about $e_{\rm disk} \approx 0.04-0.06$ with no real precession. Models with varying viscosity and disk mass indicate that disks with less mass have lower temperatures and higher disk eccentricity.
Conclusions. The fairly high disk eccentricities, as indicated in previous isothermal disk simulations, implied a more difficult planet formation in the γ Cephei system caused by the enhanced collision velocities of planetesimals. We have shown that under more realistic conditions with radiative cooling the disk becomes less eccentric and thus planet formation may be made easier. However, we estimate that the viscosity in the disk has to very low, with $\alpha \lesssim 0.001$, because otherwise the disk's lifetime will be too short to allow planet formation to occur along the core instability scenario. We estimate that the periodic heating of the disk in eccentric binaries will be observable in the mid-IR regime.

Key words. accretion, accretion disks – protoplanetary disks – hydrodynamics – radiative transfer – methods: numerical – planets and satellites: formation

1. Introduction

Presently, about 50 planets are known to reside in binary stars systems. In all systems with solar-type stars the planet orbits one of the stars while the secondary star acts as a perturber, i.e. these are in a so-called S-type configuration (Dvorak 1986). Recently, planets seem to have been detected in evolved binary star systems that are in a circumbinary (P-type) configuration (e.g. Beuermann et al. 2011). The main observational characteristic of the known planets in binary stars system have been summarized by Eggenberger et al. (2004); Raghavan et al. (2006); Desidera & Barbieri (2007). Most planets are in binaries with very large separations with semi-major axis beyond 100 AU, in particular when detected by direct imaging. Observationally, there is evidence for fewer planets in binaries with a separation of less than about 100 AU (Eggenberger et al. 2007), in accordance with the expectation that binarity constitutes a challenge to the planet formation process. Despite this, there are several systems with a quite close binary separation such as γ Cephei (Campbell et al. 1988), Gliese 86 (Queloz et al. 2000; Els et al. 2001), HD 41004 (Zucker et al. 2004), and HD 196885 (Correia et al. 2008).

As known from several theoretical studies, the presence of the secondary renders the planet formation process more difficult than around single stars. Owing to the gravitational disturbance, the protoplanetary disk is hotter and dynamically more excited such that the coagulation and growth process of planetesimals as well as the gravitational instability process in the early phase of planet formation are hindered (Nelson 2000; Thébault et al. 2004, 2006). This is particularly true for the mentioned closer binaries with an orbital separation of about 20 AU. Hence this theoretical challenge has put these tighter binaries into the focus of studies on planet formation in binary stars (Quintana et al. 2007; Paardekooper et al. 2008; Kley & Nelson 2008) and on their dynamical stability (Dvorak et al. 2004; Haghighipour 2006). The most famous example in this category is the γ Cephei system, which has been known for over 20 years to contain a protoplanet (Campbell et al. 1988; Hatzes et al. 2003). In recent years the orbital parameter of this system have been updated (Neuhäuser et al. 2007; Torres 2007) and the basic binary parameters are quoted in Table 2 (below) because γ Cephei is our standard model. At the end of the paper we will briefly discuss the α Centauri system as well.

Because planet formation occurs in disks, their dynamical structure is of crucial importance in estimating the efficiency of planetary growth processes. The prime effect of the secondary star is the truncation of the disk owing to tidal torques

(Artymowicz & Lubow 1994). The truncation radius depends on the mass ratio of the binary, its eccentricity and the viscosity in the disk. An additional effect, namely the excitation of eccentric modes in the disk, which has been noticed previously in close binary stars (Whitehurst 1988; Lubow 1991; Kley et al. 2008), has recently drawn attention in studies of planet harboring binary stars as well (Paardekooper et al. 2008; Kley & Nelson 2008). In these studies it was shown that despite the high eccentricity of a γ Cephei type binary the disk became eccentric with an average eccentricity of about $e_{\rm disk} \approx 0.12$ and a coherent disk precession (Kley & Nelson 2008). However, this leaves the question of numerical effects (Paardekooper et al. 2008). Subsequently the influence of self-gravity of the disk has been analyzed by Marzari et al. (2009a), who concluded that the inclusion of self-gravity leads to disks with lower eccentricity on average.

Interestingly, there may be observational evidence for tidal interactions between a companion on an eccentric orbit and a circumstellar disk around the primary star (van Boekel et al. 2010), as inferred from variable brightness on longer timescales. The possibility to detect an eccentric disk through spectral line observations has been analyzed recently by Regály et al. (2011).

In all simulations mentioned above, the disk has typically been modeled using a fixed radial temperature distribution. This simplifies the numerics such that no energy equation has to be solved but of course it lacks physical reality. In this work we will extend previous studies and consider a much improved treatment of the energy equation. We will do so within the two-dimensional, flat-disk approximation following D'Angelo et al. (2003) and Kley & Crida (2008). Here, the viscous heating of the disk and the radiative losses are taken into account. We will study the structure and dynamical evolution of disks with different masses and binary parameter, and will analyze the influence of numerical aspects, in particular boundary conditions. Our first target of interest will be the well-studied system γ Cephei and we will present results on the α Centauri system subsequently.

2. Model setup

We assumed that the complete system of primary star, circumstellar disk and secondary star is coplanar. Consequently, in our calculations we assumed a flat two-dimensional disk orbiting the primary. The disk is modeled hydrodynamically, under the assumption that the action of the turbulence can be described by a standard viscous stress tensor.

2.1. Physics and equations

We used cylindrical coordinates (r, φ, z) centered on the primary star where the disk lies in the equatorial, $z = 0$ plane. Because our model is two-dimensional (r, φ), we solved the vertically integrated versions of the hydrodynamical equations. In this approximation the continuity equation is

$$\frac{\partial \Sigma}{\partial t} + \nabla \cdot (\Sigma \boldsymbol{v}) = 0, \tag{1}$$

where $\boldsymbol{v} = (v_r, v_\varphi) = (v, \Omega r)$ is the velocity, and $\Sigma = \int_{-\infty}^{\infty} \rho \, \mathrm{d}z$ the surface density. As indicated, in the following we will also use v and $r\Omega$ for the radial and orbital velocity, respectively. The vertically integrated equation of radial motion is then

$$\frac{\partial (\Sigma v)}{\partial t} + \nabla \cdot (\Sigma v \boldsymbol{v}) = \Sigma r \Omega^2 - \frac{\partial p}{\partial r} - \Sigma \frac{\partial \Psi}{\partial r} + f_r, \tag{2}$$

and for the azimuthal component

$$\frac{\partial (\Sigma r^2 \Omega)}{\partial t} + \nabla \cdot (\Sigma r^2 \Omega \boldsymbol{v}) = -\frac{\partial p}{\partial \varphi} - \Sigma \frac{\partial \Psi}{\partial \varphi} + r^2 f_\varphi. \tag{3}$$

Here p is the vertically integrated pressure, Ψ the gravitational potential of both stars, and f_r and f_φ describe the radial and azimuthal forces due to the disk viscosity (Masset 2002). Owing to the motion of the primary star around the center of mass of the binary, the coordinate system is non-inertial, and indirect terms were included in the equations of motion to account for this. These are included in the potential Ψ. The gravitational influence of the disk on the binary is neglected, and the disk in non-self-gravitating. The vertically integrated energy equation reads

$$\frac{\partial e}{\partial t} + \nabla (e \boldsymbol{v}) = -p \nabla \cdot \boldsymbol{v} + Q_+ - Q_-, \tag{4}$$

where e is the internal energy density, Q_+ the heating source term and Q_- the cooling source term. To obtain a fully determined system, we additionally used the ideal gas law

$$p = \mathcal{R} \Sigma T = (\gamma - 1) e, \tag{5}$$

where T is the temperature in the midplane of the disk, γ the adiabatic index and $\mathcal{R}$ the universal gas constant divided by the mean molecular mass, which can be calculated by $\mathcal{R} = k_{\rm B}/(\mu m_{\rm u})$, where $k_{\rm B}$ is the Boltzmann constant, μ the mean molecular weight and $m_{\rm u}$ the unified atomic mass unit.

The adiabatic sound speed $c_{\rm s}$ within the disk is then given as

$$c_{\rm s} = \sqrt{\gamma \frac{p}{\Sigma}} = \sqrt{\gamma}\, c_{\rm s,iso}, \tag{6}$$

where $c_{\rm s,iso} = \sqrt{p/\Sigma}$ is the isothermal sound speed. The vertical pressure scale height H is then

$$H = \frac{c_{\rm s,iso}}{\Omega_K} = \frac{c_{\rm s}}{\sqrt{\gamma}\,\Omega_{\rm K}} = \frac{c_{\rm s}}{\sqrt{\gamma}\, v_{\rm K}} r = hr, \tag{7}$$

where $\Omega_{\rm K}$ denotes the Keplerian angular velocity around the primary and h the aspect ratio.

For the heating term Q_+ we assumed that this is solely given by viscous dissipation, and it then is given by

$$Q_+ = \frac{1}{2\nu\Sigma} \left[\sigma_{rr}^2 + 2\sigma_{r\varphi}^2 + \sigma_{\varphi\varphi}^2 \right] + \frac{2\nu\Sigma}{9} (\nabla \boldsymbol{v})^2, \tag{8}$$

where ν is the kinematic viscosity and σ denotes the viscous stress tensor, to be written in polar coordinates. The viscosity ν is given by $\nu = \alpha c_{\rm s} H$ (Shakura & Sunyaev 1973).

The cooling term Q_- describes the radiative losses from the lower and upper disk surface, which can be written as

$$Q_- = 2\sigma_{\rm R} \frac{T^4}{\tau_{\rm eff}}, \tag{9}$$

where $\sigma_{\rm R}$ is the Stefan-Boltzmann constant and $\tau_{\rm eff}$ an effective optical depth. We followed the approach of Kley & Crida (2008) and write, according to Hubeny (1990),

$$\tau_{\rm eff} = \frac{3}{8}\tau + \frac{\sqrt{3}}{4} + \frac{1}{4\tau + \tau_{\rm min}}. \tag{10}$$

The optical depth follows from $\tau = \int \rho \kappa \mathrm{d}z$, that can be approximated by $\tau \approx \rho \kappa H$ where ρ and $\kappa(\rho, T)$ are evaluated at the disk's

Table 1. Details of the various opacity regimes by type, showing the transition temperature and the constants κ_0, a and b.

#	Regime	κ_0 [cm^2/g]	a	b	$T_{\min}$ [K]	$T_{\max}$ [K]
1	Ice grains	2×10^{-4}	0	2	0	170
2	Sublimation of ice grains	2×10^{16}	0	−7	170	210
3	Dust grains	5×10^{-3}	0	1	210	$4.6 \times 10^3 \rho^{\frac{1}{15}}$
4	Sublimation of dust grains	2×10^{34}	$\frac{2}{3}$	−9	$4.6 \times 10^3 \rho^{\frac{1}{15}}$	3000
5	Molecules	2×10^{-8}	$\frac{2}{3}$	3	3000	$1.1 \times 10^4 \rho^{\frac{1}{21}}$
6	Hydrogen scattering	1×10^{-36}	$\frac{1}{3}$	10	$1.1 \times 10^4 \rho^{\frac{1}{21}}$	$3 \times 10^4 \rho^{\frac{4}{75}}$
7	bound-free & free-free	1.5×10^{20}	1	$-\frac{5}{2}$	$3 \times 10^4 \rho^{\frac{4}{75}}$	—

Notes. All values are quoted in cgs units. See Lin & Papaloizou (1985) for more details.

midplane. The vertical density profile of a disk is approximately given by a Gaussian and hence

$$\Sigma = \sqrt{2\pi}\,\rho H. \tag{11}$$

To account for the drop of opacity with vertical height we introduced a correction factor c_1 and write finally

$$\tau = \frac{c_1}{\sqrt{2\pi}}\,\kappa\Sigma. \tag{12}$$

The constant $c_1 = \frac{1}{2}$ is obtained by comparing two-dimensional disk models with the fully three-dimensional calculations as presented in Kley et al. (2009). For the Rosseland mean opacity κ we adopted power-law dependencies on temperature and density described by Lin & Papaloizou (1985) and Bell & Lin (1994), where

$$\kappa = \kappa_0 \rho^a T^b \tag{13}$$

for various opacity regimes. Each opacity regime is described by a minimum temperature $T_{\min}$ and maximum temperature $T_{\max}$, which depends on the density ρ. Table 1 lists the constants κ_0, a and b for each regime of the Lin & Papaloizou model. The temperature and density are taken from the midplane, where the density ρ is obtained from Eq. (11).

In our model we did not consider presently any radiation transport within the disk plane. This contribution is potentially important when strong gradients in temperature and density occur. In our situation this may be the case around the periastron phase of the binary. However, in our simulations the observed contrast did not seem strong enough and we did not expect a large impact on the evolution. In subsequent studies we plan to investigate this question further.

Because we are interested in the global evolution of the disk, we measured the disk eccentricity $e_{\rm disk}$ and the disk periastron $\varpi_{\rm disk}$ by first calculating for each grid cell the eccentricity vector $\boldsymbol{e}$, which is defined by

$$\boldsymbol{e} = \frac{\boldsymbol{v}\times\boldsymbol{j}}{GM} - \frac{\boldsymbol{r}}{|\boldsymbol{r}|}, \tag{14}$$

where $\boldsymbol{j} = \boldsymbol{r}\times\boldsymbol{v}$ is the specific angular momentum, G the gravitational constant, M the total mass and $\boldsymbol{r}$ the relative vector. In our two-dimensional case the specific angular momentum only has a component in z direction and therefore the eccentricity e and the longitude of periastron ϖ follow as

$$e = |\boldsymbol{e}| = \sqrt{e_x^2 + e_y^2} \tag{15}$$

$$\varpi = \mathrm{atan2}(e_y, e_x). \tag{16}$$

The global disk eccentricity $e_{\rm disk}$ and disk periastron $\varpi_{\rm disk}$ is then calculated by a mass-weighted average over the whole disk,

$$e_{\rm disk} = \left[\int_{r_{\min}}^{r_{\max}}\int_0^{2\pi} \Sigma e\, r\,\mathrm{d}\varphi\,\mathrm{d}r\right] \times \left[\int_{r_{\min}}^{r_{\max}}\int_0^{2\pi} \Sigma\, r\,\mathrm{d}\varphi\,\mathrm{d}r\right]^{-1} \tag{17}$$

$$\varpi_{\rm disk} = \left[\int_{r_{\min}}^{r_{\max}}\int_0^{2\pi} \Sigma\varpi\, r\,\mathrm{d}\varphi\,\mathrm{d}r\right] \times \left[\int_{r_{\min}}^{r_{\max}}\int_0^{2\pi} \Sigma\, r\,\mathrm{d}\varphi\,\mathrm{d}r\right]^{-1} \tag{18}$$

where the integrals are evaluated by summation over all grid cells.

2.2. Numerical considerations

The simulations were performed using the FARGO code (Masset 2000) with modifications from Baruteau (2008). The numerical method used in FARGO is a staggered mesh finite difference method. It uses operator splitting and a first-order integrator to update to velocities with the source terms (potential and pressure gradients, viscous and centrifugal accelerations). The advective terms are treated by a second-order upwind algorithm (van Leer 1977). To speed up calculations the code uses the FARGO algorithm (Masset 2000). The algorithmic details of the FARGO code have been described in Masset (2000). Because the FARGO code is based on ZEUS-2D, the basic techniques are described in Stone & Norman (1992).

The position of the secondary star is calculated by a fifth-order Runge-Kutta algorithm. To smooth shocks we used the artificial viscosity described by Stone & Norman (1992) in our simulations.

To test the code we checked that we obtained the same results when using a corotating coordinate system. In addition, several test calculations were made using the RH2D code (Kley 1989, 1999) to assure that we implemented everything correctly.

To avoid numerical problems, we implemented a surface density floor of $\Sigma_{\rm floor} = 10^{-7} \times \Sigma_0$ where $\Sigma_0 = \Sigma(1\,\mathrm{AU})|_{t=0}$ and a temperature floor of $T_{\rm floor} = 3\,\mathrm{K}$, which is about the temperature of the cosmic background radiation. In addition to the physical motivation for the floor, very low temperatures only occur in the very outer parts of the disk (see e.g. Fig. 3) where there is only very little mass that influences the dynamics of the disk. For the same reason, these cells do not contribute to the mass weighted average of the disk eccentricity. We performed test simulations with a very low temperature floor and obtained identical results.

For the simulations we typically used two boundary conditions. The open boundary condition allows outflow, but no inflow

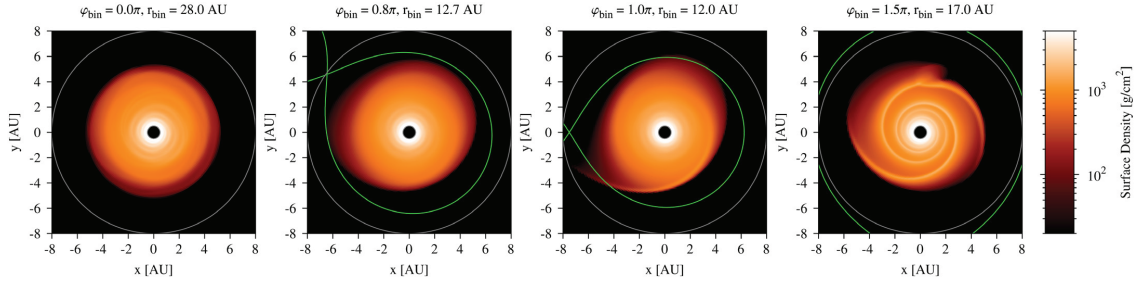

Fig. 1. Evolution of the disk within one binary period for the fully radiative standard model. The top labels in the four panels state the current position of the binary (r_{bin}, φ_{bin}) in polar coordinates. In the *first* panel the binary companion is at the apastron and has less influence on the disk. The L_1 point in this configuration is at about 17.5 AU and therefore far outside the computational domain (gray circles). In the *second* panel the binary has reduced its distance to about 12.8 AU and the Roche lobe (green curve) has shrunken dramatically and is now entirely within the computational domain. The *third* panel shows the disk with the binary at periastron. Some of the material in the disk is now outside the Roche lobe and might be lost from the system. In the *last* panel the binary's separation increases again, which makes the Roche lobe grow such that it engulfs the disk entirely. The strong tidal forces near periastron induce spiral waves in the disk that will be damped out until the binary is at apastron.

of material. It is implemented as a zero-gradient outflow condition, which reads at R_{min} as

$$\begin{aligned}\Sigma_{0j} &= \Sigma_{1j}\\ e_{0j} &= e_{1j}\\ v_{0j} &= v_{1j} = 0 \text{ if } v_{2j} > 0 \text{ and } v_{2j}, \text{ otherwise,}\end{aligned}$$

where the index 0 denotes the first inner radial ghost cells, e.g. Σ_{1j} is the first active cell in radial and the jth cell in azimuthal direction. Alternatively, the reflecting boundary condition denies exchange of quantities with the system as is implemented at R_{min} as

$$\begin{aligned}\Sigma_{0j} &= \Sigma_{1j}\\ e_{0j} &= e_{1j}\\ v_{0j} &= v_{2j}\\ v_{1j} &= 0\end{aligned}$$

and similarly at R_{max}. For the outer radial boundary we always used the standard outflow condition, while at R_{min} we typically used the reflecting condition. Below, we will investigate a possible influence of the numerical inner boundary condition.

3. The standard model

For our simulations we constructed a standard reference model using the physical parameter of the γ Cephei system. The first entries of Table 2 list the orbital parameter of this standard model based on the observations of Neuhäuser et al. (2007) and Torres (2007).

The disk parameters where chosen to be in a typical range for a possible disk around γ Cephei A, with a total mass that would allow for the formation of the observed planet of about 1.85 M_{Jup} (Endl et al. 2011) in the system. Because the tidal forces of the secondary limits the radial extent of the disk to about 6 AU (Artymowicz & Lubow 1994) we chose a slightly larger extent of the computational domain to 8 AU. This reduces artificial boundary effects. The initial density distribution is limited to 6 AU. For the outer boundary condition we always used the zero-gradient outflow boundary condition so that the material that is accelerated during periastron may leave the system freely.

Table 2. Parameters of the standard model. The top entries refer to the fixed binary parameter.

Primary star mass ($M_{primary}$)	1.4 $M_\odot$
Secondary star mass ($M_{secondary}$)	0.4 $M_\odot$
Binary semi-major axis (a)	20 AU
Binary eccentricity (e_{bin})	0.4
Binary orbital period (P_{bin})	66.6637 a
Disk mass (M_{disk})	0.01 $M_\odot$
Viscosity (α)	0.01
Adiabatic index (γ)	7/5
Mean-molecular weight (μ)	2.35
Initial density profile (Σ)	$\propto r^{-1}$
Initial temperature profile (T)	$\propto r^{-1}$
Initial disk aspect ratio (H/r)	0.05
Grid ($N_r \times N_\varphi$)	256×574
Computational domain ($R_{min} - R_{max}$)	0.5–8 AU

Notes. The following give the disk properties, and then the initial disk setup and the computational parameter are given.

The inner boundary in the standard model is typically reflecting. The resolution of the logarithmic grid is trimmed to have quadratic cells ($r\Delta\varphi/\Delta r \approx 1$).

After the initial setup at time zero, the models have to run for several binary orbits until a quasistationary state has been reached, see also Kley & Nelson (2008). This equilibration process typically takes about 15 binary periods, i.e. 1000 years for fully radiative models. Afterward the disk cycles through several states during one orbital period of the binary displayed in Fig. 1. When the binary is at apastron, the the disk is very axisymmetric, but when the binary moves toward its periastron, it starts to perturb the disk. After the binary passes its periastron, two strong tidal spiral arms develop within the disk and wind themselves to the center of the disk. Before the binary reaches its apastron, the disk spiral arms disappear. Periastron passages are also the time when most of the disk mass is lost. During the first periapse the disk looses 4.8% of its mass. This decreases during the next ten periapsis passes to about 0.1%. At the end of the simulation after 200 binary orbits, the disk mass has reduced to 0.0073 $M_\odot$, which is a loss of about 20%.

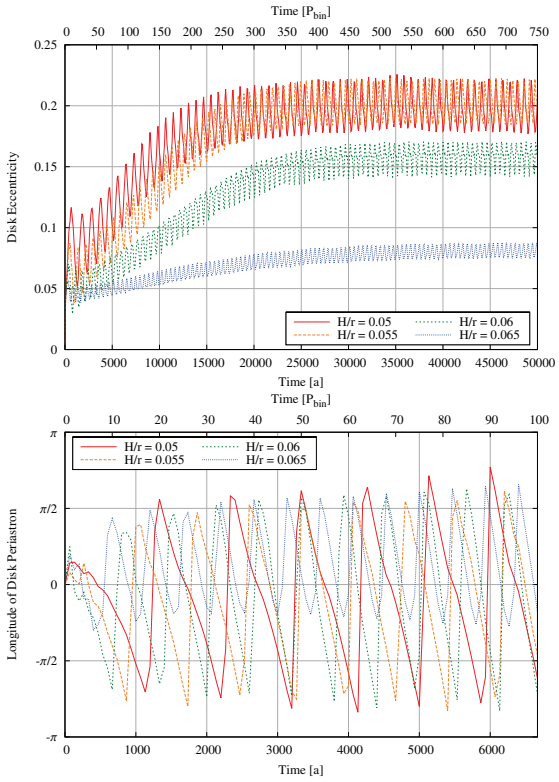

Fig. 2. Global mass-weighted disk eccentricity (*top*) and disk periastron (*bottom*), both sampled at the binary's apastron, for *isothermal* simulations of the standard model with different aspect ratios H/r. The disk eccentricity needs quite a long time to reach a quasi-equilibrium and settles at around 0.2 for an H/r of 0.05 and 0.055. High values of H/r result in a lower disk eccentricity. Note that in the lower panel a short time span is displayed for clarity.

3.1. Isothermal runs

To check our results and compare them with previous results, we first performed simulations where we kept the initial temperature stratification. In Fig. 2 we present results for constant H/r disks where we did not solve the energy equation. Shown are results for four different values of H/r, which were chosen according to our fully radiative results (see below). The disk reaches an equilibrium state after many (typically several 100) binary orbits, and the magnitude of the final average eccentricity depends on the temperature of the disk. In particular, for the disks with an H/r of about 0.05 the disk eccentricity settles at fairly high values of about 0.2. This seems to be higher than in previous simulations performed by Kley & Nelson (2008), but the parameters used for the γ Cephei system, in particular the mass ratio $q = M_{\rm secondary}/M_{\rm primary}$ of the host star and the binary companion (their $q = 0.24$ instead of our $q = 0.29$), and the binary eccentricity $e_{\rm bin}$ ($e_{\rm bin} = 0.36$ instead of $e_{\rm bin} = 0.4$) are different. Using the (older) system parameters as given by Kley et al., we were able to reproduce the results nicely (e.g. their Fig. 4).

In these isothermal runs it is clear that the two thicker, hotter disks have significantly lower mean eccentricities. The disk with $H/r = 0.065$ does not even display a coherent disk precession any more (Fig. 2, bottom panel). This drop of $e_{\rm disk}$ with increasing H/r is a consequence of the reduction of the eccentricity growth rate for thicker disks. The growth rate of the disk eccentricity is the lowest for the hottest disk with $H/r = 0.065$ and increases with decreasing H/r (Fig. 2, top panel), a finding that perfectly agrees with Kley et al. (2008). The hotter disks need therefore much more time to reach an equilibrium state. As the eccentric binary damps the growth of disk eccentricity by tidal interaction (see below), the hotter disks settle into an equilibrium state that has a lower $e_{\rm disk}$.

Table 3. Time average of the disk eccentricity $\langle e_{\rm disk}\rangle$ and precession rate $\bar{\varpi}_{\rm disk}$ for the four different *isothermal* models.

H/r	$\langle e_{\rm disk}\rangle$	$\bar{\varpi}_{\rm disk}$ $[P_{\rm bin}^{-1}]$
0.05	0.19803 ± 0.00085	−0.0844 ± 0.0018
0.055	0.20200 ± 0.00076	−0.1082 ± 0.0017
0.06	0.15800 ± 0.00054	−0.1172 ± 0.0063
0.065	0.08004 ± 0.00031	−0.1334 ± 0.0025

After about 400 binary periods, i.e. 25 000 years, the time average of the disk eccentricity $\langle e_{\rm disk}\rangle$ reaches a constant value and the disks precess with a nearly constant precession rate $\bar{\varpi}_{\rm disk}$. The values of $\langle e_{\rm disk}\rangle$ and $\bar{\varpi}_{\rm disk}$ for the four different values of H/r are given in Table 3.

3.2. Fully radiative disks: structure and dynamics

Now we include all physics, in particular the viscous heating and radiative cooling terms and solve the full set of equations as stated above. For given binary parameter and disk physics (opacity and viscosity) the dynamical state and structure of the disk is completely determined once the disk mass has been specified. The density and temperature distribution cannot be stated freely and hence the power law given in Table 2 refers only to the initial setup.

The radial disk structure is displayed in Fig. 3 where azimuthally averaged quantities of Σ, T and $e_{\rm disk}$ are displayed. The upper panel of Fig. 3 shows the surface density and temperature distribution for five different timestamps. For the initial setup, at $t = 0$ years, the surface density follows the initial r^{-1} profile in the inner region (0.5 AU–5 AU) and is lowered to the density floor in the outer region. The temperature follows the initial r^{-1} profile for the whole computational domain. After about 25 binary orbits a quasistationary state is reached where the profiles show a bend at about $r = 1.8$ AU. This change in slope, which occurs at a temperature of about 1000 K in the profiles, is a result of a change in the opacity caused by the sublimation of dust grains, which starts at about $(\rho\,{\rm g}^{-1}\,{\rm cm}^3)^{1/15} \times 4.6 \times 10^3$ K in the opacity tables (see Table 1) given by Lin & Papaloizou (1985). A second bend occurs at about $r = 4.5$ AU, which corresponds to the truncation radius of the companion's tidal forces. In the bottom panel of Fig. 3 the corresponding radial distribution of eccentricity is shown. The eccentricity is low in the inner parts of the disk and increases with larger radii. The highest values for $e(r)$ occur in the outer region $r \gtrsim 5.5$ AU, beyond the tidal truncation radius. But these regions do not play an important dynamical role because there is only very little mass left owing to the tidal forces of the secondary star. For example, the disk has a mass-weighted mean overall disk eccentricity of $e_{\rm disk} = 0.032$ after 100 binary orbits even though more than half of the radial extent of the disk has an eccentricity of ≥0.05. Remarkably the eccentricity is much lower than in the isothermal simulations

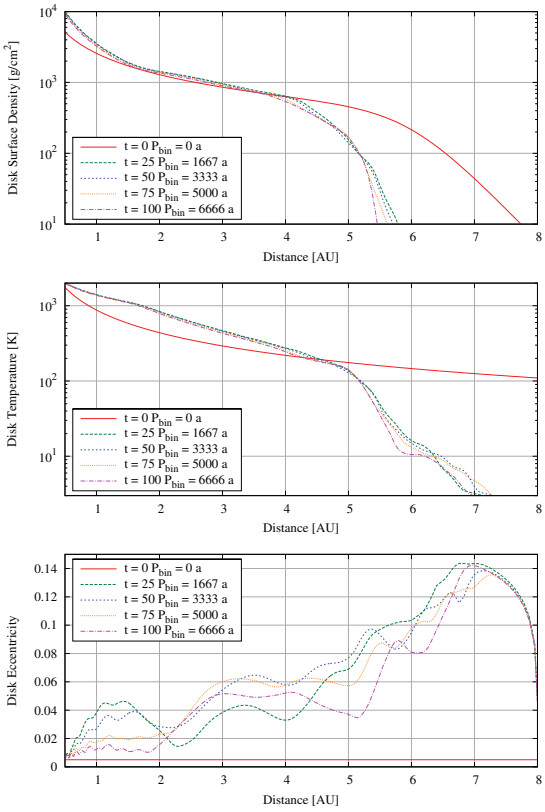

Fig. 3. Radial dependency of surface density (*top*), midplane temperature (*middle*) and disk eccentricity (*bottom*) of the *fully radiative* standard model for different timestamps. The disk ranges from 0.5 AU to about 5.5–6 AU due to tidal forces of the companion. At $t = 0$ years the disk is not fully Keplerian and thus $e_{\rm disk} > 0$.

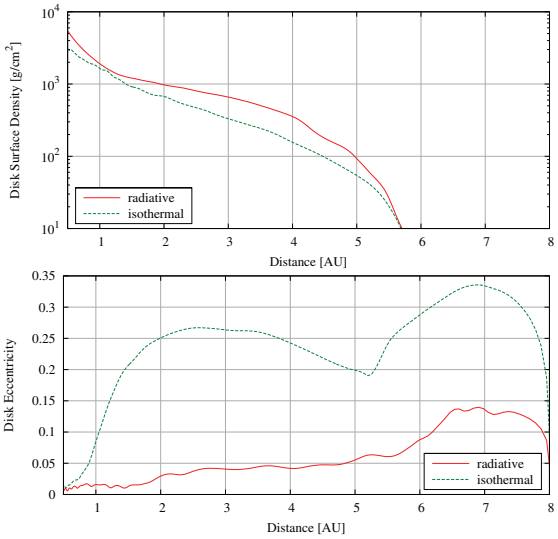

Fig. 4. Radial dependency of surface density (*top*), and disk eccentricity (*bottom*) of the $H/r = 0.05$ *isothermal* model and the *fully radiative* standard model after 750 binary orbits.

presented in Sect. 3.1. As a consequence of the lack of eccentricity there is not visible disk precession.

Figure 3 shows the radial dependency of the disk surface density and disk eccentricity of the $H/r = 0.05$ model in equilibrium after 750 binary orbits compared with the subsequently introduced fully radiative model. The surface density in the isothermal model misses the bend caused by the 1000 K change in the disk opacity and is slightly steeper than the initial r^{-1} profile. The disk eccentricity in the isothermal case is much more homogeneous with radius, as is to be expected for a coherent structure. This has already been observed by Kley & Nelson (2008).

To check for numerical dependencies we varied the location of the inner boundary of the computational domain and the grid resolution. First we chose a smaller inner boundary of $r_{\rm min} = 0.25$ AU increasing the number of radial grid points such that the spatial grid resolution remained unchanged in the overlap region. In Fig. 5 the radial dependency of the surface density and the midplane temperature at the end of the simulations differs not too much in the overlap region of both simulations, so that the effects of the inner boundary are negligible in this respect. However, the amplitude of the oscillation in the time evolution of the disk eccentricity is nearly gone (see Fig. 6). In the standard model we could see a small oscillation in the disk periastron, which also vanishes in the $r_{\rm min} = 0.25$ AU model. The non-existence of a coherent precession is also an indication of very low disk eccentricity in both cases. In additional test simulations (not displayed here), we extended the outer radius to the value of $r_{\rm max} = 12$ AU, changing the number of grid cells accordingly to maintain the resolution of the standard model. As expected, this larger radial domain does not change the results.

Then we varied the grid resolution by first doubling the grid cells to 512×1150 and doubling it again to 1024×2302 grid cells. This change in resolution has basically no impact on the disk's dynamics. As before, the disk eccentricity settles to a time averaged value of about 0.04. In all three simulations the disk periastron does not reach a state with real precession and the only change caused by the change of resolution is a small shift in time. Consequently our standard resolution of 256×574 cells seems to be sufficient to resolve the disk dynamics properly.

4. Variation of physical parameters

To study the influence of the physical conditions on the evolution of the disk, we investigated in particular the impact of the disk mass $M_{\rm disk}$, the viscosity ν, which is determined by α, the opacity κ, and the binary's eccentricity $e_{\rm bin}$.

4.1. Disk mass

The first parameter we investigated is the disk mass. In contrast to isothermal simulations our radiative simulations depend on the disk mass as the opacity depends on gas density. To analyze the influence of the disk mass on the disk's evolution, we ran four simulations with disk masses $M_{\rm disk}$ of 0.005 $M_\odot$, 0.01 $M_\odot$, 0.02 $M_\odot$ and 0.04 $M_\odot$ while keeping all other parameters unchanged.

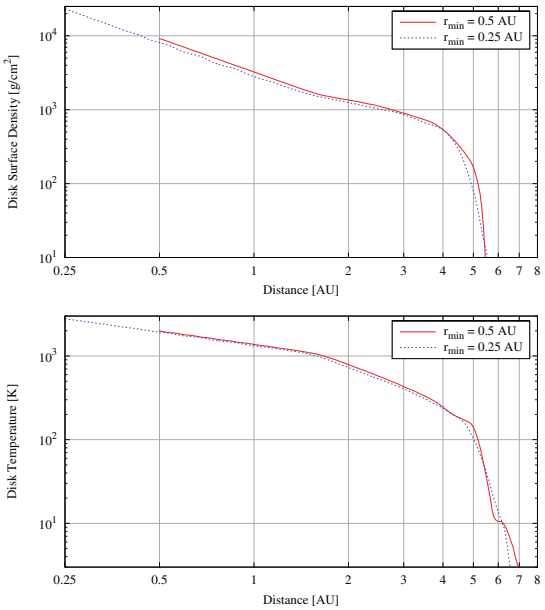

Fig. 5. Azimuthally averaged surface density (*top*) and midplane temperature (*bottom*) profiles for the radiative standard model using two different locations of the inner boundary of the computational domain. Results are displayed at 100 binary orbits (6666 years). In the overlapping region from 0.5–8 AU the profiles match very well and the region from 0.25–0.5 AU in the $r_{\rm min} = 0.25$ AU model is a consistent continuation.

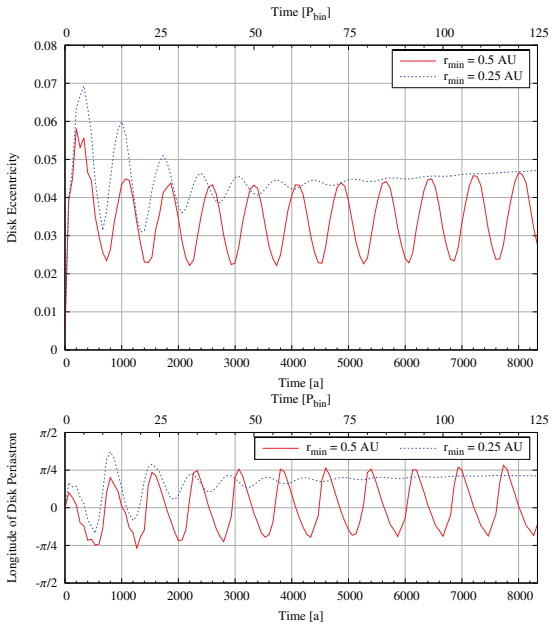

Fig. 6. Global mass-weighted disk eccentricity (*top*) and disk periastron (*bottom*), sampled at the binary's apastron, for two different inner boundary positions.

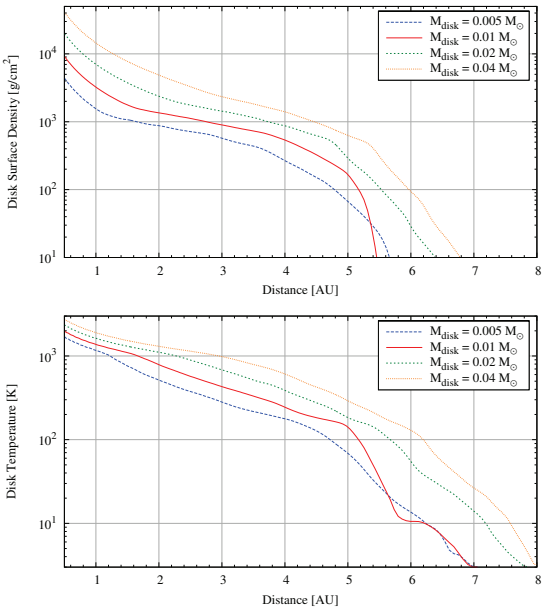

Fig. 7. Azimuthally averaged surface density (*top*) and midplane temperature (*bottom*) profiles after 100 binary orbits (6666 years) for radiative models using different initial disk masses. The profiles can be fitted using power-laws when divided into two regimes: An inner region with temperatures of less than about 1000 K and an outer region with temperatures above 1000 K because of a break in the opacity tables at about 1000 K. The inner region follows $\Sigma \propto r^{-1.49 \text{ to } -1.51}$ and $T \propto r^{-0.53 \text{ to } -0.54}$, whereas the outer region follows $\Sigma \propto r^{-0.82 \text{ to } -1.67}$ and $T \propto r^{-1.39 \text{ to } -1.58}$ for all models.

The surface density and temperature profiles after 100 binary orbits for different disk masses is displayed in Fig. 7, where the solid (red) line refers to the standard model displayed in Fig. 3. The profiles can be divided into two regimes that are separated by the 1000 K temperature line caused by the opacity (see Sect. 3.2). In each regime the surface density and temperature profiles follow a simple power-law that depends only weakly on the disk mass, and is given in the caption of Fig. 7.

Figure 8 shows the time evolution of the disk eccentricity and periastron for different disk masses. The higher the disk mass, the lower the oscillations of the the disk eccentricity, but the time average of the disk eccentricity is in the range of 0.04–0.05 for all disk masses. The disk periastron displays no real precession and with increasing disk mass it settles at about 0. This is in contrast to the isothermal simulations presented in Sect. 3.1 where we obtained a disk eccentricity $e_{\rm disk}$ of 0.2 for an aspect ratio H/r of 0.05 and a real precession of the disk periastron. There is a trend, however, that the eccentricity becomes higher for cooler disks with lower H/r. But one has to be careful here, because the aspect ratio is constant in radius and time for the isothermal simulations, but not for our radiative simulations. Figure 9 shows the aspect ratio of the disk after 100 binary orbits. All models had an initial value of $(H/r)_{\rm initial} = 0.05$ but end up with different values of H/r depending on the disk mass and the phase in the binary orbit. We note that in all models the mass of the disk reduces with time owing to the mass loss across the outer boundary. In particular, we find that after 100 binary

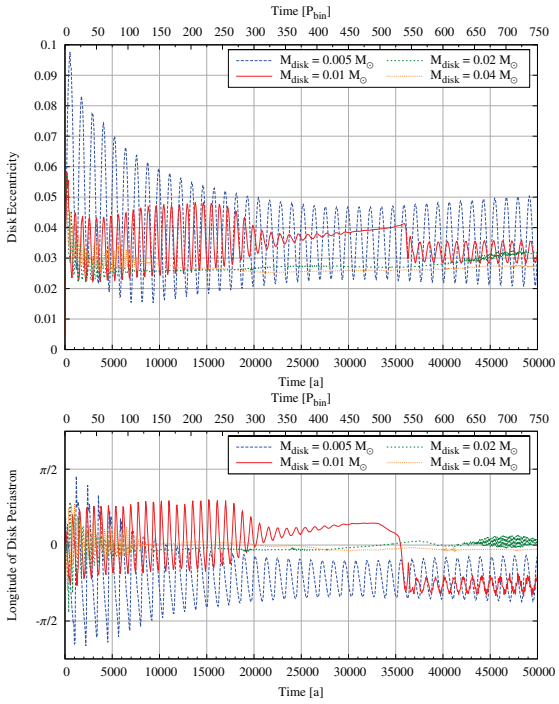

Fig. 8. Global mass-weighted disk eccentricity (*top*) and disk periastron (*bottom*), sampled at the binary's apastron, dependency for different disk masses.

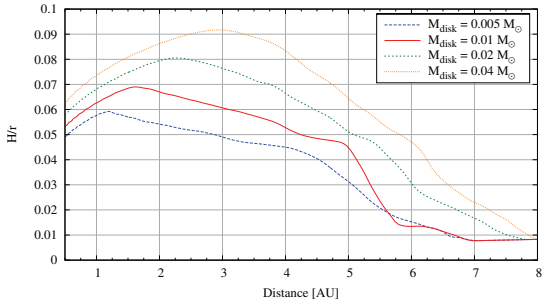

Fig. 9. H/r after 100 binary orbits (6666 years) for different disk masses.

orbits the disks have lost about 27% of their initial mass in the $M_{\rm disk} = 0.04\,M_\odot$ model, 23% in the $M_{\rm disk} = 0.04\,M_\odot$ model, 17% in the $M_{\rm disk} = 0.04\,M_\odot$ and 6% in the $M_{\rm disk} = 0.005\,M_\odot$ model. Hence, the values quoted in the text and figures always refer to the initial disk masses.

The results for $e_{\rm disk}$ in Fig. 8 show a marginal increase of the disk eccentricity for smaller disk masses. To test if this trend continues, we performed additional simulations for even smaller initial disk masses and found indeed an increased oscillatory behavior of the eccentricity, which settles eventually after about 600 binary orbits to a low eccentric state very similar to the $M_{\rm disk} = 0.025$ model, however. Hence, there does not seem to exist an obvious trend of $e_{\rm disk}$ with disk mass.

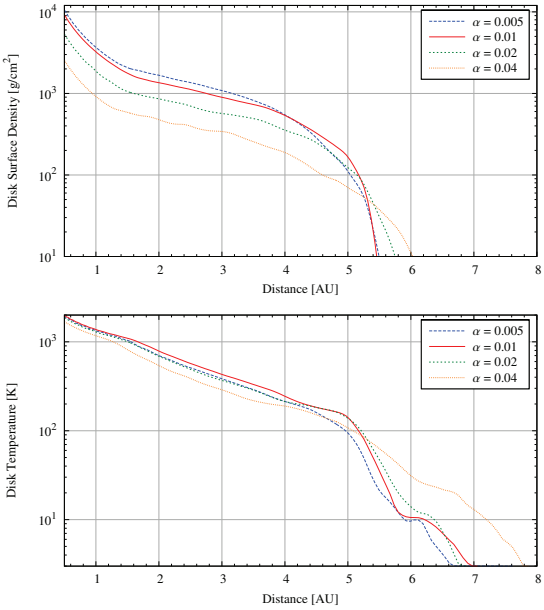

Fig. 10. Azimuthally averaged surface density (*top*) and midplane temperature (*bottom*) profiles after 100 binary orbits (6666 years) using four different values for the viscosity parameter α. The profiles can be fitted using power-laws when divided into two regimes: An inner region with temperatures of less than about 1000 K and an outer region with temperatures above 1000 K, because there is a break in the opacity tables at about 1000 K. The inner region follows $\Sigma \propto r^{-1.48\ \text{to}\ -1.53}$ and $T \propto r^{-0.53}$, whereas the outer region follows $\Sigma \propto r^{-0.78\ \text{to}\ -0.95}$ and $T \propto r^{-1.45\ \text{to}\ -1.53}$ for all α values.

4.2. Viscosity

In this section we investigate the influence of the viscosity ν. To study the dependence on ν we varied the α parameter, which determines the viscosity, $\nu = \alpha c_s H = \alpha c_s^2 \Omega_K^{-1}$ (Shakura & Sunyaev 1973), from our standard model ($\alpha = 0.01$) and kept all other parameters unchanged. We varied α from 0.005 to 0.04.

Figure 10 shows the surface density and temperature profiles after 100 binary orbits. All models started with identical disk mass, and evidently, higher α models lose the disk masses more rapidly. For example, at the displayed time at 100 binary orbits the $\alpha = 0.04$ model has lost about 71% of its initial mass, while the standard model ($\alpha = 0.01$) lost only 19%, see also Fig. 12 below. The shape of the surface density and temperature profile seems to be independent of the viscosity in the disk, as expected. Again, the profiles can be divided into two regimes that are separated by the 1000 K temperature line. The power-laws for the surface density and temperature profiles are given in the caption of Fig. 10.

Figure 11 shows the influence of α on the disk eccentricity and periastron. Higher values of α and thus high viscosities result in a calmer disk that does not react fast enough on the disturbances of the binary companion. Therefore the disk shows less oscillations in the disk eccentricity and the disk periastron remains almost constant for the higher values of α. The disk eccentricity in the model with the highest viscosity, $\alpha = 0.04$, increases to up to 0.25 within 600 binary orbits, and the disk eccentricity in the $\alpha = 0.02$ model starts to grow slowly after about

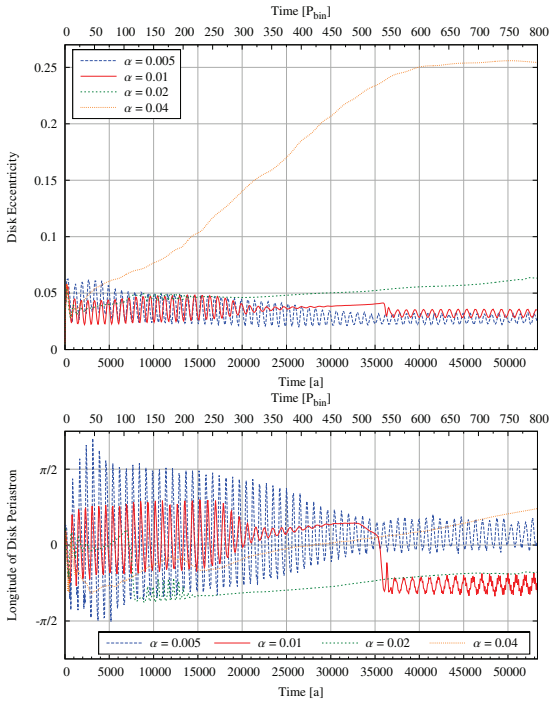

Fig. 11. Global mass-weighted disk eccentricity (*top*) and periastron (*bottom*), sampled at the binary's apastron, as a function of time for different α values for the viscosity.

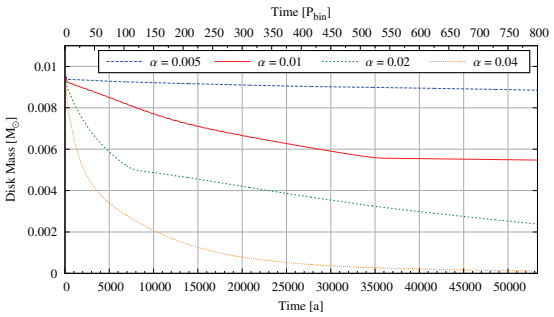

Fig. 12. Disk mass evolution for different α values for the disk viscosity.

200–300 binary orbits. This effect of a rising disk eccentricity is a direct consequence of the increasing viscosity. As shown in Fig. 12, the mass loss of the disk depends on the magnitude of the viscosity, the higher α, the faster the mass loss of the disk. For example, after 500 binary orbits the $\alpha = 0.04$ disk has lost about 97% of its initial mass. The increased mass loss for higher viscosities is a result of the stronger outward spreading of the disk, i.e. a larger truncation radius. The larger disk makes the outer parts of the disk more susceptible to the tidal perturbations of the secondary, which increase the disk eccentricity dramatically. This is in accordance with the viscosity dependence found in earlier studies, e.g. Kley et al. (2008).

4.3. Opacity

The amount of cooling in our radiative model depends on the disk's opacity. To examine the influence of the opacity model we calculated the standard model with two different opacity models leaving all other parameters unchanged. In the first calculation we used the opacity tables (see Table 1) shown by Lin & Papaloizou (1985), whereas the second calculation uses the opacity tables given by Bell & Lin (1994, their Table 3).

As expected, the opacity plays an important role and the model with the Bell & Lin opacity shows less oscillations in the disk eccentricity, but the time average is about the same as in the model with the Lin & Papaloizou opacity. This is similar to the $r_{\rm min}$ change in Sect. 3.2. The surface density and midplane temperature profiles at the end of the simulation in the simulation with the Bell & Lin opacity model differ slightly from the one shown in Fig. 3. Both models have a bend at a temperature of about 1000 K but the temperature profile in the model with the Bell & Lin opacity model is flatter and slightly lower in the region below 1000 K and slightly steeper in the region about 1000 K. In exchange, the surface density is slightly steeper and slightly higher in region the below 1000 K and matches the other model in the region above 1000 K very well.

4.4. Binary eccentricity

Another very important factor for the disk's evolution are the binary parameters. We therefore varied the binary's eccentricity in our standard model from $e_{\rm bin} = 0$ to 0.4. Because this also changes the truncation radius of the disk that is caused by the binary's tidal forces (Artymowicz & Lubow 1994), we extended the computational domain to up to 12.5 AU for the $e_{\rm bin} = 0$ model. To reach the same resolution in the computational domain of the standard model (0.5–8 AU) we increased the number of cells in radial direction to 295 in the $e_{\rm bin} = 0$ model. The $e_{\rm bin} = 0.05$, $e_{\rm bin} = 0.1$ and $e_{\rm bin} = 0.2$ models were adjusted accordingly in their computational domain and resolution in radial direction.

Figure 13 shows the time evolution of the disk eccentricity and periastron. Interestingly, the $e_{\rm bin} = 0$ and $e_{\rm bin} = 0.05$ models show the highest disk eccentricity. These high values for $e_{\rm bin} = 0$ seem to agree with Kley et al. (2008). Also, the $e_{\rm bin} = 0$ and $e_{\rm bin} = 0.05$ models are the only ones that have a real coherent disk precession with a precession rate of $-0.033\, P_{\rm bin}^{-1}$ for the $e_{\rm bin} = 0$ model and $-0.062\, P_{\rm bin}^{-1}$ for the $e_{\rm bin} = 0.05$ model. All other models with $e_{\rm bin} \geq 0.1$ show a disk eccentricity of $e_{\rm disk} < 0.1$ and no precession, which also indicates that the disk is not globally eccentric. For the low eccentric binaries it takes up to about 125 binary orbits to reach the high eccentric quasi-equilibrium disk state, which is long compared to the standard model, which reaches its quasistationary state after only about 15 binary orbits. These timescales agree well with those obtained by Kley et al. (2008) for isothermal disks. The reason why binaries with low $e_{\rm bin}$ tend to have eccentric disks is the larger disk radius in this case. This allows an easier operation of the instability according to the model of Lubow (1991).

The surface density and midplane temperature profiles after 100 binary orbits of all five models have the same slope but differ slightly in absolute values. The $e_{\rm bin} = 0.4$ models is the hottest and densest model and then the temperature and surface density decreases with decreasing binary eccentricity. The $e_{\rm bin} = 0$ model shows low oscillations in the profiles. As expected, the disk's truncation radius owing to the binary's tidal

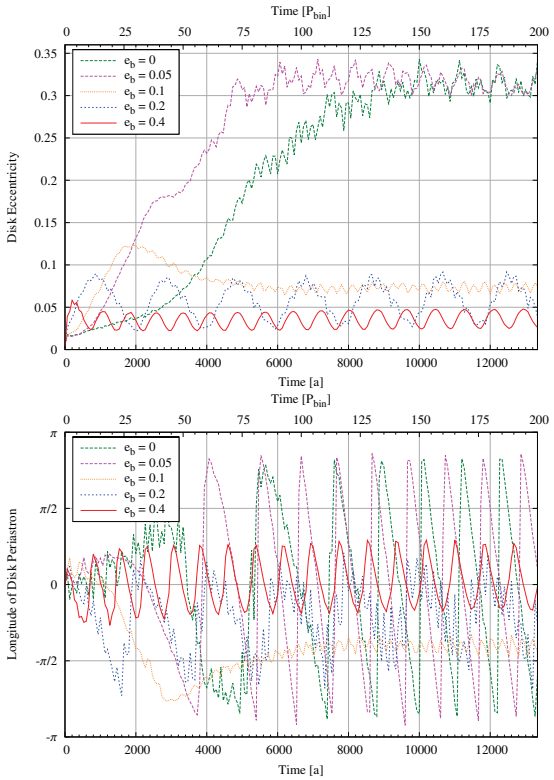

Fig. 13. Global mass-weighted disk eccentricity (*top*) and disk periastron (*bottom*), sampled at the binary's apastron, for different binary eccentricities. The low eccentricity ($e_{\rm bin} < 0.05$) models need much more time to reach their equilibrium state compared to the standard model. These are also the only models that develop a real coherent disk precession.

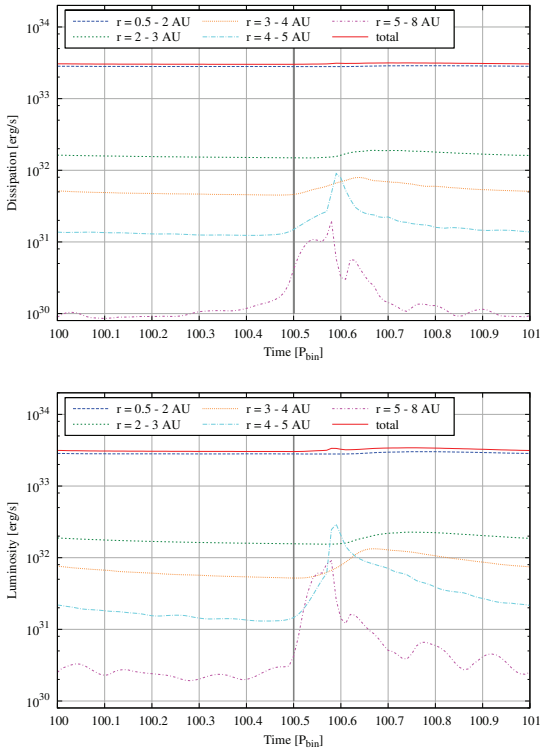

Fig. 14. Variation of disk dissipation and disk luminosity during one binary orbit. The dissipation and luminosity are calculated for five different rings ranging from 0.5–2 AU, 2–3 AU, 3–4 AU, 4–5 AU and 5–8 AU. Because the disk is truncated at about 4.5 AU (see Fig. 3), the outmost ring does not contain much mass. The solid (red) curve is the sum of all five rings. The gray line indicates the binary's periastron passage.

forces is shifted outward in the models with lower binary eccentricity.

5. Brightness variations

To identify possible observable changes in the brightness of the systems caused by perturbations in the disk, we calculated theoretical light curves for our standard model. For that purpose, we examined the time variation of the disk dissipation given by

$$D_{\rm disk} = \iint Q^{+}\,{\rm d}A, \tag{19}$$

and the disk luminosity given by

$$L_{\rm disk} = \iint Q^{-}\,d{\rm d}A = \iint 2\sigma_{\rm R}\frac{T^4}{\tau_{\rm eff}}\,{\rm d}A. \tag{20}$$

To identify the source of the brightness variations we divided the disk into five rings ranging from 0.5–2 AU, 2–3 AU, 3–4 AU, 4–5 AU and 5–8 AU. In each of these rings the disk dissipation and disk luminosity was calculated. Figure 14 displays the variation of the disk dissipation and disk luminosity of our standard model during one orbital orbit at $t = 100\,P_{\rm bin}$ where the system has already reached its quasistationary state. The periastron occurs at $t = 100.5\,P_{\rm bin}$, and is indicated by the vertical line.

When the binary is at apastron, the disk is almost uniform (see Fig. 1) and we cannot see any variations in the light curves. However, when the binary passes periastron, it starts to perturb the outer regions of the disk and two spiral arms evolve that wind themselves to the center of the disk. This results in a rise of the luminosity by 2–3 mag in the outer rings of the disk shortly after periastron passage (see Fig. 14) and after a short time also in a smaller rise in the inner rings of the disk. As the binary moves farther away from the disk, the spirals are damped out and the luminosity peak vanishes. These luminosity peaks should be observable as a 2-mag increase in the mid-infrared (MIR) because the main contributions come from the outer rings (3–5 AU) with temperatures between 150 K and 450 K.

Luminosity peaks have already been observed in the mid-infrared in the T Tau S system (van Boekel et al. 2010), a binary system that is not very different from the early stage of the γ Cephei system. Additionally, van Boekel et al. also performed some radiative simulations for the T Tau S system and pointed out that these brightness variations could be caused by the perturbations of the binary companion. However, the brightness variations found in their disk models were very weak.

Table 4. Parameters of the α Centauri model.

Primary star mass ($M_{\rm primary}$)	1.1 $M_\odot$
Secondary star mass ($M_{\rm secondary}$)	0.93 $M_\odot$
Binary semi-major axis (a)	23.4 AU
Binary eccentricity ($e_{\rm bin}$)	0.52
Binary orbital period ($P_{\rm bin}$)	79.4431 a
Disk mass ($M_{\rm disk}$)	0.01 $M_\odot$
Viscosity (α)	0.01
Adiabatic index (γ)	7/5
Mean-molecular weight (μ)	2.35
Initial density profile (Σ)	$\propto r^{-1}$
Initial temperature profile (T)	$\propto r^{-1}$
Initial disk aspect ratio (H/r)	0.05
Grid ($N_r \times N_\varphi$)	256×574
Computational domain ($R_{\rm min} - R_{\rm max}$)	0.5–8 AU

Notes. The top entries refer to the fixed binary parameter. Below we list along with the disk properties the initial disk setup and the computational parameters.

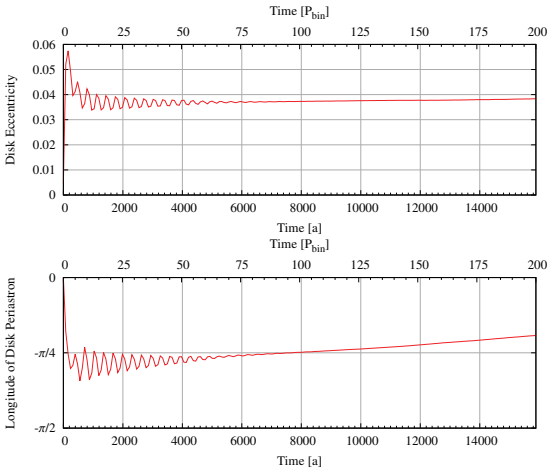

Fig. 15. Global mass-weighted disk eccentricity (*top*) and disk periastron (*bottom*), sampled at the binary's apastron for the α Centauri model.

6. α Centauri

In addition to the γ Cephei system we also performed some calculations for the α Centauri system, because it is of special interest, being the nearest star to our solar system. This system has been investigated for the possibility of planet formation, see e.g. Thébault et al. (2008). Table 4 gives an overview of the parameters of our α Centauri model based on Pourbaix et al. (2002). We tried to keep the disk parameters the same as in the γ Cephei model, so that the main difference are the mass ratio $q = M_{\rm secondary}/M_{\rm primary}$ and the binary's orbital parameters. In the γ Cephei model we have a mass ratio q of 0.28, an eccentricity $e_{\rm bin}$ of 0.4 and a semi-major axis a of 20 AU, whereas in the α Centauri model we have a mass ratio q of 0.84, an eccentricity $e_{\rm bin}$ of 0.52 and a semi-major axis a of 23.4 AU.

In Sect. 4.4 we saw that for high binary eccentricities the disk eccentricity does not reach very high values, so that we would expect a fairly low disk eccentricity for the α Centauri system. Kley et al. (2008) showed that for isothermal simulations the disk eccentricity in the quasistationary state does not depend heavily on the mass ratio q. Figure 15 shows the evolution of the disk eccentricity and periastron over time. The disk eccentricity settles after about 15 binary orbits at a rather low value of about 0.038 and the disk periastron is also at a nearly constant position.

The surface density and midplane temperature profiles for the α Centauri model can only be fitted in the inner region with $r < 1.8$ AU as a simple power-law. The surface density can be described by a $r^{-1.49}$ and the midplane temperature by a $r^{-0.53}$ power-law. In the outer region the surface density and temperature decreases rather fast to 0 until about 4 AU, where the disk is truncated by the binary's tidal forces.

7. Summary and conclusions

We have investigated the dynamics of a protostellar disk in binary star systems using specifically the orbital parameter of γ Cephei and α Centauri. We assumed a coplanar system and used a two-dimensional hydrodynamical code to evolve the non-self-gravitating disk. Extending previous simulations, we included internal viscous heating given by an α-type viscosity prescription, and radiative cooling from the disk surface.

In a first set of simulations we investigated locally *isothermal* disks for different disk temperatures. We showed that disks in binaries of the γ Cephei type with a standard thickness of $H/r = 0.05$ become eccentric ($e_{\rm disk} \approx 0.2$) showing a coherent disk precession. This agrees well with previous simulations by Kley & Nelson (2008) and Paardekooper et al. (2008). Varying the temperature in the disk, we showed that the magnitude of the disk's eccentricity becomes lower when the disk thickness increases. For disks with $H/r \gtrsim 0.065$ the mean average eccentricity has dropped below 0.08 and the disks do not show a precession anymore.

Then we studied more realistic disks with internal heating and radiative cooling, varying the disk's mass. In all cases we found relatively low eccentricities and no precession. We attribute the lack of eccentricities firstly to the increased disk height, which is, in particular for the more massive disks, higher than the standard value (see Fig. 9). Secondly, in the full radiative models the disk's dynamical behavior is more adiabatic compared to the locally isothermal case. Then, through compressional heating (pdV-work), kinetic energy is transferred to internal energy, which leads to a reduced growth of disk eccentricity. We have checked that purely adiabatic models show an even lower disk eccentricity than the radiative models. Hence, the radiative case lies between the adiabatic and isothermal, as expected.

Because the disk's energy balance is determined via the viscosity, we changed the value of the parameter α ranging from 0.005 to 0.04, all values that are consistent with the results of MHD-turbulent accretion disks. Here, we found that only the disk with the highest α becomes eccentric. The reason for this rise is the larger disk radius, which leads to an enhancement of the tidal torques from the secondary. We note that the disk's outer radius in our models still lies well inside the 3:1 resonance with the binary. According to the linear instability model by Lubow (1991), the disk eccentricity is excited through the 3:1 resonance and hence, the disk should be sufficiently large, a condition which is fulfilled only for small mass ratios, $q = M_{\rm secondary}/M_{\rm primary}$. However, as shown by Kley & Nelson (2008), disks in binary star systems with large mass ratios can

turn eccentric as well, even though the disks are small, a feature confirmed in our simulations.

The inferred short lifetime of disks with standard viscosities is slightly alarming with respect to planet formation in these systems. In the core-accretion scenario planet formation proceeds along a sequence of many steps that take a few Myr. For disks to persist this long in γ Cephei-type binaries a very low viscosity of $\alpha \lesssim 10^{-4}$ seems to be required. In the gravitational instability scenario the timescale for planet formation is much shorter and hence, this scenario may be favored by our findings. Observationally, several recent studies indeed suggest that the lifetime of disks in young binary stars is significantly reduced compared to disks around single stars (Cieza et al. 2009; Duchêne 2010; Kraus et al. 2012). Dynamically, this behavior is expected, because the perturbation of the companion star leads quite naturally to an increased mass loss of the disk, details depending on the binary separation and eccentricity.

A very critical phase in the core accretion scenario, in particular in binary stars, is the initial growth of meter to km-sized planetesimals. Here, the growth depends on the successful sticking of the two collision partners. Since the relative velocity of the bodies is increased in binary stars, planetary growth will be significantly hindered by the presence of a companion, see e.g. Thébault et al. (2006); Thebault (2011) and references therein. Here our results indicate that planetesimal growth is less negatively influenced because the disk eccentricity is reduced for more realistic radiative disks. As has been shown, eccentric disks tend to increase the mutual relative velocities of embedded objects, in particular of different sizes, because of the misaligned periastrons of the particles (Kley & Nelson 2007; Paardekooper et al. 2008). Hence, a radiative disk with a low viscosity could help to promote planetesimal growth. However, it remains to be seen how the inclusion of stellar irradiation (from both stars) influences the dynamics. Owing to the additional heating of the disk, we expect even more mass loss from the system and possibly higher disk eccentricities because the disks are more isothermal and will have a larger radius.

Previous studies have indicated that in a mutually inclined system planetesimal growth may be enhanced because planetesimals can be size-sorted in differently inclined planes (Xie & Zhou 2009; Marzari et al. 2009b). However, recently Fragner et al. (2011) showed through full 3D hydrodynamical studies that for inclined binaries the relative velocities of different sized planetesimals increases through inclinations effects. They conclude that for inclined systems planetesimal formations can take place only for very distant binary stars with $a_{\rm bin} \gtrsim 60$ AU. However, the simulations considered only isothermal disks, and it remains to be seen how radiative effects influence the disk. But full 3D radiative simulations are still beyond the present computational possibilities, because thousands of orbital timescales of the disk will have to be calculated.

Acknowledgements. We would like to thank Markus Gyergyovits for useful discussions. Tobias Müller received financial support from the Carl-Zeiss-Stiftung. Most of the simulations were performed on the bwGRiD cluster in Tübingen, which is funded by the Ministry for Education and Research of Germany and the Ministry for Science, Research and Arts of the state Baden-Württemberg. Additionally, we used the cluster of the Forschergruppe FOR 759 "The Formation of Planets: The Critical First Growth Phase" funded by the German Research Society (DFG).

References

Artymowicz, P., & Lubow, S. H. 1994, ApJ, 421, 651
Baruteau, C. 2008, Ph.D. thesis, CEA Saclay
Bell, K. R., & Lin, D. N. C. 1994, ApJ, 427, 987
Beuermann, K., Buhlmann, J., Diese, J., et al. 2011, A&A, 526, A53
Campbell, B., Walker, G. A. H., & Yang, S. 1988, ApJ, 331, 902
Cieza, L. A., Padgett, D. L., Allen, L. E., et al. 2009, ApJ, 696, L84
Correia, A. C. M., Udry, S., Mayor, M., et al. 2008, A&A, 479, 271
D'Angelo, G., Henning, T., & Kley, W. 2003, ApJ, 599, 548
Desidera, S., & Barbieri, M. 2007, A&A, 462, 345
Duchêne, G. 2010, ApJ, 709, L114
Dvorak, R. 1986, A&A, 167, 379
Dvorak, R., Pilat-Lohinger, E., Bois, E., et al. 2004, in Rev. Mex. Astron. Astrofis. Conf. Ser. 21, ed. C. Allen, & C. Scarfe, 222
Eggenberger, A., Udry, S., & Mayor, M. 2004, A&A, 417, 353
Eggenberger, A., Udry, S., Chauvin, G., et al. 2007, A&A, 474, 273
Els, S. G., Sterzik, M. F., Marchis, F., et al. 2001, A&A, 370, L1
Endl, M., Cochran, W. D., Hatzes, A. P., & Wittenmyer, R. A. 2011, in AIP Conf. Ser. 1331, ed. S. Schuh, H. Drechsel, & U. Heber, 88
Fragner, M. M., Nelson, R. P., & Kley, W. 2011, A&A, 528, A40
Haghighipour, N. 2006, ApJ, 644, 543
Hatzes, A. P., Cochran, W. D., Endl, M., et al. 2003, ApJ, 599, 1383
Hubeny, I. 1990, ApJ, 351, 632
Kley, W. 1989, A&A, 208, 98
Kley, W. 1999, MNRAS, 303, 696
Kley, W., & Crida, A. 2008, A&A, 487, L9
Kley, W., & Nelson, R. 2007 [arXiv:0705.3421]
Kley, W., & Nelson, R. P. 2008, A&A, 486, 617
Kley, W., Papaloizou, J. C. B., & Ogilvie, G. I. 2008, A&A, 487, 671
Kley, W., Bitsch, B., & Klahr, H. 2009, A&A, 506, 971
Kraus, A. L., Ireland, M. J., Hillenbrand, L. A., & Martinache, F. 2012, ApJ, 745, 19
Lin, D. N. C., & Papaloizou, J. 1985, in Protostars and Planets II, ed. D. C. Black, & M. S. Matthews, 981
Lubow, S. H. 1991, ApJ, 381, 259
Marzari, F., Scholl, H., Thébault, P., & Baruteau, C. 2009a, A&A, 508, 1493
Marzari, F., Thébault, P., & Scholl, H. 2009b, A&A, 507, 505
Masset, F. 2000, A&AS, 141, 165
Masset, F. S. 2002, A&A, 387, 605
Nelson, A. F. 2000, ApJ, 537, L65
Neuhäuser, R., Mugrauer, M., Fukagawa, M., Torres, G., & Schmidt, T. 2007, A&A, 462, 777
Paardekooper, S.-J., Thébault, P., & Mellema, G. 2008, MNRAS, 386, 973
Pourbaix, D., Nidever, D., McCarthy, C., et al. 2002, A&A, 386, 280
Queloz, D., Mayor, M., Weber, L., et al. 2000, A&A, 354, 99
Quintana, E. V., Adams, F. C., Lissauer, J. J., & Chambers, J. E. 2007, ApJ, 660, 807
Raghavan, D., Henry, T. J., Mason, B. D., et al. 2006, ApJ, 646, 523
Regály, Z., Sándor, Z., Dullemond, C. P., & Kiss, L. L. 2011, A&A, 528, A93
Shakura, N. I., & Sunyaev, R. A. 1973, A&A, 24, 337
Stone, J. M., & Norman, M. L. 1992, ApJS, 80, 753
Thebault, P. 2011, Cel. Mech. Dyn. Astron., 40
Thébault, P., Marzari, F., Scholl, H., Turrini, D., & Barbieri, M. 2004, A&A, 427, 1097
Thébault, P., Marzari, F., & Scholl, H. 2006, Icarus, 183, 193
Thébault, P., Marzari, F., & Scholl, H. 2008, MNRAS, 388, 1528
Torres, G. 2007, ApJ, 654, 1095
van Boekel, R., Juhász, A., Henning, T., et al.2010, A&A, 517, A16
van Leer, B. 1977, J. Comput. Phys., 23, 276
Whitehurst, R. 1988, MNRAS, 232, 35
Xie, J.-W., & Zhou, J.-L. 2009, ApJ, 698, 2066
Zucker, S., Mazeh, T., Santos, N. C., Udry, S., & Mayor, M. 2004, A&A, 426, 695

A&A 541, A123 (2012)
DOI: 10.1051/0004-6361/201118737

Astronomy & Astrophysics

Treating gravity in thin-disk simulations

T. W. A. Müller[1], W. Kley[1], and F. Meru[1,2]

[1] Institut für Astronomie & Astrophysik, Universität Tübingen, Auf der Morgenstelle 10, 72076 Tübingen, Germany
e-mail: Tobias_Mueller@twam.info
[2] Institute for Astronomy, ETH Zürich, Wolfgang-Pauli-Strasse 27, 8093 Zürich, Switzerland

Received 23 December 2011 / Accepted 6 March 2012

ABSTRACT

Context. In 2D-simulations of thin gaseous disks with embedded planets or self-gravity the gravitational potential needs to be smoothed to avoid singularities in the numerical evaluation of the gravitational potential or force. The softening prescription used in 2D needs to be adjusted properly to correctly resemble the realistic case of vertically extended 3D disks.
Aims. We analyze the embedded planet and the self-gravity case and provide a method to evaluate the required smoothing in 2D simulations of thin disks.
Methods. Starting from the averaged hydrodynamic equations and using a vertically isothermal disk model, we calculated the force to be used in 2D simulations. We compared our results to the often used Plummer form of the potential, which runs as $\propto 1/(r^2+\epsilon^2)^{1/2}$. For that purpose we computed the required smoothing length ϵ as a function of distance r to the planet or to a disk element within a self-gravitating disk.
Results. We find that for longer distances ϵ is determined solely by the vertical disk thickness H. For the planet case we find that outside $r \approx H$ a value of $\epsilon = 0.7H$ describes the averaged force very well, while in the self-gravitating disk the value needs to be higher, $\epsilon = 1.2H$. For shorter distances the smoothing needs to be reduced significantly. Comparing torque densities of 3D and 2D simulations we show that the modification to the vertical density stratification as induced by an embedded planet needs to be taken into account to obtain agreeing results.
Conclusions. It is very important to use the correct value of ϵ in 2D simulations to obtain a realistic outcome. In disk fragmentation simulations the choice of ϵ can determine whether a disk will fragment or not. Because a wrong smoothing length can change even the direction of migration, it is very important to include the effect of the planet on the local scale height in 2D planet-disk simulations. We provide an approximate and fast method for this purpose that agrees very well with full 3D simulations.

Key words. accretion, accretion disks – planets and satellites: formation – hydrodynamics – methods: numerical – protoplanetary disks

1. Introduction

Numerical simulations of accretion disks are often performed in the two-dimensional (2D) thin-disk approximation, because a full 3D treatment with high resolution is still a computationally demanding endeavor requiring a lot of patience. In numerical disk models with embedded planets and/or self-gravity the gravitational potential (force) needs to be smoothed because it diverges for very short mutual distances. For that purpose the potential is softened to avoid the singularities that arise, for example, from pointlike objects, such as planets embedded in disks. In full 3D simulations this smoothing may be required solely for stability purposes and can be chosen to be as small as the given numerical resolution allows. In contrast, 2D disk simulations are typically based on a vertical averaging procedure that leads to a *physically required* smoothing. Ideally, this smoothing should be calculated in a way that the 2D simulations mimic the 3D case as closely as possible. The most often used potential smoothing has a Plummer form with $\Psi \propto -1/(r^2+\epsilon^2)^{1/2}$, where r is the distance to the gravitating object and ϵ is a suitably chosen smoothing or softening length. If a vertically stratified disk has a thickness H, we would expect that somehow ϵ should depend suitably on H. In a sense, the potential is "diluted" in this case due to the disk's finite thickness.

For the planet-disk problem, Miyoshi et al. (1999) have shown with local shearing sheet simulations that owing to this dilution effect, the total torque exerted on a planet in a three dimensional disk is only about 43% of the torque obtained in the thin, unsmoothed 2D case. These authors also showed that the strength of the one-sided torque depends on the value of the smoothing, where larger ϵ lead to smaller torques. Later, Masset (2002) has studied the smoothing problem in greater detail. He has shown that good agreement of the total 2D and 3D Lindblad torques can be obtained for smoothing lengths of $\epsilon = 0.75H$, where H is the vertical scale height of the disk, see Eq. (11) below. Masset found that for the Lindblad torques this optimum ϵ/H value is independent of the planet mass and the thickness of the disk. On the contrary, for the corotation torques that are generated by material moving on horseshoe orbits, he found that the required smoothing depends on the ratio R_H/H, where R_H is the Hill radius of the planet. Masset concluded that there is no "magic" value of ϵ that generates overall agreement of 2D with 3D results.

Based on these studies, in 2D planet-disk simulations the parameter ϵ is typically chosen such that the *total* torque acting on the planet, which determines the important migration speed, is approximately equal to that obtained through 3D (linear) analysis, for example by Tanaka et al. (2002). This argument has led to the choice of $\epsilon \approx 0.3$–$0.6H$, a value very often used in these simulations (Masset 2002; de Val-Borro et al. 2006; Paardekooper & Papaloizou 2009). However, recently a very small smoothing has been advocated for 2D planet-disk simulation (Dong et al. 2011). A smoothing based on a vertical integration using

Gaussian density profiles has been used by Li et al. (2005, 2009), but they provided no details on the methodology and accuracy.

For self-gravitating disks, the conditions for fragmentation have recently attracted much attention in the context of planet formation via gravitational instability. Typically, studies are performed in full 3D (see e.g. Meru & Bate (2011b) and references therein). However, to save computational effort, 2D simulations present an interesting alternative in this context (Paardekooper et al. 2011). Here, the accurate treatment of self-gravity is very important.

The incorporation of self-gravity in 2D thin-disk calculations can be achieved by using fast Fourier transforms. Baruteau & Masset (2008) presented a method where the force is calculated directly using a smoothing length that scales linearly with radius, and they used the same smoothing, $\epsilon = 0.3H$, for the planet and self-gravity. Li et al. (2005) used this method to calculate the potential in the disk's midplane. The simultaneous treatment of an embedded planet and disk-self-gravity can be important because the latter may influence the migration properties of the planet (Pierens & Huré 2005; Baruteau & Masset 2008). For global self-gravitating disks the treatment of the potential has been analyzed in more detail by Huré & Pierens (2009), who calculated the required smoothing by comparing 3D and 2D disk models with specified density stratifications. For that purpose they compared the midplane value of the 3D potential to the 2D case and estimated from this the required smoothing length. Additionally, they considered the whole extent of the disk for their integration. They found that ϵ needs to be reduced for close separations $\approx H$, while for long distances it approaches a finite value. Huré & Pierens (2009) give an extended list of smoothing prescriptions used in the literature and we refer the reader to their paper.

Here, we will reanalyze the required smoothing in 2D disk simulations. We show that the force to be used in 2D has to be obtained by performing suitable vertical averages of the force. For the planet-disk case we extend the work by Masset (2002) and compare in detail the torque density to full 3D simulations. We present a method to approximately include the change in vertical stratification induced by the presence of the planet. With respect to self-gravitating disks we follow the work by Huré & Pierens (2009) and calculate the optimum smoothing length ϵ by performing a vertical averaging procedure for the force between two disk elements. We show that this will be important for fragmentation of gravitational unstable disks.

In the next two sections we present the vertical averaging procedure and our unperturbed isothermal disk model. In Sect. 4 we analyze the potential of an embedded planet followed by the self-gravitating case. In Sect. 6 we summarize and conclude.

2. The vertical averaging procedure

Throughout the paper we assume that the disk lies in the $z = 0$ plane and work in a cylindrical coordinate system (r, φ, z). Starting from the full 3D hydrodynamic equations the vertically averaged equations, describing the disk evolution in the $r - \varphi$ plane, are obtained by integrating over the vertical direction. The continuity equation then reads

$$\int \frac{\partial \rho}{\partial t}\,\mathrm{d}z + \int \nabla \cdot (\rho \boldsymbol{v})\,\mathrm{d}z = 0, \tag{1}$$

where $\boldsymbol{v}$ and ρ are the 3D velocity and density, respectively. This is typically written as

$$\frac{\partial \Sigma}{\partial t} + \nabla \cdot (\Sigma \boldsymbol{u}) = 0, \tag{2}$$

where

$$\Sigma = \int \rho\,\mathrm{d}z \tag{3}$$

is the surface density of the disk and

$$\boldsymbol{u} = \frac{1}{\Sigma}\int (\rho \boldsymbol{v})\,\mathrm{d}z \tag{4}$$

the vertically averaged 2D velocity in the disk's plane. The integrals extend over all z ranging from $-\infty$ to $+\infty$. The integrated momentum equation, considering only pressure and gravitational forces, then reads

$$\Sigma \frac{\mathrm{d}\boldsymbol{u}}{\mathrm{d}t} = -\nabla P - \int \rho \nabla \Psi\,\mathrm{d}z, \tag{5}$$

with the vertically integrated pressure $P = \int p\,\mathrm{d}z$, where p is the 3D pressure. From Eq. (5) it is obvious that the change in the velocities is determined by the specific force (or acceleration) that is given by the ratio of force density (the integral in Eq. (5)) and surface density Σ, i.e.

$$f = -\frac{\int \rho \nabla \Psi\,\mathrm{d}z}{\Sigma}. \tag{6}$$

We here deal with the correct treatment of the last term in Eq. (5), which describes the averaging of the potential that can be given, for example, by a central star, an embedded planet, or self-gravity

$$\Psi = \Psi_* + \Psi_\mathrm{p} + \Psi_\mathrm{sg}. \tag{7}$$

From the derivation of the momentum Eq. (5) it is clear that not the potential in the midplane matters, but a suitable averaging of the gravitational force. In the following we will analyze this averaging using density stratifications in the vertical isothermal case. Even though accretions disks are known not to be isothermal, we nevertheless prefer at this stage to use this assumption because it is still a commonly used approach that avoids solving a more complex energy equation. It leads to a Gaussian density profile that is also in more general cases a reasonable first-order approximation. Additionally, the irradiation of a central light source tends to make disks more isothermal in the vertical direction. More realistic structures will be treated in future work.

3. The locally isothermal accretion disk model

The vertical structure of accretion disks is determined through the hydrostatic balance in the direction perpendicular to the disk's midplane. In this section we present first an idealized situation, where the disk is non-self-gravitating and its structure is not influenced by an embedded planet. This allows for analytic evaluation of integrals. Then we will consider more general cases. Using the thin-disk approximation and a gravitational potential generated by a point mass M_* in the center, i.e. $\Psi_* = -GM_*/(r^2 + z^2)^{1/2}$, the vertical hydrostatic equation for long distances r from the star can be written as

$$\frac{1}{\rho}\frac{\partial p}{\partial z} = -\frac{GM_* z}{(r^2 + z^2)^{\frac{3}{2}}} \approx -\frac{GM_* z}{r^3} \equiv -\Omega_\mathrm{K}^2 z. \tag{8}$$

To obtain the vertical stratification for the density, ρ, from this equation requires an equation of state $p = p(\rho, T)$ and a detailed thermal balance, by considering, for example, internal (viscous)

heating, stellar irradiation and radiative transport through the disk. To simplify matters, often the so-called locally isothermal approximation is applied for the (numerical) study of embedded planets in disks or for self-gravitating disks. Using this approach, a costly solution of the energy equation is avoided by specifying a priori a fixed radial temperature distribution $T(r)$. At each radius, however, the temperature is assumed to be isothermal in the vertical direction. Using

$$p = \rho c_\mathrm{s}^2, \tag{9}$$

where the (isothermal) sound speed c_s is now independent of z, we obtain for the vertical disk structure a Gauss profile

$$\rho_\mathrm{G}(r,\varphi,z) = \rho_0(r,\varphi)\,\mathrm{e}^{-\frac{1}{2}\frac{z^2}{H^2}}, \tag{10}$$

where the vertical height H is defined as

$$H = \frac{c_\mathrm{s}}{\Omega_\mathrm{K}}, \tag{11}$$

and $\rho_0(r,\varphi)$ is the density in the midplane of the disk. For the vertically integrated surface density Σ one obtains in this case

$$\Sigma = \int \rho_0 \mathrm{e}^{-\frac{1}{2}\frac{z^2}{H^2}}\,\mathrm{d}z = \sqrt{2\pi} H \rho_0. \tag{12}$$

In 2D, $r-\varphi$, simulations of disks this surface density $\Sigma(r,\varphi)$ is one of the evolved quantities.

4. The potential of an embedded planet

To illustrate the necessity of potential- (or force-)smoothing we consider in this section embedded planets in locally isothermal disks that are non-self-gravitating. First we will look at an unperturbed disk whose structure is determined by the distance from the host star and is given by Eq. (10). Then we include the effects of an embedded planet on the disk structure.

4.1. Unperturbed disk

We consider the potential of a point like planet with mass M_p embedded in a 3D locally isothermal disk with a fixed Gaussian density profile, ρ_G. The planetary potential is given by

$$\Psi_\mathrm{p}(\boldsymbol{r}) = -\frac{GM_\mathrm{p}}{|\boldsymbol{r}-\boldsymbol{r}_\mathrm{p}|} = -\frac{GM_\mathrm{p}}{(s^2+z^2)^{\frac{1}{2}}}, \tag{13}$$

where $\boldsymbol{r}$ is the vector pointing to the location in the disk and $\boldsymbol{r}_\mathrm{p}$ is the vector pointing to the planet. The vector $\boldsymbol{s}$ pointing from the disk element to the projected position of the planet, i.e. in the $z=0$ plane, is denoted by

$$\boldsymbol{s} = (\boldsymbol{r}_\mathrm{p}-\boldsymbol{r}) - \langle \boldsymbol{r}_\mathrm{p}-\boldsymbol{r}, \boldsymbol{e}_z\rangle \boldsymbol{e}_z, \tag{14}$$

where $\boldsymbol{e}_z$ is the unit vector in z direction and $\langle\cdot,\cdot\rangle$ denotes the scalar product.

The force acting on each disk element is then calculated from the gradient of the potential. Since it acts along the vector $\boldsymbol{s}$, we can write for the modulus of the vertically averaged force density

$$F_\mathrm{p}(s) = -\int \rho \frac{\partial \Psi_\mathrm{p}}{\partial s}\,\mathrm{d}z = -GM_\mathrm{p} s \int \frac{\rho}{(s^2+z^2)^{\frac{3}{2}}}\,\mathrm{d}z. \tag{15}$$

The force density (with units force per area) in Eq. (15) has to be evaluated at the centers of all individual grid cells, as illustrated in Fig. 1. From there, either the total force of a disk element can be calculated by multiplying $F_\mathrm{p}(s)$ with the disk element's area $(r\Delta r\Delta\varphi)$, or one computes the specific force $f_\mathrm{p} = F_\mathrm{p}/\Sigma$, which can be used directly to update the velocities, see Eq. (6). For the density we write

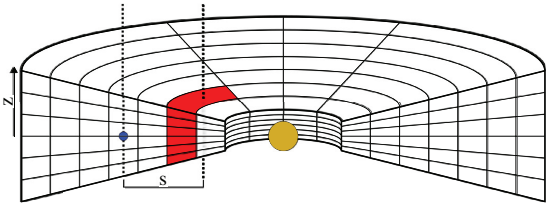

Fig. 1. Geometry of protoplanetary disk with embedded planet. We calculated the gravitational force from the planet (blue) on a vertical slice of the disk (red). For that purpose the gradient of the potential has to be vertically integrated along the dashed line that goes through the cell center. To obtain the total force exerted on the shaded disk segment, this value has to be multiplied by its area in the $r-\varphi$ plane.

$$\rho_\mathrm{G}(r,\varphi,z) = \rho_0(r,\varphi)\cdot\rho_z(z^2/H^2), \tag{16}$$

where we have assumed that the vertical dependence of ρ is a function of the quantity z^2/H^2, as stated in Eq. (10). Substituting $y = z/s$ in Eq. (15) and using a vertical stratification according to Eq. (16), we find

$$F_\mathrm{p} = -\frac{GM_\mathrm{p}\rho_0}{s}\cdot 2I_\mathrm{p}(s). \tag{17}$$

The dimensionless function $I_\mathrm{p}(s)$ is defined through an integral over half the disk

$$I_\mathrm{p}(s) = \int_0^\infty \frac{\rho_z(c^2y^2)}{(1+y^2)^{\frac{3}{2}}}\,\mathrm{d}y, \tag{18}$$

where the normalized vertical distance y and the quantity c are given by

$$y = \frac{z}{s} \quad \text{and} \quad c = \frac{s}{H}. \tag{19}$$

For the standard Gaussian vertical profile, i.e. $\rho_z(c^2y^2) = \exp\left(-\frac{1}{2}c^2y^2\right)$, the integral $I_\mathrm{p}(s)$ can be expressed as

$$I_\mathrm{p}(s) = \frac{1}{4}c^2\exp\left(\frac{c^2}{4}\right)\left[K_1\left(\frac{c^2}{4}\right) - K_0\left(\frac{c^2}{4}\right)\right], \tag{20}$$

where $K_n(x)$ are the modified Bessel functions of the second kind. For illustrating purposes we present evaluations of the force correction function I_p for simpler polynomial density stratifications in Appendix B.

In 2D numerical simulations of disks the above averaging procedure is typically not performed. Instead, an equivalent 2D potential is used in the momentum equation such that

$$\frac{\mathrm{d}\boldsymbol{u}}{\mathrm{d}t} = -\nabla\Psi_\mathrm{p}^\mathrm{2D}. \tag{21}$$

We point out that a 2D potential with the property of equation Eq. (21) cannot be the result of an averaging procedure in general as in Eq. (5) because for realistic densities

$$\nabla\Psi_\mathrm{p}^\mathrm{2D} \neq \frac{\int\rho\nabla\Psi\,\mathrm{d}z}{\Sigma}. \tag{22}$$

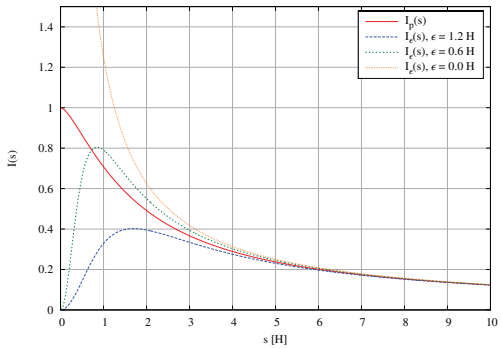

Fig. 2. Force correction function $I_p(s)$ (solid line) resulting from an integration over the vertical structure of the disk, see Eqs. ((17), (20)). Additional curves indicate the corresponding function for the 2D potential (equivalent to Eq. (24)) using different values of the smoothing parameter ϵ_p.

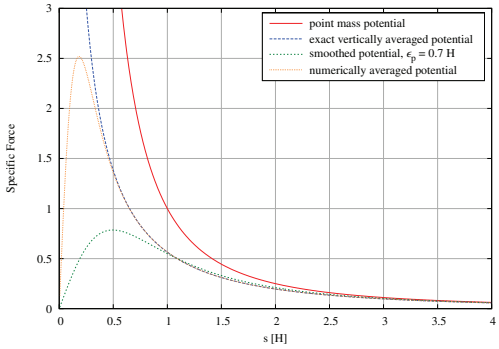

Fig. 3. Specific gravitational force F_p/Σ as a function of distance from the planet. Different approximations are shown: a) an ideal point mass (solid-red) that falls off as $1/r^2$; b) the exact averaged force according to Eqs. (25) and (20); c) the force according to the smoothed potential of Eq. (23) using here $\epsilon_p = 0.7H$; and d) a numerically integrated averaged force using 10 grid points in the vertical direction and a maximum $z_{max} = 5H$. The force is normalized such that $GM_p = 1$.

For Ψ_p^{2D} a simple smoothed version is often used, which reads

$$\Psi_p^{2D} = -\frac{GM_p}{\left(s^2 + \epsilon_p^2\right)^{\frac{1}{2}}}, \tag{23}$$

where ϵ_p is the smoothing length to the otherwise point mass potential, introduced to avoid numerical problems at the location of the planet. We will refer to this functional form of Ψ as the ϵ-potential, although it is sometimes named Plummer-potential as well. The force acting on each disk element is then calculated from the gradient of the potential.

A finite ϵ_p regularises the potential and guarantees stable numerical evolution. Additionally, it serves to account for the vertical stratification of the disk. Comparing torques acting on a planet in 2D and 3D simulations it has been suggested for the Lindblad torques that ϵ_p should be on the order of the vertical disk height, specifically $0.7H$, see Masset (2002). He pointed out, however, that for the corotation torques a lower value may be appropriate. Hence, often a value of $\epsilon = 0.6H$ is chosen. Here, we calculated the correct smoothing by a vertical average assuming an isothermal, vertically stratified disk. This will lead to a distance-dependent smoothing.

In Fig. 2 we compare the force correction obtained from the vertically averaging procedure and the 2D smoothed ϵ-potential. Specifically, we plot the function $I_p(s)$ for the Gaussian density profile together with the corresponding function for the 2D potential, which reads

$$I_\epsilon(s) = \frac{s^2}{(s^2 + \epsilon^2)^{\frac{3}{2}}} \frac{\sqrt{2\pi}H}{2}. \tag{24}$$

Because we are mainly interested in distances s up to a few H, we assume, that the disk height H does not change with radius. The unsmoothed $\epsilon_p = 0$ potential diverges as $1/s$ for short distances from the planet, leading to a $1/s^2$ force as expected for a point mass. Since the value of $I_p(s)$ remains finite for $s \to 0$, we see that a vertically extended disk reduces the divergence of the force to $1/s$. This is a clear indication that in 2D simulations the potential has to be smoothed for physical reasons alone, and that the assumption of a point mass potential will greatly overestimate the forces. As expected, the ϵ-potential strongly reduces the force for $s \to 0$ and always yields regular conditions at the location of the planet. Additionally, it appears that the value $\epsilon_p = 0.6H$ overestimates the potential slightly for $s \gtrsim H$ (green curve in Fig. 2).

Using the Gaussian isothermal density distribution, ρ_G, and the surface density Σ from Eq. (12), the force density of the planet acting on the disk can be written as

$$F_p^G = -\frac{GM_p\Sigma}{s} \frac{1}{H} \sqrt{\frac{2}{\pi}} I_p(s). \tag{25}$$

This expression could in principle be used directly in numerical simulations of planet-disk interaction. However, even though $I_p(s)$ can be solved in terms of Bessel-functions, in computational hydrodynamics this evaluation is not very efficient, because it has to be calculated once per timestep at each grid point. A possibility is to solve the integral $I_p(s)$ in Eq. (18) directly numerically using a limited number of vertical grid cells. In this case the integral is converted into a sum, where the exponential can be pre-calculated and tabulated at the corresponding nodes. For our purposes we found that only 10 vertical grid points give an adequate solution (see below). This is shown in Fig. 3 where we plot the specific force (acceleration) exerted by a planet on a disk element that is a distance s away. The force for a point mass falls off as $1/s^2$ while for small radii the exact vertically averaged force shows a $1/s$ behavior. Two approximations are displayed as well: the curve for the ϵ-potential given in Eq. (23), where we used a constant $\epsilon_p = 0.7H$. The numerically averaged curve refers to a numerical integration of $I_p(s)$ using 10 grid points in the z-range $[0, 5H]$. Note that because of the finite discretization no additional smoothing is required. Increasing the number of grid points increases the agreement with the exact averaged force even more for shorter distances s. The scaling of the distance with $1/H$ and the normalization of the force make the plot independent of the used vertical thickness of the disk. While the ϵ-potential agrees well for $s \gtrsim H$ with the exact averaged force, our numerical approximation agrees to much shorter distances. In Appendix B we show that simplified density distributions can lead to an equally good agreement. However, the advantage of the described vertical numerical integration procedure lies in its speed and in the fact that it leads directly to a regularized force for very short s. Also, it is easily generalizable, as will be shown in the next section.

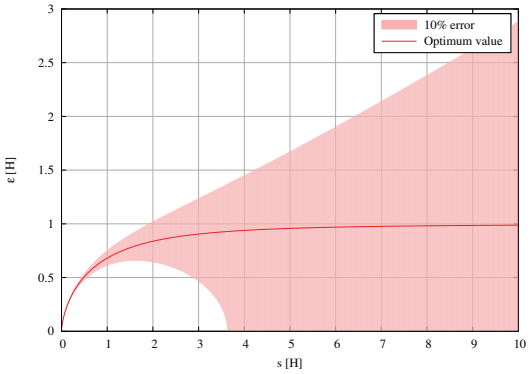

Fig. 4. Optimum value of ϵ_p in the smoothing potential of Eq. (23) as a function distance s from the planet. The shaded area illustrates which values of ϵ_p result in a force error of less than 10% with respect to the exact averaged value.

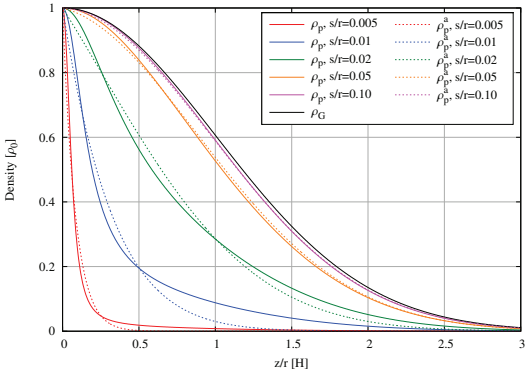

Fig. 5. Exact (see Eq. (29)) and approximate (see Eq. (30)) vertical density profiles for a disk with aspect ratio $h = 0.05$ for short distance s to a planet with mass ratio $q = 6 \times 10^{-5}$. The exact profiles are shown by the solid lines and the corresponding approximate ones in the same color but with dashed lines. For comparison the unperturbed Gaussian profile (see Eq. (10)) is shown in black for this H/r.

Because we can calculate $I_p(s)$ for the Gaussian profile numerically to any required accuracy, we can estimate the optimum $\epsilon_p(s)$ value for the smoothed potential in Eq. (23) for each point to obtain agreement with the exact averaged force. In Fig. 4 we display the correct $\epsilon_p(s)$ value against the distance. The range of ϵ_p in which the smoothed potential produces an error of less than 10% in the force compared to the correct value is illustrated by the shaded region. Obviously for very short distances it is important to use the correct ϵ_p and for long distances the exact value of ϵ_p does not play an important role. Through a Taylor expansion for $s \to \infty$ of the denominator in Eq. (18) of $I_p(s)$ it can be shown that

$$\lim_{s\to\infty} \epsilon_p(s) = H, \tag{26}$$

which can be expected because the disk has a vertical extent on the order H.

4.2. Taking the planet into account

In the previous section we have analyzed the forces acting on the planet considering an unperturbed disk with a given scale height as determined by the star, see Eq. (11). However, an embedded planet changes the disk structure, which will lead, for example, to a reduced thickness in the vicinity of the planet. This plays an important role for the torques acting on the planet. To estimate this effect we start from the vertical hydrostatic Eq. (8) taking an additional planet into account,

$$\frac{1}{\rho}\frac{\partial p}{\partial z} = -\frac{GM_* z}{(r^2+z^2)^{\frac{3}{2}}} - \frac{GM_p z}{(s^2+z^2)^{\frac{3}{2}}}, \tag{27}$$

where s is again the distance from the planet. For a vertically isothermal disk this can be integrated

$$\rho_p = \rho_0 \exp\left\{-\frac{1}{2}\frac{GM_*}{c_s^2 r^3}z^2 + \frac{GM_p}{c_s^2 s}\left[\frac{s}{(s^2+z^2)^{1/2}} - 1\right]\right\}, \tag{28}$$

where we assumed for the stellar contribution $z \ll r$, as before. Using the previous vertical thickness H (Eq. (11)) and the mass ratio $q = M_p/M_*$, this can be written as

$$\rho_p = \rho_0 \exp\left\{-\frac{1}{2}\frac{z^2}{H^2} + q\frac{r^3}{H^2 s}\left[\frac{s}{(s^2+z^2)^{1/2}} - 1\right]\right\}. \tag{29}$$

Because s is on the same order as z in the neighborhood of the planet, this equation cannot be simplified further. To still obtain an estimate of the expected effects, we *approximate* the vertical density stratification by

$$\rho_p^a = \rho_0 \exp\left\{-\left(\frac{1}{2}\frac{z^2}{H^2} + \frac{|z|}{H_p}\right)\right\}, \tag{30}$$

where we define the reduced scale height near the planet

$$H_p = \frac{4s^2H^2}{qr^3}. \tag{31}$$

This approximation for the vertical behavior of ρ_p leads to the correct limits for the integrated surface density Σ in the limits for very short and long s and is a reasonable approximation in between. From the definition of H_p in Eq. (31) we find that the distance s_t where the two scale heights are equal, i.e. $H_p = H$, is given by

$$\frac{s_t}{r} = \frac{1}{2}\left(\frac{q}{h}\right)^{1/2}, \tag{32}$$

where h is the relative scale height, $h = H/r$, of the disk. The location s_t denotes approximately a transitional distance from the planet. For $s \lesssim s_t$ the standard approximation of a Gaussian density distribution with the scale height H is no longer valid, and the influence of the planet dominates.

Figure 5 shows the exact (Eq. (29)) and the approximate (30) vertical density profiles for different distances to the planet and the comparison with the unperturbed Gaussian profile. For very short distances to the planet the effective height of the disk is much lower than in the unperturbed case. Obviously, ρ_p^a is only an approximation to ρ_p, but it captures the change in thickness of the disk, as induced by the planet, very well. We will show below that using ρ_p^a in the force calculations yields a very good approximation to the exact case.

To test how this new density-scaling influences the previous isothermal results for the planet's gravity, we calculated a corrected vertically averaged force using the modified density ρ_p according to

$$F_p(s) = -2GM_p s \int_0^{z_{max}} \frac{\rho_p}{(s^2+z^2)^{\frac{3}{2}}}\,dz. \tag{33}$$

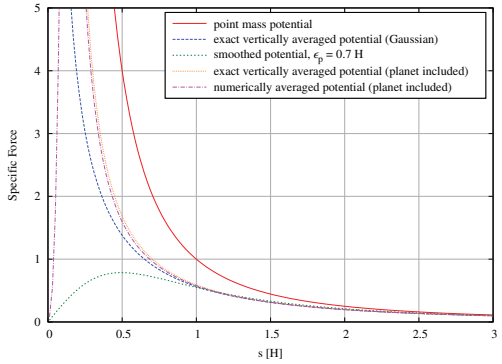

Fig. 6. Specific force F_p/Σ for different approximations. The first three curves are identical to Fig. 3 and are shown for comparison. The "exact" potential using ρ_p is shown in yellow and the approximates solution, using the simplified expression for the density ρ_p^a and only 10 vertical grid points, is shown in pink. A tapering function near the center was used for the latter to regularize the force.

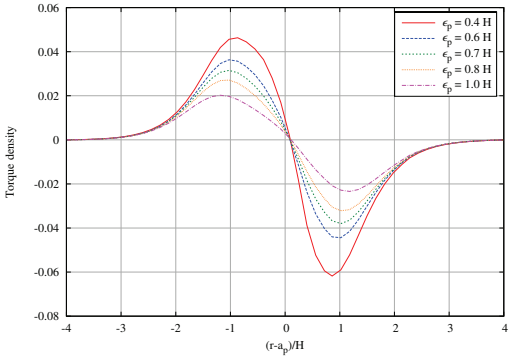

Fig. 7. Specific radial torque density in units of $(d\Gamma/dm)_0$ (see Eq. (36)) for embedded planet models using the ϵ potential with various ϵ_p. The simulations use a given $H = 0.05$, and the x-axis refers to the radial coordinate where a_p is the semi-major axis of the planet. The planet to star mass-ratio is $q = 6 \times 10^{-5}$. Other parameters of the simulations are stated in Sect. 4.3.

This integral has to be calculated numerically using an approximate z_{max}. Depending on the model to be calculated (either "exact" or approximate force), we substituted either ρ_p from Eq. (29) or the approximate ρ_p^a from Eq. (30). Since the presence of the planet alters the vertical height of the disk, z_{max} depends on the distance s from the planet. To estimate z_{max} we first define an effective vertical scale height

$$H_{eff} = \left(\frac{1}{H^2} + \frac{1}{H_p^2} \right)^{-1/2}, \tag{34}$$

which is an interpolation of the value at short and long distances from the planet. We choose to take $z_{max} = 6H_{eff}$ in the "exact" numerical evaluation where we use the density ρ_p and 1000 grid cells. In contrast, we apply $z_{max} = 3H_{eff}$ in the approximate numerical evaluation using ρ_p^a and only 10 vertical grid cells, see also Appendix A.

In Fig. 6 we display the results for the vertically integrated specific force F_p/Σ in various approximations. The first three curves (red, blue, green) correspond to those shown in Fig. 3 as an illustration. The "exact" potential using ρ_p is shown in yellow and the approximate solution using ρ_p^a in pink. The presence of the planet reduces the scale height of the disk, which leads to an enhancement of the force above the Gaussian, i.e., it diverges as s^{-2} for short distances. To regularize the approximate force, we added a tapering function that reduces it to zero in the vicinity of the planet (pink dashed-dotted curve) such that it can be used in hydrodynamic simulations, see Appendix A. Clearly the range of applicability for short s is much improved over the simple ϵ-potential. In contrast to the Gaussian approximation that uses the fixed thickness H, the force correction (with respect to the pure point mass potential) depends now on the mass of the planet as well, which enters through H_p.

4.3. Numerical simulations of planet-disk interactions

To test the formulation of the force, we performed numerical simulations of embedded planets in two and three dimensions where we use an isothermal equation of state. For this purpose we solved the 2D and 3D hydrodynamic equations for a viscous gas. We used a setup very similar to that of Kley & Crida (2008) and Kley et al. (2009). The planet with a mass ratios $M_p/M_* = 6 \times 10^{-5}$ is embedded at $r = 1$ in the disk with radial extent of 0.4–2.5. The disk is locally isothermal such that the aspect ratio H/r is constant. This implies a radial temperature gradient of $T(r) \propto r^{-1}$, while in the vertical direction T is constant. As a consequence, the unperturbed vertical density structure (in the 3D simulations) is Gaussian along the z-axis. The surface density falls off with radius as $\Sigma \propto r^{-1/2}$. We used a constant kinematic viscosity coefficient of $\nu = 10^{-5}$ in dimensionless units. This setup is such that without the planet the disk is exactly in equilibrium and would not evolve with time. At the radial boundaries damping boundary conditions were applied (de Val-Borro et al. 2006). In our simulations we used $H/r = 0.05$ and evolved the disk after the planet's insertion for about 100 orbits. To test our improved treatment of the force, we varied the planet mass and the scale height of the disk in comparison models. For the standard parameter, $h = 0.05$ and $q = 6 \times 10^{-5}$, we found for the transition distance $s_t \approx 0.35H$.

The embedded planet disturbs the disk and torques are exerted on it by the disk through gravitational back-reaction. These might lead to a change in the planet's orbital parameter. The strength of these torques will depend on the applied smoothing of the gravitational force. To illustrate the effect, it is convenient to study the radial torque distribution per unit disk mass $d\Gamma(r)/dm$, which we define here, following D'Angelo & Lubow (2010), such that the total torque Γ_{tot} is given as

$$\Gamma_{tot} = 2\pi \int \frac{d\Gamma}{dm}(r)\, \Sigma(r)\, r dr. \tag{35}$$

In other words, $d\Gamma(r)$ is the torque exerted by a disk annulus of width dr located at the radius r and having the mass dm. As $d\Gamma(r)/dm$ scales with the mass ratio squared and as $(H/r)^{-4}$, we rescale our results accordingly in units of

$$\left(\frac{d\Gamma}{dm} \right)_0 = \Omega_p^2(a_p)\, a_p^2 q^2 \left(\frac{H}{a_p} \right)^{-4}, \tag{36}$$

where the index p denotes that the quantities are evaluated at the planet's position, with the semi-major axis a_p.

In Fig. 7 we plot $d\Gamma(r)/dm$ obtained from 2D simulations using the ϵ-potential for the gravity of the planet and the standard

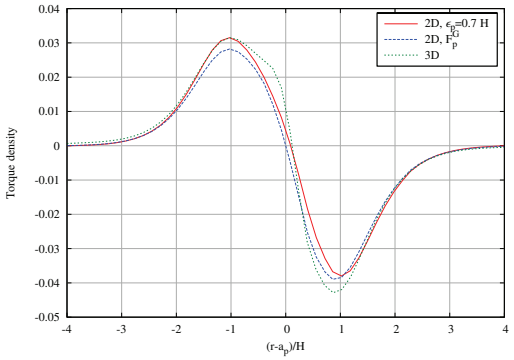

Fig. 8. Specific radial torque density in units of $(d\Gamma/dm)_0$ for embedded planet models for 2D models using ϵ-potential (red curve) and a numerically integrated force F_p^G (see Eq. (25)) that takes into account a Gaussian vertical density distribution (blue curve). The green curve refers to a full 3D model using the same physical model parameter as the 2D models. The 3D result is adapted from Kley et al. (2009) where the setup and numerics is described in more detail.

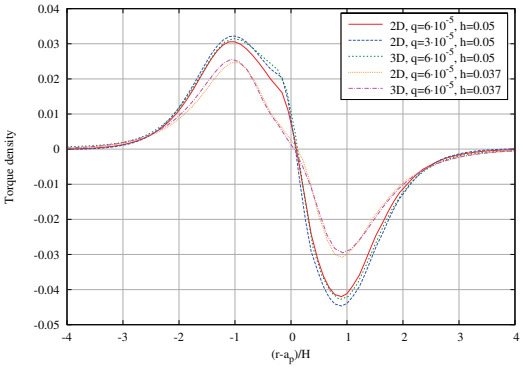

Fig. 9. Specific radial torque density in units of $(d\Gamma/dm)_0$ for 2D and 3D embedded planet models using different mass ratio and disk temperature. The first three curves represent models with the same disk temperature $H/r = 0.05$. The red curve corresponds to our standard model, the blue curve has a reduced planet mass $q = 3 \times 10^{-5}$, and the third (green curve) corresponds to a full 3D run. The next two curves (yellow and purple) refer to models with $H/r = 0.037$. The 2D runs used our approximate density distribution ρ_p^a in evaluating the gravitational force. The 3D results were adapted from Kley et al. (2009) where the setup and numerics is described in more detail.

fixed scale height H for the disk. The torque in this and the similar following plots are scaled to $(d\Gamma(r)/dm)_0$ as given in Eq. (36). Results for five values of the smoothing length are presented. Obviously, the value of ϵ_p has great impact on the amplitude of the torque density, and making the correct choice is important. We point out that the differences in the torque density also influence the total torques that determine the important migration rate. Because Γ_{tot} consists of positive and negative contributions of similar magnitude, even small errors in $d\Gamma(r)/dm$ can lead to large errors in Γ_{tot}. For the range of ϵ displayed in Fig. 7 we find a variation of Γ_{tot} larger than about a factor of 4. The best agreement in this case of $H/r = 0.05$ with 3D results is obtained for ϵ in between $0.6-0.7H$.

In Fig. 8 we compare two different force treatments for 2D simulations to a full 3D run. Results for the $\epsilon_p = 0.7H$ potential are given by the red curve, and the blue curve corresponds to the vertically averaged force F_p^G according to Eq. (25), which assumes a Gaussian vertical density profile. In magnitude the $\epsilon_p = 0.7H$ potential represents the vertically averaged results reasonably well, but it behaves differently close to the planet. The additional green curve corresponds to a full 3D (locally) isothermal simulation as presented in Kley et al. (2009) (their Fig. 10, purple curve). The 3D runs use an identical physical setup and a more realistic cubic-potential with a smoothing of $r_{sm} = 0.5$. Both 2D results are on the same order as the 3D run, but show small deviations that can lead to larger variations in the total torque, end hence the migration rate, because the positive and negative contributions to the radial torque density are of similar magnitude.

To test the applicability of our new procedure for treating the gravity in 2D simulations, we performed runs with different mass ratio and temperature in the disk. The results of 2D and 3D simulations are shown in Fig. 9, where the torque density $d\Gamma(r)/dm$ is plotted. The first set of simulations refers to $H/r = 0.05$, where we compared the standard model in 2D and 3D to a run with half the planet mass. The next two curves show results of 2D and 3D simulations for $H/r = 0.037$. Despite the indicated differences in the parameter, all models used the same physical setup as described above. The 2D runs used our approximate density distribution ρ_p^a in evaluating the gravitational force. The 3D results are adapted from Kley et al. (2009) where the setup and numerics is described in more detail. Firstly, all five curves show very similar overall behavior, confirming the scaling with $(d\Gamma(r)/dm)_0$. The reduced amplitude of the $H/r = 0.037$ models is due to the onset of gap formation. Secondly, the agreement of the 2D and 3D runs is very good indeed. For example, upon varying the scale height, the change in shape of the curves is identical in 2D and 3D runs (yellow and purple) curve. We point out that the value of ϵ to obtain the best agreement of the total torque Γ_{tot} in 2D and 3D simulations may depend on the value of H, because of the influence of the planet. Hence, it is always advisable to perform the simulations using the vertical integration of the force.

To additionally validate our simulations we compare in Fig. 10 our 2D and 3D results obtained for the standard model to an analytic fit by D'Angelo & Lubow (2010) for the same disk parameter. Although the fit has been developed for a smaller planet mass, the agreement of the two 3D results is excellent. This is interesting because our planet mass of 20 M_{Earth} is already in the range where non-linear effects should set in. The 2D torque shows the same amplitude, but small differences are visible just inside the planet. In isothermal disks the flow close to the planet is not in exact hydrostatic equilibrium anymore. However, full 3D high-resolution isothermal simulations (D'Angelo et al. 2003) have shown that vertical velocities are only large inside the Roche region of the planet. This explains the good agreement of the 2D approximation with the full 3D case.

5. The potential of a self-gravitating disk

Now we turn to full self-gravitating disks where a smoothing of the gravitational potential is required as well to account for the finite thickness of the disk. The potential at a point $\boldsymbol{r}$ generated by the whole self-gravitating disk is given by

$$\Psi_{sg}(\boldsymbol{r}) = -\int_{\text{Disk}} \frac{G\rho(\boldsymbol{r}')}{|\boldsymbol{r}-\boldsymbol{r}'|}\,\mathrm{d}\boldsymbol{r}'. \tag{37}$$

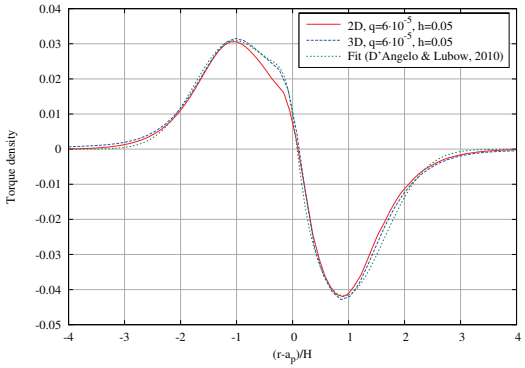

Fig. 10. Specific radial torque density in units of $(d\Gamma/dm)_0$ for 2D and 3D embedded planet models using different mass ratio and disk temperature. The first two curves are identical to those in the previous figure, and the third is a fit presented by D'Angelo & Lubow (2010) corresponding to the model with $T(r) \propto r^{-1}$ and $\Sigma(r) \propto r^{-1/2}$.

The smoothing required to obtain the potential in the midplane has been analyzed for this situation by Huré & Pierens (2009). However, if one is interested in problems of fragmentation, it is more convenient to analyze the force between to individual elements (segments) of the disk. Let us consider the force between two such disk segments that are a separated by the distance $\boldsymbol{s}$, see Fig. 11. The potential at the location $\boldsymbol{r}$ generated by a disk element located at $\boldsymbol{r}'$ which is a projected distance s away is given by

$$\Psi_{\rm sg}(\boldsymbol{r}) = -\iiint \frac{G\rho(r',\varphi',z')}{(s^2+(z-z')^2)^{\frac{1}{2}}}\,{\rm d}z'\,{\rm d}A', \tag{38}$$

where dA' is the surface element of the disk in the $r-\varphi$-plane at the point $\boldsymbol{r}'$. The vector $\boldsymbol{s}$ is defined in analogy to Eq. (14) and illustrated in Fig. 11.

The force at the location $\boldsymbol{r}$ generated by this vertically extended disk element is calculated from the gradient of the potential. The vertically averaged force density can then be written in analogy to Eq. (15) as

$$\begin{aligned} F_{\rm sg}(s) &= -\int \rho(r,\varphi,z)\frac{\partial\Psi_{\rm sg}}{\partial s}\,{\rm d}z \\ &= -Gs\iiiint \frac{\rho(r',\varphi',z')\,\rho(r,\varphi,z)}{(s^2+(z-z')^2)^{\frac{3}{2}}}\,{\rm d}z'\,{\rm d}A'\,{\rm d}z. \end{aligned} \tag{39}$$

The evaluation of this integral depends on the vertical stratification of the density at both locations $\boldsymbol{r}$ and $\boldsymbol{r}'$. As before, we consider locally isothermal disks. For weakly self-gravitating disks the density structure is then given by the Gaussian form in Eq. (10). However, similar to an embedded planet the disk's self-gravity will modify the vertical profile. Following our previous treatment of the embedded planet, we first analyzed the smoothing required for a disk that has an unperturbed Gauss profile and will then allow for modifications.

5.1. Unperturbed disk

For a locally isothermal disk and with Eq. (16) we obtain

$$F_{\rm sg}(s) = -G\rho_0(r,\varphi)\iint \rho_0(r',\varphi')\,{\rm d}A' \cdot 2I_{\rm sg}(s), \tag{40}$$

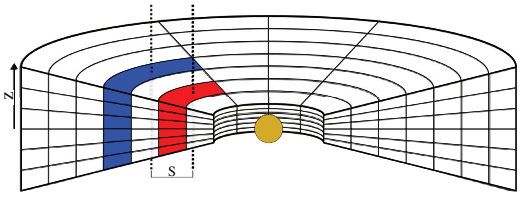

Fig. 11. Geometry of a protoplanetary disk for calculations with self-gravity. We calculate the gravitational force exerted by a vertical slice of the disk (blue) on another vertical slice of the disk (red), separated by a distance s. Two vertical integrations have to be performed along the dashed lines that go through the cell centers. To obtain the total force between the two segments, this value has to be multiplied by the corresponding areas, see also Eq. (39).

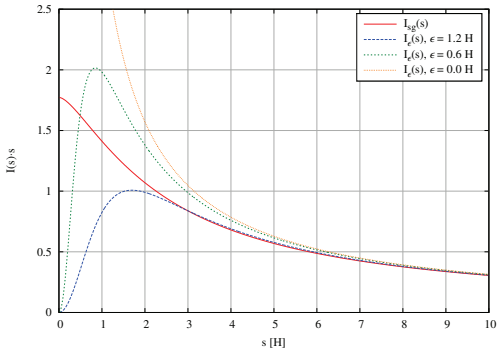

Fig. 12. Force correction function $I_{\rm sg}(s)$ multiplied by s resulting from an integration over the vertical structure of the disk, see Eqs. ((40), (41)). Additional curves indicate the corresponding function for the 2D potential (Eq. (24)) using different values of the smoothing parameter $\epsilon_{\rm sg}$.

where we defined the function $I_{\rm sg}(s)$ by

$$I_{\rm sg}(s) = \frac{1}{2}\int_{-\infty}^{\infty}\int_{-\infty}^{\infty} \frac{\rho_z(c^2y^2)\,\rho_z(c^2y'^2)}{(1+(y-y')^2)^{\frac{3}{2}}}\,{\rm d}y'\,{\rm d}y, \tag{41}$$

where the normalized vertical distance y and the quantity c are given by Eq. (19) again assuming a constant H. This integral cannot be calculated directly for the standard Gaussian profile, and we will evaluate it numerically.

In 2D numerical simulations usually a simple smoothed potential is used instead of calculating the correct averaging. This $\epsilon_{\rm sg}$-potential reads as

$$\Psi^{\rm 2D}_{\rm sg}(s) = -\iint \frac{G\Sigma(\boldsymbol{r}')}{\left(s^2+\epsilon^2_{\rm sg}\right)^{\frac{1}{2}}}\,{\rm d}A', \tag{42}$$

where $\epsilon_{\rm sg}$ is the smoothing length. The force acting on each disk element is then calculated from the gradient of $\Psi^{\rm 2D}_{\rm sg}$.

In Fig. 12 we compare the force correction obtained from the vertically averaging procedure and the 2D smoothed potential for a disk height that does not change with radius. Because $I_{\rm sg}(s)$ diverges for short distances, we multiply it by s. Because we are interested in local effects with distances s up to a few H, we assumed for the plot that the disk height H is constant. Comparing this result to the corresponding force correction function for the planet in Fig. 2, it is obvious that for the self-gravitating case a

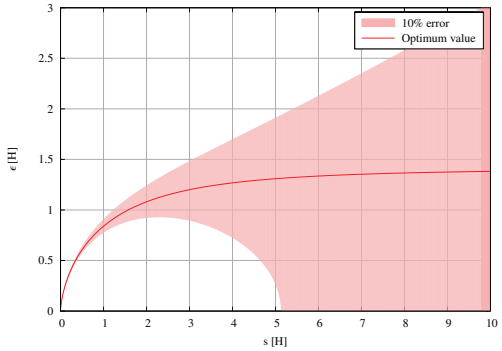

Fig. 13. Optimum value of ϵ_{sg} in the smoothing potential of Eq. (42) as a function of distance s using a Gaussian vertical stratification. The colored area illustrates which values of ϵ_{sg} result in an error of the force correction value of less than 10%.

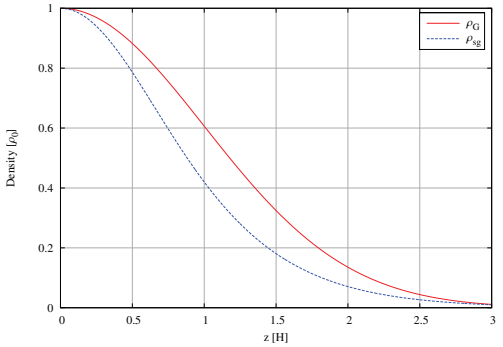

Fig. 14. Vertical density profiles of the disk with for a self-gravitating disk (see Eq. (46)) with $Q = 1$. For comparison the unperturbed Gaussian profile (see Eq. (10)) is shown in red.

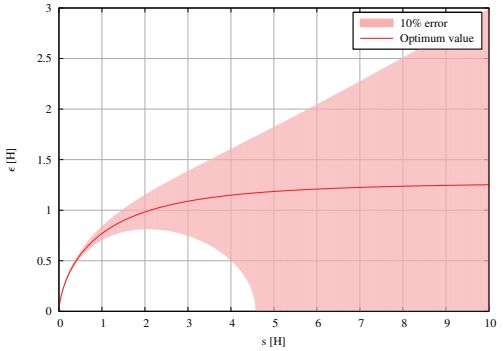

Fig. 15. Optimum value of ϵ_{sg} in the smoothing potential of Eq. (42) versus distance s using a vertical stratification caused by self-gravity with $Q = 1$. The colored area illustrates which values of ϵ_{sg} result in an error of the force correction value of less than 10%.

larger smoothing is required for the ϵ-potential than in the planet case. Here, a value of $\epsilon = 1.2$ seems to be a good choice. Lower values, already $\epsilon = 0.6$, considerably overestimate the force. We attribute this larger required smoothing with the double vertical averaging that has to be performed in this case.

From the numerically calculated $I_{sg}(s)$ for the Gaussian profile we can calculate the best $\epsilon_{sg}(s)$ value for the smoothing potential in Eq. (42) at each distance s to obtain the right force correction value. In Fig. 13 we display the optimum $\epsilon_{sg}(s)$ value versus distance. The range of ϵ_{sg} over which the smoothing potential produces an error of less than 10 % is shaded. Cleary for short distances it is crucial to use the correct value of ϵ_{sg}, whereas for long distances the influence of ϵ_{sg} becomes negligible. Because we now have to account twice for the vertical extent of the disk here compared to the planet case, we obtain a higher limiting value of

$$\lim_{s\to\infty} \epsilon_{sg}(s) = \sqrt{2}H. \tag{43}$$

This value was obtained through numerical calculation up to the sixth significant digit for $s = 1000H$, and we verified it through a Taylor expansion of the denominator in Eq. (42). As before, it is interesting that the required optimum smoothing remains finite, even for very long distances. This result agrees with Huré & Pierens (2009).

5.2. Taking the disk into account

Now we consider the correction for a disk where self-gravity has modified the vertical structure. For that purpose, we considered the case of a pure self-gravitating disk, neglecting the gravitational potential of the central mass. Assuming a large disk with a slowly varying surface density $\Sigma(r)$, then the derivate with respect to z of the disk potential given in Eq. (37) simplifies (Mestel 1963) to

$$\frac{\partial \Psi_{sg}}{\partial z} = 2\pi G\Sigma(r), \tag{44}$$

and consequently the hydrostatic Eq. (8) changes to

$$\frac{1}{\rho}\frac{\partial p}{\partial z} = -2\pi G\Sigma(r). \tag{45}$$

For a vertically isothermal disk this can be integrated (Spitzer 1942) to

$$\rho_{sg}(r,\varphi,z) = \rho_0(r,\varphi)\,\cosh^{-2}\left(\frac{z}{H_{sg}}\right), \tag{46}$$

where the vertical scale height H_{sg} is defined by

$$H_{sg} = \frac{c_s^2}{\pi G\Sigma} = \frac{c_s\Omega_K}{\pi G\Sigma}H \cong QH, \tag{47}$$

with the Toomre parameter Q (Toomre 1964). Figure 14 shows the changed vertical density profiles in the self-gravitating case compared to the unperturbed Gaussian for $H = H_{sg}$ or $Q = 1$, respectively. The self-gravitating profile is steeper and therefore, for equal surface density, the mass is consequently located nearer to the midplane of the disk. This is expected because the vertical component of the disk's gravitational potential is, with $2\pi G\Sigma(r) \sim GM/r^2$, by a factor of about r/H larger than in Eq. (8), and so the mass is more concentrated toward the midplane.

Now we can calculate the force correction function $I_{sg}(s)$ of Eq. (41) with the self-gravitating vertical density profile ρ_{sg}. In analogy to the unperturbed case, this can be used to calculate an optimum ϵ_{sg} for the ϵ-potential. In Fig. 15 we display the correct $\epsilon_{sg}(s)$ value against distance. The optimum ϵ_{sg} for

Table 1. Parameters of the disk model.

Star mass ($M_{\rm primary}$)	$1.0\,M_\odot$
Disk mass ($M_{\rm disk}$)	$0.4\,M_\odot$
Adiabatic index (γ)	5/3
Mean-molecular weight (μ)	2.4
β-Cooling (β)	20
Initial density profile (Σ)	$\propto r^{-2}$
Initial temperature profile (T)	$\propto r^{-1}$
Initial disk aspect ratio (H/r)	0.1
Grid ($N_r \times N_\varphi$)	512×1536
Computational domain ($R_{\rm min} - R_{\rm max}$)	20–250 AU

Notes. The top entry refers to host star. The following give the disk properties, and then the initial disk setup and the computational parameter are given.

this value of Q is always lower than our previous unperturbed Gaussian case. For the limit $s \to \infty$ we find a value about 10% lower. This is in consistency with the lower effective vertical scale height, because more mass is located near the midplane.

In most self-gravitating disks the vertical structure will be affect by both the central mass object and the self-gravity of the disk. Then it is to be expected that the correct $\epsilon_{\rm sg}$ is a value between the two extreme cases. The combined situation where self-gravity and the central mass both contribute has been considered by Lodato (2007). For clarity, we treat the two cases separately here.

5.3. Numerical simulations of self-gravitating disks

To demonstrate the influence of $\epsilon_{\rm sg}$ in numerical simulations, we analyzed the effects of different values of $\epsilon_{\rm sg}$ on the fragmentation conclusions of a self-gravitating disk. For that purpose, we adopted a disk model from Baruteau et al. (2011). Table 1 shows all important disk parameters. We simulated the disk twice using the `ADSG` version of the `FARGO` code (Baruteau & Masset 2008; Masset 2000) for 5000 years with values of $0.6H$ and $0.006H$ for $\epsilon_{\rm sg}$. Both models include the self-gravity of the disk and a simple β-cooling model, which is defined by

$$\frac{\partial E}{\partial t} = -\frac{E\Omega}{\beta}, \tag{48}$$

where E is the internal energy, Ω the angular velocity and β a constant. The disk must cool fast enough to be able to fragment, which is otherwise prevented by compressional heating. Gammie (2001) showed that this is the case for $\beta \lesssim 3$ and Rice et al. (2005) found later a dependency from the equation of state for β and suggested a $\beta \lesssim 7$ for $\gamma = 5/3$.

Meru & Bate (2011a) pointed out that the previous results had not converged with increasing resolution and that the critical value, $\beta_{\rm crit}$, may be higher than previously thought. They measured an $\beta_{\rm crit}$ of ~18 for their highest resolution. Because we use $\beta = 20$ in our models, we do not expect them to fragment in any case.

Another stability criterion can be described by the Toomre stability parameter Q, which is defined by

$$Q = \frac{\kappa c_{\rm s}}{\pi G \Sigma}, \tag{49}$$

where $c_{\rm s}$ is the sound speed in the disk and κ the epicyclic frequency. Toomre (1964) showed that for values of $Q \geq 1$ an axisymmetric disk should be stable. As shown in Fig. 16, the modeled disks have an initial Q value of 1.85–2.2 depending on the radial distance to the star, and thus should not be fragmenting.

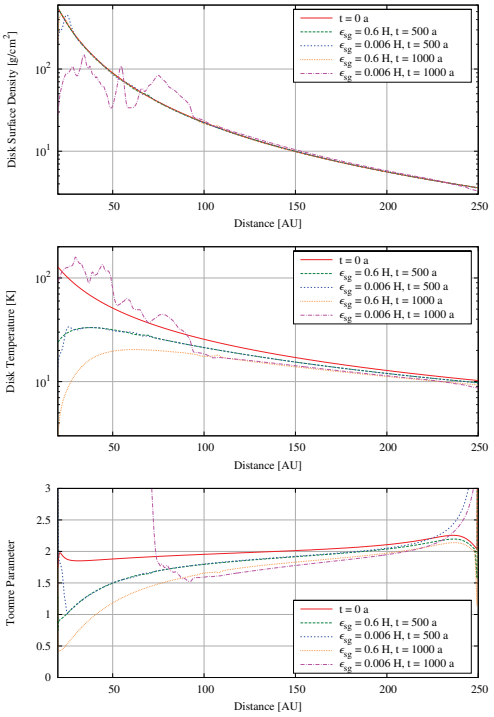

Fig. 16. Radial dependency of surface density (*top*), midplane temperature (*middle*) and Toomre parameter (*bottom*) of the two disk models with $\epsilon_{\rm sg} = 0.6H$ and $\epsilon_{\rm sg} = 0.006H$ for different timestamps. At $t = 0$ a both simulations match because they have identical start conditions. In the first 500 years they behave very similar but then their further evolution diverges drastically.

In the first 500 years both disks cool down in the central parts of the disk from about 120 K to about 30 K, resulting in Q values of 1 at the inner edge of the disk, which means that they are not Toomre-stable anymore, but still should not fragment because the cooling constant β is higher than the critical value required for fragmentation. After 500 years both simulations start to differ. The $\epsilon_{\rm sg} = 0.006H$ model fragments within about 500 years in the inner region of the disk whereas, the $\epsilon_{\rm sg} = 0.6H$ model needs about 1000 years to start developing small spiral arms in the inner region. After 5000 years two fragments have survived in the $\epsilon_{\rm sg} = 0.006H$ disk with fragment masses of 16.5 $M_{\rm Jup}$ and 8.3 $M_{\rm Jup}$. The $\epsilon_{\rm sg} = 0.6H$ model only shows spiral arms and no signs of fragmentation. Even after 50000 years we did not observe any fragments. Figure 17 shows the surface density distribution of both models after 5000 years.

In Sect. 5.1 we suggested an $\epsilon_{\rm sg}$ on the order of unity to obtain results that can compare to 3D simulations. Because the $\epsilon_{\rm sg} = 0.6H$ model did not fragment as predicted by the stability criteria, this seems to support the validity of our estimate for $\epsilon_{\rm sg}$. The very short $\epsilon_{\rm sg}$ in the $\epsilon_{\rm sg} = 0.006H$ model overestimates the gravitational forces on short distances (see Fig. 12) and therefore excites disk fragmentation.

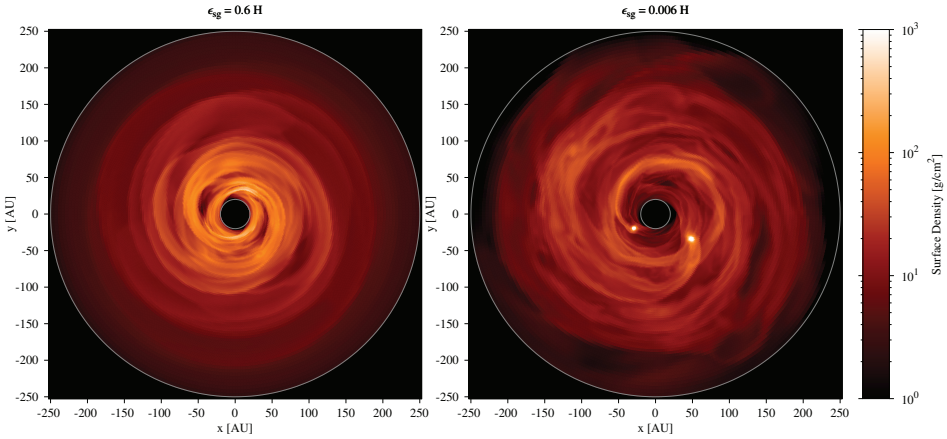

Fig. 17. Surface density of two disks after 5000 years which started from the same initial condition but with different values for the smoothing parameter ϵ_{sg} of the gravitational potential. The gray circle shows the computational domain.

6. Summary and conclusions

We analyzed the smoothing of gravity in thin 2D disk simulations for the embedded planet and self-gravitating case. Starting from the vertically averaged hydrodynamic equations, we first showed that the gravitational force has to be calculated using a density-weighted average of the 3D force, see Eq. (5). Because this depends on the density distribution, there cannot be a general equivalent 2D version of the potential (Eq. (22)). To be able to explicitly calculate the averaged force, we first used a locally isothermal disk structure in which the vertical density stratification is Gaussian.

For the embedded planet case the resulting force can be calculated analytically. In full 2D hydrodynamic simulations we compared the resulting torque density acting on the planet for the ϵ-potential (23) and the "exact" averaged force. We found that the overall magnitude of the torque is best modeled using a smoothing of $\epsilon = 0.7H$, while there remain significant differences to the full 3D case, also in the total torque. Taking the modification of the density stratification induced by the planet into account leads to a much reduced vertical thickness of the disk in the vicinity of the planet. We presented a simplified analytical form for the modified vertical density stratification with a planet, the details of the numerical implementation are given in the appendix. Using this in 2D simulations leads to very good agreement of the torque density with full 3D calculations of embedded planets on circular orbits. By varying the disk height and the mass of the planet, we showed that the torque density scales as expected with $(\mathrm{d}\Gamma(r)/\mathrm{d}m)_0$, see Eq. (36).

Because the modified density approximation that includes the planet is based on vertical hydrostatic equilibrium, it is not clear, however, whether it is valid for planets on non-circular or inclined orbits. Here, the variations occur on the orbital timescale and to establish hydrostatic equilibrium, the thermal timescale must be on the same order. In the situation of multiple planets that may interact strongly, the same restrictions may apply. Despite these restrictions, we believe that using this prescription will enhance the accuracy of 2D simulations considerably. We expect that our procedure can be generalized to the radiative case using suitable vertical averages, but this needs to be developed.

For the self-gravitating case we showed that the required smoothing, $\epsilon \approx H$, is even larger than in the planetary case. We attribute this to the necessity of a double averaging over the vertical height of the disk. Owing to the complex integration, the integrals cannot be solved analytically in this case. Taking into account self-gravity lowers the required smoothing because the vertical scale height is reduced due to the additional gravity. In more strongly self-gravitating systems, which have a Toomre parameter $Q \approx 1$, non-axisymmetric features may occur. Because the standard self-gravity solvers require a smoothing that scales with radius, one has to take an approximate average in non-axisymmetric situations. The same applies for disks that are close to the fragmentation limit. As shown by our last example, the choice of smoothing may affect the conclusions on whether the disk will fragment or not. Through detailed comparisons with full 3D simulations a suitable smoothing may be found.

Acknowledgements. We thank Clément Baruteau and Sijme-Jan Paardekooper for useful discussions. Tobias Müller received financial support from the Carl-Zeiss-Stiftung. Farzana Meru and Wilhelm Kley acknowledge the support of the German Research Foundation (DFG) through grant KL 650/8-2 within the Collaborative Research Group FOR 759: *The formation of Planets: The Critical First Growth Phase*, and Farzana Meru is supported by the ETH Zurich Postdoctoral Fellowship Programm as well as by the Marie Curie Actions for People COFUND program. Most of the simulations were performed on the bwGRiD cluster in Tübingen, which is funded by the Ministry for Education and Research of Germany and the Ministry for Science, Research and Arts of the state Baden-Württemberg, and the cluster of the Forschergruppe FOR 759 "The Formation of Planets: The Critical First Growth Phase" funded by the Deutsche Forschungsgemeinschaft. Finally, we thank the referee for the very constructive and and helpful comments.

Appendix A: Integration of the force density

Here, we briefly outline a numerically fast and convenient method to vertically integrate the force for the embedded planet case. Specifically, we plan to evaluate the force density F_p in Eq. (33), which reads

$$F_\mathrm{p}(s) = -2GM_\mathrm{p}s \int_0^{z_\mathrm{max}} \frac{\rho_\mathrm{p}}{(s^2+z^2)^{\frac{3}{2}}}\,\mathrm{d}z. \tag{A.1}$$

As pointed out in the text, we used for the (approximate) numerical integration a maximum z of $z_\mathrm{max} = 3H_\mathrm{eff}$, with H_eff given by

Eq. (34). The interval $[0, z_{\max}]$ is divided into N_z equal intervals with the size $\Delta z = z_{\max}/N_z$. The integral in Eq. (A.1) is replaced with the following sum

$$\int_0^{z_{\max}} \frac{\rho_p \, dz}{(s^2+z^2)^{\frac{3}{2}}} \rightarrow \sum_{k=1}^{N_z} \frac{\rho_p(z_k)\,\Delta z}{(s^2+z_k^2+r_s^2)^{\frac{3}{2}}}, \tag{A.2}$$

where the N_z nodes are located at $z_k = (k-1/2)\Delta z$. We introduce a small smoothing, r_s, here to keep the sum regular at short distances s. In the simulation presented in the paper we used $r_s = 0.1 R_{\rm Hill}$ throughout, which is much shorter than the unperturbed vertical height H. In the 2D hydrodynamic simulations we used $N_z = 10$, which makes the method feasible numerically.

The specific force, or acceleration (F_p/Σ), is then obtained by dividing through the integrated surface density

$$\Sigma = 2 \sum_{k=1}^{N_z} \rho_p(z_k)\,\Delta z, \tag{A.3}$$

using the same nodes. In 2D simulations Σ is one of the evolved quantities and this relation can be used to calculate the otherwise unknown midplane density ρ_0. Because the vertical number of grid points is very small ($N_z = 10$), the method is reasonably fast and can be used in numerical planet-disk simulations. Additionally, it only needs to be evaluated in the vicinity of the planet and could be omitted farther out. Nevertheless, despite the coarseness of the integration, the agreement with the "exact" force and torque is excellent. For numerical stability we smooth the resulting force using the following tapering function

$$f_{\rm taper}(s) = \frac{1}{\exp\left[-(s-r_t)/(0.2 r_t)\right]+1} \tag{A.4}$$

with the tapering cutoff-length r_t, for which we used in our simulations $r_t = 0.2 R_{\rm Hill}$. The purple curve in Fig. 6 exactly corresponds to the procedure described here, using the stated parameter.

Finally, we point out that for the stellar contribution to the potential

$$\Psi_*(\boldsymbol{r}) = -\frac{GM_*}{|\boldsymbol{r}-\boldsymbol{r}_*|} = -\frac{GM_*}{(r^2+z^2)^{\frac{1}{2}}}, \tag{A.5}$$

a very similar vertical averaging needs to be performed. However, because the vertical profile is always Gaussian, the nodes can be precomputed and the exponential function has only to be evaluated once for the N_z nodes per grid point and timestep.

Appendix B: Approximate vertical density profiles

To simplify some estimates and obtain an idea of the functional behavior of the forces, it is useful to study simpler vertical density stratifications. Here, we present results for a parabolic and quartic behavior. The corresponding density stratifications read

$$\rho_z^{(2)} = \left[1 - \frac{1}{2}\left(\frac{z}{H^{(2)}}\right)^2\right] \tag{B.1}$$

for the parabolic form, and

$$\rho_z^{(4)} = \left[1 - \frac{1}{2}\left(\frac{z}{H^{(4)}}\right)^2 + \frac{1}{16}\left(\frac{z}{H^{(4)}}\right)^4\right] \tag{B.2}$$

for the quartic form. The vertical heights $H^{(2)}$ and $H^{(4)}$ of the models are specified such that the corresponding surface and midplane densities match the isothermal case, see Eq. (12). We obtain $H^{(2)} = 3/4\sqrt{\pi}\,H$ and $H^{(4)} = 15/16\sqrt{\pi/2}\,H$. Figure B.1 shows all three vertical density profiles in comparison.

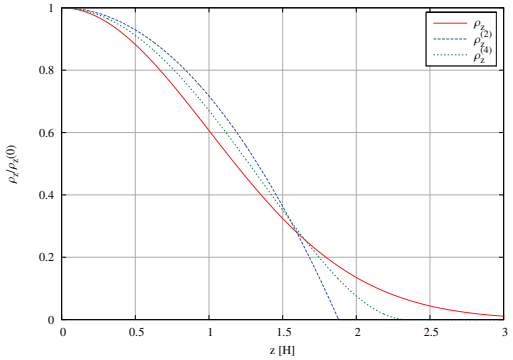

Fig. B.1. Gaussian vertical profile ρ_z (solid line) compared with the parabolic vertical profile $\rho_z^{(2)}$ and fourth-order vertical profile $\rho_z^{(4)}$. They all have the same area below the curves and yield the identical surface density.

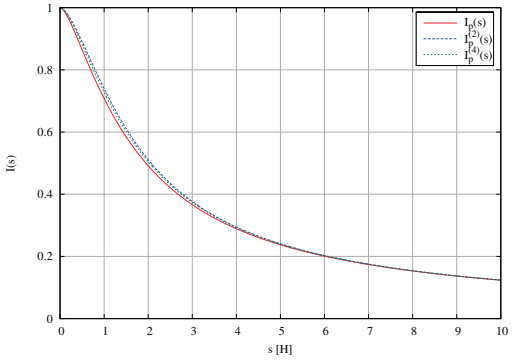

Fig. B.2. Force correction functions for different vertical density profiles. $I_p(s)$ is the numerically calculated force correction function for the Gaussian vertical profile ρ_z. $I_p^{(2)}(s)$ and $I_p^{(4)}(s)$ are the analytically calculated force correction functions for the parabolic vertical profile $\rho_z^{(2)}$ and the fourth-order vertical profile $\rho_z^{(4)}$.

These density stratifications are then used to calculate the vertically integrated force and to obtain the corresponding force correction functions. Here, the vertical integrations extend to that $z_{\max}$ value where the density vanishes. For the two distributions we find $z_{\max}^{(2)} = \sqrt{2}\,H^{(2)}$ and $z_{\max}^{(4)} = 2H^{(4)}$. For the second-order integral we find

$$I_p^{(2)}(s) = \sqrt{1+\frac{1}{2}c_2^2} - \frac{1}{2}c_2^2 \,\mathrm{arcsinh}\left(\frac{\sqrt{2}}{c_2}\right), \tag{B.3}$$

and for the fourth-order integral

$$I_p^{(4)}(s) = \frac{3c_4^2+8}{16}\sqrt{c_4^2+4} - \frac{c_4^2}{2}\left(1+\frac{3c_4^2}{16}\right)\mathrm{arcsinh}\frac{2}{c_4}. \tag{B.4}$$

Here, we defined $c_2 = s/H^{(2)}$ and $c_4 = s/H^{(4)}$. As Fig. B.2 illustrates, for the unperturbed disk (without a planet) these functions agree reasonably well with the Gaussian value also for smaller

separations s. For long distances all studied force correction functions ($I_\mathrm{p}, I_\epsilon, I_\mathrm{p}^{(2)}$ and $I_\mathrm{p}^{(4)}$) approach each other. These simpler profiles may be also useful in the study of self-gravitating disks.

References

Baruteau, C., & Masset, F. 2008, ApJ, 678, 483
Baruteau, C., Meru, F., & Paardekooper, S.-J. 2011, MNRAS, 416, 1971
D'Angelo, G., & Lubow, S. H. 2010, ApJ, 724, 730
D'Angelo, G., Kley, W., & Henning, T. 2003, ApJ, 586, 540
de Val-Borro, M., Edgar, R. G., Artymowicz, P., et al. 2006, MNRAS, 370, 529
Dong, R., Rafikov, R. R., Stone, J. M., & Petrovich, C. 2011, ApJ, 741, 56
Gammie, C. F. 2001, ApJ, 553, 174
Huré, J.-M., & Pierens, A. 2009, A&A, 507, 573
Kley, W., & Crida, A. 2008, A&A, 487, L9
Kley, W., Bitsch, B., & Klahr, H. 2009, A&A, 506, 971
Li, H., Li, S., Koller, J., et al. 2005, ApJ, 624, 1003
Li, H., Lubow, S. H., Li, S., & Lin, D. N. C. 2009, ApJ, 690, L52
Lodato, G. 2007, Nuovo Cimento Riv. Ser., 30, 293
Masset, F. 2000, A&AS, 141, 165
Masset, F. S. 2002, A&A, 387, 605
Meru, F., & Bate, M. R. 2011a, MNRAS, 411, L1
Meru, F., & Bate, M. R. 2011b, MNRAS, 410, 559
Mestel, L. 1963, MNRAS, 126, 553
Miyoshi, K., Takeuchi, T., Tanaka, H., & Ida, S. 1999, ApJ, 516, 451
Paardekooper, S.-J., & Papaloizou, J. C. B. 2009, MNRAS, 394, 2283
Paardekooper, S.-J., Baruteau, C., & Meru, F. 2011, MNRAS, 416, L65
Pierens, A., & Huré, J.-M. 2005, A&A, 433, L37
Rice, W. K. M., Lodato, G., & Armitage, P. J. 2005, MNRAS, 364, L56
Spitzer, Jr., L. 1942, ApJ, 95, 329
Tanaka, H., Takeuchi, T., & Ward, W. R. 2002, ApJ, 565, 1257
Toomre, A. 1964, ApJ, 139, 1217

A&A 546, A99 (2012)
DOI: 10.1051/0004-6361/201219719

Astronomy & Astrophysics

Low-mass planets in nearly inviscid disks: numerical treatment

W. Kley[1], T. W. A. Müller[1], S. M. Kolb[1], P. Benítez-Llambay[2], and F. Masset[3]

[1] Institut für Astronomie & Astrophysik, Universität Tübingen, Auf der Morgenstelle 10, 72076 Tübingen, Germany
e-mail: wilhelm.kley@uni-tuebingen.de
[2] Instituto de Astronomía Teórica y Experimental, IATE (CONICET), Observatorio Astronómico, Universidad Nacional de Córdoba, Laprida 854, X5000BGR, Córdoba, Argentina
[3] Instituto de Ciencias Físicas, Universidad Nacional Autónoma de México, Apdo. Postal 48-3, 62251 Cuernavaca, Morelos, Mexico

Received 30 May 2012 / Accepted 9 August 2012

ABSTRACT

Context. Embedded planets disturb the density structure of the ambient disk, and gravitational back-reaction possibly will induce a change in the planet's orbital elements. Low-mass planets only have a weak impact on the disk, so their wake's torque can be treated in linear theory. Larger planets will begin to open up a gap in the disk through nonlinear interaction. Accurate determination of the forces acting on the planet requires careful numerical analysis. Recently, the validity of the often used fast orbital advection algorithm (FARGO) has been put into question, and special numerical resolution and stability requirements have been suggested.
Aims. We study the process of planet-disk interaction for low-mass planets of a few Earth masses, and reanalyze the numerical requirements to obtain converged and stable results. One focus lies on the applicability of the FARGO-algorithm. Additionally, we study the difference of two and three-dimensional simulations, compare global with local setups, as well as isothermal and adiabatic conditions.
Methods. We study the influence of the planet on the disk through two- and three-dimensional hydrodynamical simulations. To strengthen our conclusions we perform a detailed numerical comparison where several upwind and Riemann-solver based codes are used with and without the FARGO-algorithm.
Results. With respect to the wake structure and the torque density acting on the planet, we demonstrate that the FARGO-algorithm yields correct a correct and stable evolution for the planet-disk problem, and that at a fraction of the regular cpu-time. We find that the resolution requirements for achieving convergent results in unshocked regions are rather modest and depend on the pressure scale height H of the disk. By comparing the torque densities of two- and three-dimensional simulations we show that a suitable vertical averaging procedure for the force gives an excellent agreement between the two. We show that isothermal and adiabatic runs can differ considerably, even for adiabatic indices very close to unity.

Key words. accretion, accretion disks – planet-disk interactions – methods: numerical – hydrodynamics – protoplanetary disks

1. Introduction

Very young planets that are still embedded in the protoplanetary disk will disturb the ambient density by their gravity. This will lead to gravitational torques that can alter the orbital elements of the planet. For massive enough planets, the wake becomes nonlinear, and gap formation sets in. In numerical simulations of embedded planets, different length scales have to be resolved, in particular when studying low-mass planets. On the one hand, the global structure has to be resolved to be able to obtain the correct structure of the wakes, i.e. the spiral arms generated by the planet, which requires a sufficiently large radial domain. The libration of co-orbital material on horseshoe streamlines requires a full azimuthal extent of $2\,\pi$ radians to be properly captured. On the other hand, the direct vicinity of the planet has to be resolved to study detail effects, such as horseshoe drag or accretion onto the planet.

To ease computational requirements, often planet-disk simulations are performed in the two-dimensional (2D) thin disk approximation, because a full three-dimensional (3D) treatment with high resolution is still very time-consuming. However, even under this reduced dimensionality, the problem is still computationally very demanding. The main reason is the strongly varying timestep size caused by the differentially rotating disk. Because the disk is highly supersonic with (azimuthal) Mach numbers of about 10 to 50, the angular velocity at the inner disk will limit the timestep of the whole simulation, even though the planet or other regions of interest are located much farther out. Changing to a rotating coordinate system will not help too much owing to the strong differential shear. To solve this particular problem and speed up the computation, Masset (2000a) has developed a fast orbital advection algorithm (FARGO). This method consists of an analytic, exact shift in the hydrodynamical quantities by approximately the average azimuthal velocity. The transport step utilizes only the residual velocity, which is close to the local sound speed. Depending on the grid layout and the chosen radial range, a very large speed-up can be achieved, while at the same time the intrinsic numerical diffusion of the scheme is highly reduced (Masset 2000a,b).

The original version of the algorithm has been implemented into the public code FARGO, which is very often used in planet-disk and related simulations. The accuracy of the FARGO-algorithm has been demonstrated in a detailed planet-disk comparison project utilizing embedded Neptune and Jupiter mass planets (de Val-Borro et al. 2006). There, it has been shown that it leads to identical density profiles near the planet and total

torques acting on the planet. Meanwhile, similar orbital advection algorithms have been implemented into a variety of different codes in two and three spatial dimensions, e.g. NIRVANA (Ziegler & Yorke 1997; Kley et al. 2009), ATHENA (Gardiner & Stone 2008; Stone & Gardiner 2010), and PLUTO (Mignone et al. 2007, 2012). Despite these widespread applications, it has been claimed recently that usage of the FARGO-algorithm (here in connection with ATHENA) may lead to an unsteady behavior of the flow near the planet, which even affects the wake structure of the flow farther away from the planet (Dong et al. 2011b).

In the same paper, Dong et al. (2011b) note that a very high numerical grid resolution is required to obtain a resolved flow near the planet. In particular, they analyze the smooth, unshocked wake structure close to the planet and infer that a minimum spatial resolution of about 256 gridcells per scale height H, of the disk is needed to obtain good agreement with linear studies. New simulations with a moving mesh technique also seem to indicate the necessity of very high resolutions (Duffell & MacFadyen 2012).

Because a robust, fast, and reliable solution technique is mandatory in these types of simulations, we decided to address the planet-disk problem for a well defined standard setup, which is very close to the one used in Dong et al. (2011b). To answer the question of the validity of the FARGO-algorithm and estimate the resolution requirements, we applied several different codes to an identical problem. These range from classical second-order upwind schemes (e.g. RH2D, FARGO) to modern Riemann-solvers such as PLUTO. The characteristics of these codes are specified in Appendix A.

Another critical issue in planet-disk simulations is the selection of a realistic treatment of the gravitational force between the disk and the planet. Because the planet is typically treated as a pointmass and located within the numerical grid, regularization of the potential is required. In addition, physical smoothing is required to account for the otherwise neglected vertical thickness of the disk. The magnitude of this smoothing is highly relevant, since it influences the torques acting on the planet (Masset 2002), and the smoothing parameter has even entered analytical torque formulas (Masset & Casoli 2009; Paardekooper et al. 2010). Because the 2D equations are obtained by a vertical averaging procedure, the force should be calculated by a suitable vertical integration as well. This approach has been undertaken recently by Müller et al. (2012), who show that the smoothing length is indeed determined by the vertical thickness of the disk, and is roughly on the order of 0.7 H. They show in addition that the change of the disk thickness induced by the presence of the planet has to be taken into account. Because in recent simulations very short smoothing lengths have been used in 2D simulations (Dong et al. 2011b; Duffell & MacFadyen 2012), we compare our 2D results on the standard problem to an equivalent 3D setup and infer the required right amount of smoothing.

Finally, we performed additional simulations for different equations of state. The first set of simulations deals with the often used locally isothermal setup, while in comparison simulations we explore the outcome of adiabatic runs. This is important because some codes may not allow for treating an isothermal equation of state. Here, we use different values for the ratio of specific heat γ. In particular, a value of γ very close to unity has often been quoted as closely resembling the isothermal case. We show that this statement can depend on the physical problem. In particular, in flows where the conservation of the entropy along streamlines is relevant, there can be strong differences between an isothermal and an adiabatic flow, regardless of the value chosen for γ. For the planet-disk problem this has already been shown by Paardekooper & Mellema (2008).

In the following Sect. 2 we describe the physical and numerical setup of our standard model, and present the numerical results in Sect. 3. The validity of the FARGO-algorithm is checked in Sect. 4. Alternative setups (nearly local, 2D versus 3D, adiabatic) are discussed in Sect. 5. The transition of the wake into a shock front is discussed in Sect. 6, and in the last section, we summarize our results.

2. The physical setup

We study planet-disk interaction for planets of the very low masses that are embedded in a protoplanetary disk. Most of our results shown refer to 2D simulations, using the vertically integrated hydrodynamic equations. For validation and comparison purposes, some additional full 3D models were performed using a similar physical setup. In all cases, we assumed that the disk lies in the $z = 0$ plane and used, for the 2D models, a cylindrical coordinate system (r, φ, z), while in the 3D case we used spherical polar coordinates (R, φ, θ).

We considered locally isothermal, as well as adiabatic models. In the first case, the thermal structure of the disk was kept fixed, and for the standard model we chose a constant aspect ratio, $h = H/r$. Here r is the distance to the star and H the local vertical scale height of the disk

$$H = \frac{c_\mathrm{s}}{\Omega_\mathrm{K}}, \tag{1}$$

where c_s is the isothermal sound speed and $\Omega_\mathrm{K} = (GM_*/r^3)^{1/2}$ is the Keplerian angular velocity around the star. During the computations the orbital elements of the planet remained fixed at their initial values; i.e., we assumed no gravitational backreaction of the disk on the planet or the star. This allows the problem to be formulated scale free in dimensionless units. The planet, whose mass is specified in terms of its mass ratio $q = M_\mathrm{p}/M_*$, is placed on a circular orbit at the distance $r = 1$ and has angular velocity $\Omega_\mathrm{p} = 1$; i.e., one planetary orbit in these units is 2π. The initial surface density Σ_0 is constant and can be chosen arbitrarily since it scales out of the equations.

In the 2D case, the basic equations for the flow in the $r - \phi$ plane are given by equation of continuity

$$\frac{\partial \Sigma}{\partial t} + \nabla \cdot (\Sigma \boldsymbol{u}) = 0, \tag{2}$$

the momentum equation

$$\frac{\partial \Sigma \boldsymbol{u}}{\partial t} + \nabla \cdot (\Sigma \boldsymbol{u}\, \boldsymbol{u}) = -\nabla P + \Sigma F_\mathrm{ext}, \tag{3}$$

and the equation of energy

$$\frac{\partial e}{\partial t} + \nabla \cdot (e \boldsymbol{u}) = -P \nabla \cdot \boldsymbol{u}. \tag{4}$$

Here, e is the energy density (energy per surface area), and $P = (\gamma - 1)e$ denotes the vertically integrated pressure. In the isothermal case the energy equation is not evolved and the pressure reduces to $P = \Sigma c_\mathrm{s}^2$, where $c_\mathrm{s}(r)$ is a given function. The external force

$$F_\mathrm{ext} = F_* + F_\mathrm{p} + F_\mathrm{inertial}, \tag{5}$$

contains the gravitational specific forces (accelerations) exerted by the star, the planet, and the inertial specific forces due to the accelerated and rotating coordinate system.

Table 1. Physical and numerical parameter for the 2D standard model, which consists of a locally isothermal, 2D disk with an embedded planet.

Parameter	Symbol	Value
mass ratio	$q = M_\mathrm{p}/M_*$	6×10^{-6}
aspect ratio	$h = H/r$	0.05
nonlinearity parameter	$\mathcal{M} = q^{1/3}/h$	0.36
kinematic viscosity	ν	10^{-8}
potential smoothing	ϵ_p	0.1 H
radial range	$r_\mathrm{min} - r_\mathrm{max}$	0.6–1.4
angular range	$\phi_\mathrm{min} - \phi_\mathrm{max}$	0–2π
number of gridcells	$N_r \times N_\phi$	256×2004
spatial resolution	Δr	$H/16$
damping range at r_min		0.6–0.7
damping range at r_max		1.3–1.4

For the gravitational force generated by the central star and the inertial part of the force, we use standard expressions. The planetary force is more crucial because it influences, for example, the magnitude of the torque generated by the planet. In our 2D standard model, we derive it from a smoothed potential and use the very common form

$$\Psi_\mathrm{p}^\mathrm{2D} = -\frac{GM_\mathrm{p}}{\left(s^2 + \epsilon_\mathrm{p}^2\right)^{\frac{1}{2}}}, \tag{6}$$

where s is the distance from the planet to the gridpoint under consideration, and ϵ_p the smoothing length to the otherwise point mass potential. It is introduced to avoid numerical problems at the location of the planet. Then, $F_\mathrm{p} = -\nabla\Psi_\mathrm{p}^\mathrm{2D}$. Alternatively, we use in the 2D simulations a vertically averaged version of F_p, following Müller et al. (2012), which we outline in more detail below.

Even though we use a nonzero but very low viscosity, we do not specify those terms explicitly in the above equations, as for example in Kley (1999). The viscosity is so low, that it does not influence the flow on the relevant scales but is just included to enhance stability and smoothness of the flow. In the inviscid case, the dynamical evolution of the system is controlled by the planet-to-star massratio q and the pressure scale height H. A dimensional analysis by Korycansky & Papaloizou (1996) has shown that the relevant quantity is the nonlinearity parameter

$$\mathcal{M} = \frac{q^{1/3}}{h}. \tag{7}$$

2.1. The standard model

The standard model refers to a 2D disk with a locally isothermal setup, where the temperature is a given function of radius, which does not evolve in time. The parameters for our standard model are specified in Table 1. The first two quantities, the mass and the aspect ratio, determine the problem physically. Since we intend to model the linear case in the standard model, we chose a small planet with $q = 6 \times 10^{-6}$, which refers to a $2M_\mathrm{Earth}$ planet for a solar-mass star. We assume $h = 0.05$ for the disk's thickness. For later purposes, we list the nonlinearity parameter in the third row, which is 0.36 here. All results are a function of q and H only, if we assume a vanishing viscosity. In the present situation, where we indeed model the inviscid case, we nevertheless chose a small nonzero kinematic viscosity $\nu = 10^{-8}$, given in units of $a_\mathrm{p}^2\,\Omega_\mathrm{K}(a_\mathrm{p})$. This is equivalent to an α-value of 4×10^{-6} for a $H/r = 0.05$ disk, a value that is considered to be much lower than even a purely hydrodynamic viscosity in the disk. We opted for the very low nonzero value for numerical purposes. For the planetary gravitational potential $\Psi_\mathrm{p}^\mathrm{2D}$, we chose a value of $\epsilon = 0.1H$ in the standard model. We selected this small value for ϵ, primarily for comparison reasons to make contact to the recent simulations of Dong et al. (2011b,a), who suggest a very small smoothing length. Below we demonstrate that, for physical reasons, a much larger smoothing is required, which can be obtained by a suitable vertical averaging procedure (Müller et al. 2012).

A whole annulus is modelled with a radial range from $r_\mathrm{min} = 0.6$ to $r_\mathrm{max} = 1.4$. We chose this domain size to capture all of the torque-producing region, which has a radial range of typically a few vertical scale heights, see e.g. D'Angelo & Lubow (2010). The computational domain is covered by an equidistant grid that has 256×2004 gridcells. This results in a resolution of $H/16$ at the location of the planet for the standard model. To reduce or even avoid reflection from the inner and outer boundaries we applied a damping procedure where, within a specified radial range, all dynamical variables are damped towards their initial values. Specifically, we used the prescription described in de Val-Borro et al. (2006), and write

$$\frac{\mathrm{d}X}{\mathrm{d}t} = -\frac{X(t) - X_0}{\tau}\,R(r), \tag{8}$$

where $X \in \{\Sigma, u_r\}$, and $R(r)$ is a ramping function increasing quadratically from zero to unity (at the actual boundary) within the radial damping regions. The relaxation time τ is given by a fraction of the orbital periods T_orb at r_min and r_max. Here, we use a value of $\tau = 0.03T_\mathrm{orb}$. For more details on the procedure, see de Val-Borro et al. (2006). We note that it is sufficient to only damp the radial velocity u_r (plus u_θ in 3D simulations), which may be useful in radiative simulations where the density stratification may not be known a priori. In test simulations (not displayed here) that use a wider radial range, we have found identical results for the torque and wake structure induced by the planet.

2.2. Initial setup and boundary conditions

The initialization of the variables Σ, T, u_r, u_ϕ was chosen such that without the planet the system would be in an equilibrium state. Here, we chose a constant Σ_0, and a temperature gradient such that the aspect ratio $h = H/r$ is constant. That results in $T(r) \propto r^{-1}$, which is fixed for the (locally) isothermal models. The radial velocity is zero initially, $u_r = 0$, and for u_ϕ we assume a nearly Keplerian azimuthal flow, corrected by the pressure gradient

$$u_\phi(t = 0) = r\Omega_\mathrm{K}\left(1 - h^2\right)^{1/2}. \tag{9}$$

The planet with mass ratio q is placed at $r = 1$ and $\phi = \pi$, i.e. in the middle of the computational domain. For some models the gravitational potential of the planet is slowly switched on within the first five orbital periods, while others do not use this ramping procedure for the potential. For low-mass planets, the results that are typically evaluated at $30\,T_\mathrm{orb}$ (i.e. $t = 30 \cdot 2\pi$), and there is no difference between these two options.

Near the inner and outer radial boundaries the solution is damped towards the initial state, using the procedure as described above. In addition we use reflecting boundaries directly at r_min and r_max. In the azimuthal direction we use periodic boundaries.

2.3. Numerical methods and codes

Because one goal of this paper is to verify the accuracy of numerical methods, we applied several different codes to this physical problem. The 2D case was run using the following codes FARGO, NIRVANA, RH2D, and PLUTO. All of these are finite volume codes utilizing a second-order spatial discretization. Additionally, all are empowered with the orbital advection speed-up known as the FARGO-algorithm, as developed by Masset (2000a), but can be used without this algorithm as well. The first three codes in the list have been used and described in de Val-Borro et al. (2006). The last code, PLUTO, is a multidimensional Riemann-solver based code for magnetohydrodynamical flows (Mignone et al. 2007), which has been empowered recently with the FARGO-algorithm (Mignone et al. 2012).

In the standard 2D setup, the simulations were performed in a cylindrical coordinate system that corotates with the embedded planet, and the star is located at the origin. This implies that inertial forces, such as Coriolis and centrifugal force, as well as an acceleration term to compensate for the motion of the star, have to be included in the external force term $F_{\rm ext}$. Additionally, the FARGO-algorithm is applied, which leads to a speedup of around ten for the standard model, and possibly even more for the higher resolution models. For testing purposes the FARGO-algorithm can be alternatively switched on or off.

The 3D models are run in spherical polar coordinates. For reference we quote the inertial terms and their conservative treatment in Appendix C. These are run using the following codes FARGO3D, NIRVANA, and PLUTO, where FARGO3D is a newly developed 3D extension of FARGO. For a description see Appendix A. For the timestep we typically use 0.5 of the Courant number (CFL). In Sect. 4 we describe the outcome of the comparison in more detail.

3. Results for the standard case

To set the stage and illustrate the important physical effects, we first present the results of our simulations for the 2D standard case using the parameters according to Table 1. For the simulations in this section we used the RH2D code unless otherwise stated. Below, we discuss the variations from the standard model.

After the insertion of the planet, the planet's gravitational disturbance generates two wakes in the form of trailing spiral arms. The basic structure of the surface density, Σ, is shown in Fig. 1. As seen from the plot, the damping procedure ensures that reflections by the radial boundaries are minimized. There is indication of vortex formation as can be seen by the additional structure on the righthand side of Fig. 1. Vortices induced by the planet occur for low-viscosity disks and have already been seen in earlier simulations (see e.g. Li et al. 2005; de Val-Borro et al. 2006; Li et al. 2009). Here, we do not discuss this issue any further.

The relevant quantity to study the physical consequences of the interaction of the embedded planet with the ambient disk is the gravitational torque exerted on the planet by the disk. For that purpose it is very convenient to calculate the radial torque distribution per unit disk mass, $\mathrm{d}\Gamma(r)/\mathrm{d}m$, which we define here, following D'Angelo & Lubow (2010), through the definition of the total torque, $\Gamma_{\rm tot}$, acting on the planet

$$\Gamma_{\rm tot} = 2\pi \int \frac{\mathrm{d}\Gamma}{\mathrm{d}m}(r)\,\Sigma(r)\,r\mathrm{d}r. \tag{10}$$

Here, $\mathrm{d}\Gamma(r)$ is the torque exerted on the planet by a disk annulus of width $\mathrm{d}r$ located at the radius r and having mass $\mathrm{d}m$. Because

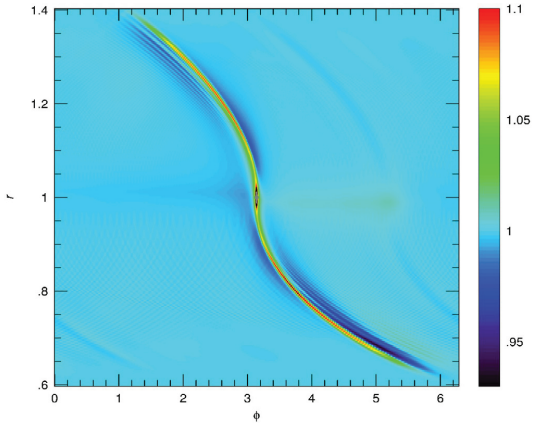

Fig. 1. Density structure of the 2D standard model as generated by an embedded planet with $q = 6 \times 10^{-6}$ in a disk having the aspect ratio $H/r = 0.05$. Shown is the configuration after $30\,T_{\rm orb}$. The density is scaled linearly.

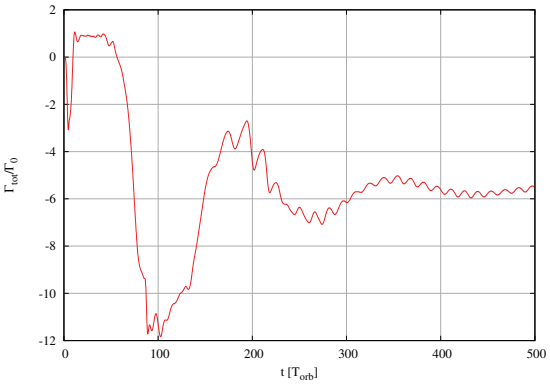

Fig. 2. Total torque, $\Gamma_{\rm tot}$, in units of Γ_0 (see Eq. (12)), acting on the planet vs. time for the 2D standard model. Shortly after insertion, the torque is positive and approximately constant between 10 and 40 orbits. At later times it saturates due to mixing of the material within the horseshoe region.

$\mathrm{d}\Gamma(r)/\mathrm{d}m$ scales with the mass ratio squared and as $(H/r)^{-4}$, we rescale our results accordingly in units of

$$\left(\frac{\mathrm{d}\Gamma}{\mathrm{d}m}\right)_0 = \Omega_{\rm p}^2(a_{\rm p}) a_{\rm p}^2 q^2 \left(\frac{H}{a_{\rm p}}\right)^{-4}, \tag{11}$$

where the index p denotes that the quantities are evaluated at the location of the planet, which has the semi-major axis $a_{\rm p}$. The time evolution of the total torque, $\Gamma_{\rm tot}$, is displayed in Fig. 2 for the first 500 orbits. The total torque is stated in units of

$$\Gamma_0 = \Sigma_0\,\Omega_{\rm p}^2(a_{\rm p}) a_{\rm p}^4 q^2 \left(\frac{H}{a_{\rm p}}\right)^{-2}. \tag{12}$$

In this simulation, the planetary potential has been ramped up during the first five orbits. After insertion of the planet, the total torque becomes first positive and remains constant at this level for about 30 orbits. In this phase the co-orbital torque, in particular the horseshoe drag, is fully unsaturated and gives rise

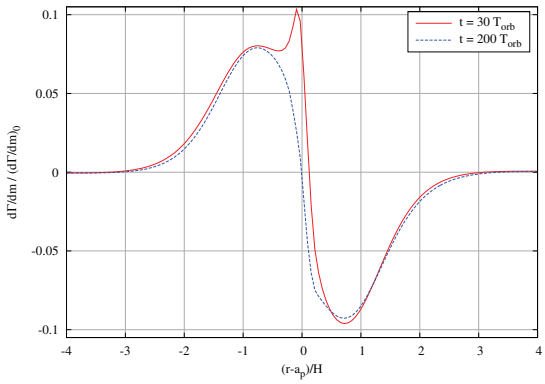

Fig. 3. Radial torque density in units of $(\mathrm{d}\Gamma/\mathrm{d}m)_0$ (see Eq. (11)) at 30 and 200 $T_{\rm orb}$ for the 2D standard model. The torque enhancement and spike near $r = 1$ at $t = 30\,T_{\rm orb}$ is due to the unsaturated corotation torque. At later times, here shown at $t = 200\,T_{\rm orb}$, only the Lindblad contributions due to the spiral arms remain.

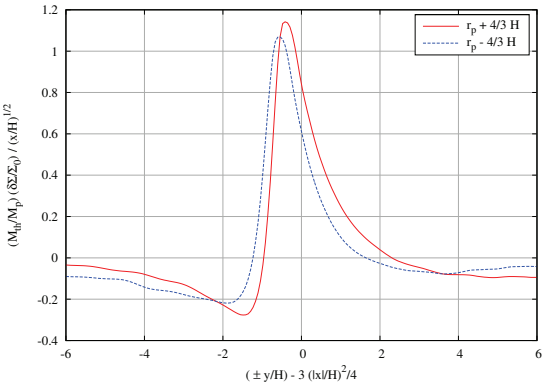

Fig. 4. Normalized azimuthal density profile of the inner and outer wakes at radial distances $\pm 4/3H$ away from the planet at 30 $T_{\rm orb}$ for the isothermal 2D standard model. The coordinates x and y refer to local Cartesian coordinates, see Eq. (15). The "plus" sign in the x-axis label refers to the blue curve at $r_{\rm p} - 4/3H$, and the "minus" sign to the red curve at $r_{\rm p} + 4/3H$. The upstream side of the wake is to the left for both curves.

to a total positive torque. In our situation of an isothermal disk this comes about because of a nonvanishing vortensity gradient across the horseshoe region, which generates a strong positive corotation torque (Goldreich & Tremaine 1979) in this case. The vortensity, which is defined as vorticity divided by surface density, is given here by

$$\zeta = \frac{(\nabla \times \boldsymbol{u})|_z}{\Sigma}. \tag{13}$$

As can be seen from this definition, the radial gradient of ζ is $\propto r^{-3/2}$ for a constant Σ disk, which leads to the strong vortensity-related torque. However, owing to the different libration speeds, the material within the corotation region mixes, and the gradients of potential vorticity and entropy are wiped out in the absence of viscosity (Balmforth & Korycansky 2001; Masset 2001). Consequently, the torques drop again and oscillate on timescales close to the libration time towards a negative equilibrium value, which is given by the Lindblad torques generated by the spiral arms. This saturation of the vortensity-related torque related torque has been analyzed, for example, by Ward (2007) through an analysis of streamlines within the horseshoe region for an inviscid disk, and later through 2D hydrodynamic simulations by Masset & Casoli (2010) and Paardekooper et al. (2011). The strength of the (positive) corotation torque depends strongly on the smoothing of the gravitational potential. For the chosen small $\epsilon = 0.1$ this results in a positive total torque. For more realistic values of $\epsilon \approx 0.6$–0.7, $\Gamma_{\rm tot}$ will usually be negative, see Sect. 5.2.

To study the spatial origin of the torques we analyzed the radial torque density for the standard model. In Fig. 3 the torque density $\mathrm{d}\Gamma/\mathrm{d}m$, according to Eq. (11) is displayed vs. radius in units of $(\mathrm{d}\Gamma/\mathrm{d}m)_0$. Two snapshots are displayed, one at $t = 30\,T_{\rm orb}$ where the torque is fully unsaturated and one at $t = 200\,T_{\rm orb}$ where the torque is saturated. We note that, for the torque calculation, we used a tapering function near the planet to avoid contributions of material that is bound to the planet, or is so close that it yields large torque fluctuations due to numerical discretization effects. We use the form as given in Crida et al. (2008) which reads as

$$f(s) = \left[\exp\left(-\frac{s - r_{\rm t}}{0.1 r_{\rm t}}\right) + 1\right]^{-1}, \tag{14}$$

with a tapering length of $r_{\rm t} = 0.8\,R_{\rm H}$. Here, $R_{\rm H} = (q/3)^{1/3} a_{\rm p}$ is the Hill radius of the planet. Such tapering is particularly useful for massive planets that form a disk around them (Crida et al. 2009). Around lower mass planets, with $\mathcal{M} \lesssim 0.6$, circumplanetary disks do not form (Masset et al. 2006) and a large tapering is not required. Indeed, we found that for values of $r_{\rm t}$ in the range of 0.4–1.0 $R_{\rm H}$ there is not a large difference in the measured torques in equilibrium. For example, the variations in the total torque in Fig. 2 are less than 5%.

The torque density in the fully saturated phase, at $t = 200\,T_{\rm orb}$ (Fig. 3, blue line), is positive inside of the planet and negative outside of the planet. The positive contribution of this Lindblad torque comes from the inner spiral arm, and the negative part from the outer one. The distribution at the earlier time, $t = 30\,T_{\rm orb}$, shows an additional contribution and spike just inside of the planet. This part is due to the horseshoe drag, which is subject to the described saturation process.

To study the wake properties generated by the planet, we used here a quasi-Cartesian local coordinate system centered on the planet to allow direct comparison to previous linear results. Specifically, we define

$$x = (r - r_{\rm p}) \quad \text{and} \quad y = (\phi - \phi_{\rm p}) r_{\rm p}. \tag{15}$$

In Fig. 4 the relative density perturbations for the inner and outer wakes are shown along the azimuth. They are displayed at a radial distance of $x = \pm 4/3H$ from the location of the planet. For the normalization of the perturbed density we first define the thermal mass of the planet

$$M_{\rm th} = \left(\frac{c_{\rm s}^3}{G\Omega}\right)_{\rm p} = h^3\, M_*, \tag{16}$$

where the quantities have to be evaluated at the location of the planet. Then, the ratio of the planet mass to the thermal mass is given by

$$\frac{M_{\rm p}}{M_{\rm th}} = \frac{q}{h^3} = \mathcal{M}^3. \tag{17}$$

Now, we follow Dong et al. (2011b) and scale $\delta\Sigma = \Sigma(\phi) - \Sigma_0$ by the planet mass (in units of $M_{\rm th}$) and normalize by x/H.

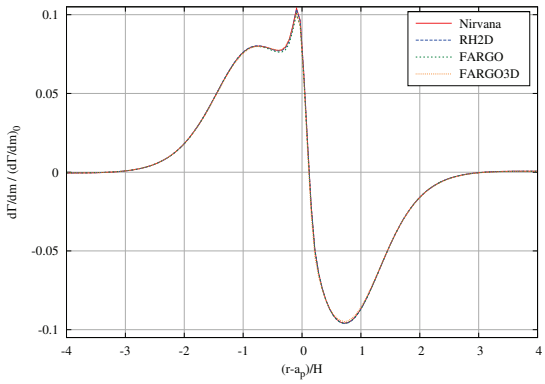

Fig. 5. Radial torque density of the 2D standard-problem in units of $(d\Gamma/dm)_0$ at 30 T_{orb} for different codes at the standard resolution.

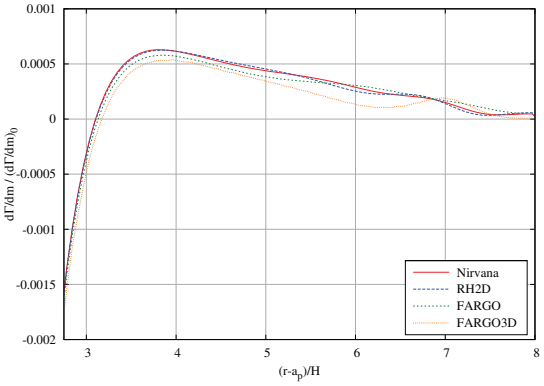

Fig. 6. Radial torque density in units of $(d\Gamma/dm)_0$ at 30 T_{orb} for the standard setup for various code. This is an enlargement of Fig. 5.

Owing to the radial temperature variation and the cylindrical geometry, the inner and outer wake differ in their appearance. However, the general shape and magnitude are very similar to the linear results that have been obtained for the local shearing sheet model (see Goodman & Rafikov 2001; Dong et al. 2011b). Differences in the amplitude are presumably due to a different normalization. Because our results (in all simulations and with all codes) are consistently by a factor of 3/2 greater than those of Dong et al. (2011b), we suspect that they might have used the normalization of M_{th} as given by Goodman & Rafikov (2001), which differs exactly by this factor. At the displayed distance from the planet, the wake is expected to be in the linear regime, which results in a smooth maximum. For this reason we do not expect a strong dependence on the numerical resolution. In the following, we only use the outer wake to check for possible variations due to setup, numerical methods, and resolution.

4. Testing numerics

To validate our results and demonstrate that the FARGO-algorithm yields accurate results, we varied the numerical setup, and used several different codes on the same physical problem. In this section we describe our studies in more detail.

4.1. Using different codes on the 2D standard model

To support our findings on the torque density and wake form and to demonstrate the accuracy of the used codes, we ran the 2D standard model in the isothermal and the adiabatic version using all of the above codes. All simulations use the FARGO-setup and were run in the same (standard) resolution. The isothermal results for the torque density are shown in Figs. 5 and 6, where the latter displays an enlargement of the first. Clearly, the results agree extremely well between the different codes. This includes the standard Lindblad torques, as well as the detailed structure of the corotation torque. The `FARGO3D` code was used in its 2D version for this test.

Recently, it has been shown by Dong et al. (2011b) and Rafikov & Petrovich (2012) that the torque density $\Gamma(r)$ changes sign at a certain distance from the planet in contrast to the standard linear results (Goldreich & Tremaine 1979). Here, we show that this effect is reproduced in our simulations, for all codes. In Fig. 6 we show that this reversal occurs at a distance $r_{\pm} \approx 3.1H$ away from the planet in good agreement with the linear results of Rafikov & Petrovich (2012). Again, all codes agree well on this feature, with only `FARGO3D` showing small deviations.

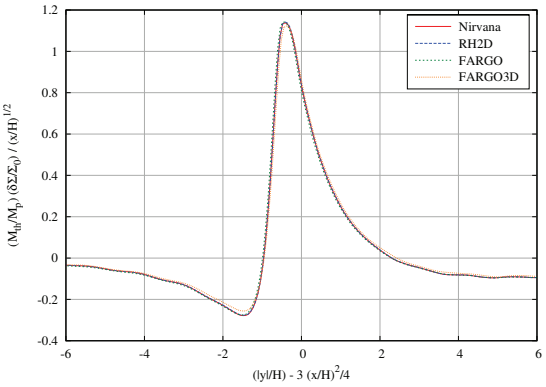

Fig. 7. Normalized azimuthal density profile of the outer wake at the radius $r_p + 4/3H$ at 30 T_{orb} for different codes at the standard resolution.

The corresponding wake form at $x = r_p + 4H$ is displayed in Fig. 7. It is identical for all four cases, which shows the consistency and accuracy of the results and codes.

4.2. The FARGO treatment

In Fig. 8 the wake form is analyzed for three different numerical uses of the FARGO-algorithm on the 2D standard setup. The first, a red curve, corresponds to the standard reference case using a corotating coordinate system and the FARGO-algorithm. For the second, the blue curve, the simulation was performed in the inertial frame and using FARGO. In the mechanism of the algorithm, the quantities in each ring are first shifted according to the overall mean angular velocity of the ring, and then advected using the residual velocity (Masset 2000a). As a result, theoretically it should not matter whether the coordinate system is rotating or not. This is exactly what we find in our simulations, since the blue curve is very similar to the red one. Small differences can be produced by the planetary potential, which is time dependent in the latter case, as the planet is moving, and

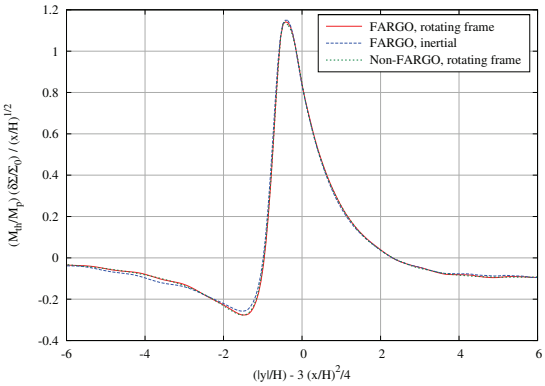

Fig. 8. Normalized azimuthal density profile of the outer wake at the radius $r_p + 4/3H$ at 30 T_{orb} for the code RH2D using different timesteps and a non-rotating frame.

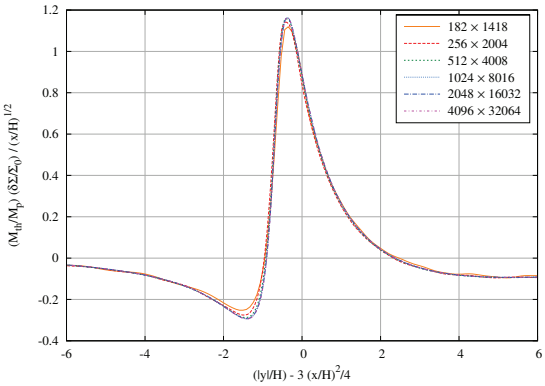

Fig. 9. Normalized azimuthal density profile of the outer wake at the radius $r_p+4/3H$ at 30 T_{orb} using the FARGO-code at different resolutions.

it lies at different locations with respect to the numerical grid. Also, the number of timesteps used until 30 T_{orb} are identical for two runs (12 866 steps). The third, the green curve, corresponds to a model in the corotating frame without using the FARGO-algorithm. Because of the small timestep size in this case, over ten times more timesteps had to be used in this case (137 750 steps). Nevertheless, the wake form is identical. These runs indicate that the FARGO-algorithm captures the physics of the system correctly. At the same time, it comes with a much larger timestep, thereby much reducing the computational cost. This also applies to modern Riemann-solvers such as PLUTO, as shown in Sect. 5.4.

4.3. Testing numerical resolution

To estimate the effect of numerical resolution, we ran the 2D standard model using gridsizes ranging from 182 × 1418 all the way to 4096×32 064. This is equivalent to grid resolutions of $H/10$ to $H/256$. As shown in Fig. 9, the results are nearly identical at all resolutions. The first two, lower resolution cases have a slightly lower trough just in front of the wake and a smaller amplitude. As discussed later in Sect. 6, the results for the different

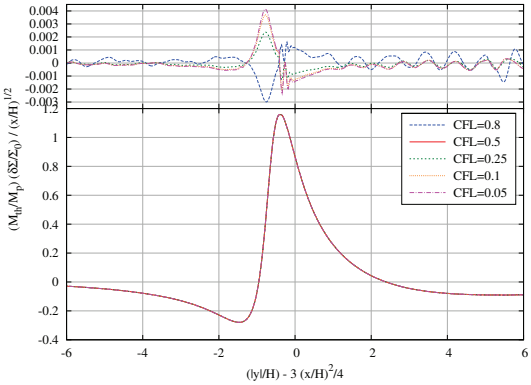

Fig. 10. Normalized azimuthal density profile of the outer wake at the radius $r_p+4/3H$ at 30 T_{orb} using the FARGO-code with different Courant-numbers (CFL). The physical setup differs slightly from the standard problem and is described in Sect. 4.4. In the upper panel the differences of the individual runs with respect to the standard, CFL = 0.5, are displayed.

resolutions are this similar because at this distance to the planet the wake is in the linear regime and has not steepened to a shock wave yet. The resolution requirements at the shock front is analyzed in Sect. 6.

4.4. Testing timestep and stability

Finally, we would like to comment on possible timestep limitations due to the gravitational force generated by the planet. In our simulations we never found any unsteady evolution when using orbital advection. In contrast, the results of Dong et al. (2011b) indicate an unsteady behavior for longer timesteps. They attribute possible instabilities to a violation of an additional gravity-related timestep criterion and advocate using very small timesteps, which would render the FARGO-algorithm inapplicable in very many cases.

To test this statement specifically, we performed a suite of simulations on a very similar setup to the one used by Dong et al. (2011b) in their Fig. 12. Owing to the difficulty of RH2D and FARGO to use a Cartesian local setup, we used here a computational domain exactly as before with a gridsize of 1024 × 8016, which gives a resolution of 64 gridcells per scale-height H. The planet mass is 1.33 M_{Earth}, which is equivalent to a mass ratio $q = 4 \times 10^{-6}$ or $M_p = 3.2 \times 10^{-2}\ M_{th}$. For the potential smoothing we chose $\epsilon = 0.08H$, which yields a planetary potential that is nearly identical to that of Dong et al. (2011b). In Fig. 10 we display the results (using FARGO) for different timestep sizes as indicated by the corresponding Courant-number. The CFL = 0.5 case corresponds to our standard case. We made the timestep longer (CFL = 0.8) as well as shorter, down to CFL = 0.05. All cases yield identical results and do not show any sign of instability. In the upper panel the differences of the individual runs with respect to the standard, CFL = 0.5, are displayed. The performed runs with the RH2D, FARGO, and FARGO3D codes yield identical results, again with no signs of unsteady behavior. Here, FARGO3D was run in the 2D version, both with the setup as indicated above and with the local setup of Table 3, with resolution $h/64$. For all our runs, past the first two orbits the wake profile at $x = 1.33H$ has achieved convergence to better than the 1% level, regardless of the value of the

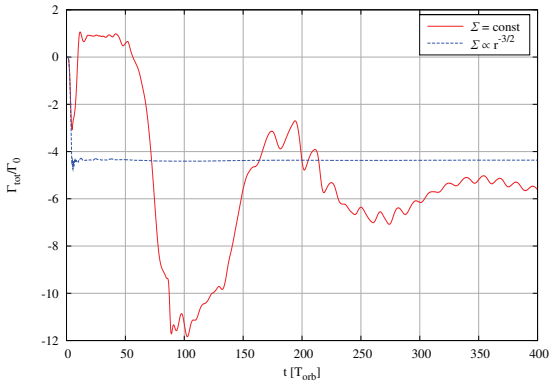

Fig. 11. Total torque $\Gamma_{\rm tot}$, in units of Γ_0 (see Eq. (12)), acting on the planet vs. time. Shown are the 2D standard model (red) and a globally isothermal case (blue), with a different density profile, such that the potential vorticity gradient vanishes.

timestep size. In Appendix B we reanalyzed possible stability requirements in the presence of gravity and find indeed stability for the timestep sizes used with the FARGO-algorithm.

For these runs we switched off the physical viscosity completely. We find that the result for the wake displayed in Fig. 10 is, in fact, due to the special scaling of the axes, identical to that of the standard problem as shown in the previous plots. Additionally, we have not seen any sign of unsteady behavior. All of this indicates that our low value of the kinematic viscosity, $\nu = 10^{-8}$ (in dimensionless units), is essentially negligible.

5. Using alternative setups

To illustrate how variations in individual properties of the standard model influence the outcome, we performed additional simulations, which are described in this section.

5.1. Different radial stratification

As shown above, in the initial evolution after embedding the planet the total torque is positive owing to a strong positive horseshoe drag. The strength of this effect depends on the radial gradients of potential vorticity, entropy (for simulations with energy equation), and temperature (Baruteau & Masset 2012). To minimize this effect, we present an additional, alternative setup where the gradients of potential vorticity (vortensity) and temperature vanish exactly. For this reason, we chose a setup with a density gradient $\Sigma \propto r^{-3/2}$ and T = const. The time evolution of the total torque for this model is displayed with the standard case in Fig. 11. Clearly, after the short switch-on period of the planet mass, the total torque is negative and constant throughout the evolution. This demonstrates that, for this density profile, $\Sigma \propto r^{-3/2}$, which resembles (coincidently) the minimum mass solar nebula, there is indeed no corotation torque present, and the flow settles directly to the Lindblad torque. The final value for the total Lindblad torque differs slightly for the two models due to the different gradients in density and temperature. We note that for this setup, with a vanishing vortensity gradient, there are also no vortices visible during the initial evolution.

Table 2. Numerical parameter for the 3D standard model.

Parameter	Symbol	Value
smoothing radius	$r_{\rm sm}$	$0.25R_{\rm H}$
radial range	$R_{\rm min} - R_{\rm max}$	0.6–1.4
angular range	$\phi_{\rm min} - \phi_{\rm max}$	$0–2\pi$
meridional range	$\theta_{\rm min} - \theta_{\rm max}$	82°–90°
number of gridcells	$N_r \times N_\phi \times N_\theta$	$256 \times 2004 \times 39$
spatial resolution	Δr	$H/16$
damping range at $R_{\rm min}$		0.6–0.7
damping range at $R_{\rm max}$		1.3–1.4

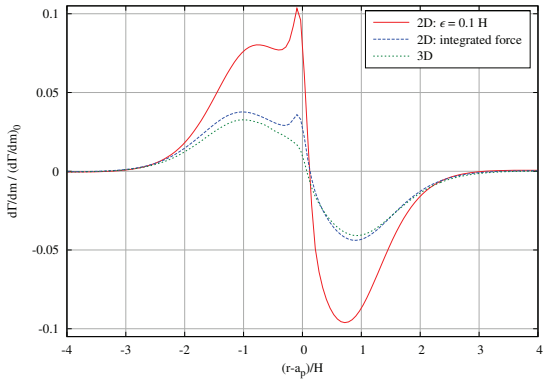

Fig. 12. Radial torque density in units of $(d\Gamma/dm)_0$ at 30 $T_{\rm orb}$ for 2D and 3D simulations of the standard setup. The red curve corresponds to that in Fig. 3, the blue line to a 2D model with a vertical integrated gravitational force, and the green to the 3D model (using `NIRVANA`).

5.2. Comparing 2D and 3D simulations

The setup of the described standard case reduces the physical planet-disk problem to two dimensions. However, even though the disk may be thin, corrections are nevertheless expected because of its finite thickness. We investigated this by performing full 3D simulations using the same physical setup as in the standard 2D model. The treatment of the inertial forces is outlined in Appendix C. The additional numerical parameters are listed in Table 2. The spatial extent and numerical resolution are identical to the 2D model. The initialization of the 3D density was chosen such that the surface density is constant throughout. In the vertical direction the density profile was initialized with a Gaussian profile as expected for vertically isothermal disks. The temperature is constant on cylinders. For the gravitational potential of the planet we chose the so-called cubic-form (Kley et al. 2009), which is exact outside a smoothing radius $r_{\rm sm}$ and smoothed by a cubic polynomial inside of $r_{\rm sm}$. The advantage of this form lies in the fact that in 3D simulations the smoothing is required only numerically, and the cubic potential allows us to have the exact potential outside a specified radius, here $r_{\rm sm}$. To calculate the torque the same tapering function (Eq. (14)) as has been used before.

In Fig. 12 we show the normalized torque density $d\Gamma/dm$ for 2D simulations in comparison to a full 3D simulation using the same physical setup. Due to the finite vertical extent, the torques of the 3D model are substantially less than for the corresponding 2D setup. As Müller et al. (2012) have shown recently, this discrepancy can be avoided by performing a suitable vertical

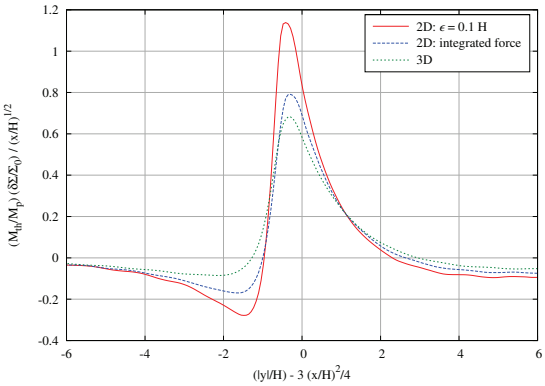

Fig. 13. Normalized azimuthal density profile of the outer wake at the radius $r_p + 4/3H$ at 30 T_{orb} for 2D and 3D simulations of the standard setup. The color coding is identical to Fig. 12.

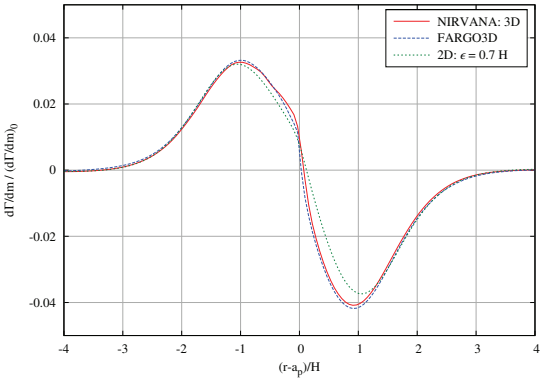

Fig. 14. Radial torque density in units of $(d\Gamma/dm)_0$ at 30 T_{orb} for the 3D and 2D simulations of the standard setup. Compared are two 3D simulations (using NIRVANA and FARGO3D) with a 2D simulation, using $\epsilon = 0.7$.

averaging procedure of the gravitational force. Specifically, the force acting on each disk element in a 2D simulation is calculated from the projected force that acts in the midplane of the disk. Denoting the distance of the disk element to the planet with s, the force density (force per area) is given by

$$F_p(s) = -\int \rho \frac{\partial \Psi_p}{\partial s}\, dz = -GM_p s \int \frac{\rho}{(s^2+z^2)^{\frac{3}{2}}}\, dz, \qquad (18)$$

where Ψ_p is the physical 3D potential generated by the planet. For the vertical density stratification, a Gaussian density profile can be assumed for a vertically isothermal disk as a first approximation. However, the change in the vertical density as induced by the planet has to be taken into account. The results using this averaging prescription in an approximate way (Müller et al. 2012) is also shown additionally in Fig. 12. The overall behavior and magnitude is very similar to the full 3D results. For comparison, a 2D model using a fixed $\epsilon = 0.7H$ (instead of $0.1H$ of the standard model) for Ψ_p^{2D} yields similar amplitude as the full 3D model but a slightly different shape (see Fig. 14).

In Fig. 13 we show the corresponding wake profile for the 2D and 3D setups. For the 3D case, the surface density is obtained by integration along the θ direction at constant spherical radii, R. Here, the wake amplitude of the full 3D model is again reduced in contrast to the flat 2D case, with $\epsilon = 0.1$. The 2D model using the integrated force algorithm yields here again a better agreement. The 3D results displayed in these plots were obtained with NIRVANA, but using the new code FARGO3D yields identical results, as demonstrated in Fig. 14.

These results demonstrate clearly that the ϵ-parameter in the 2D planetary potential (Ψ_p^{2D}) cannot be chosen arbitrarily small, but has to be similar to the scale height H of the disk. Near the planet, a reduction is required to account for the reduced thickness, see Müller et al. (2012). As a result, the value of $\epsilon = 0.1\,H$ as chosen for the standard setup is too small to yield good agreement with vertically stratified disks, and serves here only as a numerical illustration to connect to previous linear and numerical results (Goodman & Rafikov 2001; Dong et al. 2011b). As shown by Müller et al. (2012), a value of $\epsilon = 0.7\,H$ yields similar amplitudes to the 3D case, in particular for the Lindblad torque, see Fig. 14. However, as can be seen from the figure, for the ϵ-potential the relative strengths of the inner and outer torques differ from the full 3D and the 2D vertically integrated case.

Table 3. Setup for the alternative quasi-local model.

Parameter	Symbol	Value
mass ratio	$q = M_p/M_*$	3.2×10^{-8}
aspect ratio	$h = H/r$	0.01
nonlinearity parameter	$\mathcal{M} = q^{1/3}/h$	0.32
potential smoothing	ϵ_p	$0.06H$
radial range	$r_{min} - r_{max}$	0.94–1.06
angular range	$\phi_{min} - \phi_{max}$	−0.32–0.32 rad
number of gridcells	$N_r \times N_\phi$	384×2048
spatial resolution	Δr	$H/32$

Notes. The parameters have been chosen according to Dong et al. (2011b).

5.3. Using a quasi-local setup

To demonstrate the agreement of our simulations with previously published local results, e.g. by Dong et al. (2011b,a), we changed the computational setup, which is listed briefly in Table 3. Despite using cylindrical coordinates, the setup is in fact identical to a model used by Dong et al. (2011b). The very small thickness H of the disk and the small planet mass minimize curvature effects and make the problem more local. The nonlinearity parameter for this local model is $\mathcal{M} = 0.32$, which is similar to the standard case. This quasi-local model was run in a 2D and 3D setup using FARGO3D. The 3D case was run again in spherical polar coordinates with the same spatial resolution as in the 2D setup of Table 3. For the gravitational smoothing a length of two gridcells was chosen, which is equivalent here to $\epsilon = 0.06\,H$. For the 2D simulations we used RH2D and FARGO, while for the 3D simulations we used NIRVANA and FARGO3D. All these codes are based on the standard ZEUS-method and are enhanced with the FARGO-speedup, see Appendix A for details.

In Fig. 15 we compare the torque density of the 2D standard model to the quasi-local model. In a local setup any corotation torques saturate very quickly, possibly due to the very small (quasi-periodic) domain in the angular direction. To match this condition, the standard model is shown here at $200T_{orb}$ when the corotation torques have nearly saturated. The overall shape and magnitude of the two models is qualitatively in very good agreement, which supports the scaling with $(d\Gamma/dm)_0$. For the

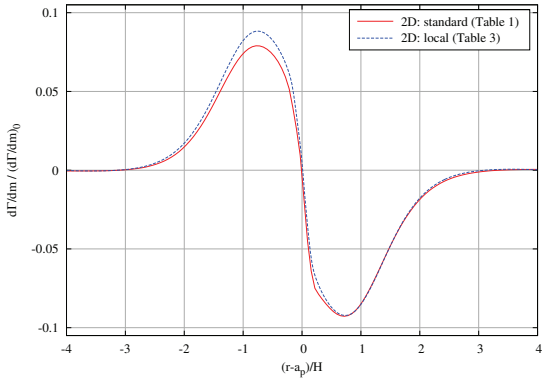

Fig. 15. Radial torque density in units of $(d\Gamma/dm)_0$. The standard setup with $q = 6 \times 10^{-6}, h = 0.05$ at 200 T_{orb} is compared to the quasi-local model with $q = 3.2 \times 10^{-8}, h = 0.01$ at 30 T_{orb}. The local calculation utilizes the FARGO3D-code in the 2D setup.

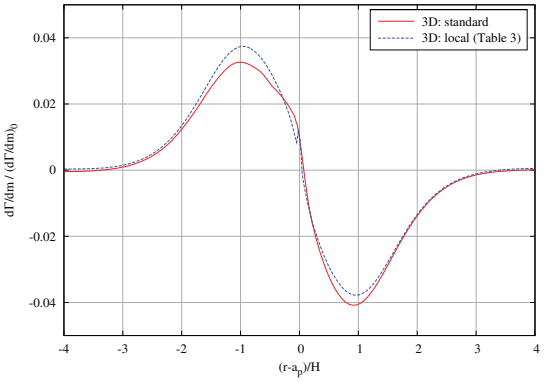

Fig. 17. Radial torque density in units of $(d\Gamma/dm)_0$ for full 3D models. Compared is the standard setup with $q = 6 \times 10^{-6}$, $h = 0.05$ at 30 T_{orb} (using NIRVANA) to the quasi-local model with $q = 3.2 \times 10^{-8}$, $h = 0.01$ at 30 T_{orb} (using FARGO3D).

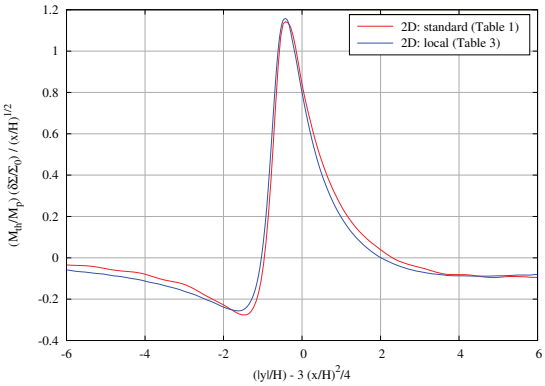

Fig. 16. Normalized azimuthal density profile of the outer wake at the radius $r_p + 4/3H$ at 30 T_{orb}. Compared is the standard setup with $q = 6 \times 10^{-6}$, $h = 0.05$ to the quasi-local model with $q = 3.2 \times 10^{-8}$, $h = 0.01$.

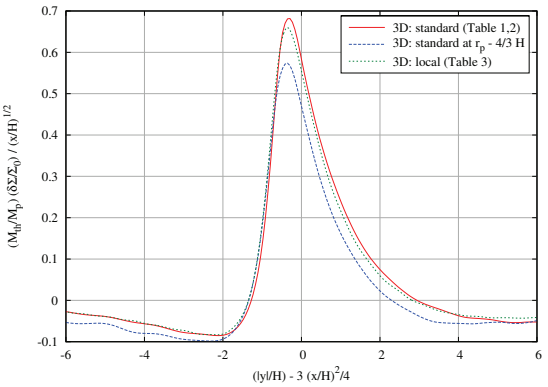

Fig. 18. Normalized azimuthal density profile of the outer and inner wake at the radii $r_p \pm 4/3H$ for full 3D models. Compared is the standard setup with $q = 6 \times 10^{-6}$, $h = 0.05$ at 30 T_{orb} for the outer and inner wakes, to the quasi-local model with $q = 3.2 \times 10^{-8}$, $h = 0.01$ at 30 T_{orb}, only at the outer wake.

local models a symmetric shape with respect to the location of the planet is expected, while for standard model the outer torques are greater in magnitude. This can explain some differences.

In Fig. 16 we compare the wake form of the standard model (as shown in Figs. 4, 13) to the more local alternative model for the 2D setup. The two curves agree very well indeed, despite the huge difference in parameters for the planet mass and the disk scale height. We attribute the small differences to curvature effects. We note that, thanks to the local character of this setup, the curves for inner and outer wakes at $r_p \pm 4/3$ look identical for the quasi-local model.

In Fig. 17 we compare the torque density of the 3D standard model to the 3D quasi-local model. As in the 2D case, now the overall shape and magnitude of the two models are again qualitatively in good agreement. The local model shows a symmetric shape with respect to the location of the planet, as expected. For both cases a similar reduction of amplitude is seen in comparison to the 2D case.

In Fig. 18 we compare the wake form of the standard model to the local alternative model for the full 3D setup. This time the two curves for the outer wake again agree very well, despite the huge difference in parameters. The profile for the inner wake of the standard model deviates from the outer wake as for the previous 2D setup. For the local model, inner and outer wakes are again identical, as expected.

5.4. Adiabatic simulations

The assumption of isothermality is only satisfied approximately in protoplanetary disks. Because cooling times can be long, it may be more appropriate to take the energy equation into account. To study the influence of the equation of state on the outcome, we performed purely adiabatic simulations, which solve the energy equation (Eq. (4)), together with an ideal equation of state. The result of such an approach is presented in Fig. 19, where the radial torque density is displayed for the standard isothermal model, along with two adiabatic models using $\gamma = 1.4$ and 1.01. The adiabatic results require rescaled units because the adiabatic sound speed is greater than the isothermal

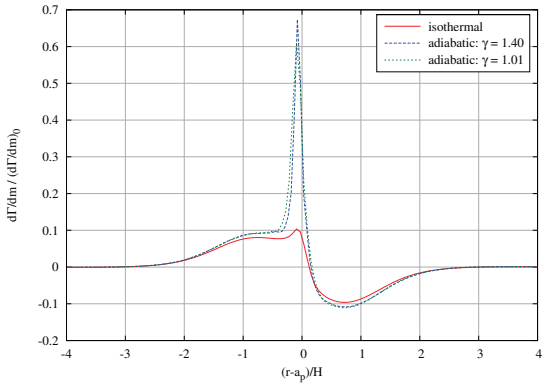

Fig. 19. Radial torque density in units of $(d\Gamma/dm)_0$ (see Eq. (11)) at 30 T_{orb} for the 2D standard model for an isothermal and an adiabatic setup using $\gamma = 1.01$ and $\gamma = 1.40$. The units for $(d\Gamma/dm)_0$ and H have been changed for the adiabatic runs, such that $H \to \gamma H$.

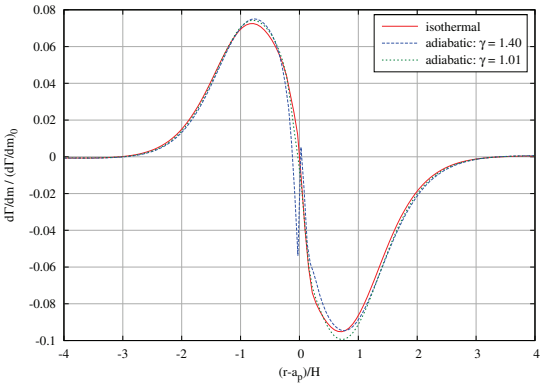

Fig. 20. Radial torque density in units of $(d\Gamma/dm)_0$ (see Eq. (11)) at 500 T_{orb} for the 2D standard model for an isothermal and an adiabatic setup using $\gamma = 1.01$ and $\gamma = 1.40$. The units for $(d\Gamma/dm)_0$ and H have been rescaled as in Fig. 19.

one by a factor $\sqrt{\gamma}$. As a result, the pressure scale length is increased by the same factor, which enters (through H) the units for $(d\Gamma/dm)_0$ and Γ_0. Obviously, there is a huge difference in the horseshoe torque between isothermal and adiabatic runs, while the Lindblad contributions are similar, once correctly scaled. The adiabatic runs yield similar results for the two γ values throughout. The strong torque enhancement in these adiabatic simulations comes from the entropy-related part of the corotation torque, which is driven by a radial gradient of entropy across the horseshoe region (Baruteau & Masset 2008).

This result is interesting because sometimes an isothermal situation is mimicked with an adiabatic simulation using a γ-value very close to unity. In particular, this may be required by those Riemann solvers that do not allow isothermal conditions to be treated. Our results show that such an approach has to be treated very carefully, as shown already by Paardekooper & Mellema (2008). They argue that compressional heating near the planet plays an important role in determining the torques. Additionally, in an adiabatic situation the entropy is conserved along streamlines, which is not the case for isothermal flows. Reducing the value of γ even further yields the same results. In general, an adiabatic flow with $\gamma \to 1$ approaches truly isothermal flow only in the the case of a *globally* constant temperature.

After a few libration times the horseshoe region is well mixed, and the entropy and potential vorticity gradients across the horseshoe regions are wiped out, so the horseshoe torques disappear and the Lindblad contributions remain. This situation is displayed in Fig. 20 for an evolutionary time of 500 orbits. Now, the isothermal model agrees well with the adiabatic one.

We also applied several codes on the adiabatic setup. In Fig. 21 we display the same results for the adiabatic situation using $\gamma = 1.01$. Again, all codes agree very closely, even though now the numerical methodology is vastly different, because some use a second order upwind scheme (`RH2D` and `FARGO`) while `PLUTO` uses a Riemann-solver. Only very near to the planet do the results differ slightly.

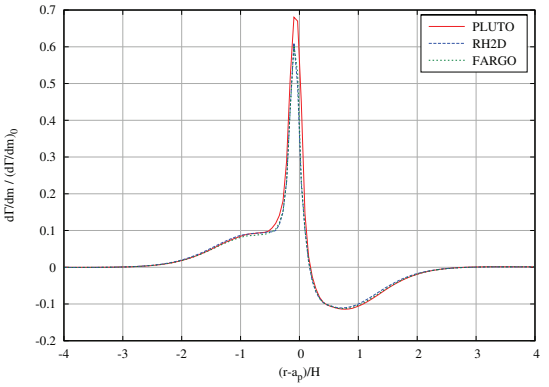

Fig. 21. Radial torque density in units of $(d\Gamma/dm)_0$ (see Eq. (11)) at 30 T_{orb} for the adiabatic standard model using an ideal equation of state with $\gamma = 1.01$. Three different codes have been used, `RH2D` and `FARGO` are 2nd-order upwind schemes and `PLUTO` is a Riemann solver.

6. Shock formation

For the damping of the wake, it is important where the transition to a shock occurs. As a shock indicates a discontinuous change in the fluid variables, numerical codes often have difficulty resolving the structure in detail. To analyze this, we plot in Fig. 22 the maximum density in the wake as a function of radius for various resolutions of the computational grid. At the radius of the planet, the density obviously has its maximum, and it drops on both sides. The previous curves for the wake profile were taken near the minimum value of the density maximum. Here, all resolutions show an identical maximum of the wake amplitude. As we demonstrated in Sect. 4.3, the form of the wake thus does not depend very strongly on resolution at a distance of $|x| = 4/3H$.

Farther away from the planet, beyond a distance $|x| \gtrsim 2H$ the curves begin to differ for the various resolutions. This clearly indicates the nonconvergence of the simulations. We attribute this to the formation of a shock wave. In fact, at a distance $x_s \approx 2H$ from the location of the planet, the speed of the wake becomes supersonic with respect to the local Keplerian flow. The criterion as given by Goodman & Rafikov (2001) indicates a shock formation at a distance of $\approx 2.9H$ from the planet for our nonlinearity parameter, $\mathcal{M} = 0.36$, which consistent with our findings.

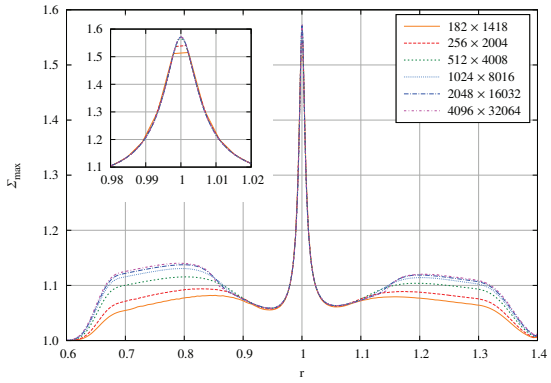

Fig. 22. Maximum of the density in the spiral wake as a function of radius for the 2D isothermal standard model at 30 $T_{\rm orb}$. Different numerical resolutions are shown using FARGO.

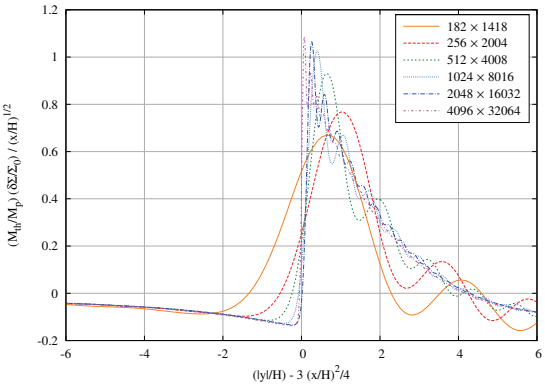

Fig. 23. Normalized azimuthal density profile of the outer wake at the radii $r_{\rm p} + 5H$ at 30 $T_{\rm orb}$ for the 2D isothermal standard model. Different numerical resolutions are shown.

At very high spatial resolutions, i.e. above a grid resolution of 64 gridcells per scale height (1024 × 8016), the curves begin to converge in the shock region. Far away from the planet, the damping action of the boundary condition begins to set in beyond $|x| \approx 6H$ ($r = 1.3$), and the curves coincide again.

In Fig. 23 the azimuthal density profile is shown at a radial location $r = r_{\rm p}+5H = 1.25$. At this location the wake is expected to have turned into a shock wave. Owing to the trailing nature of the wake, we define the variable y here slightly different from before through

$$y = (\phi - \phi_{\rm p})\, r.$$

From the figure it is obvious that the wake has turned into a shock at this location. At our standard resolution (256 × 2004) there is no indication of any shock front. The overall form is very smooth with the presence of large oscillations behind the wake. With increasing numerical resolution the shock becomes resolved better and better, but only at the very highest resolution does the wake turn into a discontinuous jump. The oscillations behind the front diminish and move closer to the front with increasing resolution. Numerical experiments show that these oscillations can be damped out by increasing the strength of viscosity. However, this also smears out the shock front. It has been suggested that these oscillations stem from the chosen numerical scheme and occur for very weak shocks (Rein 2010).

7. Summary

Through a series of 2D and 3D simulations using different computational methods and codes we have explored in detail the numerical requirements for studies of the planet-disk problem. In our analysis we focused on the torque density acting on the planet and the structure of the wake generated by the planet.

With respect to the applicability of the fast orbital advection algorithm, FARGO, we have shown that it leads to consistent numerical results that agree extremely well with non-FARGO studies. The achievable gain in speed can be significant. For the setup used here we found a speed-up of more than a factor of 10. The method works well in the presence of embedded planets, does not show any signs of unsteady behavior, and can be applied in two or three spatial dimensions. Since it is also applicable in conjunction with magnetic fields, new possibilities for numerical studies of turbulent accretion disks open up (Mignone et al. 2012).

We extend previous treatments of the gravitational potential of embedded planets (Masset 2002; Müller et al. 2012) to very low-mass planets in extremely thin disks. We confirmed that, for physical reasons, the planetary potential has to be smoothed in 2D simulations with about $\epsilon = 0.6\,H - 0.7\,H$. Models where the gravitational force is obtained directly through a vertical integration always yield reasonable agreement with full 3D simulations. The use of very short smoothing lengths below $\epsilon = 0.6\,H$ in 2D simulations is not recommended, because then the forces in the vicinity of the planet are strongly overestimated, which results in an unphysical enhancement of the torque and wakes that are too strong.

Through a careful resolution study, we showed that the smooth wake structure at distances below about 2 H of the planet can be resolved well and consistently, already with the very low resolution of 8 to 16 cells per scale height. The results are clearly converged for 32 gridcells per H. For longer distances from the planet, the spiral wake turns into a shock wave, and much higher resolution may be required. We found that around a resolution of about 100 gridcells per H convergence can be achieved. Because this high resolution is only required near the spiral shocks and the flow is relatively smooth outside, numerical methods that adaptively refine this crucial region may be the method of choice in the future.

For adiabatic flows we confirmed earlier findings (Paardekooper & Mellema 2008) that the unsaturated horseshoe drag shows a strong deviation from the isothermal case. Using the appropriate scaling, the adiabatic corotation torques are independent of γ and do not converge to the isothermal case, even in the limit $\gamma \to 1$. As a result, the procedure of modelling the isothermal case with simulations of γ close to unity has to be treated with care. In the final saturated case, where all the corotation effects have been wiped out, isothermal and adiabatic results agree perfectly, once the correction to the sound speed has been applied.

In Appendix B we show that we do not find any additional timestep criterion due to the planetary potential, and we also do not notice any unstable evolution in the case of using the orbital advection. The question why using the ATHENA-code instabilities occur in the simulations (Dong et al. 2011b) may be connected to the treatment of orbital advection in that code

(Stone & Gardiner 2010), which is apparently different from the implementation in the FARGO-code. One should also notice that the conservative treatment of Coriolis forces is mandatory in such simulations to properly conserve angular momentum (Kley 1998).

We have demonstrated that the planet-disk interaction problem may be regarded as a very good test to validate an implementation of orbital advection, because it admits a nearly analytic solution to which a code output can be compared. This is not the case for simulations of turbulent disks, where no such known solutions exist. We hope that the presented results and comparison simulations may serve as a useful reference for other researchers in this field.

Acknowledgements. Tobias Müller received financial support from the Carl-Zeiss-Stiftung. Wilhelm Kley acknowledges the support of the German Research Foundation (DFG) through grant KL 650/8-2 within the Collaborative Research Group FOR 759: *The formation of Planets: The Critical First Growth Phase*. Some simulations were performed on the bwGRiD cluster in Tübingen, which is funded by the Ministry for Education and Research of Germany and the Ministry for Science, Research and Arts of the state Baden-Württemberg, and the cluster of the Forschergruppe FOR 759 "The Formation of Planets: The Critical First Growth Phase" funded by the Deutsche Forschungsgemeinschaft. Pablo Benítez-Llambay acknowledges the financial support of CONICET and the computational resources provided by IATE. We acknowledge fruitful discussions with Ruobing Dong and Roman Rafikov.

Appendix A: The codes

For our comparison simulations we utilized the following codes:
NIRVANA: In its original (FORTRAN) version a ZEUS-like second-order upwind scheme (Ziegler & Yorke 1997), with the option of fixed nested grids and magneto-hydrodynamics (MHD). It can be used in two or three dimensions and can use different coordinate systems. Recently, it has been improved to include radiative transport and the FARGO-treatment (Kley et al. 2009).

RH2D: A 2D radiation hydrodynamics code for different coordinate systems, originally developed for treating the boundary layer in accretion disks (Kley 1989) and later adapted to the planet disk problem (Kley 1999).

FARGO: A 2D, special purpose code for disk simulations that first featured the FARGO-algorithm (Masset 2000a). The code is publicly available at: `http://fargo.in2p3.fr/`, and has been used frequently in planet-disk and related simulations.

FARGO3D: A code based on similar algorithms to the standard FARGO-code, but aimed at being more versatile, as it includes Cartesian, cylindrical and spherical geometries, in one, two or three dimensions, with arbitrary grid limits. Its hydrodynamical core has been written from scratch, and it includes an MHD solver based on the method of characteristics and constrained transport. It is parallelized using the Message Passing Interface (MPI) and a slab domain decomposition. It is intended in the near future to run distinctly on clusters of CPUs or GPUs, and it will be made publicly available as the successor to the FARGO-code.

PLUTO: A multidimensional Riemann-solver based code for MHD flows (Mignone et al. 2007), which can also be used in the purely hydrodynamic setup. Additionally, it has been empowered recently by the FARGO-algorithm (Mignone et al. 2012). PLUTO is also freely available at `http://plutocode.ph.unito.it`.

The first three codes in the list have been used and described in an earlier code comparison project on the planet-disk problem (de Val-Borro et al. 2006). There, more massive planets of Neptune and Jupiter mass embedded in viscous and inviscid disks have been studied for a large number of codes, the focus was on the gap structure of the disk, and the total torques have been analyzed.

Appendix B: Timestep limitation in the presence of gravity

Numerically, we expect that possibly gravity might cause problems if, due to the gravitational acceleration g, a parcel of material travels more than about half a gridcell of length Δx in one timestep Δt. This requires the additional gravitational criterion

$$\Delta t_{\rm G} \le \left(\frac{\Delta x}{g}\right)^{1/2}. \tag{B.1}$$

Using now the smoothed planetary potential of Eq. (6) we find that the maximum force is given by

$$g_{\rm max} = \frac{GM_{\rm p}}{\epsilon^2}\, k \tag{B.2}$$

with $k = 2/3^{3/2} \approx 0.4$. To obtain the strongest limitation on Δt we substitute $g_{\rm max}$ in Eq. (B.1) and obtain

$$\Delta t_{\rm G} \le \Omega_{\rm K}^{-1}\, \mathcal{M}^{-1/2} \left(\frac{2\Delta x\, \epsilon^2}{k\, H^3}\right)^{1/2}. \tag{B.3}$$

We compare this limit now to the regular Courant condition when using orbital advection which is given by

$$\Delta t_{\rm C} = \frac{\Delta x}{c_{\rm s}}, \tag{B.4}$$

and find

$$\frac{\Delta t_{\rm G}}{\Delta t_{\rm C}} = \mathcal{M}^{-1/2} \left(\frac{2\epsilon^2}{kH\Delta x}\right)^{1/2}. \tag{B.5}$$

If there should be no additional timestep limitation generated by the gravity then this ratio should be larger than one. Writing now for the grid resolution $\Delta x = H/N$ we finally find that

$$N \ge \frac{k}{2}\, \frac{H^2}{\epsilon^2}\, \mathcal{M} \tag{B.6}$$

for stability. With $k = 0.4$, $\epsilon = 0.1H$, and $\mathcal{M} = 0.36$ we find for the necessary resolution $N \approx 10$. This is indeed fulfilled even for our lowest resolution. We point out that this limit formally only applies to flows without pressure (dust). If around the planet the envelope is hydrostatic, no additional criterion is required. Switching on the planetary potential slowly will ensure stability throughout the evolution as will an initial atmosphere around the planet (Duffell & MacFadyen 2012).

Appendix C: The 3D hydrodynamic equations in a rotating frame

For reference we state here the 3D hydrodynamic equations in a rotating coordinate frame. In a coordinate system rotating with the (constant) angular velocity $\mathbf{\Omega}$, omitting pressure terms, any external forces (eg. gravitation) and viscosity, the momentum equation reads as

$$\frac{\partial \boldsymbol{u}}{\partial t} + \boldsymbol{u}\nabla\boldsymbol{u} = -2\mathbf{\Omega}\times\boldsymbol{u} + \frac{1}{2}\nabla\left[(\mathbf{\Omega}\times\boldsymbol{r})^2\right]. \tag{C.1}$$

We now use spherical polar coordinates (r, φ, θ), where r is the radial coordinate, φ the azimuthal angle, and θ the usual polar coordinate measured from the z-axis. NOTE, that we use in this Appendix the same symbol r for the spherical radial coordinate. For rotation around the z-axis, $\mathbf{\Omega} = \Omega\mathbf{e}_z$, the individual equations are

$$\frac{\partial u_r}{\partial t} + \boldsymbol{u}\nabla u_r = \frac{1}{r}\left(u_\varphi^2 + u_\theta^2\right) + r\Omega^2\sin^2\theta + 2u_\varphi\Omega\sin\theta, \tag{C.2}$$

$$\frac{\partial u_\varphi}{\partial t} + \boldsymbol{u}\nabla u_\varphi = -\frac{u_r u_\varphi}{r} - \frac{u_\theta u_\varphi\cot\theta}{r} - 2\Omega\left(\sin\theta u_r + \cos\theta u_\theta\right), \tag{C.3}$$

$$\frac{\partial u_\theta}{\partial t} + \boldsymbol{u}\nabla u_\theta = -\frac{u_r u_\theta}{r} + \frac{u_\varphi^2\cot\theta}{r} + 2\Omega u_\varphi\cos\theta + \Omega^2 r\sin\theta\cos\theta. \tag{C.4}$$

Introducing the angular velocity ω through

$$u_\varphi = r\sin\theta\,\omega, \tag{C.5}$$

we may write for the three equations (C.2–C.4)

$$\frac{\partial u_r}{\partial t} + \boldsymbol{u}\nabla u_r = \frac{u_\theta^2}{r} + r\sin^2\theta\,(\omega+\Omega)^2, \tag{C.6}$$

$$\frac{\partial u_\varphi}{\partial t} + \boldsymbol{u}\nabla u_\varphi = -\left(\omega + 2\Omega\right)\left(\sin\theta u_r + \cos\theta u_\theta\right), \tag{C.7}$$

$$\frac{\partial u_\theta}{\partial t} + \boldsymbol{u}\nabla u_\theta = -\frac{u_r u_\theta}{r} + r\sin\theta\cos\theta\,(\omega+\Omega)^2. \tag{C.8}$$

One sees that in the radial and meridional (θ) momentum equation only the centrifugal part ($\omega + \Omega$) and occurs in the angular momentum (φ) equation only the Coriolis term (2Ω).

C.1. Conservative treatment of Coriolis terms in the angular momentum equation

Defining the *total* specific angular momentum

$$h_\mathrm{t} = r^2\sin^2\theta\,(\omega+\Omega) \tag{C.9}$$

and using the continuity equation (in 3D) we may write

$$\frac{\partial\rho h_\mathrm{t}}{\partial \mathrm{t}} + \nabla\cdot(\rho h_\mathrm{t}\boldsymbol{u}) = 0 \tag{C.10}$$

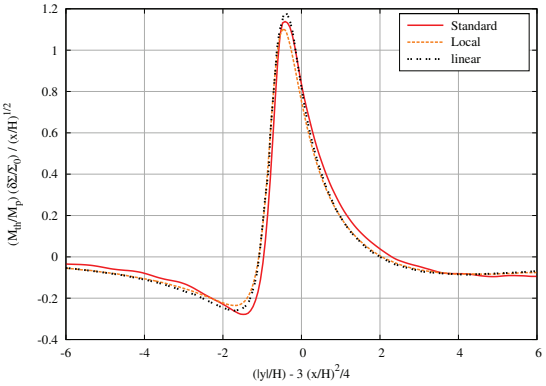

Fig. D.1. Normalized azimuthal density profile of the outer wake at the radius $r_\mathrm{p} + 4/3H$ at 30 T_orb. Compared is the standard setup with $q = 6\times10^{-6}, h = 0.05$ and the quasi-local model with $q = 3.2\times10^{-8}, h = 0.01$ to the linear theoretical results of Goodman & Rafikov (2001).

for the angular momentum Eq. (C.7). Expanding h_t this may be written as

$$\frac{\partial\left[\rho r\sin\theta\left(u_\varphi + r\Omega\sin\theta\right)\right]}{\partial t} + \nabla\cdot\left[\rho r\sin\theta\left(u_\varphi + r\Omega\sin\theta\right)\boldsymbol{u}\right] = 0. \tag{C.11}$$

The validity of (C.11) can be easily checked by expanding the terms and making use of the continuity equation. Then one arrives at Eq. (C.7). In a numerical method that evolves u_φ, Eq. (C.11) should be used to solve the angular momentum transport conservatively.

Appendix D: Comparing to linear results

After submission of the original manuscript, Ruobing Dong generously supplied us with the data of the linear results of Goodman & Rafikov (2001). In Fig. D.1 we compare their data to our results for the 2D simulations using the standard setup of Table 1 and the quasi-local setup of Table 3. The overall agreement of our full nonlinear results with the linear case is very good. The small differences between the results are comparable to what Dong et al. (2011b) found in their study. We note that their vertical scaling differs by a factor of 3/2.

References

Balmforth, N. J., & Korycansky, D. G. 2001, MNRAS, 326, 833
Baruteau, C., & Masset, F. 2008, ApJ, 672, 1054
Baruteau, C., & Masset, F. 2012, in Tidal effects in Astronomy and Astrophysics, Lect. Notes Phys., to be published
Crida, A., Sándor, Z., & Kley, W. 2008, A&A, 483, 325
Crida, A., Baruteau, C., Kley, W., & Masset, F. 2009, A&A, 502, 679
D'Angelo, G., & Lubow, S. H. 2010, ApJ, 724, 730
de Val-Borro, M., Edgar, R. G., Artymowicz, P., et al. 2006, MNRAS, 370, 529
Dong, R., Rafikov, R. R., & Stone, J. M. 2011a, ApJ, 741, 57
Dong, R., Rafikov, R. R., Stone, J. M., & Petrovich, C. 2011b, ApJ, 741, 56
Duffell, P. C., & MacFadyen, A. I. 2012, ApJ, 755, 7
Gardiner, T. A., & Stone, J. M. 2008, J. Comput. Phys., 227, 4123
Goldreich, P., & Tremaine, S. 1979, ApJ, 233, 857
Goodman, J., & Rafikov, R. R. 2001, ApJ, 552, 793
Kley, W. 1989, A&A, 208, 98

Kley, W. 1998, A&A, 338, L37
Kley, W. 1999, MNRAS, 303, 696
Kley, W., Bitsch, B., & Klahr, H. 2009, A&A, 506, 971
Korycansky, D. G., & Papaloizou, J. C. B. 1996, ApJS, 105, 181
Li, H., Li, S., Koller, J., et al. 2005, ApJ, 624, 1003
Li, H., Lubow, S. H., Li, S., & Lin, D. N. C. 2009, ApJ, 690, L52
Masset, F. 2000a, A&AS, 141, 165
Masset, F. S. 2000b, in Disks, Planetesimals, and Planets, eds. G. Garzón, C. Eiroa, D. de Winter, & T. J. Mahoney, ASP Conf. Ser., 219, 75
Masset, F. S. 2001, ApJ, 558, 453
Masset, F. S. 2002, A&A, 387, 605
Masset, F. S., & Casoli, J. 2009, ApJ, 703, 857
Masset, F. S., & Casoli, J. 2010, ApJ, 723, 1393
Masset, F. S., D'Angelo, G., & Kley, W. 2006, ApJ, 652, 730
Mignone, A., Bodo, G., Massaglia, S., et al. 2007, ApJS, 170, 228
Mignone, A., Flock, M., Stute, M., Kolb, S. M., & Muscianisi, G. 2012, A&A, 545, A152
Müller, T. W. A., Kley, W., & Meru, F. 2012, A&A, 541, A123
Paardekooper, S.-J., & Mellema, G. 2008, A&A, 478, 245
Paardekooper, S.-J., Baruteau, C., Crida, A., & Kley, W. 2010, MNRAS, 401, 1950
Paardekooper, S.-J., Baruteau, C., & Kley, W. 2011, MNRAS, 410, 293
Rafikov, R. R., & Petrovich, C. 2012, ApJ, 747, 24
Rein, H. 2010, Ph.D. Thesis, University of Cambridge [arXiv:1012.0266]
Stone, J. M., & Gardiner, T. A. 2010, ApJS, 189, 142
Ward, W. R. 2007, in Lunar and Planetary Institute Science Conference Abstracts, 38, 2289
Ziegler, U., & Yorke, H. W. 1997, Comp. Phys. Commun., 101, 54

A&A 560, A40 (2013)
DOI: 10.1051/0004-6361/201322503

Astronomy & Astrophysics

Modelling accretion in transitional disks

Tobias W. A. Müller and Wilhelm Kley

Institut für Astronomie & Astrophysik, Universität Tübingen, Auf der Morgenstelle 10, 72076 Tübingen, Germany
e-mail: Tobias_Mueller@twam.info

Received 19 August 2013 / Accepted 14 October 2013

ABSTRACT

Context. Transitional disks are protoplanetary disks around young stars that display inner holes in the dust distribution within a few au that are accompanied by some gas accretion onto the central star. These cavities could possibly be created by the presence of one or more massive planets that opened a large gap or even cleared the whole inner region.
Aims. If the gap is created by planets and gas is still present in it, then there should be a flow of gas past the planet into the inner region. It is our goal to study in detail the mass accretion rate into this planet-created gap in transitional disks and in particular the dependency on the planet's mass and the thermodynamic properties of the disk.
Methods. We performed 2D hydrodynamical simulations using the grid-based FARGO code for disks with embedded planets. We added radiative cooling from the disk surfaces, radiative diffusion in the disk midplane, and stellar irradiation to the energy equation to have more realistic models.
Results. The mass flow rate into the gap region depends, for given disk thermodynamics, non-monotonically on the mass of the planet. Generally, more massive planets open wider and deeper gaps which would tend to reduce the mass accretion into the inner cavity. However, for larger mass planets the outer disk becomes eccentric and the mass flow rate is enhanced over the low mass cases. As a result, for the isothermal disks the mass flow is always comparable to the expected mass flow of unperturbed disks $\dot{M}_\mathrm{d}$, while for more realistic radiative disks the mass flow is very small for low mass planets ($\leq 4\,M_\mathrm{jup}$) and about 50% of $\dot{M}_\mathrm{d}$ for larger planet masses. The critical planet mass that allows the disk to become eccentric is much larger for radiative disks than for purely isothermal cases.
Conclusions. Massive embedded planets can reduce the mass flow across the gap considerably, to values of about an order of magnitude smaller than the standard disk accretion rate, and can be responsible for opening large cavities. The remaining mass flow into the central cavity is in good agreement with the observations.

Key words. accretion, accretion disks – protoplanetary disks – planet-disk interactions – methods: numerical – hydrodynamics – planets and satellites: formation

1. Introduction

The early stages of planet formation take place in protoplanetary disks around young stars and the growing and evolving planets shape the structure of the disks. One important observational goal is the detection of signatures that give direct hints of the presence of planets in such disks. One class of systems that have been linked to planets are the so-called transitional disks that show a deficiency in the IR excess in their spectral energy distribution (SED) and/or show an extended inner hole in the disk in direct images. In recent years many of these transitional disks have been discovered, for example by the *Spitzer* Space Telescope (Muzerolle et al. 2010; Kim et al. 2013). The occurrence rate of transitional disks rises monotonically with age from about 1% at an age of one million years to about 20% at 8 million years (Muzerolle et al. 2010) and so they are potentially very interesting indicators of the late phase in the planet formation process. Disks with gaps or completely cleared inner cavities usually fshow mass accretion onto the star, but with accretion rates $\dot{M}$ typically an order of magnitude smaller than that of a continuous disk (Kim et al. 2013). As there is a clear decrease in $\dot{M}$ from continuous disks over disks with gaps to disks with cavities, Kim et al. (2013) suggest that the presence of substellar companions (planets) may be the most likely explanation of the properties of transitional disks.

Growing planets can open gaps within the disk after accumulating a sufficient amount of mass, and so they constitute a natural possible explanation (Lin & Papaloizou 1993). Indeed, single planet simulations of embedded planets could show the formation of large inner cavities with a reduced mass flow through the inner hole (Quillen et al. 2004; Varnière et al. 2006). In these simulations, a massive Jupiter-like planet opened a gap in the disk and the inner cavity was cleared out rapidly through mass flow through the inner boundary onto the star. While it was possible to produce a deep cavity, it has been pointed out that this may be due to the special outflow boundary condition used at the inner edge (Crida et al. 2007). Additional clearing of the inner disk in the case of one embedded planet region may also be mediated by disk photo-evaporation (Alexander & Armitage 2009), which has been investigated in simulations by Rosotti et al. (2013). Here, the timescale of the evaporation process has to be chosen such that it is compatible with the observed long life times of accretion in T Tau disks (Zhu et al. 2011). Because it is known that multiple planets can clear out much deeper and wider gaps than single planets (Kley 2000), it has been suggested that the large gaps and inner cavities may be caused by the presence of multiple (up to four) planets (Dodson-Robinson & Salyk 2011; Zhu et al. 2011). In this scenario, however, mass transfer has to occur across the planets and the system has to be dynamically stable over long timescales.

The recent observations presented by Mayama et al. (2012) that show a kind of spiral arm connecting the outer disk through the cleared area with the star strengthened these hints of planets within transitional disks. In either case, multiple planets or a single planet, the important question is, how strong is the mass flow from the outer disk across the planet into the inner cavity onto the star?

Even though the option of multiple planets has been suggested as a possible cause for the observed properties of transitional disks, we will nevertheless focus in this paper of the effect of single embedded planets in the disk. As pointed out above, even in the presence of multiple planets it is necessary for mass to flow from the outer disk into the inner gap region to provide for the observed accretion signatures onto the star. Here, we focus on the dynamics of single massive planets that are surrounded by an outer accretion disk and no inner counterpart. For smaller mass planets ($<M_{\rm jup}$) the mass accretion rate across a gap has been analysed by Lubow & D'Angelo (2006). This single planet could be considered the outermost in a multi-planet system. Our simulations will give important information about the mass flow from the outer disk into this planetary system.

We are particularly interested in the amount of mass that can flow across massive planets into the inner cavity. For this purpose we have performed a detailed analysis of this process considering planets of different masses. Additionally, we have improved on the thermodynamics of the disk and consider isothermal as well as radiative disks with and without irradiation from the central star.

In Sect. 2 we describe our physical and numerical modelling of the process. The standard model is described in Sect. 3. In Sect. 4 we present the results of the isothermal runs for different planet masses together with some numerical tests. This is followed in Sect. 5 by the radiative results that are compared to even more extended models that include irradiation in Sect. 6.

2. Model set-up

2.1. Physics and equations

We assumed an infinitesimally thin disk around the star and therefore solved the vertically integrated versions of the hydrodynamical equations. For the coordinate system we chose cylindrical coordinates (r, φ, z), centred on the star where the disk lies in the equatorial $z = 0$ plane.

The vertically integrated versions of the continuity equation and the equations of motions in the $r - \varphi$ plane can be found in Müller & Kley (2012, Sect. 2.1). Here, we included an energy equation to allow for a more realistic thermodynamic treatment of the disk. The vertically integrated energy equation reads

$$\frac{\partial e}{\partial t} + \nabla \cdot (e\boldsymbol{v}) = -p\nabla \cdot \boldsymbol{v} + Q_+ - Q_-, \tag{1}$$

where e is the internal energy density, Q_+ the heating source term, and Q_- the cooling source term.

The cooling term Q_- is given by the vertically integrated divergence of the radiative flux,

$$F = -\frac{4\sigma_{\rm R}}{3\rho\kappa}\nabla T^4, \tag{2}$$

where $\sigma_{\rm R}$ is the Stefan-Boltzmann constant, ρ the density, κ the Rosseland mean opacity and T the temperature. It can be written as

$$\begin{aligned} Q_- &= -\int_{-\infty}^{\infty} \nabla \cdot F \,{\rm d}z = -\int_{-\infty}^{\infty} \nabla \cdot \left(-\frac{16\sigma_{\rm R}}{3\rho\kappa} T^3 \nabla T\right) {\rm d}z \\ &= -\int_{-\infty}^{\infty} \frac{\partial}{\partial z}\left(-\frac{16\sigma_{\rm R}}{3\rho\kappa} T^3 \frac{\partial}{\partial z} T\right) {\rm d}z \\ &\quad -\int_{-\infty}^{\infty}\left[\frac{1}{r}\frac{\partial}{\partial r} r\left(-\frac{16\sigma_{\rm R}}{3\rho\kappa} T^3 \frac{\partial}{\partial r} T\right) + \frac{1}{r}\frac{\partial}{\partial \varphi}\frac{1}{r}\left(-\frac{16\sigma_{\rm R}}{3\rho\kappa} T^3 \frac{\partial}{\partial \varphi} T\right)\right] {\rm d}z \\ &\approx -Q_{\rm rad} - 2H\,\nabla \cdot (K\nabla T)\,. \end{aligned} \tag{3}$$

Here $Q_{\rm rad}$ describes the radiative losses from the disk surfaces which is calculated using suitably averaged opacities (Müller & Kley 2012, Sect. 2.1), and the second term corresponds to the radiative diffusion in plane of the disk; $H = c_{\rm s}/\Omega_{\rm K}$ is the pressure scale height given by the midplane sound speed, $c_{\rm s}$, and the Keplerian rotational angular velocity, $\Omega_{\rm K}$, of the disk. The coefficient of the radiative diffusion in the r–φ plane is given by $K = -\frac{16\sigma_{\rm R}}{3\rho\kappa} T^3$.

The heating term Q_+ consists of the viscous dissipation $Q_{\rm visc}$ and the irradiation from the star $Q_{\rm irrad}$. The stellar irradiation to one surface of the disk can be approximated by

$$Q_{\rm irrad} = \beta\sigma_{\rm R} T_{\rm star}^4 \left(\frac{R_{\rm star}}{r}\right)^2 \tag{4}$$

(Günther et al. 2004), where $T_{\rm star}$ is the effective photospheric temperature of the star and $R_{\rm star}$ the radius of the star. The factor β accounts for the non-perpendicular impact of the irradiation from the star onto the disk.

2.2. Numerical considerations

We used the adiabatic version of the FARGO code (Masset 2000; Baruteau 2008). For the radiative cooling $Q_{\rm rad}$ from Eq. (3) we used our implementation from Müller & Kley (2012). The radiative diffusion source term is solved separately after the rest of the source-terms as a flux-limited diffusion equation for the temperature (Kley 1989; Kley & Crida 2008). We solve it implicitly using a successive over-relaxation (SOR) method. For the stellar irradiation we implemented the approximation by Günther et al. (2004).

The planet in the disk has a Plummer type gravitational potential to account for the vertical extent of the disk and to avoid numerical problems of a point-mass potential. We used a smoothing value of $\epsilon = 0.6H$ as this describes the vertically averaged forces very well (Müller et al. 2012).

To avoid numerical problems the density cannot fall below a minimum value of $\Sigma_{\rm floor} = 10^{-7} \cdot \Sigma_0$, where Σ_0 is the reference density at $r = r_{\rm jup} = 5.2$ au, and the temperature is always at least $T_{\rm floor} = 3$ K, which is about the temperature of the cosmic background radiation.

Because the disk has an abrupt end at the inner edge of the computational domain, the stellar irradiation produces here artificial high temperatures because of the large amount of energy deposited. To account for this we introduced an estimated horizontal optical depth $\tilde{\tau}$ by rescaling the vertical optical depth τ (see Müller & Kley 2012, Eq. (12)) by the radial extent of the corresponding grid cell

$$\tilde{\tau}_{i,j} = \tau_{i,j} \frac{r_{i+1} - r_i}{(hr)_{i,j}}, \tag{5}$$

where $h = H/r$ is the aspect ratio of the disk. If $\tilde{\tau}_{i,j} < 1$ we set $Q_{\rm irrad} = 0$. This simple procedure keeps the temperatures within the gap region regular and allows for standard heating in the outer parts of the disk.

2.3. Boundary conditions

To maintain a given disk structure in the outer parts of the disk we implemented the damping mechanism by de Val-Borro et al. (2006), where specified quantities like radial velocity and angular velocity are damped towards their initial values. This damping is described by

$$\frac{\mathrm{d}\xi}{\mathrm{d}t} = -\frac{\xi - \xi_0}{\tau} R(r)^2, \tag{6}$$

where $\xi \in \{\Sigma, v_r, v_\varphi, e\}$, τ is the damping timescale, and $R(r)$ is a linear ramp-function rising from 0 to 1 from the damping star radius to the outer radius of the computational domain. To be able to measure the mass loss rate in our models we only damped the velocity components within $0.9\,r_{\rm max}$ to $r_{\rm max}$ using a time factor of $\tau = 3 \times 10^{-2} \cdot 2\pi\,\Omega_{\rm K}(r_{\rm max})^{-1}$.

In addition to the damping we used a reflecting boundary condition at the outer edge so that no mass could escape through the outer boundary. For the inner edge we used a zero-gradient outflow boundary condition and measured the amount of mass lost through this boundary to calculate the mass accretion rate onto the star. The details of the implementation of the boundary conditions can be found in Müller & Kley (2012, Sect. 2.2).

3. The standard model

Our model consists of a planet with a varying mass of 1 to 16 Jupiter masses ($M_{\rm jup}$) orbiting a Sun-like star with a semi-major axis of $1\,r_{\rm jup} = 5.2$ au. The planet is fixed in its circular orbit and therefore cannot change its orbital parameters during the simulation. Beyond $r_{\rm jup}$ the star is surrounded by a gaseous disk that extends up to $r_{\rm max} = 5\,r_{\rm jup}$, the outer edge of the computational domain. The inner radius depends on the model and ranges from 0.7 to $0.9\,r_{\rm jup}$, where we chose for the main part of our models $r_{\rm min} = 0.7$. The gas disk is set up initially as if there were no planet with a simple surface density power-law profile of $r^{-0.5}$ and a temperature power-law profile of r^{-1}. To prevent strong shock waves in the initial phase of the simulations the planet's mass is ramped up slowly over 50 orbits. All the models were run for a total simulation time of 5000 planetary orbits. For the viscosity we used a constant kinematic viscosity $\nu = 10^{15}$ cm^2 s^{-1} that corresponds to an α-value of about 4×10^{-3} at the reference radius. Table 1 summarizes the parameters of the standard model.

4. Isothermal simulations

For the first set of simulations we used a locally isothermal approach keeping the initial temperature stratification throughout the whole simulation fixed. We assumed a constant aspect ratio $H/r = 0.05$, that corresponds to a temperature profile of r^{-1} with 137 K at the inner edge and 24 K at the outer edge of the disk. Similar simulations have been performed by Kley & Dirksen (2006) for a constant surface density profile; they damped the surface density at the outer edge of the disk.

Table 1. Parameters of the standard disk model.

Star mass ($M_{\rm star}$)	$1\,M_\odot$
Star radius ($R_{\rm star}$)	$1\,R_\odot$
Planet mass ($M_{\rm p}$)	$4\,M_{\rm jup}$
Adiabatic index (γ)	$\frac{7}{5}$
Mean-molecular weight (μ)	2.35
Surface density (Σ_0)	888.723 g cm^{-2}
Viscosity (ν)	1×10^{15} cm^2 s^{-1}
Initial density profile (Σ)	$\propto r^{-1/2}$
Initial temperature profile (T)	$\propto r^{-1}$
Initial disk aspect ratio (H/r)	0.05
Grid ($N_r \times N_\varphi$)	256×1024
Computational domain ($r_{\rm min} - r_{\rm max}$)	0.7–5 $r_{\rm jup}$

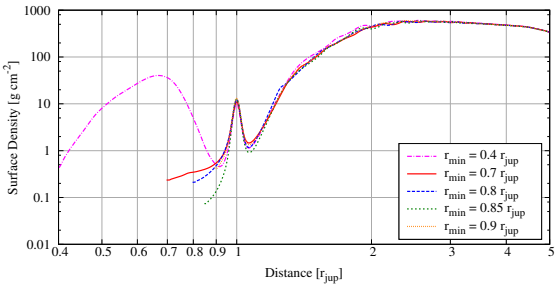

Fig. 1. Azimuthally averaged radial profile of surface density of the isothermal set-up after 5000 orbits with a planet of $M_{\rm p} = 4\,M_{\rm jup}$.

4.1. Inner radius dependency

In this first set of simulations, a fixed planet mass of $M_{\rm p} = 4\,M_{\rm jup}$ was assumed, while the location of the inner radius was varied to check its influence. The L_1 point lies at about 0.896 au and so all radii were chosen in such a way that the Roche-Lobe of the planet is fully included in the computational domain. Kley & Dirksen (2006) showed, that for planets with $M_{\rm p} \geq 3\,M_{\rm jup}$ the disks become eccentric after a very long time (>1000 orbits). Figures 1 and 2 show the azimuthally averaged surface density and disk eccentricity profiles after 5000 orbits for $M_{\rm p} = 4\,M_{\rm jup}$ and five different inner radii. For the eccentricity we calculated first a mass weighted average of each grid cell and then averaged over the azimuthal direction. We note that the models are in different phases of their eccentricity oscillation as shown in Fig. 5. The gap opened by the planet at $r = 1\,r_{\rm jup}$ is clearly visible and the gas in the vicinity has eccentric orbits with an eccentricity of up to 0.22. The eccentricities for all models are very similar. The model with the smallest inner radius shows a slightly smaller eccentricity just outside of the planet inside the gap. This does not influence the mass flow across the planet, however. The eccentricity can also be noticed in the surface density plot show in Fig. 3. In this r-φ plot, circular motions are represented by horizontal lines. However, the gas at the outer edge of the gap has wavelike perturbations which visualize the eccentricity of its orbit. This is similar to Fig. 1 of Kley & Dirksen (2006) where the outer disk also becomes eccentric.

These quasi-stationary states of the disks need a rather long time to establish. Figure 4 shows the disk mass evolution and Fig. 5 the disk eccentricity evolution of the disks over the total

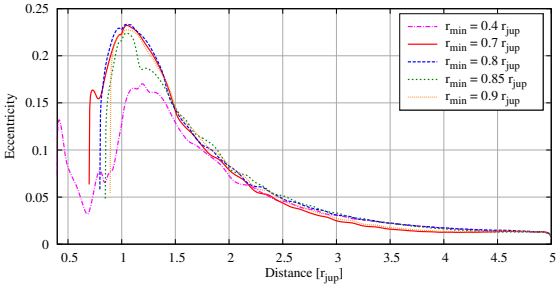

Fig. 2. Azimuthally averaged radial profile of eccentricity of the isothermal set-up after 5000 orbits with a planet of $M_p = 4\,M_{jup}$.

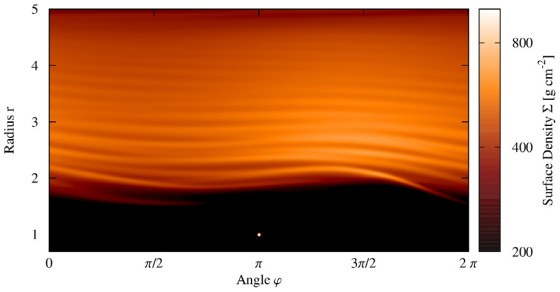

Fig. 3. Surface density of the isothermal set-up after 5000 orbits with a planet of $M_p = 4\,M_{jup}$ and an inner radius of $r_{min} = 0.7$ jup. The planet is located at the angle of π in this $r - \phi$ representation.

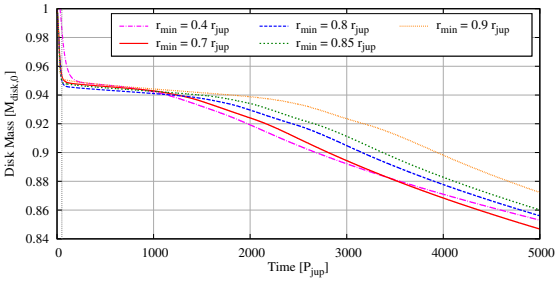

Fig. 4. Total disk mass over time for the isothermal set-up with a planet mass of $M_p = 4\,M_{jup}$. The vertical dotted line at $t = 50\,P_{jup}$ marks the time when the planet has reached its full mass.

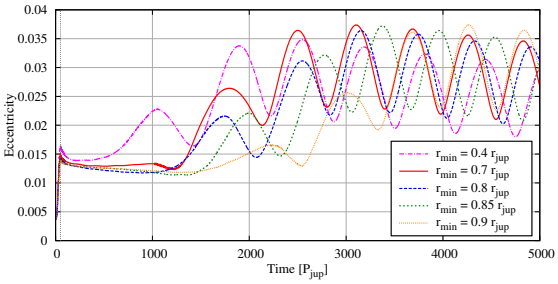

Fig. 5. Global disk eccentricity over time for the isothermal set-up with a planet mass of $M_p = 4\,M_{jup}$. The vertical dotted line at $t = 50\,P_{jup}$ marks the time when the planet has reached its full mass.

simulation time of 5000 orbits. The planet's mass is ramped up during the first 50 orbits which is indicated by the dotted vertical line. For about the first 1000 orbits (depending on the inner radius), the disk evolution is very smooth with a nearly constant mass content and small eccentricity. After this time the disk becomes eccentric and thereby loses more mass through the inner boundary. The simulations with smaller computational domain (larger r_{min}) need some more time to develop the disk eccentricity, but after that display a similar evolution.

Figure 6 shows the normalized mass accretion rate through the inner boundary of the computational domain using a moving average over 50 orbits. The normalized mass flow $-\dot{M}(t)/M_{disk}(t)$ is shown where the actual mass of the disk is used, as the surface density Σ and therefore the disk mass M_{disk} cancel out of the equations in locally isothermal simulations. During the first ~1000 orbits the mass accretion rate is almost constant at about $5 \times 10^{-6}\,M_{disk}\,P_{jup}^{-1}$. However, as soon as the disk becomes eccentric (see Fig. 5) the mass accretion rate starts to increase as more mass is crossing the planetary orbit and flows through the inner boundary at r_{min}.

The initial mass loss through the inner boundary is smaller than the standard mass accretion rate of stationary, viscous accretion disks as given by

$$\dot{M}_{disk} = 3\pi\nu\Sigma_0 = 8.37 \times 10^{18}\ \mathrm{g\,s^{-1}} = 1.33 \times 10^{-7} M_\odot\ \mathrm{a^{-1}} = 1.58 \times 10^{-6} M_\odot\,P_{jup}^{-1}. \quad (7)$$

After the disk becomes eccentric, it seems to converge against the value, which is indicated by the horizontal dashed line.

We note that all the figures with normalized mass accretion rates are displayed in units of P_{jup}^{-1}, whereas accretion rates are usually given in $M_\odot\,\mathrm{a^{-1}}$. The 0.7 r_{jup} models have an initial disk mass of 0.12 $M_\odot$, and because the disks lose less than 20% of their mass during the simulation time of 5000 orbits (see Fig. 4), one can get a rough estimate of the mass accretion rate in $M_\odot\,\mathrm{a^{-1}}$ by dividing the values in the figures by a factor of

$$\frac{1}{M_{disk}} = \frac{1}{0.12\,M_\odot}\,\frac{11.86\,\mathrm{a}}{P_{jup}} = 98.86\,\mathrm{a}\,M_\odot^{-1}\,P_{jup}^{-1} \approx 100. \quad (8)$$

The shapes of the time-dependent curves (Figs. 4–6) appear to be shifted in time, because the disks with the smaller inner computational radii need more time to loose the mass in the outer disk. This leads to a surface density enhancement at the outer edge of the gap and subsequently to stronger eccentricity excitations.

4.2. Planet mass dependency

The final state of the simulations are not strongly dependent on the minimum radius of the computational domain. So we chose $r_{min} = 0.7\,r_{jup}$ for the following simulations to compare different planet masses. As shown by Kley & Dirksen (2006), the outer disk turns eccentric for planetary masses larger than about 3 M_{jup}. So we varied the planet mass from 1 M_{jup} to 16 M_{jup} by doubling it each step. Figures 7 and 8 show again the radial profiles of the surface density and the eccentricity at the end of simulation after 5000 orbits. We note that the models are in different phases of their global eccentricity oscillation as shown in Fig. 10. For example, in Fig. 8 the 16 M_{jup} model shows a maximum eccentricity of about 0.35, whereas the maximum eccentricity varies between 0.32 and 0.4 during one period of the oscillation. In agreement with the previous results,

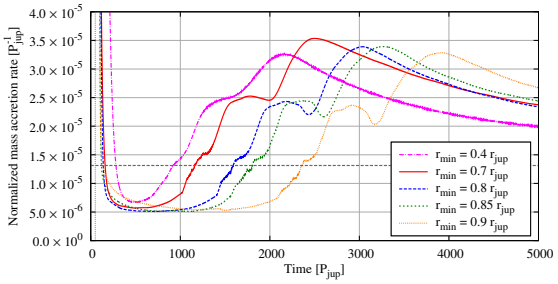

Fig. 6. Normalized mass accretion rate over time for the isothermal set-up with a planet mass of $M_\mathrm{p} = 4\,M_\mathrm{jup}$. The values are plotted as a moving average over 50 orbits to remove jitter. The vertical dotted line at $t = 50\,P_\mathrm{jup}$ marks the time when the planet has reached its full mass and the horizontal dashed line is the gas accretion rate given by Eq. (7).

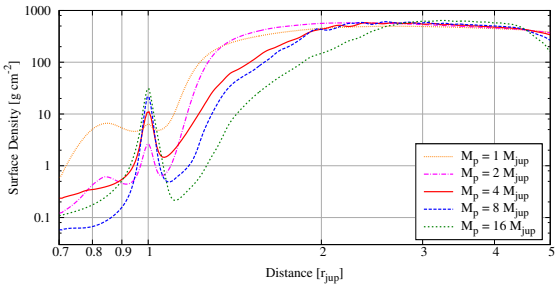

Fig. 7. Azimuthally averaged radial profile of surface density of the isothermal set-up after 5000 orbits with an inner radius of the computational domain of $r_\mathrm{min} = 0.7\,r_\mathrm{jup}$.

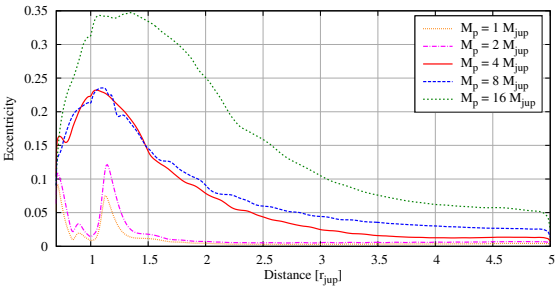

Fig. 8. Azimuthally averaged radial profile of eccentricity of the isothermal set-up after 5000 orbits with an inner radius of the computational domain of $r_\mathrm{min} = 0.7\,r_\mathrm{jup}$.

the simulations with the small mass planets, 1 and 2 M_jup, do not show any significant disk eccentricity. Beyond a planet mass of about 3−4 M_jup the disk becomes eccentric. As expected, the more massive planets form a much wider gap in the disk, and the eccentricity of the disk is much higher for the 4 M_jup and more massive planets.

In Figs. 9 and 10 the disk mass and disk eccentricity over time are shown. The average disk eccentricity increases clearly with the planetary mass. It is easy to see that the higher the planet mass is, the faster the disk eccentricity starts to grow and that the mass loss starts earlier. Whereas the previously examined example of the 4 M_jup planet needs about 1000 orbits until the disk eccentricity grows, the lower mass planet models do

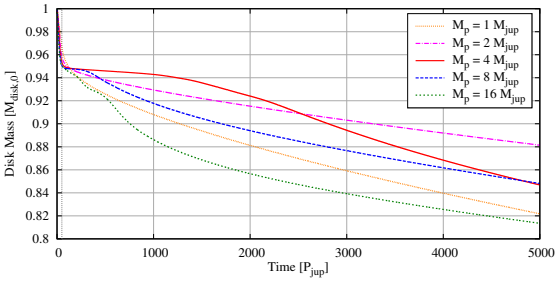

Fig. 9. Total disk mass over time for the isothermal set-up with an inner radius of the computational domain of $r_\mathrm{min} = 0.7\,r_\mathrm{jup}$. The vertical dotted line at $t = 50\,P_\mathrm{jup}$ marks the time when the planet has reached its full mass.

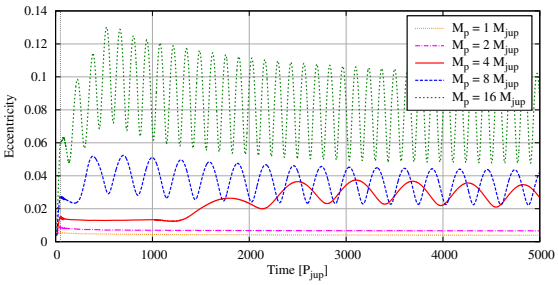

Fig. 10. Global disk eccentricity over time for the isothermal set-up with an inner radius of the computational domain of $r_\mathrm{min} = 0.7\,r_\mathrm{jup}$. The vertical dotted line at $t = 50\,P_\mathrm{jup}$ marks the time when the planet has reached its full mass.

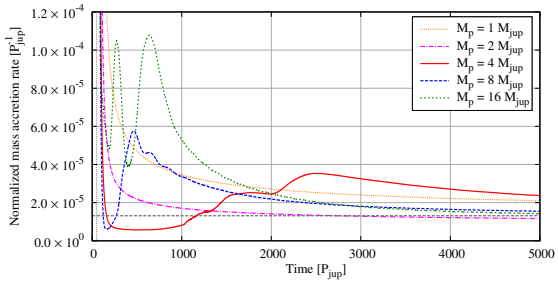

Fig. 11. Normalized mass accretion rate over time for the isothermal set-up with an inner radius of the computational domain of $r_\mathrm{min} = 0.7\,r_\mathrm{jup}$. The values are plotted as a moving average over 50 orbits to remove jitter. The vertical dotted line at $t = 50\,P_\mathrm{jup}$ marks the time when the planet has reached its full mass and the horizontal dashed line is the gas accretion rate given by Eq. (7).

not develop a noteworthy eccentricity at all. The models with more massive planets start to develop much large eccentricities almost instantly. The normalized mass accretion rate is displayed in Fig. 11. There is no clear trend that with increasing planet mass the mass accretion rate grows or shrinks because there are two competing effects. The growing disk eccentricity favours the mass transport across the planet into the inner cavity of the disk whereas the larger gap due to the larger planet mass hinders mass transport through this gap. All the mass accretion rates are of the order of the typical disk accretion rates from Eq. (7).

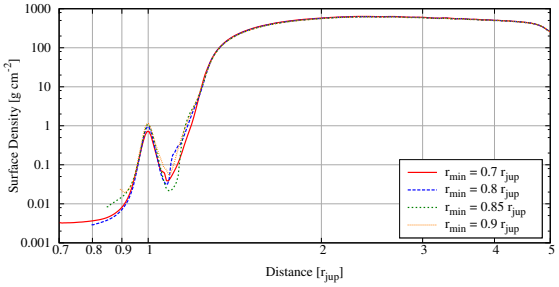

Fig. 12. Azimuthally averaged radial profile of surface density of the radiative set-up after 5000 orbits with a planet of $M_p = 4\,M_{jup}$.

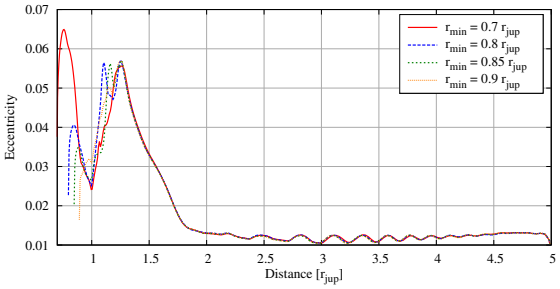

Fig. 13. Azimuthally averaged radial profile of eccentricity of the radiative set-up after 5000 orbits with a planet of $M_p = 4\,M_{jup}$.

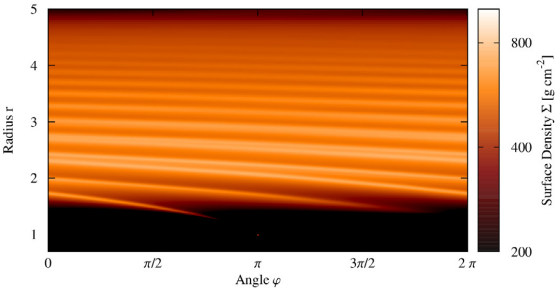

Fig. 14. Surface density of the radiative set-up after 5000 orbits with a planet of $M_p = 4\,M_{jup}$ and an inner radius of $r_{min} = 0.7$ jup. The planet is located at the angle of π.

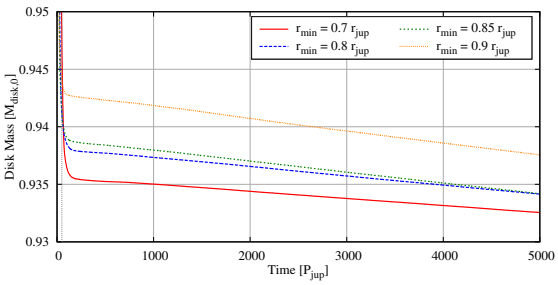

Fig. 15. Total disk mass over time for the radiative set-up with a planet mass of $M_p = 4\,M_{jup}$. The vertical dotted line at $t = 50\,P_{jup}$ marks the time when the planet has reached its full mass.

5. Radiative simulations

In Sect. 4 we performed locally isothermal simulations and maintained the initial temperature stratification throughout the whole simulation. In this section we extend the set-up and also solve for the energy equation (Eq. (1)), but neglect the radiative diffusion ($2H\,\nabla\,(K\nabla T) = 0$), because in standard accretion disk models this term is much smaller than the vertical cooling. Additionally, we neglect stellar irradiation ($Q_{irrad} = 0$). We redid the same set of calculations (except for the $r_{min} = 0.4\,r_{jup}$ case) as in the isothermal case for a direct comparison of the results.

5.1. Inner radius dependency

Figures 12 and 13 show the surface density and eccentricity profiles at the end of the simulation. Whereas the shape of surface density profile does not look too different from the isothermal models shown in Fig. 1, the absolute values within the gap are about a magnitude smaller. All models display a much lower total eccentricity. The planets also open a gap that can be seen in Fig. 14, but compared with to the isothermal case (Fig. 3) the outer edge of the gap is much less distorted because of the much smaller eccentricity. Only within the gap does a significant eccentricity develop and it is a factor of three to four smaller than in the isothermal simulations (see Fig. 3).

The global disk eccentricity is more or less constant over time and it reaches its final, very small value shortly after the planet has been ramped up. The value of 0.013 at the end of the simulation is about the same as the value for the first stage in the isothermal evolution (Fig. 5). Because of the small constant value of the disk eccentricity there is a small mass loss through the inner edge of the simulation region, which can be seen in the disk mass over time simulation shown in Fig. 15. As in the isothermal models, the mass loss at the start of simulation is dependent on the exact position of the inner boundary, but for the rest of the simulation the results are only shifted.

The normalized mass accretion rate shown in Fig. 16 is therefore almost constant except for some jitter. For the $0.7\,r_{jup}$ model we obtain an average value of $(6.604 \pm 0.008) \times 10^{-7} P_{jup}^{-1}$ after 1000 orbits. Assuming a constant disk mass (see Eq. (8)), this corresponds to a mass accretion rate of $(6.680 \pm 0.008) \times 10^{-9} M_\odot\,a^{-1}$, which fits very well to observational data (Kim et al. 2013). Interestingly, it is now much smaller than the value given by Eq. (7) in contrast to the isothermal simulations, as the disk is much less eccentric and therefore pushes less mass through the gap. In addition, the disk can radiate its energy away and is therefore much cooler which also hinders mass transport through the gap. In the next section we present a comparison of the temperatures in the isothermal and radiative disks.

Figure 17 shows a zoomed version of Fig. 14 with a different scaling of the surface density. Within the gap almost no gas is left (<0.001 g cm^{-2}), but the spiral arm induced by the planet is clearly visible.

5.2. Planet mass dependency

For the comparison of different planet masses we again chose $r_{min} = 0.7\,r_{jup}$ for the inner boundary. Figures 18 and 19 display the surface density and eccentricity profiles at the end of the simulation. As in the isothermal, case the more massive planets open a deeper gap in the disk. In the isothermal simulations, the disk eccentricity profiles were much larger for masses $M_p \geq 4\,M_{jup}$, whereas in the radiative models this is only the

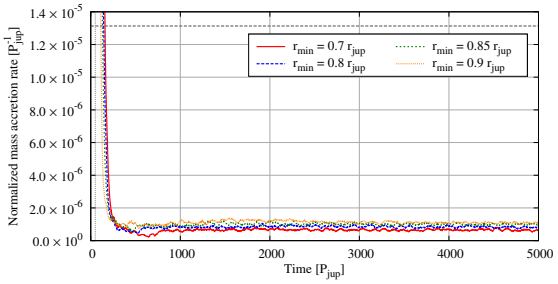

Fig. 16. Normalized mass accretion rate over time for the radiative set-up with a planet mass of $M_p = 4\,M_{jup}$. The values are plotted as a moving average over 50 orbits to remove jitter. The vertical dotted line at $t = 50\,P_{jup}$ marks the time when the planet has reached its full mass and the horizontal dashed line is the gas accretion rate given by Eq. (7).

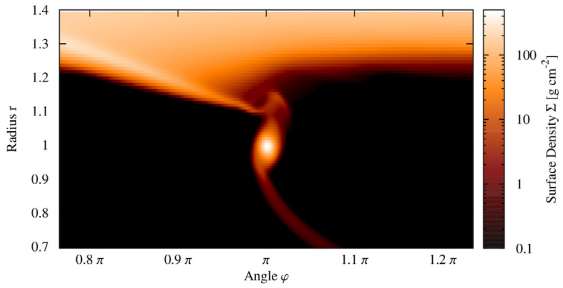

Fig. 17. Surface density of the radiative set-up after 5000 orbits with a planet of $M_p = 4\,M_{jup}$ and an inner radius of $r_{min} = 0.7$ jup. The planet is located at the angle of π.

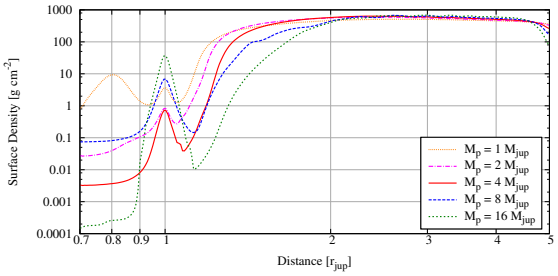

Fig. 18. Azimuthally averaged radial profile of surface density of the radiative set-up after 5000 orbits with an inner radius of the computational domain of $r_{min} = 0.7\,r_{jup}$.

case for masses $M_p \geq 8\,M_{jup}$. In addition, all eccentricities are smaller than those seen in the isothermal case. We note again, that the models are in different phases of their eccentricity oscillation as shown in Fig. 22. Because the temperature profile can also change during the simulation, Fig. 20 shows the radial temperature profile at the end of the simulation. The temperature in the gap is rather low and therefore we can see the deeper gaps for the more massive planets even in the temperature profile. The maximum temperature is always at the outer edge of the gap and is dependent on the planet's mass. The edge temperature is the highest for the $4\,M_{jup}$ and lower for higher and smaller planet masses.

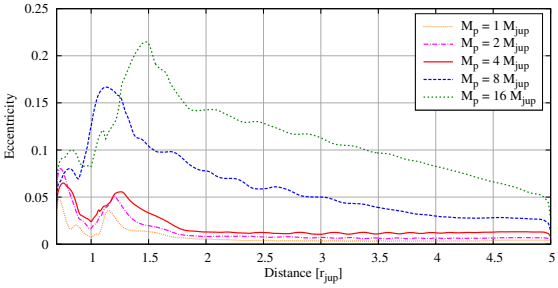

Fig. 19. Azimuthally averaged radial profile of eccentricity of the radiative set-up after 5000 orbits with an inner radius of the computational domain of $r_{min} = 0.7\,r_{jup}$.

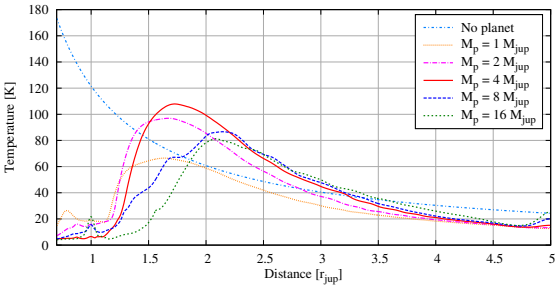

Fig. 20. Azimuthally averaged radial profile of temperature of the radiative set-up after 5000 orbits with an inner radius of the computational domain of $r_{min} = 0.7\,r_{jup}$.

The global disk mass evolution is shown in Fig. 21. The mass loss through the inner edge now depends on two factors. On the one hand, the mass flow through the gap will be increased by the disk's eccentricity as in the isothermal case. The global disk eccentricity evolution in time as shown in Fig. 22 is similar to that of the isothermal case. In the radiative case the planet mass required to reach a certain disk eccentricity is higher than in the isothermal case. On the other hand thermal pressure changes the depth of the gap which may lead to an enhanced mass flow across the gap. This is also mass dependent as already seen in Fig. 20. Figure 23 now shows the normalized mass accretion rate for the radiative models. As both effects interact we can see no clear trend for the mass accretion rate. For the two lowest mass planets (1 and 2 M_{jup}), the mass accretion rates are highest because they have the smallest gap size (see Fig. 18). The 4 M_{jup} case has a wider and deeper gap with no disk eccentricity and shows a much smaller accretion rate. For the 8 M_{jup} case the disk becomes eccentric and the mass flow increases again, while for the 16 M_{jup} case the gap widens substantially such that the mass flow rate becomes very small.

5.3. Disk mass dependency

In the isothermal models the normalized mass accretion rate was independent of the disk mass M_{disk} because as the surface density Σ cancels out of the equations. Therefore, the mass accretion rate scales with the same factor as the surface density, for example if we decrease the surface density by a factor of 10, the mass accretion rate decreases by a factor of 10.

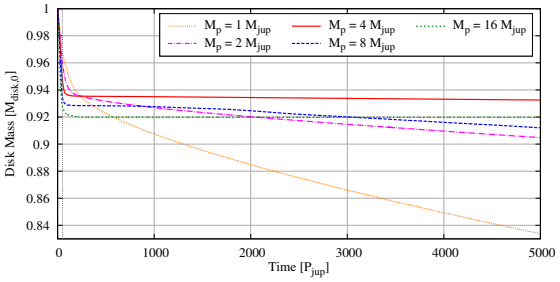

Fig. 21. Total disk mass over time for the radiative set-up with an inner radius of the computational domain of $r_{\rm min} = 0.7\,r_{\rm jup}$. The vertical dotted line at $t = 50\,P_{\rm jup}$ marks the time when the planet has reached its full mass.

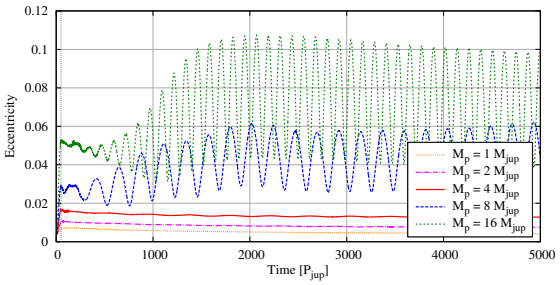

Fig. 22. Global disk eccentricity over time for the radiative set-up with an inner radius of the computational domain of $r_{\rm min} = 0.7\,r_{\rm jup}$. The vertical dotted line at $t = 50\,P_{\rm jup}$ marks the time when the planet has reached its full mass.

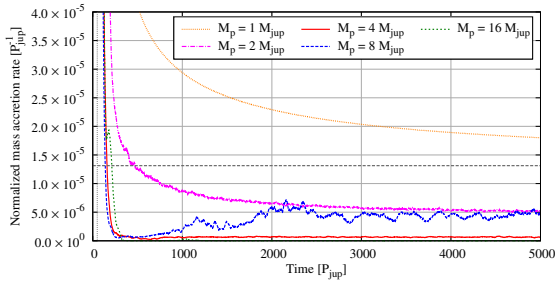

Fig. 23. Normalized mass accretion rate over time for the radiative set-up with an inner radius of the computational domain of $r_{\rm min} = 0.7\,r_{\rm jup}$. The values are plotted as a moving average over 50 orbits to remove jitter. The vertical dotted line at $t = 50\,P_{\rm jup}$ marks the time when the planet has reached its full mass and the horizontal dashed line is the gas accretion rate given by Eq. (7).

In the radiative case, however, this is no longer true. Figure 24 shows the normalized mass accretion rates and the mass accretion rates for different disk masses. The normalized mass accretion rates (upper panel of Fig. 24) seem to scale in the wrong direction at first sight. For example, the $M_{\rm disk} = 0.12\,M_\odot$ model has a smaller normalized mass accretion rate than the $M_{\rm disk} = 0.012\,M_\odot$ model, but if we calculate the mass accretion rates (lower panel of Fig. 24) with Eq. (8) the trend flips as expected and the $M_{\rm disk} = 0.12\,M_\odot$ model has a larger mass accretion rate than the $M_{\rm disk} = 0.012\,M_\odot$ model, but it does not

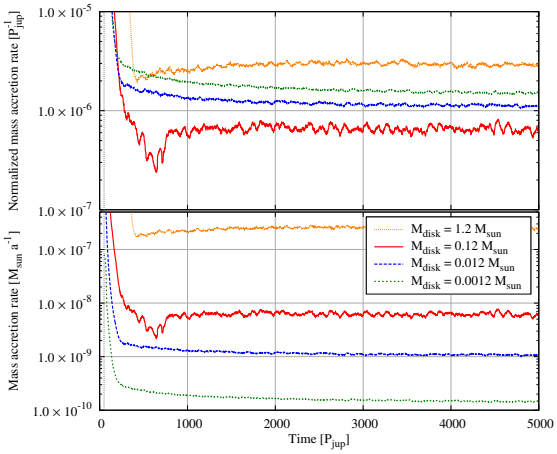

Fig. 24. Normalized mass accretion rate over time (*upper panel*) and mass accretion rate over time (*lower panel*) for the radiative set-up with an inner radius of the computational domain of $r_{\rm min} = 0.7\,r_{\rm jup}$ and a planet mass of $M_{\rm p} = 4\,M_{\rm jup}$. The values are plotted as a moving average over 50 orbits to remove jitter. The vertical dotted line at $t = 50\,P_{\rm jup}$ marks the time when the planet has reached its full mass.

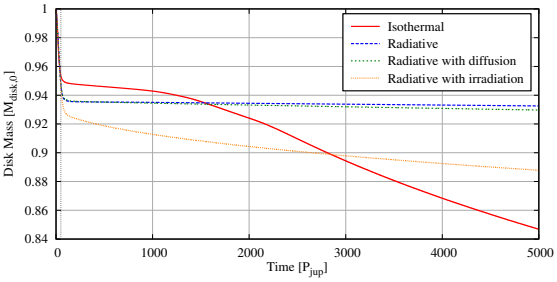

Fig. 25. Total disk mass over time for different set-ups with an inner radius of the computational domain of $r_{\rm min} = 0.7\,r_{\rm jup}$ and a planet mass of $M_{\rm p} = 4\,M_{\rm jup}$. The vertical dotted line at $t = 50\,P_{\rm jup}$ marks the time when the planet has reached its full mass.

scale with the same factor as the disk mass. For the rest of the simulations we used the $M_{\rm disk} = 0.12\,M_\odot$ model.

6. Comparison of different models

In this section we extend our models again for radiative diffusion and stellar irradiation and compare the following four different models: the isothermal set-ups from Sect. 4 with a constant temperature stratification throughout the simulation, the radiative set-ups from Sect. 5 where we solve the energy equation with viscous dissipation and radiative cooling, the radiative with diffusion set-ups where we also solve the radiative diffusion in the r–φ plane, and the radiative with irradiation set-ups where we include radiative diffusion and stellar irradiation. As radiative diffusion and stellar irradiation are very costly in terms of computation time we ran those models only with an inner radius of $r_{\rm min} = 0.7\,r_{\rm jup}$ and planet masses of $M_{\rm p} = 4\,M_{\rm jup}$ and $M_{\rm p} = 8\,M_{\rm jup}$.

Figures 25 and 26 show the disk mass and disk eccentricity evolution over the whole simulation for the $M_{\rm p} = 4\,M_{\rm jup}$ models.

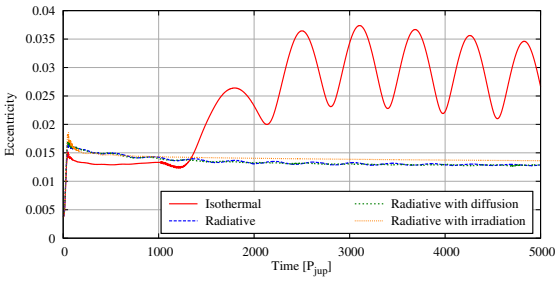

Fig. 26. Global disk eccentricity over time for different set-ups with an inner radius of the computational domain of $r_{\rm min} = 0.7\,r_{\rm jup}$ and a planet mass of $M_{\rm p} = 4\,M_{\rm jup}$. The vertical dotted line at $t = 50\,P_{\rm jup}$ marks the time when the planet has reached its full mass.

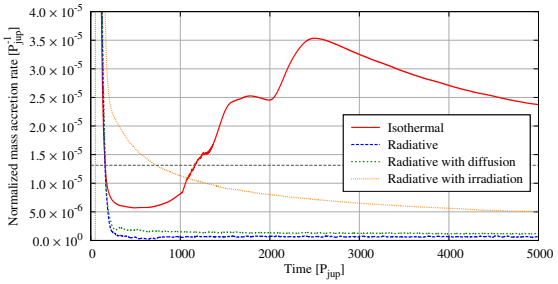

Fig. 27. Normalized mass accretion rate over time for different set-ups with an inner radius of the computational domain of $r_{\rm min} = 0.7\,r_{\rm jup}$ and a planet mass of $M_{\rm p} = 4\,M_{\rm jup}$. The vertical dotted line at $t = 50\,P_{\rm jup}$ marks the time when the planet has reached its full mass and the horizontal dashed line is the gas accretion rate given by Eq. (7).

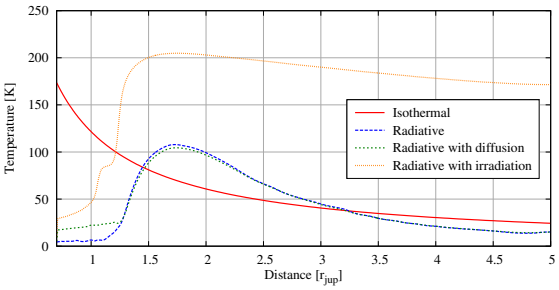

Fig. 28. Azimuthally averaged radial profile of temperature of the isothermal, radiative, radiative with diffusion and radiative with irradiation set-up after 5000 orbits with an inner radius of the computational domain of $r_{\rm min} = 0.7\,r_{\rm jup}$ and a planet mass of $M_{\rm p} = 4\,M_{\rm jup}$.

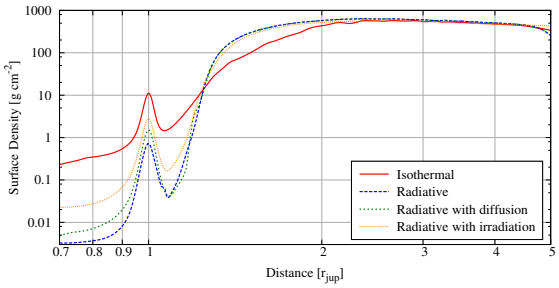

Fig. 29. Azimuthally averaged radial profile of the surface density of the isothermal, radiative, radiative with diffusion and radiative with irradiation set-up after 5000 orbits with an inner radius of the computational domain of $r_{\rm min} = 0.7\,r_{\rm jup}$ and a planet mass of $M_{\rm p} = 4\,M_{\rm jup}$.

The isothermal model shows a huge difference in both plots. The disk loses much more mass and becomes significantly more eccentric. Between the radiative model and the radiative with diffusion model there is barely a visible difference, so that the neglect of the radiative diffusion in accretion disk simulations is a valid assumption. The addition of irradiation increases the mass loss again because the disk is much hotter, but it does not play an important role for the global disk eccentricity.

The normalized mass accretion rate of all models in shown in Fig. 27. As already seen in Fig. 25, the mass loss of the isothermal model is much larger than all the other models. The radiative with diffusion model has a slightly larger accretion rate than the radiative model, but both are smaller than the standard mass accretion rate of stationary accretion disks (Eq. (7)). The accretion rate of the radiative with irradiation model needs much more time to converge and is significantly larger than those of the other two radiative models.

Therefore, the mass accretion in the irradiative model must be driven by thermal pressure through the gap, as the eccentricity is the same. This can be seen in Fig. 28, which shows the temperature profiles of all models after 5000 orbits. The isothermal model still has the unchanged initial condition, whereas the radiative models show a temperature drop in the gap. The radiative with diffusion set-up shows a slightly higher temperature in the gap as heat is diffused into the gap from the outer edge. The temperature of radiative with irradiation is much higher overall, especially in the outer regions, but the gradient on the outer edge of the gap is also much steeper and therefore has pushed more material through the gap.

In Fig. 29, we display the surface density at the final state after 5000 orbits for all our models. In the outer part of the disk, all models show comparable surface densities. In the inner gap region, the densities are typically 3 to 4 orders of magnitude smaller than in the outer disk. As expected by the mass accretion rates, the isothermal and irradiated models show an enhanced density in the gap region. In contrast, the radiative models have a surface density about an order of magnitude smaller inside the gap. For the most realistic irradiated models, the density contrast is about 4 orders in magnitude. For models with the 8 $M_{\rm jup}$ planet the principal surface density structure is very similar for the radiative models.

7. Summary and conclusions

We have performed hydrodynamic simulations of transitional disks where the inner edge is formed by a very massive planet and studied the mass flow rate of the gas from the outer disk into the inner cavity. For comparison, we have studied locally isothermal disks as well as viscously heated radiative disks including irradiation from the central star.

We find that the mass flow past the planet is largest for the isothermal models. These have a much higher temperature in the inner regions of the disk and the corresponding pressure gradient is partly responsible for the high mass flow. The second contribution comes from the eccentricity of the disk for planet masses beyond roughly 3 $M_{\rm jup}$. The disk has its largest eccentricity near

its inner edge, and reaches about 0.2 for the 4 and 8 $M_{\rm jup}$ planets and up to 0.35 for the 16 $M_{\rm jup}$ planet in the isothermal disk. For larger radii the disk eccentricity slowly declines. For eccentric disks the planet passes periodically through the disk which leads to the enhanced mass accretion into the inner gap. The asymmetries in recent observations (e.g. Mayama et al. 2012) can be explained by these eccentricities or by a vortex within the disk (Ataiee et al. 2013).

In the radiative cases, there are two reasons why the mass mass accretion rate is generally much smaller. First, the temperature is much smaller in the gap region which leads to a smaller pressure effect, and second the radiative models have a smaller disk eccentricity than the isothermal models. The maximum disk eccentricity is around 0.2 for the most massive 16 $M_{\rm jup}$ planet. The reduction in eccentricity comes about because the emission of radiation from the disk surfaces leads to an energy leakage of the eccentric modes of the disk. The model including stellar irradiation shows again a larger mass flow which is still smaller than the purely isothermal disk.

The surface density contrast between the outer and inner disk is interesting. In the eccentric disk case we find a contrast of about four orders of magnitude which is even larger in the non-eccentric disk cases. Despite this large contrast in surface density, the mass accretion rate past the planet into the gap changes by much less. For the isothermal models it is always comparable to the typical disk accretion rate (see Fig. 11) in contrast to the observations that show a reduction of about an order of magnitude compared to stationary disks (Kim et al. 2013). However, for the more realistic radiative cases, the mass accretion rate can be reduced by over an order of magnitude, if the disk is not eccentric, i.e. if the planet is smaller than about 5 $M_{\rm jup}$. This mass flow rate is in good agreement with the observations (Kim et al. 2013). For larger mass planets and eccentric disks the mass flow rate is about 40% of the standard equilibrium disk value (see Fig. 23).

Our model contains several restrictions that could be improved on in subsequent works. The models are only 2D because 3D runs over this extended simulation time of several thousand orbits are not feasible at the present time. We estimate that because of the large mass of the planets and the deep gaps that are opened, the differences between 2D and 3D may be not too large. For Jupiter-mass planets the gaps are nearly indistinguishable (Kley et al. 2001) in 2D and 3D. Furthermore, the planets cannot accrete material from their surroundings. Because of the strong decline of the density in the gap, this effect may be more important for low mass planets as well. It may play a role, however, in the eccentric disk case where it could lead to higher planet masses than otherwise reachable (Kley & Dirksen 2006).

In our models we kept the planet fixed in a circular orbit, while it is known that the planets will tend to migrate because of the torques of the outer disk. For circular planets in non-eccentric disks, the migration will be directed inwards. However, the eccentric disk for more massive planets will make the orbit the slightly eccentric and the migration rate slows considerably (D'Angelo et al. 2006). For $e \geq 0.2$, the migration may be even outwards, but these high planetary eccentricities are only reached for very massive planets beyond 10 $M_{\rm jup}$ (Papaloizou et al. 2001). However, all these results are only obtained using locally isothermal disks. The question of planetary migration and possible eccentricity growth will have to be addressed in future simulations. In our case, we might consider the simulated single planet being the outermost planet in a multiple system. Our results should then give a good approximation of the expected mass flow of the gas into the gap.

We also did not include any dust particles within the models. Rice et al. (2006) showed that the outer edge of the gap acts as a filter for larger particles ($\gtrsim$10 μm). However, the simulations by Rice et al. are only locally isothermal. The question whether this filter mechanism also works within more realistic, radiative simulations will also have to be addressed in future simulations.

Acknowledgements. Tobias Müller received financial support from the Carl-Zeiss-Stiftung. Wilhelm Kley acknowledges the support of the German Research Foundation (DFG) through grant KL 650/8-2 within the Collaborative Research Group FOR 759: The Formation of Planets: The Critical First Growth Phase. We thank Andres Carmona for very fruitful discussions. We thank the referee for providing constructive comments which helped to improve this paper. Most of the simulations were performed on the bwGRiD cluster in Tübingen, which is funded by the Ministry for Education and Research of Germany and the Ministry for Science, Research and Arts of the state Baden-Württemberg, and the cluster of the Collaborative Research Group FOR 759.

References

Alexander, R. D., & Armitage, P. J. 2009, ApJ, 704, 989
Ataiee, S., Pinilla, P., Zsom, A., et al. 2013, A&A, 553, L3
Baruteau, C. 2008, Ph.D. Thesis, CEA Saclay
Crida, A., Morbidelli, A., & Masset, F. 2007, A&A, 461, 1173
D'Angelo, G., Lubow, S. H., & Bate, M. R. 2006, ApJ, 652, 1698
de Val-Borro, M., Edgar, R. G., Artymowicz, P., et al. 2006, MNRAS, 370, 529
Dodson-Robinson, S. E., & Salyk, C. 2011, ApJ, 738, 131
Günther, R., Schäfer, C., & Kley, W. 2004, A&A, 423, 559
Kim, K. H., Watson, D. M., Manoj, P., et al. 2013, ApJ, 769, 149
Kley, W. 1989, A&A, 208, 98
Kley, W. 2000, MNRAS, 313, L47
Kley, W., & Crida, A. 2008, A&A, 487, L9
Kley, W., & Dirksen, G. 2006, A&A, 447, 369
Kley, W., D'Angelo, G., & Henning, T. 2001, ApJ, 547, 457
Lin, D. N. C., & Papaloizou, J. C. B. 1993, in Protostars and Planets III, eds. E. H. Levy & J. I. Lunine, 749
Lubow, S. H., & D'Angelo, G. 2006, ApJ, 641, 526
Masset, F. 2000, A&AS, 141, 165
Mayama, S., Hashimoto, J., Muto, T., et al. 2012, ApJ, 760, L26
Müller, T. W. A., & Kley, W. 2012, A&A, 539, A18
Müller, T. W. A., Kley, W., & Meru, F. 2012, A&A, 541, A123
Muzerolle, J., Allen, L. E., Megeath, S. T., Hernández, J., & Gutermuth, R. A. 2010, ApJ, 708, 1107
Papaloizou, J. C. B., Nelson, R. P., & Masset, F. 2001, A&A, 366, 263
Quillen, A. C., Blackman, E. G., Frank, A., & Varnière, P. 2004, ApJ, 612, L137
Rice, W. K. M., Armitage, P. J., Wood, K., & Lodato, G. 2006, MNRAS, 373, 1619
Rosotti, G. P., Ercolano, B., Owen, J. E., & Armitage, P. J. 2013, MNRAS, 430, 1392
Varnière, P., Blackman, E. G., Frank, A., & Quillen, A. C. 2006, ApJ, 640, 1110
Zhu, Z., Nelson, R. P., Hartmann, L., Espaillat, C., & Calvet, N. 2011, ApJ, 729, 47

The Astrophysical Journal, 782:26 (18pp), 2014 February 10 doi:10.1088/0004-637X/782/1/26

CALCULATING THE HABITABLE ZONES OF MULTIPLE STAR SYSTEMS WITH A NEW INTERACTIVE WEB SITE*

Tobias W. A. Müller[1] and Nader Haghighipour[1,2]
[1] Institute for Astronomy and Astrophysics, University of Tübingen, Auf der Morgenstelle 10, D-72076 Tübingen, Germany
[2] Institute for Astronomy and NASA Astrobiology Institute, University of Hawaii-Manoa, Honolulu, HI 96822, USA
Received 2013 October 31; accepted 2013 December 28; published 2014 January 22

ABSTRACT

We have developed a comprehensive methodology and an interactive Web site for calculating the habitable zone (HZ) of multiple star systems. Using the concept of spectral weight factor, as introduced in our previous studies of the calculations of HZ in and around binary star systems, we calculate the contribution of each star (based on its spectral energy distribution) to the total flux received at the top of the atmosphere of an Earth-like planet, and use the models of the HZ of the Sun to determine the boundaries of the HZ in multiple star systems. Our interactive Web site for carrying out these calculations is publicly available at http://astro.twam.info/hz. We discuss the details of our methodology and present its application to some of the multiple star systems detected by the *Kepler* space telescope. We also present the instructions for using our interactive Web site, and demonstrate its capabilities by calculating the HZ for two interesting analytical solutions of the three-body problem.

Key words: astrobiology – atmospheric effects – planetary systems

Online-only material: color figures

1. INTRODUCTION

It is widely accepted that stars form in clusters. Surveys of star-forming regions have indicated that approximately 70% of all stars in our galaxy are in binary or multiple star systems (Batten et al. 1989). An examination of 164 nearest G-dwarfs by Duquennoy & Mayor (1991), for instance, has shown that 62 of these stars are in binaries, 7 are in triplets, and 2 are members of two quadruple star systems. In the past few years, the *Kepler* space telescope has also detected many binary and multiple star systems. The *Kepler* Eclipsing Binary Catalog lists more than 2100 eclipsing binaries (Slawson et al. 2011) among which ∼20% are within triple star systems.

A survey of the currently known planet-hosting stars indicates that slightly more than 8% of these stars have stellar companions (Rein 2012). While the majority of these stars are in binaries, some are also in triple and quadruple systems. For instance, Kepler 64, which has a binary stellar companion and is host to a circumbinary planet (Schwamb et al. 2013), is in fact a member of a quadruple stellar system. The M star Gliese 667 (Anglada-Escudé et al. 2012; Delfosse et al. 2013), which is known to host at least seven planets, is part of a triple stellar system. The star 16 Cyg (Cochran et al. 1997), the first multiple star system discovered to host a planet, consists of three stellar components.

The discovery of planets in multiple star systems has raised the question that whether such planetary systems can be habitable. As the habitability of a planet (and, therefore, the system's habitable zone (HZ)), in addition to the size, atmospheric composition, and orbital dynamics of the planet, depends also on the total flux received at the top of the planet's atmosphere, the stellar multiplicity plays an important role in determining the range and location of the system's HZ. Depending on their surface temperatures and orbital characteristics, each star of the system will have a different contribution to the total flux at the location of the planet. Within the context of binary stars, during the past few years this topic has been addressed by Mason et al. (2013), Liu et al. (2013), Kane & Hinkel (2013), Eggl et al. (2013), Eggl et al. (2012), and Quarles et al. (2012).

Recently, Haghighipour & Kaltenegger (2013, hereafter HK13) and Kaltenegger & Haghighipour (2013, hereafter KH13) studied this concept within the context of binary star systems. These authors have shown that as the atmosphere of a planet interacts differently with the incident radiation from stars with different spectral energy distributions (SEDs), the contribution of each star of the binary to the total flux received by the planet will be different. In other words, considering the direct summation of the fluxes of the two stars as the total flux received at the top of the planet's atmosphere, and using that quantity to calculate the total insulation on the planet's surface will not be a correct approach and will result in an inaccurate value for the planet's equilibrium temperature. The fact that the planet's atmosphere responds differently to stellar radiations with different incident energy indicates that the contribution of each star to the total flux received at the top of the planet's atmosphere has to be weighted according to the star's SED. As shown by HK13 and KH13, such a weight factor will be a function of the star's effective temperature and will have different forms for different models of the Sun's HZ. Considering the latest models of the habitability of Earth as presented by Kopparapu et al. (2013a, 2013b), HK13 and KH13 derived a formula for the *spectral weight factor* of a star based on the star's effective temperature, and presented an analytical formalism for calculating the HZ in S-type and P-type binary stars systems.

In this paper, we follow the same approach as presented by these authors and generalize their methodology to calculate the HZ in systems with $N \geqslant 2$ stars. Although in order to maintain stability, most multi-star systems have evolved into hierarchical configurations and have developed large stellar separations (which depending on the effective temperatures of their stars may imply minimal contribution from one star in the extent of the HZ around others), as we will explain in next sections, it proves useful to develop a self-consistent and comprehensive methodology that can be used to calculate the HZ of any system with more than one stellar component. The latter constitutes the main goal of this paper. We consider the HZ to be

* http://astro.twam.info/hz

Table 1
Values of the Coefficients of Equation (2) from Kopparapu et al. (2013b)

	Narrow HZ		Empirical HZ	
	Runaway Greenhouse	Maximum Greenhouse	Recent Venus	Early Mars
$F_{\rm Sun}$	1.06	0.36	1.78	0.32
$d_{\rm Sun}$ (AU)	0.97	1.67	0.75	1.77
a	1.2456×10^{-4}	5.9578×10^{-5}	1.4335×10^{-4}	5.4471×10^{-5}
b	1.4612×10^{-8}	1.6707×10^{-9}	3.3954×10^{-9}	1.5275×10^{-9}
c	-7.6345×10^{-12}	-3.0058×10^{-12}	-7.6364×10^{-12}	-2.1709×10^{-12}
d	-1.7511×10^{-15}	-5.1925×10^{-16}	-1.1950×10^{-15}	-3.8282×10^{-16}

a region where an Earth-like planet (that is, a rocky planet with a $CO_2/H_2O/N_2$ atmosphere and sufficiently large water content) can permanently maintain liquid water on its solid surface. This definition of the HZ assumes that similar to Earth, the planet has a dynamic interior and a geophysical cycle similar to Earth's carbonate silicate cycle that naturally regulates the abundance of CO_2 and H_2O in its atmosphere. The boundaries of the HZ are then associated with an H_2O-dominated atmosphere for its outer boundary and a CO_2-dominated atmosphere for its inner limit. Between those limits on a geologically active planet, climate stability is established by a feedback mechanism through which the concentration of CO_2 in the atmosphere varies inversely with planetary surface temperature.

It is important to note that in a multiple star system, the close approach of each star of the system to a planet can substantially affect the contribution of that star to the overall flux received by the planet. Also, the interaction between the star and the planet can affect the orbital motion of the planet, and therefore, its habitability. This all implies that the (instantaneous) shape of the HZ in a multiple star system will vary during the motion of the stars. In the next sections, we discuss this in more detail and explain how our methodology treats this matter properly.

In Section 2, we present the generalization of the calculation of a binary HZ to a system of N stars. In Section 3, we demonstrate the time-variation of the HZ in a multiple star system by applying our methodology to some of the systems from the *Kepler* catalog. Motivated by the *Habitable Zone Gallery* (http://hzgallery.org, Kane & Gelino 2012) which provides information about the HZ around single stars, we present in Section 4 our fully interactive Web site for calculating the HZ in binary and multiple star systems. We also demonstrate in this section how to use our Web site by calculating the HZ of two analytical solutions of the three-body problem. In Section 5, we conclude this study by summarizing the results.

2. CALCULATION OF THE HABITABLE ZONE

As mentioned in the previous section, we consider the HZ to be the region where a fictitious Earth-like planet with a $CO_2/H_2O/N_2$ atmosphere, and similar geophysical and geodynamical properties as those of Earth can maintain liquid water on its solid surface. As the capability of retaining liquid water depends on the planet's equilibrium temperature, and because this temperature depends on the total flux received by the planet, the statement above is equivalent to considering the HZ to be the region where the total flux received at the top of the atmosphere of a fictitious Earth-like planet is equal to that of Earth received from the Sun. To calculate this flux for a star in a multiple star system, we generalize the methodology presented by HK13 and KH13 (which has been developed for binary star systems) to systems with N number of stars. Using Equation (1) in KH13 and Equation (3) in HK13, that implies,

$$F_{\rm total} = \sum_{i=1}^{N} W_i\,(T_{\rm star})\,\frac{L_i/L_\odot}{d_i^2}. \quad (1)$$

In this equation, $F_{\rm total}$ is the total flux received by the planet, L_i is the luminosity of star i in units of the solar luminosity ($L_\odot$), d_i is the distance of the planet to the ith star in astronomical units (AU), and $W_i(T_{\rm star})$ is the spectral weight factor which accounts for the different SED of the ith star compared to the Sun. The quantity $T_{\rm star}$ is the effective stellar temperature.

The value of the spectral weight factor $W(T)$, in addition to the star's effective temperature, depends also on the models of the Sun's HZ. We consider the models recently developed by Kopparapu et al. (2013a, 2013b) for which the spectral weight factor of a star with an effective temperature in the range of $2600\,{\rm K} \leqslant T_{\rm star} \leqslant 7200\,{\rm K}$, is given by (HK13; KH13)

$$W(T_{\rm star}) = \left[1 + \alpha\,(T_S)\,d_{\rm Sun}^2\right]^{-1}. \quad (2)$$

In this equation, $T_S = T_{\rm star} - 5780$ K is the star's temperature-difference compared to the Sun, and

$$\alpha(T_S) = a\,T_S + b\,T_S^2 + c\,T_S^3 + d\,T_S^4. \quad (3)$$

The quantities a, b, c, and d in Equation (3) are constant coefficients with values that depend on the conditions that determine the inner and outer boundaries of the Sun's HZ. Table 1 shows these values.

As mentioned earlier, to calculate the HZ of a multiple star system, we compare the total flux received by a fictions Earth-like planet with that received by Earth from the Sun. From Equation (1), that means

$$\sum_{i=1}^{N} W_i\,(T_{\rm star})\,\frac{L_i/L_\odot}{d_i^2} = \frac{L_\odot}{l_{\rm x-Sun}^2}, \quad (4)$$

where x = (In, Out), and $l_{\rm x-Sun}$ denotes the boundaries of the Sun's HZ. To determine the location and range of the HZ of a multiple star system, the distances d_i have to be calculated for different values of $l_{\rm x-Sun}$ by solving a set of differential equations corresponding to the motion of the stellar N-body system along with the algebraic equation (4).

To determine the values of $l_{\rm x-Sun}$, we follow HK13 and KH13, and consider a *narrow* HZ corresponding to the region between the runaway greenhouse and the maximum greenhouse limits in the most recent Sun's HZ model by Kopparapu et al. (2013a, 2013b). As this model does not include cloud feedback, the boundaries of the narrow HZ in our definition do not include the feedback from clouds as well. To mimic the effects of clouds

Table 2
Values of the Spectral Weight Factor

T (K)	2800	3500	4500	5500	5636	5780	6407	7400	8500
$W_{\rm in}$ (narrow)	1.200	1.184	1.132	1.033	1.017	1.000	0.929	0.844	0.843
$W_{\rm out}$ (narrow)	1.529	1.417	1.237	1.048	1.024	1.000	0.906	0.809	0.807
$W_{\rm in}$ (empirical)	1.194	1.164	1.102	1.023	1.012	1.000	0.952	0.899	0.901
$W_{\rm out}$ (empirical)	1.614	1.462	1.249	1.050	1.025	1.000	0.903	0.799	0.771

(and have a more realistic definition for the HZ), HK13 and KH13 introduced the *empirical* (nominal) HZ as the region with an inner boundary at the Recent Venus limit and an outer boundary at the limit of Early Mars in the model by Kopparapu et al. (2013a, 2013b). These boundaries have been derived using the fluxes received by Mars and Venus at 3.5 and 1.0 Gyr ago, respectively. At these times, the two planets did not show indications for liquid water on their surfaces (Kasting et al. 1993). We follow HK13 and KH13, and consider also the empirical HZ, as the second range for determining the values of $l_{\rm x-Sun}$. In these definitions, the locations of the HZs are determined based on the flux received by the planet (Kasting et al. 1993; Selsis et al. 2007; Kaltenegger & Sasselov 2011; Kopparapu et al. 2013a).

It is important to note that, except for some special orbital configurations of the stars (e.g., when the stars orbit the center of mass of the system so close to one another that the system's HZ can only exist around the entire stellar system, as in HK13), it may not be possible to determine a distinct inner or outer edge for the HZ of a multiple star system. The motions of the stars cause the HZ of the system to be dynamic and change boundaries and locations as the stars move over the time. For this reason, in order to determine the location of the HZ of the system, at any given time, we consider a large grid of points over the entire system and calculate the flux at each grid point using Equation (1). We then mark those points of the grid for which the value of the total flux satisfies the following condition, as a point of the system's HZ:

$$\frac{L_\odot}{l^2_{\rm In-Sun}} \leqslant \sum_{i=1}^{N} W_i\,(T_{\rm star})\,\frac{L_i/L_\odot}{d_i^2} \leqslant \frac{L_\odot}{l^2_{\rm Out-Sun}}. \qquad (5)$$

We repeat this process for one complete orbital period of the system by increasing the time in small increments and allowing the stars to move in their orbits. When calculating the HZ, we do not consider whether the orbit of the fictitious Earth-like planet will stay stable. As explained in the next sections, we determine the stability of the HZ by direct integration of the orbit of an Earth-mass planet at different locations in the HZ. As a result, in some systems, some or all of the HZ will be dynamically unstable (see HK13 for several examples). In the following, we present a sample of our calculations as well as the instructions to our interactive HZ-calculator Web site.

3. EXAMPLES

To demonstrate the application of our methodology, we calculate the HZ of two multiple stars systems KIC 4150611 and KID 5653126 from the *Kepler* space telescope catalog. As explained below, these systems have stellar and orbital characteristics that allow for exploring effects of luminosity and distance on the range of the HZ. We calculate the narrow and empirical HZs in these systems, and show the results for one complete orbit. Following HK13 and KH13, and from the model by Kopparapu et al. (2013a, 2013b), we consider the narrow HZ (without cloud feedback) of a Sun-like star to extend from 0.97 AU to 1.67 AU, and its empirical HZ to be from 0.75 AU to 1.77 AU. Animations of the time-variation of the HZs of our systems can be found at http://astro.twam.info/hz-multi.

3.1. KIC 4150611

The KIC 4150611 (HD 181469, HIP 94924) is a system of five stars consisting of a triplet with an A and two K stars, and a binary with two F stars. The A–KK and FF systems form a visual pair with a separation of 1.″1. The A–KK triplet has an orbital period of 94.2 days, and the orbital period of the inner KK binary is 1.522 days. The effective temperatures of the A and K stars are 8500 K and 4500 K, respectively (A. Prša 2013, private communication). We consider here only the A–KK system and use our methodology to calculate the location and time-evolution of its HZ (given the large separation between this system and the FF binary, the effect of the latter is negligible).

As shown by Equation (5), the calculation of the HZ requires the knowledge of the luminosity, semimajor axis, and spectral weight factor of each star. To calculate the semimajor axis and luminosity of the A and K stars, we consider the A star to be 1.5 $M_\odot$ (corresponding to the lower limit of the mass of a star of spectral type A) and the mass of each K star to be 0.7 $M_\odot$. Using these values of the mass combined with the orbital periods of the KK binary and A–KK system as given above, the semimajor axis of the KK binary will be 0.029 AU and that of the A–KK system will be equal to 0.58 AU. The luminosities are calculated using the mass-luminosity relation, $L = M^{3.5}$. For the values of the stellar masses considered here, the luminosity of the A star will be equal to 4.134 $L_\odot$ and that of the K stars will be 0.287 $L_\odot$. To calculate the spectral weight factor $W(T)$ for each star, we use Equation (2). It is important to note that this equation is model-dependent and has been derived based on the model of the Sun's HZ by Kopparapu et al. (2013a, 2013b), which is valid for stellar temperatures ranging from 2600 K to 7200 K. The latter means that Equation (2) may not be applicable when calculating the spectral weight factor of the A star (8500 K). However, because the purpose of our calculations is to demonstrate our methodology and how it is used to determine the HZ of multiple star systems, we assume that the model by Kopparapu et al. (2013a, 2013b) will maintain the functional form of its temperature dependence (i.e., Equation (3)) for higher values of stellar temperature, and extrapolate this model to effective stellar temperatures of 8500 K. We then calculate the spectral weight factor of each star using Equation (2). Table 2 shows these values for the system's A and K stars.

Given the short period of the KK binary (1.522 days), the stand-alone HZ of this system (i.e., assuming it is isolated and not part of a triple or larger stellar system) will be only at circumbinary distances. Following the methodology by HK13,

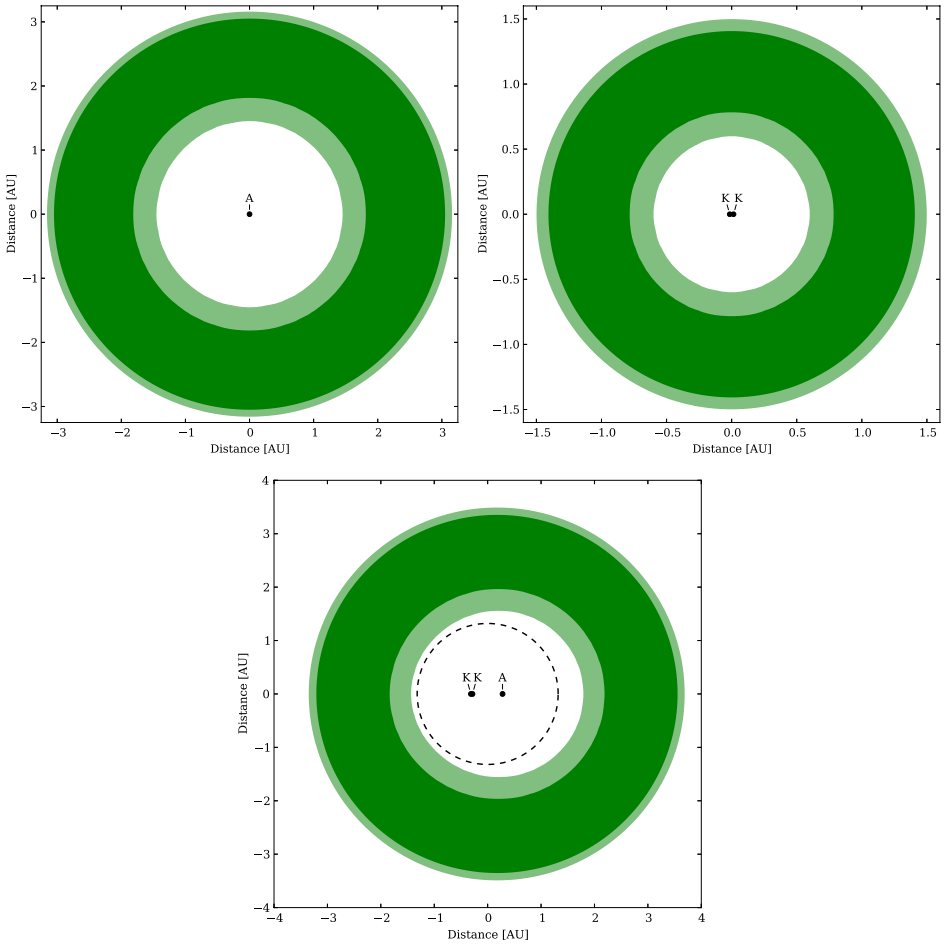

Figure 1. Graphs of the HZs of the A–KK triplet in the KIC 4150611 system and its components. The top left panel shows the HZ of the A star, the top right panel shows that of the KK binary, and the bottom panel shows the HZ of the A–KK triple star system. Here and in subsequent figures, the dark green corresponds to the narrow and the light green corresponds to the empirical HZs. The dashed circle shows the boundary of stability. Interior to this boundary, planetary orbits will become unstable. An animation of the HZ of this system can be found at http://astro.twam.info/hz-multi.

(A color version of this figure is available in the online journal.)

this HZ extends from 0.6 AU to 1.5 AU from the center of mass of the binary. The top right panel of Figure 1 shows this region. The dark green in this and subsequent figures corresponds to the narrow and the light green corresponds to the empirical HZ. Similarly, assuming that the A star is isolated and not part of a multiple star system, its single-star HZ, shown in the top left panel of Figure 1, will extend from 1.3 AU to 3.1 AU. As the distance between the A star and the center of mass of the KK binary in the A–KK system is 20 times larger than the semimajor axis of the binary K stars, one would expect that the effect of the A star on the stand-alone HZ of the KK binary, if not negligible, to be very small. However, as shown in the bottom panel of Figure 1, when these three stars are considered to be in their current orbital configuration, and assuming that the orbits are co-planar and circular, the higher luminosity of the A star dominates and causes the entire HZ around the KK binary to disappear. In this case, the HZ of the A–KK system is primarily due to the A star although the KK binary does seem to have some small effect. An animation of the HZ of this system can be found at http://astro.twam.info/hz-multi.

To determine the orbital stability of an Earth-like planet in the HZ of the A–KK system, we distributed 100,000 non-interacting Earth-mass objects between 0.5 AU and 3 AU around the center of mass of the system, and integrated their orbits for 5000 periods of the A star using a fifth-order *N*-body integrator (Cash & Karp 1990). The bodies were initially set to be in non-eccentric Keplerian orbits. The timesteps of the integrations were taken to be 1/100 of the period of the inner KK binary. Figure 2 shows the distribution of the Earth-like planets at the beginning (top panel, blue) and end (bottom panel, red) of the simulations. As shown here, at the end of the simulations, a lack of particles appears for distances smaller than 1.32 AU (shown by the vertical dashed line in Figure 2), implying that the orbit of an Earth-mass planet in these regions will be unstable.

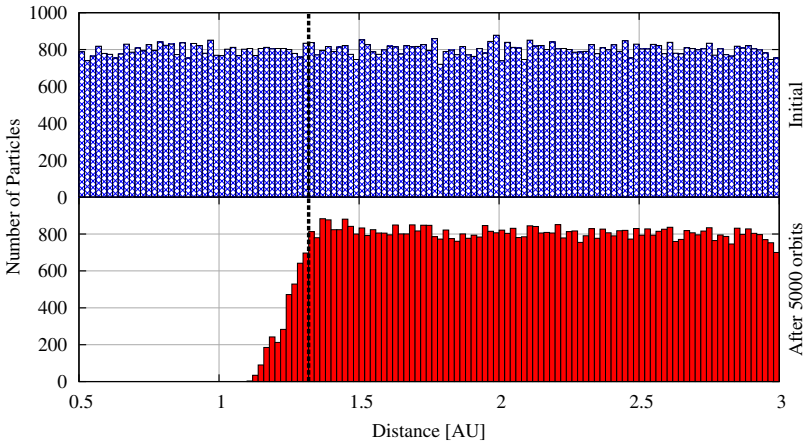

Figure 2. Results of the integrations of the orbits of non-interacting Earth-mass planets around the center of mass of the KIC 4150611 system. The top panel (blue histogram) shows the initial distribution of planets and the bottom panel (red histogram) corresponds to their distribution after integrating their orbits for 5000 orbital periods of star A around the KK binary. The dashed line shows the boundary of orbital stability at 1.32 AU.

(A color version of this figure is available in the online journal.)

We, therefore, considered 1.32 AU as the stability limit, and have shown this by the dashed circles in Figure 1.

As mentioned above, the stability integrations were carried out for only 5000 orbits of the A star. To determine whether this time of integration was sufficient, we assumed that the triple star system of A–KK can be approximated by a binary star system with the A star as its primary and a secondary with a mass equal to the sum of the masses of the two K stars ($0.7+0.7 = 1.4\,M_{\odot}$). We recall that the distance between the A star and the center of mass of the KK binary is 20 times larger than the binary semimajor axis. In this *auxiliary* binary system, an Earth-mass planet in the HZ will have a circumbinary orbit. As shown by Dvorak (1986), Dvorak et al. (1989), and Holman & Wiegert (1999), for such planetary orbits, the stability limit is given by

$$a_{\rm min} = a(1.60 + 5.10\,e - 2.22\,e^2 + 4.12\,\mu - 4.27\,e\mu - 5.09\,\mu^2 + 4.61\,e^2\mu^2), \quad (6)$$

where $a_{\rm min}$ is the minimum semimajor axis for a planetary orbit to be stable, a is the binary semimajor axis, e is the binary eccentricity and $\mu = M_{\rm Pr}/(M_{\rm Pr}+M_{\rm Sec})$ with $M_{\rm Pr}$ and $M_{\rm Sec}$ being the masses of the primary and secondary stars, respectively. Considering that in the actual A–KK system, the orbits are circular and the A star is at 0.58 AU from the KK binary ($a = 0.58$ AU), the stability limit obtained from Equation (6) is at $a_{\rm min} = 1.39$ AU. This value is in good agreement with the 1.32 AU stability limit obtained from our numerical simulations, indicating that stability integrations have been carried out for a sufficient amount of time.

3.1.1. Effect of the Eccentricity of the A Star

The fact that the high luminosity of the A star stripped the KK binary from its HZ motivated us to examine how the HZ of the entire triple system would change, and at what stage the HZ around the KK binary would re-appear, had the A star been at farther distances. We, therefore, increased the radial distance of the A star from the center of mass of the system, and determined the smallest distance ($r_1 = 2.8$ AU) for which the inner edge of the empirical HZ re-appeared around the KK binary. We continued increasing the radial distance of the A star until the smallest value ($r_2 = 6.45$ AU) for which the outer boundary of the empirical HZ of the KK binary re-appeared. Beyond this distance, the two HZs of the A star and KK binary will separate. To study the HZ of the triple system in the intermediate distances, we considered two cases. In the first case, we assumed the closest and farthest distances of the A star to be $0.5r_1$ and $1.5r_1$, respectively, and calculated the semimajor axis and eccentricity of an elliptical orbit for the A star for which these distances could be the periastron and apastron ($a_1 = 2.8$ AU, $e_1 = 0.5$). Figure 3 shows four snapshots of the HZ of this system during the orbital motion of the A star. From the top right panel and in a counterclockwise rotation, the panels correspond to the A star to be at angles 0°, 63°, 110°, and 180° with respect to the horizontal line passing through zero on the vertical axis. The dashed circles correspond to the outer boundaries of planetary stability (planets interior to the dashed circles will be stable). Around the A star, this boundary is at 0.34 AU, and around the KK binary is at 0.32 AU. The inner boundary of stability around the entire system is at approximately 10.18 AU (outside this limit, planets will have stable orbits). As shown here, while the A star is still the dominating factor in establishing the boundaries of the narrow HZ, there are distances where the inner region of the empirical HZ of the KK binary is solely due to the luminosities of its two stars. For an animation of the HZ of this system see http://astro.twam.info/hz-multi.

In the second case, we considered the closest and farthest distances of the A star to be $0.5r_2$ and $1.5r_2$, respectively. The corresponding elliptical orbit of the A star in this case has a semimajor axis of 5.48 AU and an eccentricity of 0.412. Figure 4 shows the evolution of the HZ during the motion of the A star. From the top right panel and in a counterclockwise rotation, the panels correspond to 0°, 19°, 86°, and 180°, respectively. The outer boundaries of planetary orbit stability are at 0.8 AU around the A star and 0.77 AU around the KK binary. The inner stability limit around the entire system is at 18.95 AU. As shown here, beyond certain distances, the HZ of the KK binary reappears, and the HZ of the triple system consists of

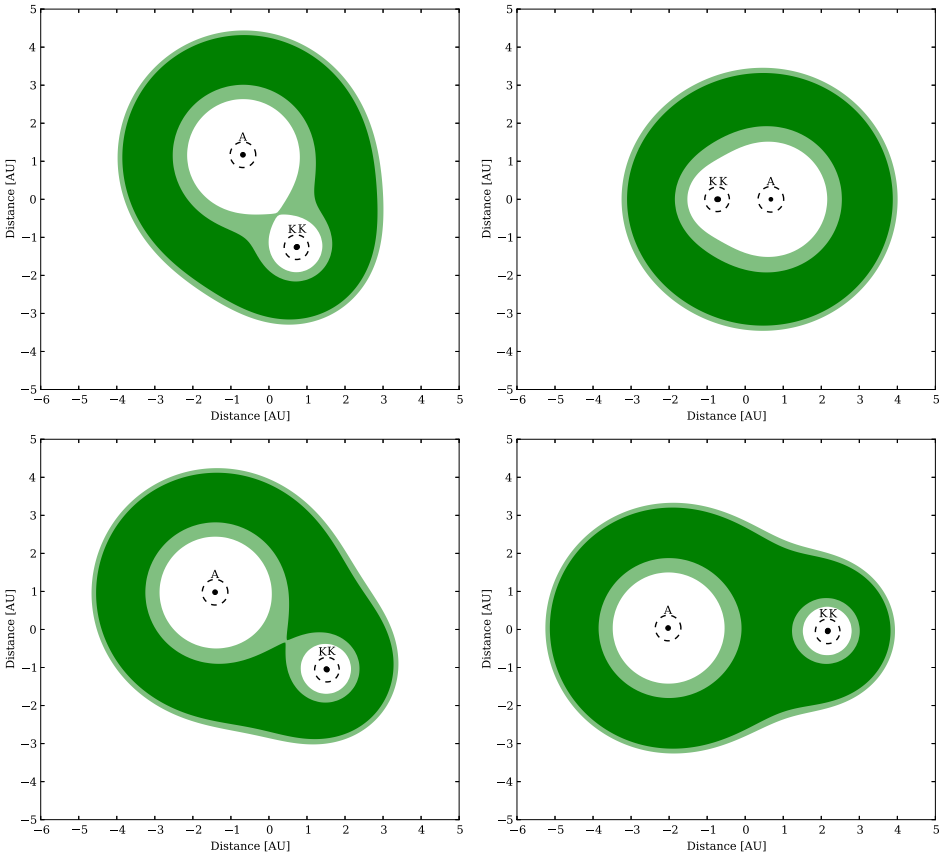

Figure 3. Time-evolution of the HZ of the A–KK triplet in the KIC 4150611 system when the orbit of the A star has a semimajor axis of 2.8 AU and an excentricity of 0.5. From top right panel and in a counterclockwise rotation, the panels correspond to the A star being at 0°, 63°, 110°, and 180° with respect to the horizontal line passing through zero on the vertical axis. The dashed circles correspond to the outer boundary of the stability of planetary orbits. An animation of the HZ of this system can be found at http://astro.twam.info/hz-multi.

(A color version of this figure is available in the online journal.)

two separate HZs corresponding to those of the A star and KK binary, respectively. An animation of the HZ of this system can be found at http://astro.twam.info/hz-multi.

3.2. KID 5653126

The A–KK triplet in the multiple star system KIC 4150611 provided an interesting case for studying how the HZ of a binary can be affected by a highly luminous farther companion. To study the reverse situation, that is, the possible effect of a less luminous farther star on the HZ of a binary with more luminous components, we considered the hierarchical triple star system KID 5653126. This system consists of a close binary (hereafter labeled as A and B) with a period of 38.5 days and a farther companion (hereafter labeled as C) orbiting the AB binary in an 800 day orbit. The stellar properties of this system are unknown. To ensure that the farther companion would be a less luminous star, we consider the star A to be similar to the primary of the Kepler 47 system and stars B and C to be similar to the primary and secondary stars of Kepler 64, respectively. Table 3 shows the values of the mass, luminosity, and effective temperatures of these stars. From the values of the mass and orbital periods

Table 3
The AB–C Triplet in KID 5653126 System

Star	A	B	C
Mass ($M_\odot$)	1.043	1.528	0.4
Luminosity ($L_\odot$)	0.84	4.54	0.02
Temperature (K)	5636	6407	3561

of the system, the AB binary will have a semimajor axis of $a_{AB} = 0.31$ AU and that of star C, with respect to the center of mass of the binary system, will be $a_C = 2.42$ AU. In contrary to the A–KK triplet in the KIC 4150611 system, the separation of star C is only 7.8 times larger than the semimajor axis of the inner binary AB, implying that this star may have a noticeable effect on the HZ of the binary system.

Figure 5 shows the HZ of the system when the binary AB and star C are in circular orbits. Starting from the upper right panel and counterclockwise, the figures show the evolution of the HZ during one revolution of the star C around the binary when this star is at 0°, 60°, 120°, 180°, 240° and 330°, respectively. As shown here, while the HZ of the system is primarily due to the

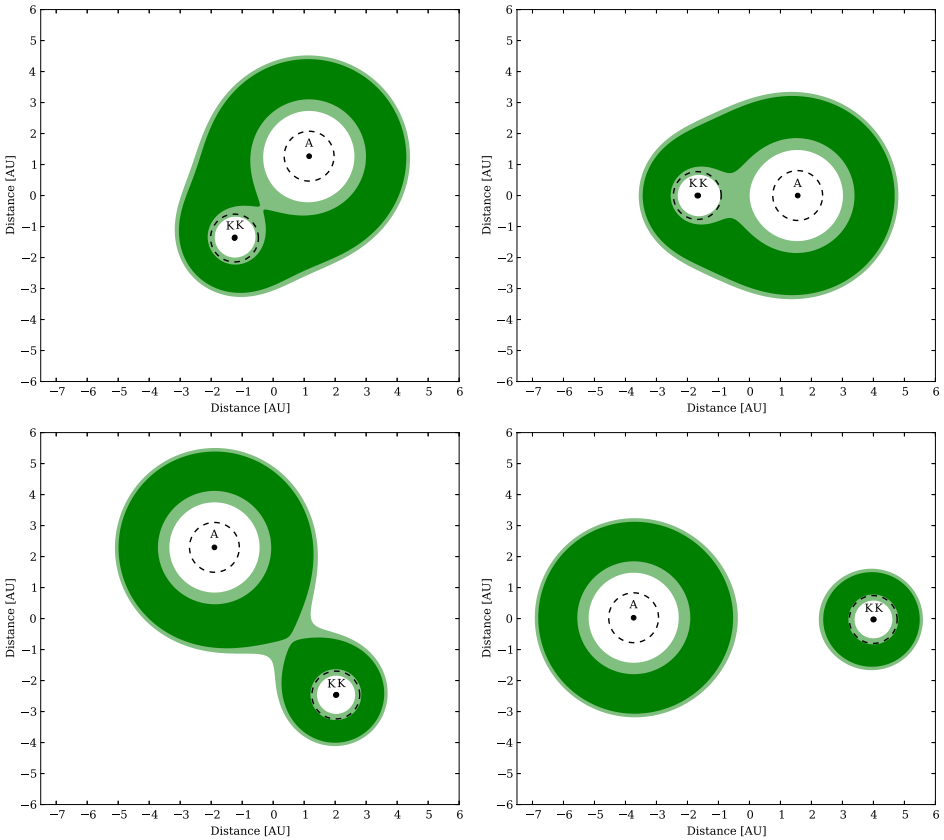

Figure 4. Time-evolution of the HZ of the A–KK triplet in the KIC 4150611 system when the orbit of the A star has a semimajor axis of 5.48 AU and an excentricity of 0.412. From top right panel in a counterclockwise rotation, the panels correspond to the A star being at 0°, 19°, 86°, and 180° with respect to the horizontal line passing through zero on the vertical axis. The dashed circles correspond to the outer boundary of the stability of planetary orbits. An animation of the HZ of this system can be found at http://astro.twam.info/hz-multi.

(A color version of this figure is available in the online journal.)

AB binary, the radiation from star C excludes the region around this star from the system's narrow HZ and slightly extends the empirical HZ of the AB binary to farther distances (animations of the HZ at http://astro.twam.info/hz-multi).

To determine the stability of an Earth-like planet in the HZ of the KID 5653126 system, similar to the case of KIC 4150611, we distributed a large number of non-interacting, Earth-mass planets around the center of mass of the AB–C system, and integrated their orbits for 10,000 orbital periods of the star C using the *N*-body integrator explained in Section 3.1. Figure 6 shows the distributions of the Earth-mass planets at the beginning and end of the integrations. The top panel of this figure corresponds to the stability around the entire system and the bottom panel is for the stability around the star C. As shown here, the stability limit around the system's center of mass is at approximately 5.225 AU (shown by a dashed line in the top panel of Figure 6 and by a dashed circle in Figure 5), indicating that the majority of the HZ of the system is unstable. As indicated by the bottom panel of Figure 6, however, a small region of stability exists interior to 0.348 AU around the star C (shown by a dashed line in the bottom panel of Figure 6 and a dashed circle around this star in Figure 5) where an Earth-mass planet can have a stable orbit in a small portion of the empirical HZ around this star.

To determine whether the above-mentioned integration time was sufficient for calculating the stability limit around the entire three stars, we approximated the AB–C system with a circular P-type binary. In this binary, the mass of the primary star is equal to the sum of the masses of stars A and B, and the binary semimajor axis is 2.42 AU. Using Equation (6), the stability limit of this P-type system will be at ∼5 AU, which is in a very good agreement with the 5.225 AU that was obtained from direct integrations.

To examine whether the time of the integration was sufficient for calculating the stability limit around the star C, we approximate the AB–C system with an S-type binary, considering star C to be the primary star. As shown by Holman & Wiegert (1999) and Rabl & Dvorak (1988), the critical stability limit around each star of an S-type binary (interior to which a planet will have a long-term stable orbit) can be calculated using

$$a_{\max} = a(0.464 - 0.38\,\mu - 0.631\,e + 0.586\,\mu e + 0.15\,e^2 - 0.198\,\mu e^2). \quad (7)$$

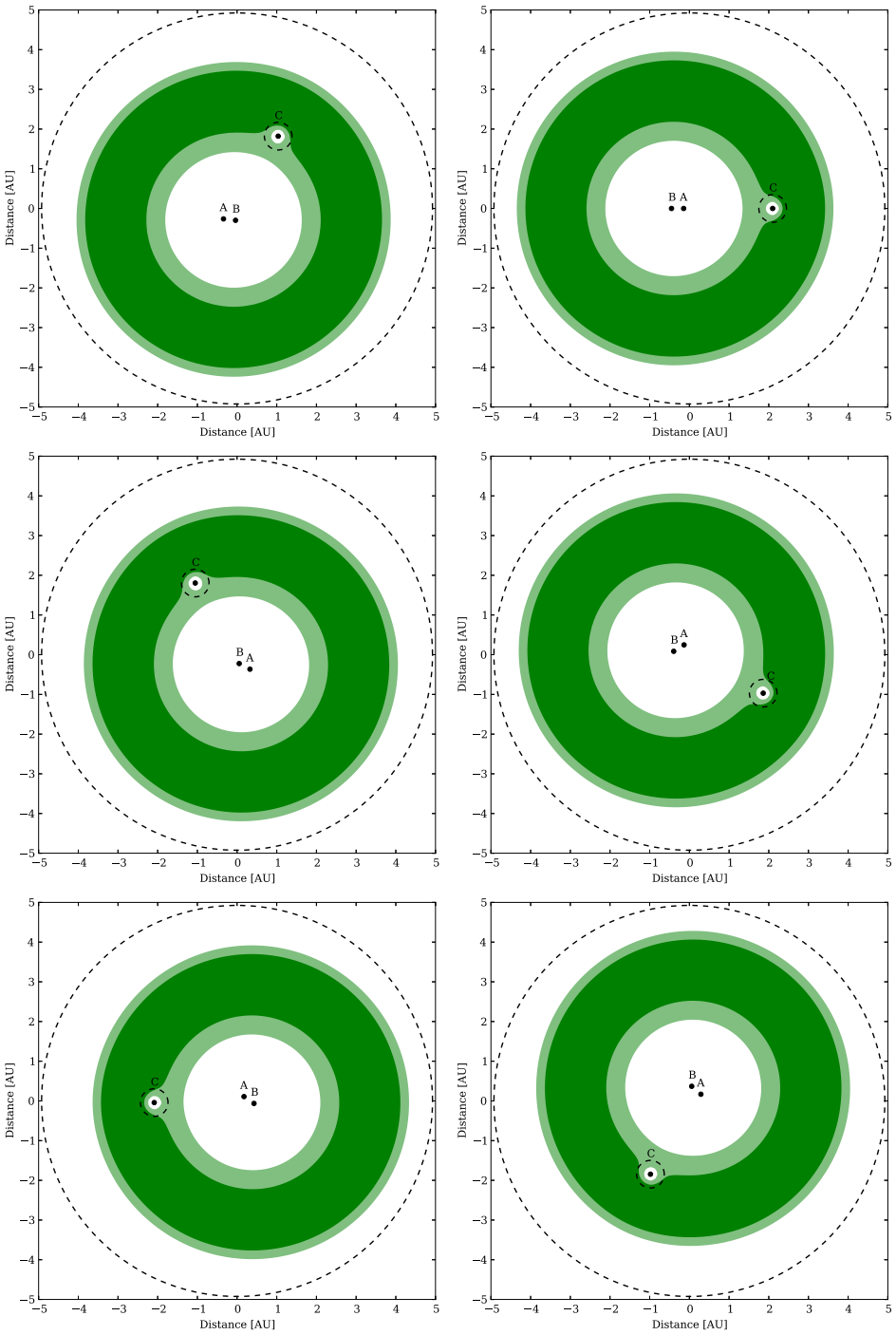

Figure 5. Graphs of the HZ of the KID 5653126 system when the three stars are in circular orbits. From the top right panel and counterclockwise, the figures show the changes in the boundaries of the HZ during one revolution of the star C when this star is at 0°, 60°, 120°, 180°, 240° and 330°, respectively. The dashed circles corresponds to the limits of planetary orbit stability (see Figure 6). An animation of the HZ of this system can be found at http://astro.twam.info/hz-multi.

(A color version of this figure is available in the online journal.)

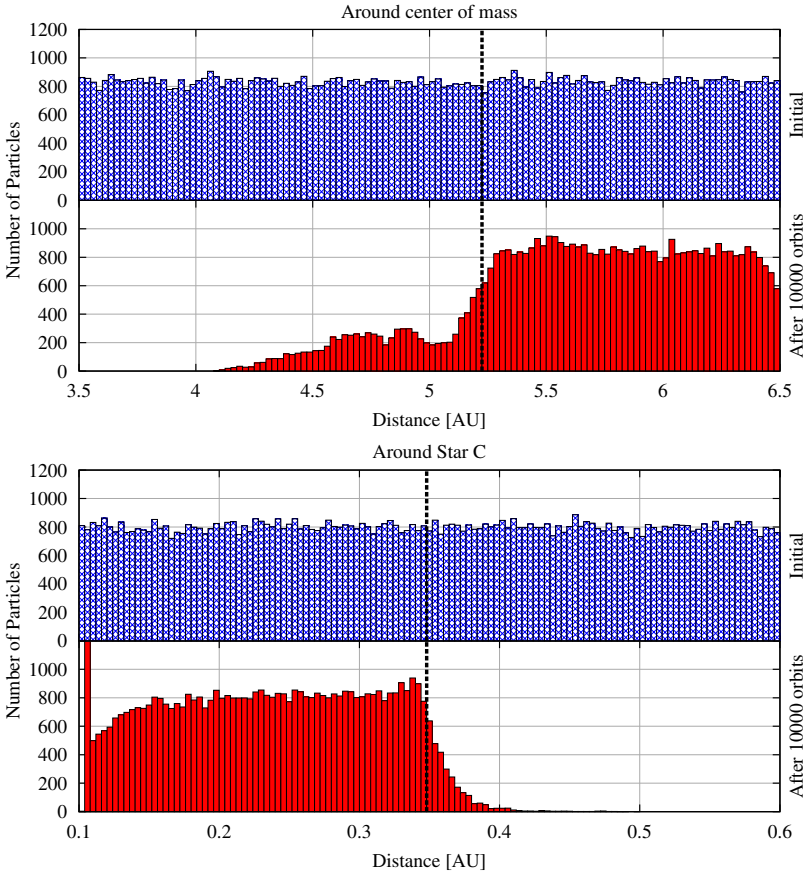

Figure 6. Results of the integrations of non-interacting Earth-mass planets around the center of mass of the KID 5653126 system (top) and around the star C (bottom). In each panel, the upper graph (blue histogram) shows the initial distribution of the planets and the lower graph (red histogram) corresponds to their distribution after integrating their orbits for 10,000 orbital periods of the star C around the binary AB. The dashed line shows the boundary of orbital stability at 5.225 AU around the center of mass, and at 0.348 AU around star C.

(A color version of this figure is available in the online journal.)

Considering a circular binary with a semimajor axis of 2.42 AU and a mass-ratio of $\mu = (M_A + M_B)/(M_A + M_B + M_C)$, the outer boundary of the stable region around star C will be at 0.328 AU. This is in a very good agreement with the 0.348 AU limit obtained from direct integrations confirming that the time of integrations for our stability analysis was sufficient.

3.2.1. Effect of the Eccentricity of the Star C

The fact that during its motion around the AB binary, the star C removes part of the HZ of the system that is in its vicinity motivated us to examine how the HZ would change if the orbit of this star were eccentric. Similar to the case of KIC 4150611, we considered two cases. In the first case, we determined the values of the semimajor axis and eccentricity of star C for which this star would break away from the inner part of the empirical HZ of the system while having a periastron distance equal to 2.42 AU and an apastron interior to the outer edge of the system's empirical HZ. In this case $a_C = 3.01$ AU, and $e_C = 0.195$. Figure 7 shows the HZ of the system in one orbit of the star C around the binary. From the upper right panel and in a counterclockwise rotation, the panels correspond to star C at 0°, 60°, 180° and 309°. As shown here, the inner part of the empirical HZ of the system expands temporarily as the star C moves away from this region. The outer edge of the HZ is also extended to larger distances as this star approaches its apastron position. Figure 8 shows the outer boundary of orbital stability for Earth-mass planets around star C. Integrations were carried out for 1000 orbital periods of planet C. As indicated by the vertical dashed line, planets with semimajor axes smaller than 0.362 AU will have stable orbits around this star. Figure 7 shows this region with a dashed circle around star C. As shown in this figure, the empirical HZ around this star maintains stability for planetary orbits as this star rotates around the AB binary. For an animation of the HZ of this system, we refer the reader to the Web site http://astro.twam.info/hz-multi.

In the second case, we considered the star C to have a semimajor axis equal to 2.42 AU and changed the value of its orbital eccentricity until this star left the HZ of the binary ($e_C = 0.7$). Figure 9 shows this for half of the orbital period of star C. From top right and in a counterclockwise rotation, the

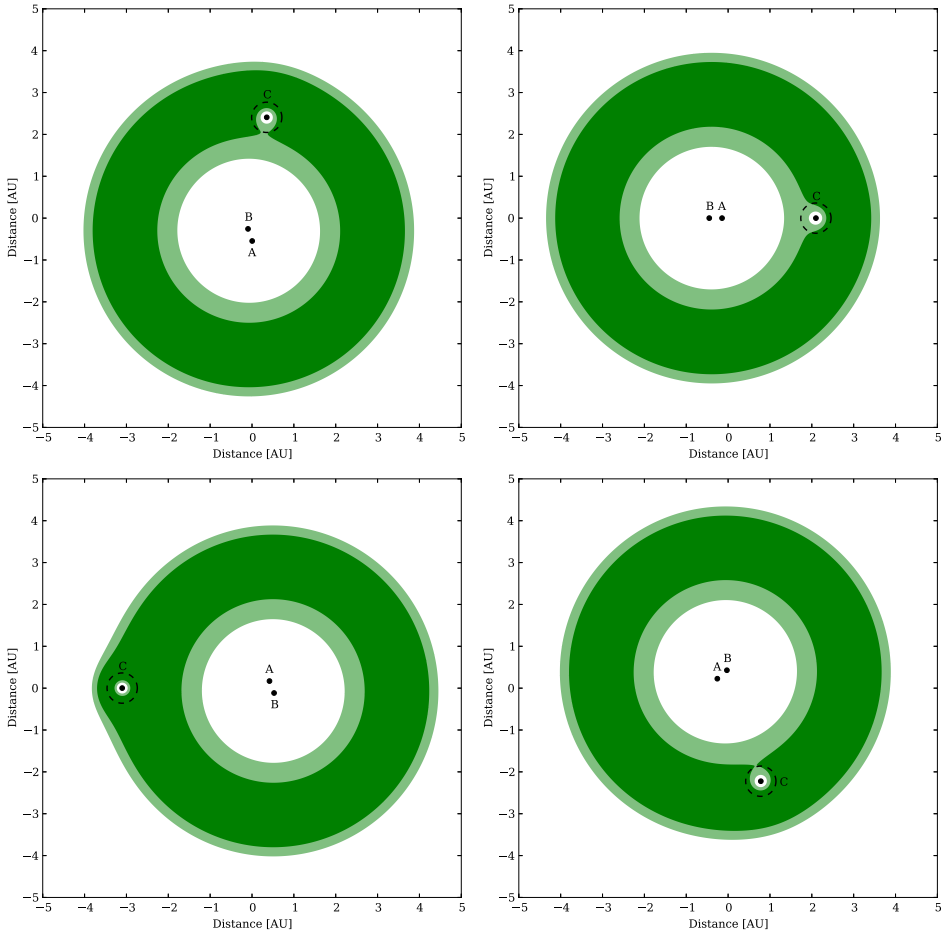

Figure 7. Graphs of the HZ of the KID 5653126 system when the star C has a semimajor axis of 3.01 AU and an eccentricity of 0.195. From the top right panel and in a counterclockwise rotation, the panels correspond to the star C being at , 0°, 60°, 180°, and 309°, respectively. An animation of the HZ of this system can be found at http://astro.twam.info/hz-multi.

(A color version of this figure is available in the online journal.)

panels show this star at 0°, 26°, 28°, 41°, 52°, 73°, 117°, 150°, and 154°. As shown here, the motion of star C disturbs the HZ of the AB binary by either excluding regions of it that are around this star, or extending its inner and outer boundaries. The capability of the HZ of the AB binary to accommodate stable planetary orbits is also affected by the motion of the star C. Except for when this star is either entirely inside the inner boundary of the system's empirical HZ or is outside the HZ of the AB binary, the stability of the system's HZ is limited to only a small region around star C. When star C is separated from the AB binary, planetary stability is maintained in both HZs. However, as this star enters the inner boundary of the empirical HZ of the system, the stability region around it becomes unstable due to the perturbation of the AB binary. This all means that during the motion of the stars around their center of mass, an Earth-like planet may not maintain a long-term stable orbit in the HZ of the system. For more details, we refer the reader to the Web site http://astro.twam.info/hz-multi where animations of the time-variations of the HZs shown in Figures 7 and 9 can be found.

4. INTERACTIVE WEB SITE

To streamline the calculations of the HZ in binary and multiple star systems, we have developed an interactive Web site where by inputting the orbital and physical properties of the stars, the HZ of the system is calculated for the time at which the stars are in the configuration that corresponds to their prescribed orbital parameters. The Web site can be found at

http://astro.twam.info/hz.

Figure 10 shows a screenshot of the Web site. As shown on the top of the figure, the Web site gives the option for the calculations to be performed for a binary or a multiple star system. We chose to separate these two cases because in calculating the HZ of binary star systems, the Web site has

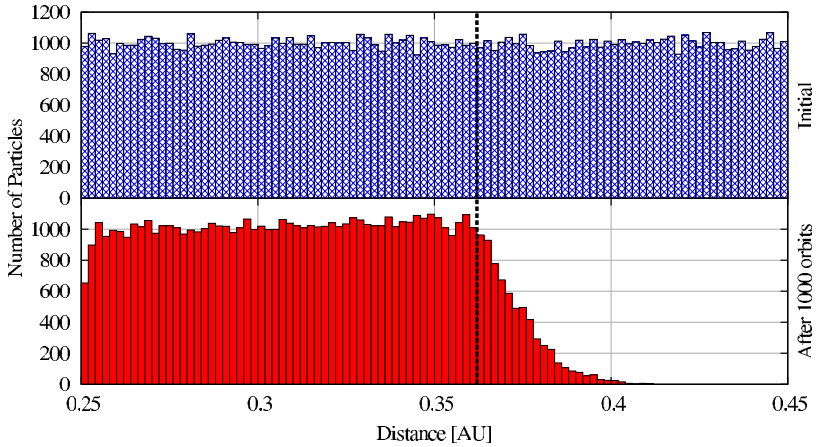

Figure 8. Results of the integrations of non-interacting Earth-mass planets around star C in the system of Figure 7. The upper panel (blue histogram) shows the initial distribution of the planets and the lower panel (red histogram) corresponds to their distribution after integrating their orbits for 10,000 orbital periods of star C. The dashed line shows the outer boundary of orbital stability at 0.362 AU.

(A color version of this figure is available in the online journal.)

the capability of using Equations (6) and (7) to determine the boundaries of planetary stability as well. However, for a stellar system with more than two stars, the stability limits can be obtained only by direct integration of the equation of motion of planetary bodies at different locations in the system. Also, for binary stars, the Web site offers the choice of setting the value of the mean-anomaly, which can be used to obtain snapshots of the HZ during the rotation of the two stars around their common center of mass.

The next set of input parameters are the effective temperature, luminosity, and mass of each star as well as the star's position. The temperature and luminosity of a star are used to calculate its spectral weight factor and the boundary of the system's HZ. The mass of each star is used to calculate boundaries of planetary stability in binary star systems, and for the calculation of the center of mass in multiple star systems. Since the value of the spectral weight factor and the locations of the boundaries of the HZ are model-dependent, the Web site offers the option to choose between three models of the Sun's HZ: The model by Kasting et al. (1993),[3] Selsis et al. (2007), and Kopparapu et al. (2013b). The remaining input parameters are for determining the range of plotting the HZ and its resolution.

After entering all parameters and choosing the options, the HZ of the system can be displayed by clicking on the "Render" button. The Web site has been programed to stop the calculations and ask for reducing the resolution if the calculations take longer than 10 s. Once the HZ of the system is calculated, the displayed image can be saved as a vectorized PDF file, or a rasterized PNG image. Figure 10 shows as an example the input parameters and the calculated HZ of a GKM triple star system. In the next section, we show the application of the Web site by calculating the HZ of some interesting analytical solutions to the three-body problem. We would like to emphasize that the systems studied in the next section have been chosen for the mere purpose of demonstrating the use of our interactive Web site. We, therefore, will not be concerned about the possibility of the formation of terrestrial-class planets in these systems, and the orbital stability of Earth-like bodies in their HZs (although when possible, we will address the latter).

[3] The calculations of the spectral weight factor for this model is carried out using the formulas given by Underwood et al. (2003).

Table 4
Values of the Mass, Luminosity, Temperature, and the Components of the Position and Velocity Vectors of the Equilateral Three-star Systems shown in Figures 11 and 12

	Circular			Elliptical		
	A	B	C	A	B	C
T (K)	3500	5500	7400	3500	5500	7400
L ($L_\odot$)	0.028	0.063	6.6	0.028	0.063	6.6
M ($M_\odot$)	0.4	0.5	1.6	0.4	0.5	1.6
a (AU)	5.32	5.13	2.19	2.96	2.85	1.21
e	0	0	0	0.8	0.8	0.8
X (AU)	3.64	−0.14	−3.64	3.36	−0.14	−3.64
Y (AU)	−3.88	2.18	−3.88	−3.88	2.18	−3.88
$V_X/2\pi$ (AU day^{-1})	0.33	−0.19	0.33	0.13	−0.08	0.15
$V_Y/2\pi$ (AU day^{-1})	0.29	−0.01	−0.31	0.14	−0.005	−0.13

4.1. Interesting Examples: Equilateral Three-star System

Among the currently known solutions of the general three-body problem, only a few are stable. The most well-known stable solutions are the equilateral configurations were three stars (with different masses) rotate around their common center of mass in an equilateral triangle at all times. The orbits of the stars can be circular or elliptical. In the latter configuration, the distances between the stars vary with time whereas in the circular case, the distances stay constant.

We calculated the HZ of the system using our interactive Web site for different values of the mass, luminosity and temperature of the three stars, and for the model of the Sun's HZ by Kopparapu et al. (2013a, 2013b). Table 4 shows a sample of our systems for a circular (Figure 11) and an elliptical

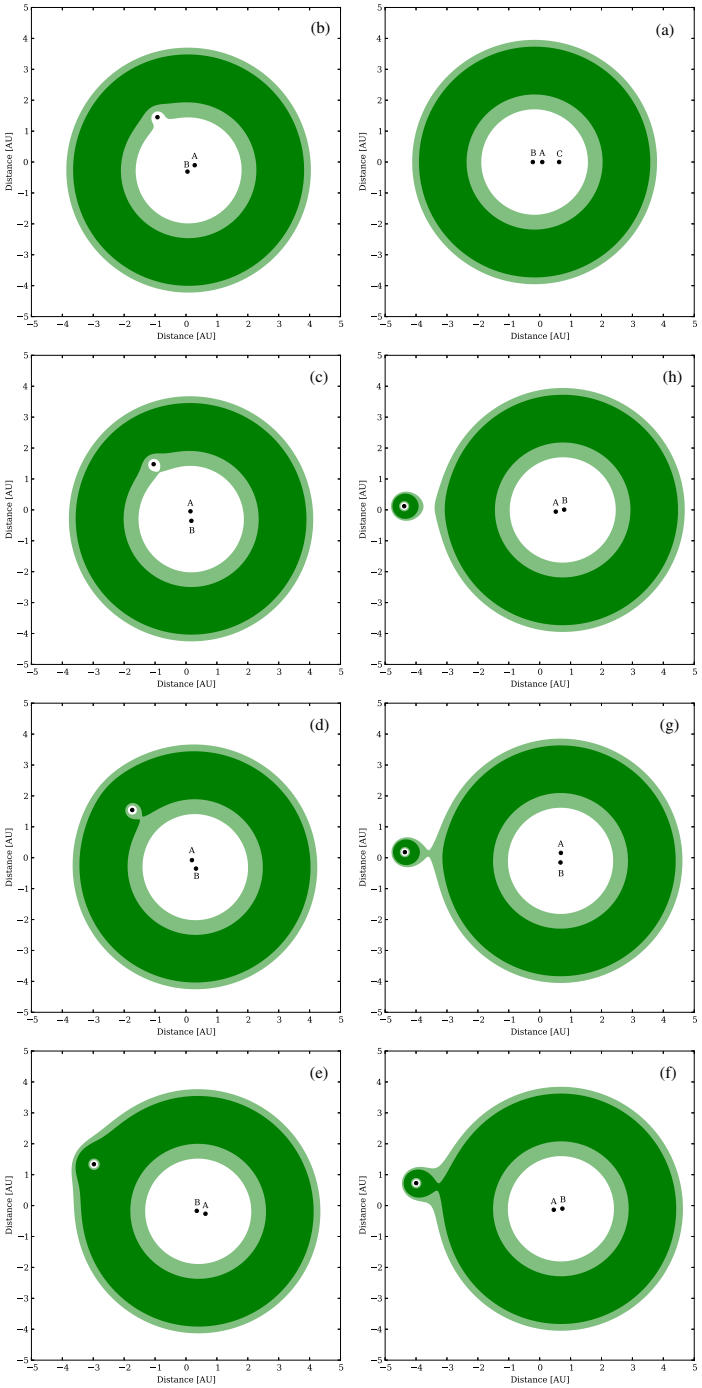

Figure 9. Graphs of the HZ of the KID 5653126 system when the star C has a semimajor axis of 2.42 AU and an eccentricity of 0.7. From the top right panel and in a counterclockwise rotation (from (a) to (h)), the panels correspond to the star C being at 0°, 26°, 28°, 41°, 52°, 73°, 117°, 150°, and 154°, respectively. An animation of the HZ of this system can be found at http://astro.twam.info/hz-multi.

(A color version of this figure is available in the online journal.)

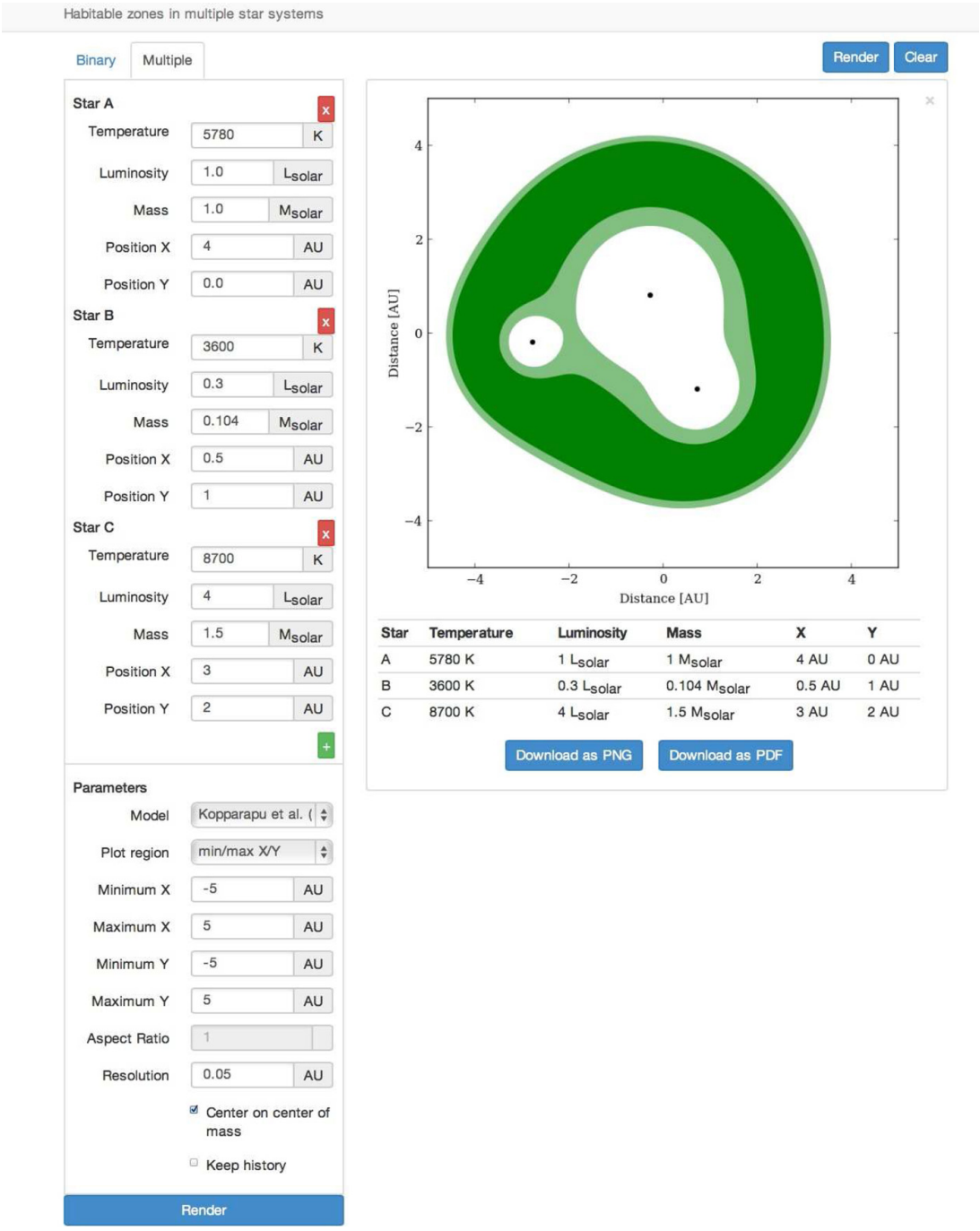

Figure 10. Screenshot of the interactive Web site http://astro.twam.info/hz for calculating the HZ of binary and multiple star systems. (A color version of this figure is available in the online journal.)

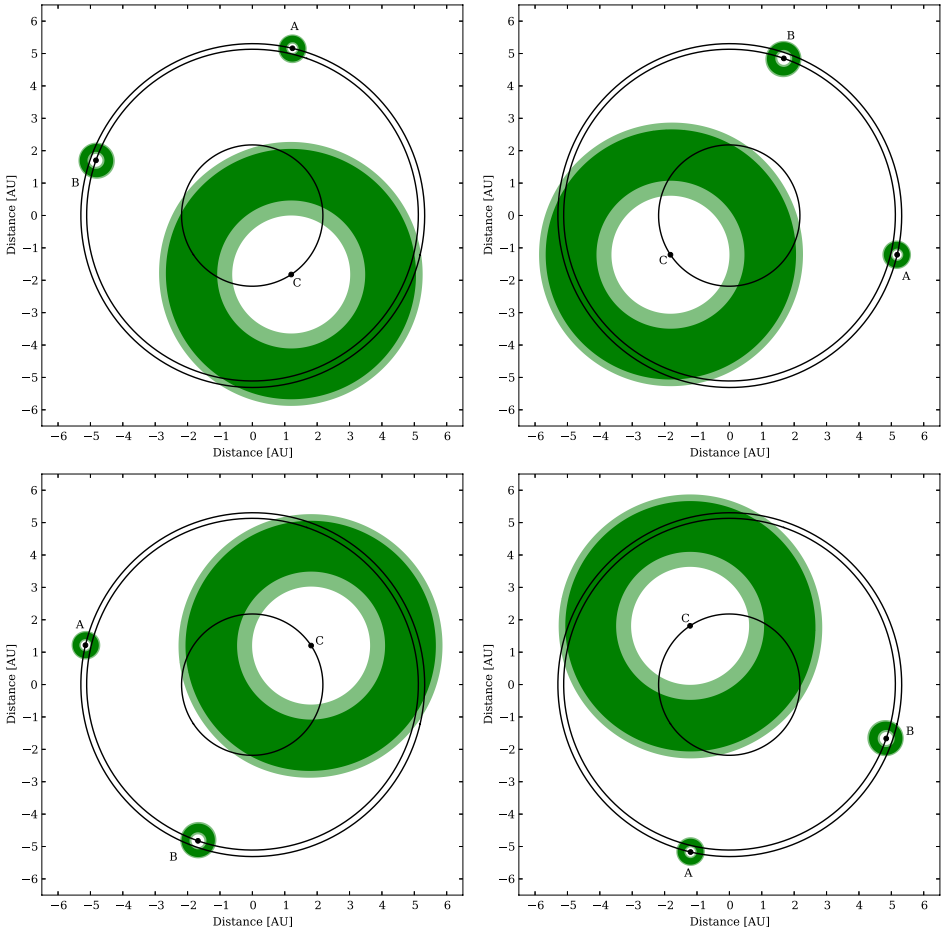

Figure 11. Habitable zone of a triple star system with the stars on an equilateral triangle as an analytical solution to the general three-body problem. From the top right panel and counterclockwise, the figures show the evolution of the HZ of the system for one complete revolution around its center of mass. The stars masses, luminosities, and temperatures as well as their initial positions and velocities are given in Table 4. The orbits of the stars around the center of mass (0, 0) are shown in black. An animation of the HZ of this system can be found at http://astro.twam.info/hz-multi.

(A color version of this figure is available in the online journal.)

(Figure 12) configuration. The initial positions (X, Y) and velocities (V_X, V_Y) of the stars are also shown. Figure 11 shows four snapshots of the HZ of the circular case along with the orbits of the stars (black, solid circles) for one complete revolution of the system (from the top right panel and in a counterclockwise rotation). Since in this configuration, the distances between the stars do not change, one would expect that for the types of the stars considered here, the mutual stellar interactions will be so small that planetary orbits maintain stability in the stars' individual HZs. Figure 12, shows similar stars in an elliptical configurations. As shown here, although at times during their orbital motions, the stars are so far away from one another that they maintain their individual HZs, their subsequent close approaches causes the HZ of the system to change and the interactions among them may become so strong that the orbits of Earth-mass objects in the HZ will become unstable. Animations of the time-evolution of the HZ of the system can be found at http://astro.twam.info/hz-multi.

4.2. Interesting Examples: Three Stars in a Figure-eight Orbit

Another interesting solution to the general three-body problem is when three equal-mass bodies revolve around their center of mass in a figure-eight orbit (Moore 1993; Chenciner & Montgomery 2000). Although such orbital configuration is unlikely to appear in nature, it would be interesting to calculate its HZ and determine how it evolves as the stars move in their orbits.

Using our interactive Web site, we calculated the HZ of such systems for different values of the mass and temperature of each star. Results of stability analysis indicated that in general in a triple star system in a figure-eight orbit, the orbit of an Earth-mass planet will be stable at large distances around the entire system and in a small region around each star where the perturbations of other stars do not affect its motion. Figure 13 shows the results of these integrations for a system with three Sun-like stars ($T = 5780$ K). Integrations were carried out for

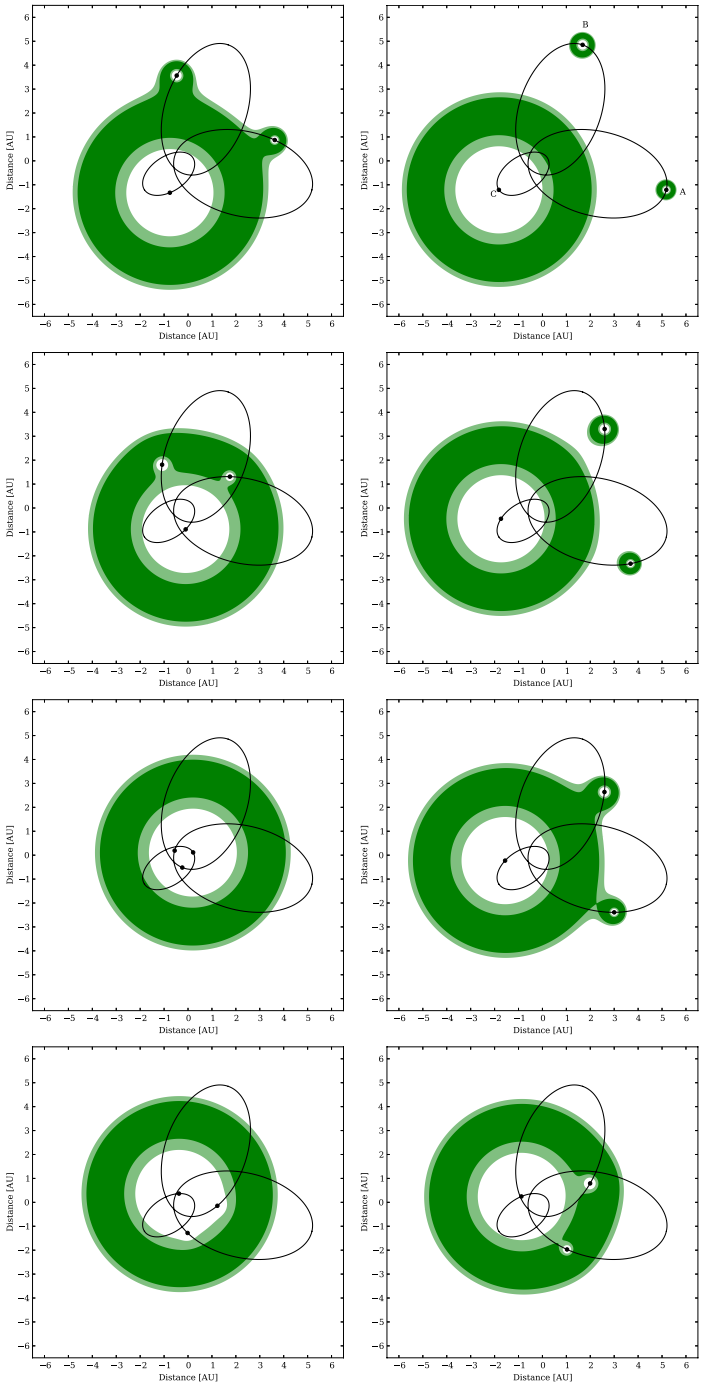

Figure 12. HZ of the same triple star systems as in Figure 11 with stars being in elliptical orbits. From the top right panel and counterclockwise, the figures show the evolution of the HZ of the system for one complete revolution around its center of mass. The stars masses, luminosities, and temperatures as well as their initial positions and velocities are given in Table 4. The orbits of the stars around the center of mass (0, 0) are shown in black. An animation of the HZ of this system can be found at http://astro.twam.info/hz-multi.

(A color version of this figure is available in the online journal.)

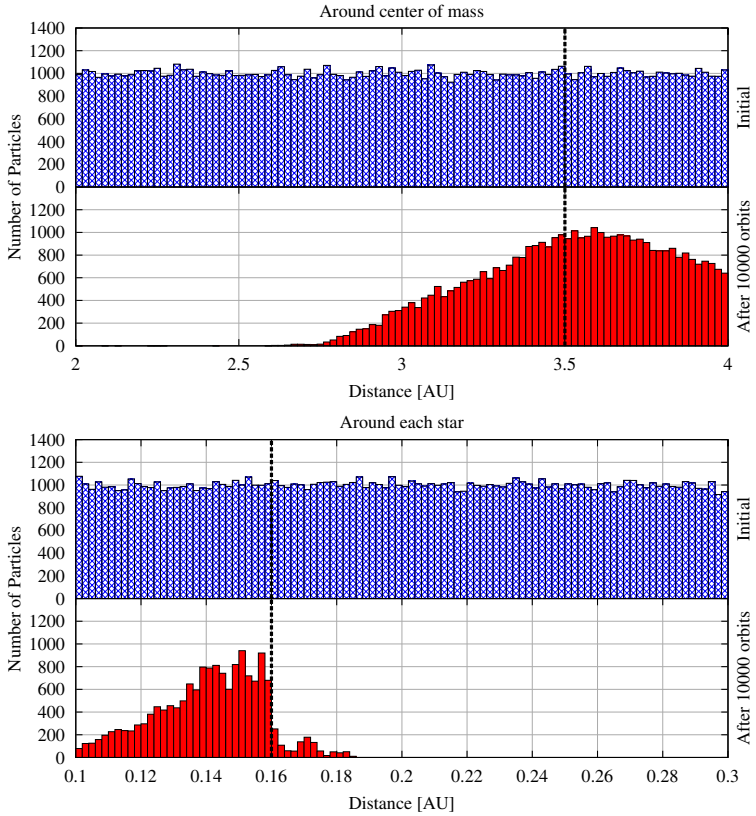

Figure 13. Results of the integrations of non-interacting Earth-mass planets around the center of mass of a triple stars system with Sun-like stars in a figure-eight orbit. The blue histograms show the initial distribution of the planets and the red histograms correspond to their distribution after integrating their orbits for 10,000 orbital periods of one star around the center of mass of the system (the orbital periods of all stars around the center of mass are identical). As shown here, Earth-mass planets initially at distances larger than 3.5 AU (top panel) and interior to 0.160 AU (bottom panel) around each star, maintained their orbits for the duration of the integration. (A color version of this figure is available in the online journal.)

Table 5
Values of the Mass, Luminosity, Temperature, and the Components of the Position and Velocity Vectors of the Three-star Systems shown in Figures 14 and 15

	Sun-like stars			M stars		
	A	B	C	A	B	C
T (K)	5780	5780	5780	2800	2800	2800
L ($L_\odot$)	1.0	1.0	1.0	0.0095	0.0095	0.0095
M ($M_\odot$)	1.0	1.0	1.0	0.25	0.25	0.25
X (AU)	−0.97	0	0.97	−0.61	0	0.61
Y (AU)	0.24	0	−0.24	0.15	0	−0.15
$V_X/2\pi$ (AU day^{-1})	0.47	−0.93	0.47	0.29	−0.59	0.29
$V_Y/2\pi$ (AU day^{-1})	0.43	−0.86	0.43	0.27	−0.54	0.27

10,000 orbital period of one star around the center of mass of the system. The values of the initial positions (X, Y) and velocities (V_X, V_Y) of these stars are given in Table 5. As indicated by the vertical dashed line in the figure, the regions of planetary stability are at distances larger than 3.5 AU around the entire system, and smaller than 0.160 AU, around each star. Figure 14 shows the HZ of this system for one orbital period (starting from the upper right panel and counterclockwise). The dashed circles in this figure correspond to the above-mentioned stability limits. Given the luminosities of the stars, the HZ of the system encompasses the entire triple stars system and its outer boundary is inside the stability limit. The latter implies that an Earth-like planet will not be able to maintain a stable orbit in this HZ.

Although the HZ of the three-star system in Figure 14 is dynamically unstable, the fact that small regions of stability exist in close distances around each star motivated us to calculate the HZ of the system for cool and low-mass stars. Figure 15 shows the results for three 0.25 solar-masses M dwarfs with luminosities of 0.0095 $L_\odot$ and temperatures of $T = 2800$ K. From the top right panel and counterclockwise, the figure corresponds to one complete revolution of the system. The integrations of the motion of Earth-mass objects indicated that the planetary stability is limited to distances larger than 2.20 AU around the entire system, and smaller than 0.101 AU around each star (the dashed circles in Figure 15). As shown here, while during the motion of the stars, the HZ of the system extends to larger distances, only a small region of the empirical HZ around each star maintains planetary stability. Animations

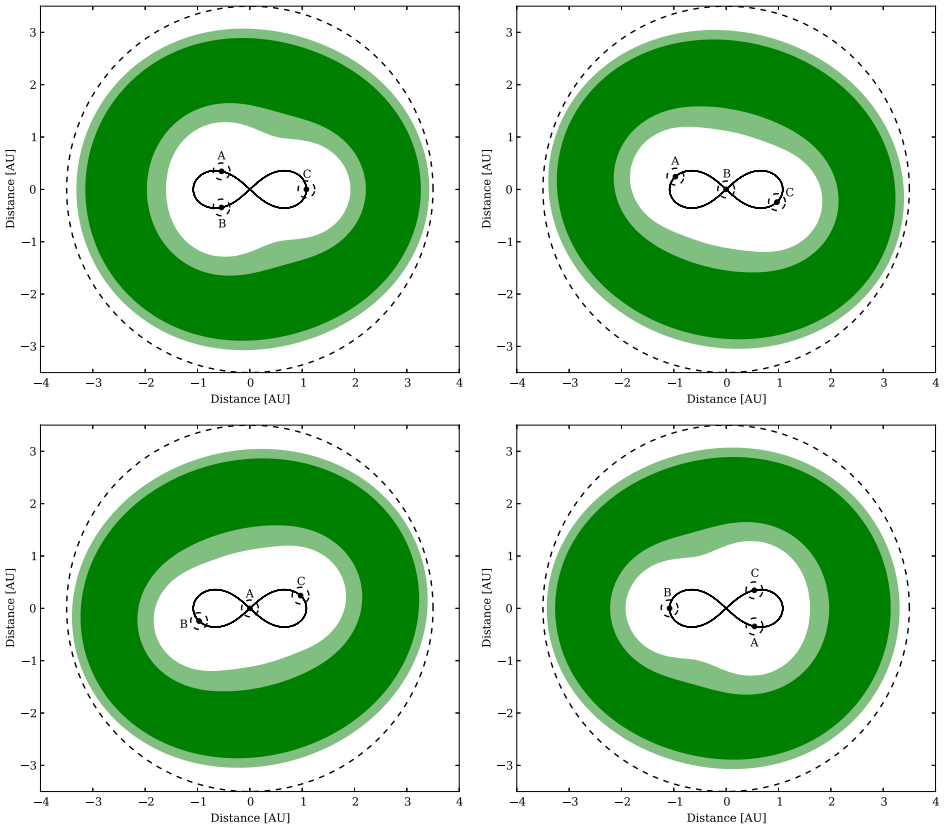

Figure 14. HZ of a triple star system with Sun-like stars in a figure-eight orbit. From the top right panel, and in a counterclockwise rotation, the figures show the evolution of the HZ of the system for one complete revolution around its center of mass. The initial orbital elements and velocities of the stars are given in Table 5. The dashed circles correspond to the boundaries of planetary orbit stability. As shown here, the HZ encompasses the entire system and is dynamically unstable. An animation of the HZ of this system can be found at http://astro.twam.info/hz-multi.

(A color version of this figure is available in the online journal.)

of the time-evolution of the HZ of the system can be found at http://astro.twam.info/hz-multi.

5. SUMMARY

We presented a general methodology for calculating the HZ of multiple star systems. We used the concept of spectral weight factor as introduced by HK13 and KH13, and calculated the total flux received at the top of the atmosphere of an Earth-like planet. By comparing this flux with that received at the top of Earth's atmosphere from the Sun, we determined regions corresponding to narrow and empirical HZ in and around multiple stars systems. To demonstrate the applicability of our methodology, we calculated the HZ of two triple star systems and studied the effects of high and low luminosity stars on the HZ around the other stellar components. To streamline the calculations of HZ in binary and multiple star systems, we developed an interactive Web site where by inputting the physical and dynamical properties of the stars, the HZ of the system is obtained.

We would like to note that the HZ, as calculated in this study is in fact an instantaneous HZ. In our calculations, we did not consider the effect of the eccentricity of the stellar and planetary orbits. When the orbit of the planet and/or those of the stars are eccentric, the close approaches of the stars to the planet will affect the total flux received at the top of the planet's atmosphere, and therefore changes the locations where the planet can be habitable (i.e., the boundaries of the system's HZ). In an actual system with an Earth-like planet, these effects have to be taken into consideration, and the region of the habitability of the planet has to be determined by averaging the flux received by the planet over the longest orbital period of the system. Such calculations have to be applied to actual systems in a case by case basis.

We thank the anonymous referee for constructive comments which have improved our manuscript. T.M. received financial support from the Carl-Zeiss-Stiftung. N.H. acknowledges support from the NASA ADAP grant NNX13AF20G, NASA Astrobiology Institute under Cooperative Agreement NNA09DA77 at the Institute for Astronomy, University of Hawaii, *HST* grant HST-GO-12548.06-A, and Alexander von Humboldt Foundation. Support for program HST-GO-12548.06-A was provided by NASA through a grant from the Space Telescope Science Institute, which is operated by the Association of Universities

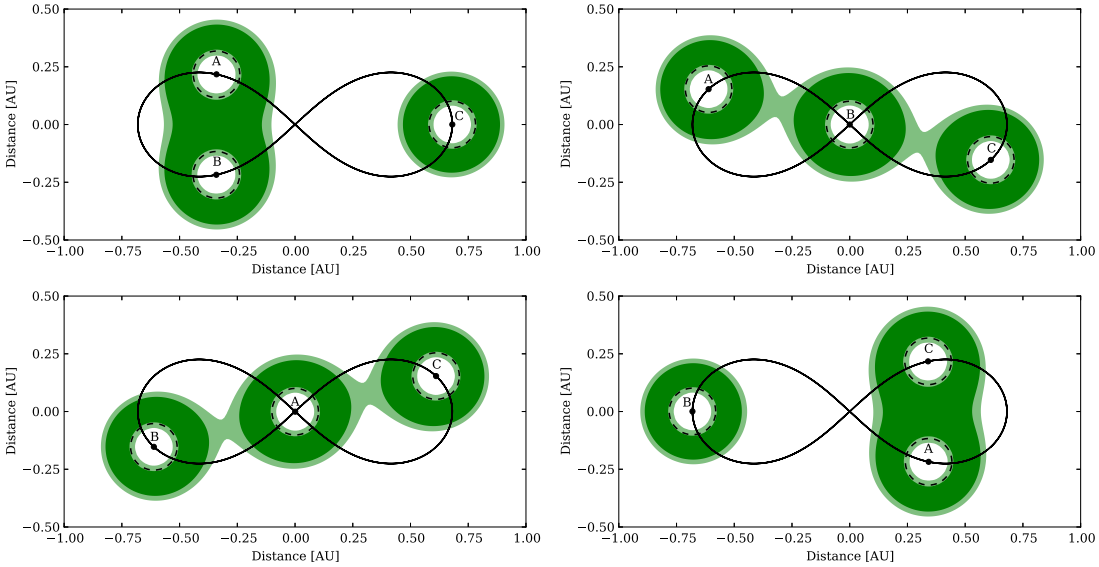

Figure 15. HZ of a system of three 0.25 solar-mass M stars in a figure-eight orbit. From the top right panel and in a counterclockwise rotation, the figures show the evolution of the HZ of the system for one complete revolution around its center of mass. The initial orbital elements and velocities of the stars are given in Table 5. The dashed circles show the boundaries of the regions of planetary stability around each star (∼0.101 AU). As shown here, Earth-like planets can have stable orbits in a small region in the empirical HZ around each star. An animation of the HZ of this system can be found at http://astro.twam.info/hz-multi.

(A color version of this figure is available in the online journal.)

for Research in Astronomy, Incorporated, under NASA contract NAS5-26555. N.H. is also thankful to the Computational Physics group at the Institute for Astronomy and Astrophysics, University of Tübingen for their kind hospitality during the course of this project.

REFERENCES

Anglada-Escudé, G., Arriagada, P., Vogt, S. S., et al. 2012, ApJL, 751, L16
Batten, A. H., Fletcher, J. M., & MacCarthy, D. G. 1989, , PDAO, 17, 1
Cash, J. R., & Karp, A. H. 1990, ACM Trans. Math. Softw., 16, 201
Chenciner, A., & Montgomery, R. 2000, AnMat, 152, 881
Cochran, W. D., Hatzes, A. P., Butler, R. P., & Marcy, G. W. 1997, ApJ, 483, 457
Delfosse, X., Bonfils, X., Forveille, T., et al. 2013, A&A, 553, A8
Duquennoy, A., & Mayor, M. 1991, A&A, 248, 485
Dvorak, R. 1986, A&A, 167, 379
Dvorak, R., Froeschle, C., & Froeschle, C. 1989, A&A, 226, 335
Eggl, S., Pilat-Lohinger, E., Funk, B., Georgakarakos, N., & Haghighipour, N. 2013, MNRAS, 428, 3104
Eggl, S., Pilat-Lohinger, E., Georgakarakos, N., Gyergyovits, M., & Funk, B. 2012, ApJ, 752, 74
Haghighipouir, N., & Kaltenegger, L. 2013, ApJ, 777, 166
Holman, M. J., & Wiegert, P. A. 1999, AJ, 117, 621
Kaltenegger, L., & Haghighipour, N. 2013, ApJ, 777, 165
Kaltenegger, L., & Sasselov, D. 2011, ApJL, 736, L25
Kane, S. R., & Gelino, D. 2012, PASP, 124, 323
Kane, S. R., & Hinkel, N. R. 2013, ApJ, 762, 7
Kasting, J. F., Whitmire, D. P., & Reynolds, R. T. 1993, Icar, 101, 108
Kopparapu, R. K., Ramirez, R., Kasting, J. F., et al. 2013a, ApJ, 765, 131
Kopparapu, R. K., Ramirez, R., Kasting, J. F., et al. 2013b, ApJ, 770, 82
Liu, H-G., Zhang, H., & Zhou, J-L. 2013, ApJL, 767, L38
Mason, P. A., Zuluaga, J. I., Clark, J. M., & Cuartas-restrepo, P. A. 2013, ApJL, 774, L26
Morre, C. 1993, PhRvL, 70, 3675
Quarles, B., Musielak, Z. E., & Cuntz, M. 2012, ApJ, 750, 14
Rabl, G., & Dvorak, R. 1988, A&A, 191, 385
Rein, H. 2012, arXiv:1211.7121
Schwamb, M. E., Orosz, J. A., Carter, J. A., et al. 2013, ApJ, 768, 127
Selsis, F., Kasting, J. F., Levrard, B., et al. 2007, A&A, 476, 1373
Slawson, R. W., Prša, A., Welsh, W. F., et al. 2011, AJ, 142, 160
Underwood, D. R., Jones, B. W., & Sleep, P. N. 2003, IJAsB, 2, 289

4. Summary

Throughout this work I studied different problems in the context of planet formation and in particular the case of planet formation in binary stars. This was done using numerical simulations mainly with the `FARGO` code.

In the first paper (Müller and Kley, 2012) we addressed the problem of planet formation in close binary systems using the examples of γ Cephei and α Centauri. We extended previous work which was done primarily with locally isothermal simulations by adding an energy equation and local radiative cooling. The additional physical effects result in less eccentric disks which facilitates planet formation as the relative velocities between dust within the disk are decreased.

The second paper (Müller et al., 2012) analyzed the numerical treatment of gravity forces in two-dimensional simulations due to an embedded planet in the protoplanetary disk or the self-gravity within the protoplanetary disk. As planets are usually treated as point masses their gravitational potential needs to be smoothed to avoid singularities within the potential. The smoothing also accounts for the finite height of the disk in the vicinity of the planet. In the case of a self-gravitating disk the gravitational potential needs also to be smoothed to account for the finite height of the disk and to avoid overestimating gravitational forces on short distances. To estimate the values for the smoothing parameter we compared the smoothed torques on the planet to analytically known torques and the smoothed forces between cells to vertically integrated forces.

In the third paper (Kley et al., 2012) we investigated spatial resolution and timestep issues concerning the FARGO algorithm rose by Dong et al. (2011). We showed that the FARGO algorithm can be applied to the given problems without any constraints on resolution and time steps. This was done by doing a comprehensive comparison between five different codes on the problem suggested by Dong et al. (2011).

The forth paper (Müller and Kley, 2013) deals with mass accretion in transitional disks. Transitional disks are protoplanetary disks with an inner cavity but nevertheless show mass accretion onto the star. We showed that planets at the outer edge of the cavity may transfer mass through the gap onto the star. This was done using locally isothermal and radiative simulations which also included stellar irradiation. Isothermal models showed similar mass accretion rates to the standard mass accretion rate of stationary, viscous accretion disks whereas the radiative and irradiated models show much smaller accretion rates.

In the last paper (Müller and Haghighipour, 2014) we described a way to calculate habitable zones in multiple star systems based on one-dimensional climate models by Kopparapu et al. (2013a,b). Therefore we extended previous work done by Kaltenegger and Haghighipour (2013) and Haghighipour and Kaltenegger (2013). We showed that the concept of an inner and outer radius of the habitable zone in multiple star systems is obsolete and presented an alternative definition. To simplify calculations of the habitable zones in multiple star systems

we presented an interactive website.

4.1. Outlook

The simulations done on the γ Cephei and α Centauri system in Müller and Kley (2012) did not include self-gravity and stellar irradiation. With the in-depth analysis of gravitational smoothing in Müller et al. (2012) it is now possible to include the effects of self-gravity in these models correctly. Also the addition of radiative diffusion (Appendix A.1) and stellar irradiation (Appendix A.2), which were successfully used in the simulations of Müller and Kley (2013) can improve the models.

As all the simulations where only done using the two-dimensional `FARGO` code, some of the models should be compared to fully three-dimensional models to check if the gravitational smoothing and stellar irradiation provide similar results.

The protoplanetary disks in these simulations can get eccentric and thus the relative velocities between particles within the disk increase. To simulate the evolution of particles and their relative velocities in the disk further simulations need to be done. This can be done using the particle treatment (Appendix A.3) that I implemented into the `FARGO` code.

A. Appendix

Most of the simulations done in this thesis we performed using the FARGO code, which is freely available at http://fargo.in2p3.fr. The FARGO code is a grid-based, staggered mesh code which uses the same techniques as the ZEUS-2D (Stone and Norman, 1992) code with the addition of the FARGO algorithm (Masset, 2000) to speed-up calculations. It uses operator splitting and a first-order integrator to update velocities with the source terms. The advective terms are treated by a second-order upwind algorithm (van Leer, 1977). We used the modified version of Baruteau (2008) with self-gravity and an energy equation.

In this chapter, some of the additions we made to the FARGO code are described.

A.1. Radiative Diffusion

The vertically integrated energy equation reads as

$$\frac{\partial \Sigma c_v T}{\partial t} + \nabla \left(\Sigma c_v T \mathbf{v} \right) = -p \nabla \mathbf{v} + Q_+ - \int_{-\infty}^{\infty} \nabla F \, dz, \tag{A.1.1}$$

where Σ is the surface density, c_v the specific heat, T the mid-plane temperature, p the vertically integrated pressure, $\mathbf{v}$ the two-dimensional velocity, Q_+ the heating terms and F the two-dimensional radiative flux, which reads as

$$F = -\frac{4\sigma_\mathrm{R}}{3\rho\kappa} \nabla T^4 \tag{A.1.2}$$

where σ_R is the Stefan-Boltzmann constant, ρ the density and κ the Rosseland mean opacity. The last term of Equation A.1.1 can be approximated as

$$-\int_{-\infty}^{\infty} \nabla F \, dz = -\int_{-\infty}^{\infty} \nabla \left(-\frac{16\sigma_\mathrm{R}}{3\rho\kappa} T^3 \nabla T \right) dz \tag{A.1.3}$$

$$= -\int_{-\infty}^{\infty} \frac{\partial}{\partial z} \left(-\frac{16\sigma_\mathrm{R}}{3\rho\kappa} T^3 \frac{\partial}{\partial z} T \right) dz$$

$$-\int_{-\infty}^{\infty} \left[\frac{1}{r} \frac{\partial}{\partial r} r \left(-\frac{16\sigma_\mathrm{R}}{3\rho\kappa} T^3 \frac{\partial}{\partial r} T \right) + \frac{1}{r} \frac{\partial}{\partial \varphi} \frac{1}{r} \left(-\frac{16\sigma_\mathrm{R}}{3\rho\kappa} T^3 \frac{\partial}{\partial \varphi} T \right) \right] dz \tag{A.1.4}$$

$$\approx -Q_\mathrm{rad} - 2H \left[\frac{1}{r} \frac{\partial}{\partial r} r \left(-\frac{16\sigma_\mathrm{R}}{3\rho\kappa} T^3 \frac{\partial}{\partial r} T \right) + \frac{1}{r} \frac{\partial}{\partial \varphi} \frac{1}{r} \left(-\frac{16\sigma_\mathrm{R}}{3\rho\kappa} T^3 \frac{\partial}{\partial \varphi} T \right) \right] \tag{A.1.5}$$

$$= -Q_\mathrm{rad} + H \left[\frac{1}{r} \frac{\partial}{\partial r} \left(rK \frac{\partial}{\partial r} T \right) + \frac{1}{r} \frac{\partial}{\partial \varphi} \frac{1}{r} \left(K \frac{\partial}{\partial \varphi} T \right) \right], \tag{A.1.6}$$

where Q_rad describes the radiative losses from the disk surfaces (Müller and Kley, 2012, Section 2.1) and

$$K = \frac{32\sigma_\mathrm{R}}{3\rho\kappa} T^3 = \frac{32\sqrt{2\pi}\sigma_\mathrm{R}}{3\Sigma\kappa} H T^3 \tag{A.1.7}$$

is the diffusion coefficient of the radiative diffusion in the r–φ plane. To treat optically thick and thin regions correctly we use a flux-limited diffusion approach (Levermore and Pomraning, 1981; Levermore, 1984). Therefore the factor $\frac{1}{3}$ in K is replaced by a flux-limiter λ given by Kley (1989). The flux-limiter depends on the local physical conditions of the gas and approaches $\frac{1}{3}$ for optically thick regions and reduces the flux to $4\sigma_\mathrm{R} T^4$ in the optically thin regions.

The radiative diffusion part of Equation A.1.6 can be written as a diffusion equation, which reads as

$$\frac{\partial \Sigma c_v T}{\partial t} = H \frac{1}{r} \frac{\partial}{\partial r} \left(rK \frac{\partial}{\partial r} T \right) + H \frac{1}{r} \frac{\partial}{\partial \varphi} \frac{1}{r} \left(K \frac{\partial}{\partial \varphi} T \right). \tag{A.1.8}$$

This can be discretized on the staggered mesh as

$$\frac{T_{i,j}^{n+1}-T_{i,j}^{n}}{dt} = \frac{H}{\Sigma_{i,j}c_v}\left[\frac{2}{r_{i+\frac{1}{2}}^2-r_{i-\frac{1}{2}}^2}\left(\frac{T_{i+1,j}-T_{i,j}}{r_{i+1}-r_i}(rK)_{i+\frac{1}{2},j}-\frac{T_{i,j}-T_{i-1,j}}{r_i-r_{i-1}}(rK)_{i-\frac{1}{2},j}\right)\right.$$
$$\left.+\frac{1}{r_i^2}\frac{1}{\Delta\varphi^2}\left(\left(T_{i,j+1}-T_{i,j}\right)K_{i,j+\frac{1}{2}}-\left(T_{i,j}-T_{i,j-1}\right)K_{i,j-\frac{1}{2}}\right)\right] \tag{A.1.9}$$

If we bring all terms with the $n+1$ timestep on the right side and factor them by the different cell values of T we get a linear system of equations:

$$\begin{aligned}
T_{i,j}^{n} = {} & T_{i,j}^{n+1} \\
& + T_{i-1,j}^{n+1}\underbrace{\left(-dt\frac{H}{\Sigma_{ij}c_v}\frac{2}{r_{i+\frac{1}{2}}^2-r_{i-\frac{1}{2}}^2}\frac{(rK)_{i-\frac{1}{2},j}}{r_i-r_{i-1}}\right)}_{A_{ij}} \\
& + T_{i+1,j}^{n+1}\underbrace{\left(-dt\frac{H}{\Sigma_{ij}c_v}\frac{2}{r_{i+\frac{1}{2}}^2-r_{i-\frac{1}{2}}^2}\frac{(rK)_{i+\frac{1}{2},j}}{r_{i+1}-r_i}\right)}_{C_{ij}} \\
& + T_{i,j-1}^{n+1}\underbrace{\left(-dt\frac{H}{\Sigma_{ij}c_v}\frac{1}{r_i^2}\frac{1}{\Delta\varphi^2}K_{i,j-\frac{1}{2}}\right)}_{D_{ij}} \\
& + T_{i,j+1}^{n+1}\underbrace{\left(-dt\frac{H}{\Sigma_{ij}c_v}\frac{1}{r_i^2}\frac{1}{\Delta\varphi^2}K_{i,j+\frac{1}{2}}\right)}_{E_{ij}} \\
& + T_{i,j}^{n+1}\left(dt\frac{H}{\Sigma_{ij}c_v}\frac{2}{r_{i+\frac{1}{2}}^2-r_{i-\frac{1}{2}}^2}\left(\frac{(rK)_{i-\frac{1}{2},j}}{r_i-r_{i-1}}+\frac{(rK)_{i+\frac{1}{2},j}}{r_{i+1}-r_i}\right)\right. \\
& \qquad \left.+\left(dt\frac{H}{\Sigma_{ij}c_v}\frac{1}{r_i^2}\frac{1}{\Delta\varphi^2}\left(K_{i,j-\frac{1}{2}}+K_{i,j+\frac{1}{2}}\right)\right)\right) \qquad \text{(A.1.10)} \\
= {} & A_{ij}T_{i-1,j}^{n+1}+C_{ij}T_{i+1,j}^{n+1}+D_{ij}T_{i,j-1}^{n+1}+E_{ij}T_{i,j+1}^{n+1} \\
& + \underbrace{\left(1-A_{ij}-C_{ij}-D_{ij}-E_{ij}\right)}_{B_{ij}}T_{i,j}^{n+1} \qquad \text{(A.1.11)} \\
= {} & A_{ij}T_{i-1,j}^{n+1}+C_{ij}T_{i+1,j}^{n+1}+D_{ij}T_{i,j-1}^{n+1}+E_{ij}T_{i,j+1}^{n+1}+B_{ij}T_{i,j}^{n+1} \qquad \text{(A.1.12)}
\end{aligned}$$

This linear system of equations can be solved by any linear equation solver. We use a successive over-relaxation algorithm to solve it. Therefore we iterate over

$$\tilde{T}_{i,j}^{k+1} = (1-\omega)\tilde{T}_{i,j}^{k} - \frac{\omega}{B_{i,j}}\left[A_{i,j}\tilde{T}_{i-1,j}^{k}+C_{i,j}\tilde{T}_{i+1,j}^{k}+D_{i,j}\tilde{T}_{i,j-1}^{k}+E_{i,j}\tilde{T}_{i,j+1}^{k}-T_{i,j}^{k}\right] \tag{A.1.13}$$

until $\tilde{T}$ converges. If we use open boundary conditions at the inner or outer radius of the disk we set the corresponding temperature values to T_{floor} at each iteration. T_{floor} is usually $\approx 3\,\text{K}$ to account for the cosmic background radiation.

A.2. Stellar irradiation

The irradiation from the star to one side of the disk can be approximated by

$$Q_{\text{irrad}} = \alpha \sigma_{\text{R}} T_{\text{star}}^4 \left(\frac{r_{\text{star}}}{r} \right)^2 \tag{A.2.1}$$

(Günther et al., 2004), where T_{star} is the effective photosphere temperature of the star and r_{star} the radius of the star. The factor α accounts for the non-perpendicular impact of the irradiation from the star onto the disk.

The implementation of this is done in the following way: First of all, the factor α is calculated for each cell by

$$\alpha_{i,j} = \begin{cases} dH_{i,j} \left[(dH_{i,j})^2 + (r_{i+1} - r_{i-1})^2 \right]^{-\frac{1}{2}} & dH_{i,j} < 0 \\ 0 & dH_{i,j} \geq 0 \end{cases}, \tag{A.2.2}$$

where $dH_{i,j} = (hr)_{i+1,j} - (hr)_{i-1,j}$ is the difference in height of the current cell. α is only non-zero when the slope is positive and thus not shadowed.

To further improve the shadow effect a depth buffer is used. Therefore a maximum angle $\vartheta_{\max}$ and a resolution in ϑ direction is specific in the configuration file. A buffer with $N_\varphi \times N_\vartheta$ integer values is created, where N_φ is the number of cells in φ direction and N_ϑ the number of cells in ϑ direction. Each value is filled with the radial index of maximum radius which is visible by direct line of sight in this direction. The advantage of this method is that it can be trivially parallelized with the `FARGO` parallelization method of rings. Each process can calculate its own maximum radius and later on the maximum of all local maximum radii can be taken to get the global maximum radius. For each cell the visibility can be determined by calculating the index

$$k_{i,j} = \min \left\{ N_\vartheta, \arctan \frac{h_{i,j}(N_\vartheta - 1)}{\vartheta_{\max}} \right\}, \tag{A.2.3}$$

which corresponds to the height of the cell and then looking up the maximum visible radius in the depth buffer. The visibility

$$\eta_{i,j} = \begin{cases} 1 & i < \text{depthBuffer}[i,k] \\ 0 & \text{otherwise} \end{cases} \tag{A.2.4}$$

then defines if a cell is visible or not. To avoid discontinuities by abrupt shadowing the actual visibility is calculated as a mean of all surrounding cells.

As the initial profiles used in the simulations usually do not account for stellar irradiation, it is a good idea to slowly ramp up the stellar irradiation. This can be done by multiplying Q_{irrad} by a factor

$$f(t) = \begin{cases} 1.0 - \left(\cos \frac{t\pi}{2t_{\text{ramp}}} \right)^2 & t \leq t_{\text{ramp}} \\ 0 & \text{otherwise} \end{cases}, \tag{A.2.5}$$

where t_{ramp} is the ramp-up time.

To avoid depositing too much energy in the optically thin regions, we estimate a horizontal optical depth $\tilde{\tau}$ by calculating the vertical optical depth

$$\tau_{i,j} = \frac{1}{\sqrt{2\pi}} \kappa_{i,j} \Sigma_{i,j} \,, \tag{A.2.6}$$

where κ is the Rosseland mean opacity and Σ the surface density, and rescaling it by the size of the cell:

$$\tilde{\tau}_{i,j} = \tau_{i,j} \frac{r_{i+1} - r_i}{(hr)_{i,j}} \,. \tag{A.2.7}$$

If $\tilde{\tau}_{i,j} < 1$ we set $Q_{\rm irrad} = 0$.

Composing everything together $Q_{\rm irrad}$ can be written as

$$Q_{{\rm irrad},i,j} = \begin{cases} 2\, f(t)\, \eta_{i,j}\, \alpha_{i,j}\, \sigma_{\rm R} T_{\rm star}^4 \left(\frac{r_{\rm star}}{r_i}\right)^2 & \tilde{\tau}_{i,j} \geq 1 \\ 0 & \text{otherwise} \end{cases} . \tag{A.2.8}$$

A.3. Particles

The FARGO code has a built-in N-body solver for the motion of the stars and planets. It is implemented as a fifth-order Runge-Kutta integrator. When running FARGO in parallel the position of the stars and planets is needed in all processes and therefore the N-body problem is solved on each process separately.

This is not needed for the study of particles within the disk and so we implemented an additional N-body solver into the FARGO code, which is optimized for handling hundreds of thousands particles. We also use a fifth-order Runge-Kutta integrator proposed by Cash and Karp (1990). Each particle is only calculated by one process, more precisely by that process which stores the corresponding gas cells of the particle's current position. If a particle leaves the computational domain of one process it is handed over to the next process.

The particles can not interact, meaning they only feel the gravity of the stars and planets, but not of other particles. The inclusion of the gravitational potential of the gaseous disk is optional as it is computationally very costly.

In addition to the gravitational forces, the particle feels the gas drag. It is given by (Landau and Lifshitz, 1959; Whipple, 1972)

$$\mathbf{F}_{\mathrm{drag}} = -\frac{1}{2}\, C_{\mathrm{D}}\, \pi r_{\mathrm{p}}^2\, \rho_{\mathrm{g}}\, v_{\mathrm{rel}} \mathbf{v}_{\mathrm{rel}} \tag{A.3.1}$$

where r_{p} is the radius of the particle, ρ_{g} the density of the gas and $\mathbf{v}_{\mathrm{rel}}$ the relative velocity between the particle and the gas. The drag coefficient is a dimensionless constant and is given by (Whipple, 1972; Weidenschilling, 1977)

$$C_{\mathrm{D}} = \begin{cases} 24\,\mathrm{Re}^{-1} & \mathrm{Re} \leq 1 \quad \text{(Stoke's law)} \\ 24\,\mathrm{Re}^{-\frac{3}{5}} & 1 < \mathrm{Re} < 800 \\ 0.44 & \mathrm{Re} \geq 800 \quad \text{(Newtonian)} \end{cases}, \tag{A.3.2}$$

where Re is the Reynolds number of the gas. It can be calculated by

$$\mathrm{Re} = \frac{2\,\rho_{\mathrm{g}}\, r_{\mathrm{p}}\, v_{\mathrm{rel}}}{\eta}, \tag{A.3.3}$$

where η is the dynamic viscosity of the gas. It is given by (Adachi et al., 1976)

$$\eta = \frac{m_{\mathrm{g}}\, v_{\mathrm{therm}}}{3\,\sigma}, \tag{A.3.4}$$

where $m_{\mathrm{g}} = \mu\, m_0$ and $v_{\mathrm{therm}} = \sqrt{\frac{8 k_B T}{\pi m_{\mathrm{g}}}}$ are the mean mass and mean thermal velocity of the gas molecules and σ their collisional cross section. The collisional cross section is about $\pi \left(1.5 \times 10^{-8}\,\mathrm{cm}\right)^2$ for molecular hydrogen.

We assume that the sizes of the particles are larger than the mean free path of the gas molecules and therefore neglect the Epstein regime. A combined approach to include both regimes is described in Haghighipour and Boss (2003).

To calculate the drag force for the particles the gas quantities (density ρ, temperature T and velocity $\mathbf{v}$) need to be known at the position of the particles. As they are only specified for

the grid points they have to be interpolated. For each quantity we identify the nearest grid point in r and φ direction. Q_{mm}, Q_{mp}, Q_{pm} and Q_{pp} are the nearest values to the point (r, φ), where the first index specifies the radial direction and the second the azimuthal direction and the index m means *minus* and specifies the cell left or below and the index p stands for *plus* and specifies the cell right or above. We can first interpolate azimuthally by

$$Q_{\mathrm{m}} = \frac{(r_{\mathrm{m}}\varphi_{\mathrm{p}} - r_{\mathrm{m}}\varphi)\, Q_{\mathrm{mm}} + (r_{\mathrm{m}}\varphi - r_{\mathrm{m}}\varphi_{\mathrm{m}})\, Q_{\mathrm{mp}}}{r_{\mathrm{m}}\varphi_{\mathrm{p}} - r_{\mathrm{m}}\varphi_{\mathrm{m}}}, \tag{A.3.5}$$

$$Q_{\mathrm{p}} = \frac{(r_{\mathrm{p}}\varphi_{\mathrm{p}} - r_{\mathrm{p}}\varphi)\, Q_{\mathrm{pm}} + (r_{\mathrm{p}}\varphi - r_{\mathrm{p}}\varphi_{\mathrm{m}})\, Q_{\mathrm{pp}}}{r_{\mathrm{p}}\varphi_{\mathrm{p}} - r_{\mathrm{p}}\varphi_{\mathrm{m}}}. \tag{A.3.6}$$

Afterwards we interpolate radially by

$$Q = \frac{(r_{\mathrm{p}} - r)\, Q_{\mathrm{m}} + (r - r_{\mathrm{m}})\, Q_{\mathrm{p}}}{r_{\mathrm{p}} - r_{\mathrm{m}}}. \tag{A.3.7}$$

The values of r and φ have to be taken on the corresponding grids. If $\varphi_{\mathrm{p}} > 2\pi$ or $\varphi_{\mathrm{m}} > 2\pi$ it is a good idea to shift everything by $-\pi$ to avoid problems.

A.4. FARGO Viewer

As the FARGO code has no graphical user interface all the output data is provided in binary data files. To visualize the certain gas quantities and positions of stars, planets and particles I developed an OpenGL based viewer. The FARGO Viewer is freely available at https://github.com/twam/FARGO-Viewer.

The FARGO Viewer can visualize the simulations from arbitrary point of views, with or without the underlaying grid. Stars and planets can be displayed with the respective orbits. It also allows the visualization of particles within the disk as discussed in Appendix A.3. It can loop through all the time steps of the simulation by itself and write out the current visualization as PNG files for easy video generation.

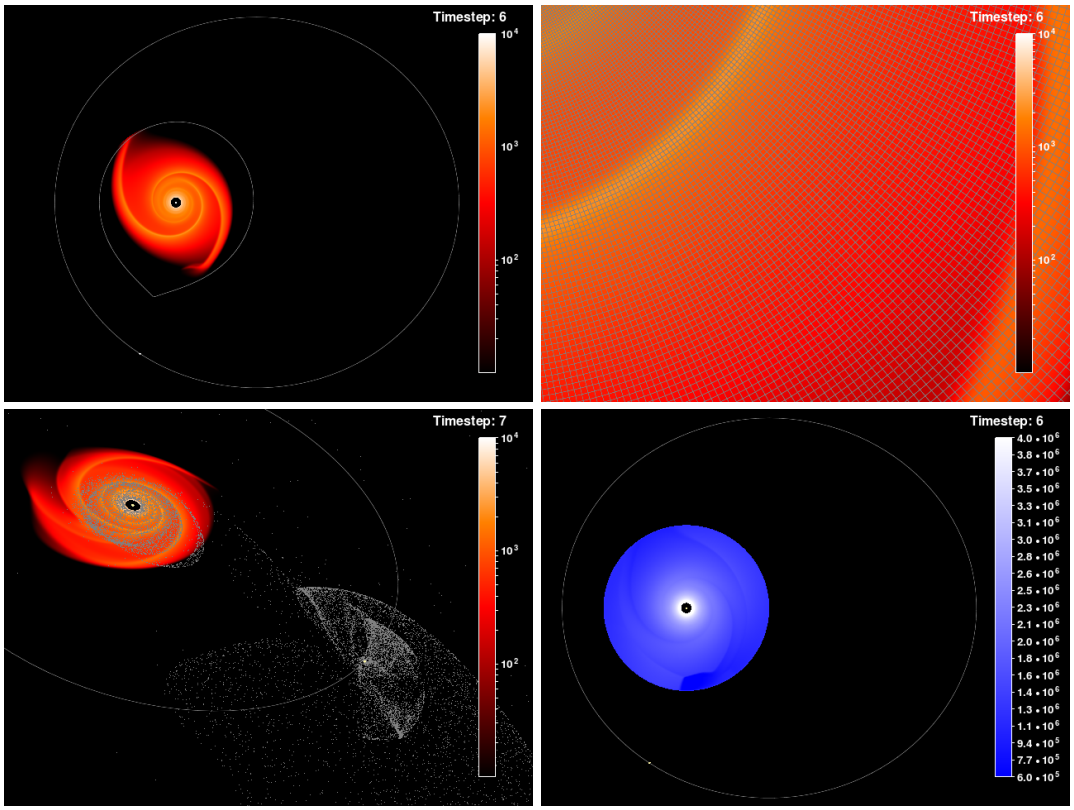

Figure A.1.: Screenshots of the FARGO Viewer showing a γ Cephei simulation. The upper left panel shows the surface density of the disk, the orbits and positions of the stars and the Roche-Lobe of the primary star. The upper right panel shows the surface density at a zoomed view such that the single grid cells are visible. Note the logarithmic grid with a much higher resolution in the top left corner. The lower left panel shows the particles within the simulation. The lower right panel shows the azimuthal velocity of the gas.

Acknowledgements

While working on this graduate thesis I was excellently supervised by Prof. Dr. Wilhelm Kley. He encouraged me to graduate and to apply for a fellowship. In addition he sent me to several conferences to present my work, which allowed me to meet many of the colleagues of my field in person. The discussions on these occasions were very fruitful for my work.

I also want to thank the Carl-Zeiss-Stiftung for granting me a fellowship. Their commitment to science allowed me to focus on my research full-time. Therefore, I am very thankful!

I benefited from the good atmosphere within the Computational Physics group at the Institute for Astronomy and Astrophysics Tübingen. The colleagues were always open to questions and discussions and helped to make the stay at the institute an unforgettable time. I will miss the time at our *cutting edge research office* with Philipp Buchegger, Marius Hertfelder and Alexander Seizinger.

Special thanks go to my whole family, in particular to my girlfriend Anneke, my deceased mother Luise, my father Gerd and his wife Dagmar and my brothers Thomas and Markus, for supporting me during my graduation.

Bibliography

I. Adachi, C. Hayashi, and K. Nakazawa.
The gas drag effect on the elliptical motion of a solid body in the primordial solar nebula.
Progress of Theoretical Physics, 56:1756–1771, December 1976.
doi:10.1143/PTP.56.1756.

Y. Alibert, C. Mordasini, and W. Benz.
Migration and giant planet formation.
Astronomy & Astrophysics, 417:L25–L28, April 2004.
doi:10.1051/0004-6361:20040053.

G. Anglada-Escudé, P. Arriagada, S. S. Vogt, E. J. Rivera, R. P. Butler, J. D. Crane, S. A. Shectman, I. B. Thompson, D. Minniti, N. Haghighipour, B. D. Carter, C. G. Tinney, R. A. Wittenmyer, J. A. Bailey, S. J. O'Toole, H. R. A. Jones, and J. S. Jenkins.
A Planetary System around the nearby M Dwarf GJ 667C with At Least One Super-Earth in Its Habitable Zone.
The Astrophysical Journal, 751:L16, May 2012.
doi:10.1088/2041-8205/751/1/L16.

P. Artymowicz and S. H. Lubow.
Dynamics of binary-disk interaction. 1: Resonances and disk gap sizes.
The Astrophysical Journal, 421:651–667, February 1994.
doi:10.1086/173679.

C. Baruteau.
Toward predictive scenarios of planetary migration.
PhD thesis, CEA Saclay, 2008.

A. P. Boss.
Giant planet formation by gravitational instability.
Science, 276:1836–1839, 1997.
doi:10.1126/science.276.5320.1836.

A. G. W. Cameron.
Physics of the primitive solar accretion disk.
Moon and Planets, 18:5–40, February 1978.
doi:10.1007/BF00896696.

B. Campbell, G. A. H. Walker, and S. Yang.
A search for substellar companions to solar-type stars.
The Astrophysical Journal, 331:902–921, August 1988.
doi:10.1086/166608.

J. R. Cash and A. H. Karp.

A variable order Runge-Kutta method for initial value problems with rapidly varying right-hand sides.
ACM Transactions on Mathematical Software, 16:201–222, 1990.
doi:10.1145/79505.79507.

A. C. M. Correia, S. Udry, M. Mayor, A. Eggenberger, D. Naef, J.-L. Beuzit, C. Perrier, D. Queloz, J.-P. Sivan, F. Pepe, N. C. Santos, and D. Ségransan.
The ELODIE survey for northern extra-solar planets. IV. HD 196885, a close binary star with a 3.7-year planet.
Astronomy & Astrophysics, 479:271–275, February 2008.
doi:10.1051/0004-6361:20078908.

X. Delfosse, X. Bonfils, T. Forveille, S. Udry, M. Mayor, F. Bouchy, M. Gillon, C. Lovis, V. Neves, F. Pepe, C. Perrier, D. Queloz, N. C. Santos, and D. Ségransan.
The HARPS search for southern extra-solar planets. XXXIII. Super-Earths around the M-dwarf neighbors Gl 433 and Gl 667C.
Astronomy & Astrophysics, 553:A8, May 2013.
doi:10.1051/0004-6361/201219013.

R. Dong, R. R. Rafikov, J. M. Stone, and C. Petrovich.
Density Waves Excited by Low-mass Planets in Protoplanetary Disks. I. Linear Regime.
The Astrophysical Journal, 741:56, November 2011.
doi:10.1088/0004-637X/741/1/56.

X. Dumusque, F. Pepe, C. Lovis, D. Ségransan, J. Sahlmann, W. Benz, F. Bouchy, M. Mayor, D. Queloz, N. Santos, and S. Udry.
An Earth-mass planet orbiting α Centauri B.
Nature, 491:207–211, November 2012.
doi:10.1038/nature11572.

A. Eggenberger, S. Udry, G. Chauvin, J.-L. Beuzit, A.-M. Lagrange, D. Ségransan, and M. Mayor.
The impact of stellar duplicity on planet occurrence and properties. I. Observational results of a VLT/NACO search for stellar companions to 130 nearby stars with and without planets.
Astronomy & Astrophysics, 474:273–291, October 2007.
doi:10.1051/0004-6361:20077447.

S. G. Els, M. F. Sterzik, F. Marchis, E. Pantin, M. Endl, and M. Kürster.
A second substellar companion in the Gliese 86 system. A brown dwarf in an extrasolar planetary system.
Astronomy & Astrophysics, 370:L1–L4, April 2001.
doi:10.1051/0004-6361:20010298.

C. F. Gammie.
Nonlinear Outcome of Gravitational Instability in Cooling, Gaseous Disks.
The Astrophysical Journal, 553:174–183, May 2001.
doi:10.1086/320631.

R. Günther, C. Schäfer, and W. Kley.
Evolution of irradiated circumbinary disks.
Astronomy & Astrophysics, 423:559–566, August 2004.

doi:10.1051/0004-6361:20040223.

N. Haghighipour and A. P. Boss.
On Pressure Gradients and Rapid Migration of Solids in a Nonuniform Solar Nebula.
The Astrophysical Journal, 583:996–1003, February 2003.
doi:10.1086/345472.

N. Haghighipour and L. Kaltenegger.
Calculating the Habitable Zone of Binary Star Systems. II. P-type Binaries.
The Astrophysical Journal, 777:166, November 2013.
doi:10.1088/0004-637X/777/2/166.

A. P. Hatzes, W. D. Cochran, M. Endl, B. McArthur, D. B. Paulson, G. A. H. Walker, B. Campbell, and S. Yang.
A Planetary Companion to γ Cephei A.
The Astrophysical Journal, 599:1383–1394, December 2003.
doi:10.1086/379281.

J.-M. Huré and A. Pierens.
A local prescription for the softening length in self-gravitating gaseous discs.
Astronomy & Astrophysics, 507:573–579, November 2009.
doi:10.1051/0004-6361/200912348.

International Astronomical Union.
IAU 2006 General Assembly: Result of the IAU Resolution votes, August 2006.
URL `http://www.iau.org/public_press/news/detail/iau0603/`.

B. M. Johnson and C. F. Gammie.
Nonlinear Outcome of Gravitational Instability in Disks with Realistic Cooling.
The Astrophysical Journal, 597:131–141, November 2003.
doi:10.1086/378392.

L. Kaltenegger and N. Haghighipour.
Calculating the Habitable Zone of Binary Star Systems. I. S-type Binaries.
The Astrophysical Journal, 777:165, November 2013.
doi:10.1088/0004-637X/777/2/165.

J. F. Kasting, D. P. Whitmire, and R. T. Reynolds.
Habitable Zones around Main Sequence Stars.
Icarus, 101:108–128, January 1993.
doi:10.1006/icar.1993.1010.

K. H. Kim, D. M. Watson, P. Manoj, W. J. Forrest, J. Najita, E. Furlan, B. Sargent, C. Espaillat, J. Muzerolle, S. T. Megeath, N. Calvet, J. D. Green, and L. Arnold.
Transitional Disks and Their Origins: An Infrared Spectroscopic Survey of Orion A.
The Astrophysical Journal, 769:149, June 2013.
doi:10.1088/0004-637X/769/2/149.

W. Kley.
Radiation hydrodynamics of the boundary layer in accretion disks. I - Numerical methods.
Astronomy & Astrophysics, 208:98–110, January 1989.

W. Kley and G. Dirksen.

Disk eccentricity and embedded planets.
Astronomy & Astrophysics, 447:369–377, February 2006.
doi:10.1051/0004-6361:20053914.

W. Kley and R. P. Nelson.
Planet formation in binary stars: the case of γ Cephei.
Astronomy & Astrophysics, 486:617–628, August 2008.
doi:10.1051/0004-6361:20079324.

W. Kley, J. C. B. Papaloizou, and G. I. Ogilvie.
Simulations of eccentric disks in close binary systems.
Astronomy & Astrophysics, 487:671–687, August 2008.
doi:10.1051/0004-6361:200809953.

W. Kley, T. W. A. Müller, S. M. Kolb, P. Benítez-Llambay, and F. Masset.
Low-mass planets in nearly inviscid disks: numerical treatment.
Astronomy & Astrophysics, 546:A99, October 2012.
doi:10.1051/0004-6361/201219719.

R. K. Kopparapu.
A Revised Estimate of the Occurrence Rate of Terrestrial Planets in the Habitable Zones around Kepler M-dwarfs.
The Astrophysical Journal, 767:L8, April 2013.
doi:10.1088/2041-8205/767/1/L8.

R. K. Kopparapu, R. Ramirez, J. F. Kasting, V. Eymet, T. D. Robinson, S. Mahadevan, R. C. Terrien, S. Domagal-Goldman, V. Meadows, and R. Deshpande.
Habitable Zones around Main-sequence Stars: New Estimates.
The Astrophysical Journal, 765:131, March 2013a.
doi:10.1088/0004-637X/765/2/131.

R. K. Kopparapu, R. Ramirez, J. F. Kasting, V. Eymet, T. D. Robinson, S. Mahadevan, R. C. Terrien, S. Domagal-Goldman, V. Meadows, and R. Deshpande.
Erratum: 'Habitable Zones around Main-sequence Stars: New Estimates'.
The Astrophysical Journal, 770:82, June 2013b.
doi:10.1088/0004-637X/770/1/82.

G. P. Kuiper.
On the Origin of the Solar System.
Proceedings of the National Academy of Science, 37:1–14, January 1951.
doi:10.1073/pnas.37.1.1.

L. D. Landau and E. M. Lifshitz.
Fluid mechanics.
Pergamon Press, 1959.

C. D. Levermore.
Relating Eddington factors to flux limiters.
Journal of Quantitative Spectroscopy and Radiative Transfer, 31:149–160, February 1984.
doi:10.1016/0022-4073(84)90112-2.

C. D. Levermore and G. C. Pomraning.

A flux-limited diffusion theory.
The Astrophysical Journal, 248:321–334, August 1981.
doi:10.1086/159157.

S. H. Lubow.
A model for tidally driven eccentric instabilities in fluid disks.
The Astrophysical Journal, 381:259–267, November 1991.
doi:10.1086/170647.

S. H. Lubow and G. D'Angelo.
Gas Flow across Gaps in Protoplanetary Disks.
The Astrophysical Journal, 641:526–533, April 2006.
doi:10.1086/500356.

C. Marois, B. Macintosh, T. Barman, B. Zuckerman, I. Song, J. Patience, D. Lafrenière, and R. Doyon.
Direct Imaging of Multiple Planets Orbiting the Star HR 8799.
Science, 322:1348–, November 2008.
doi:10.1126/science.1166585.

C. Marois, B. Zuckerman, Q. M. Konopacky, B. Macintosh, and T. Barman.
Images of a fourth planet orbiting HR 8799.
Nature, 468:1080–1083, December 2010.
doi:10.1038/nature09684.

F. Marzari, H. Scholl, P. Thébault, and C. Baruteau.
On the eccentricity of self-gravitating circumstellar disks in eccentric binary systems.
Astronomy & Astrophysics, 508:1493–1502, December 2009.
doi:10.1051/0004-6361/200912251.

F. Masset.
FARGO: A fast eulerian transport algorithm for differentially rotating disks.
Astronomy and Astrophysics Supplement, 141:165–173, January 2000.
doi:10.1051/aas:2000116.

S. Mayama, J. Hashimoto, T. Muto, T. Tsukagoshi, N. Kusakabe, M. Kuzuhara, Y. Takahashi, T. Kudo, R. Dong, M. Fukagawa, M. Takami, M. Momose, J. P. Wisniewski, K. Follette, L. Abe, E. Akiyama, W. Brandner, T. Brandt, J. Carson, S. Egner, M. Feldt, M. Goto, C. A. Grady, O. Guyon, Y. Hayano, M. Hayashi, S. Hayashi, T. Henning, K. W. Hodapp, M. Ishii, M. Iye, M. Janson, R. Kandori, J. Kwon, G. R. Knapp, T. Matsuo, M. W. McElwain, S. Miyama, J.-I. Morino, A. Moro-Martin, T. Nishimura, T.-S. Pyo, E. Serabyn, H. Suto, R. Suzuki, N. Takato, H. Terada, C. Thalmann, D. Tomono, E. L. Turner, M. Watanabe, T. Yamada, H. Takami, T. Usuda, and M. Tamura.
Subaru Imaging of Asymmetric Features in a Transitional Disk in Upper Scorpius.
The Astrophysical Journal, 760:L26, December 2012.
doi:10.1088/2041-8205/760/2/L26.

M. Mayor and D. Queloz.
A Jupiter-mass companion to a solar-type star.
Nature, 378:355–359, November 1995.
doi:10.1038/378355a0.

H. Mizuno.
Formation of the Giant Planets.
Progress of Theoretical Physics, 64:544–557, August 1980.
doi:10.1143/PTP.64.544.

T. W. A. Müller and N. Haghighipour.
Calculating the Habitable Zone of Multiple Star Systems.
The Astrophysical Journal, 782:26, February 2014.
doi:doi:10.1088/0004-637X/782/1/26.

T. W. A. Müller and W. Kley.
Circumstellar disks in binary star systems. Models for γ Cephei and α Centauri.
Astronomy & Astrophysics, 539:A18, March 2012.
doi:10.1051/0004-6361/201118202.

T. W. A. Müller and W. Kley.
Modelling accretion in transitional disks.
Astronomy & Astrophysics, 560:A40, December 2013.
doi:10.1051/0004-6361/201322503.

T. W. A. Müller, W. Kley, and F. Meru.
Treating gravity in thin-disk simulations.
Astronomy & Astrophysics, 541:A123, May 2012.
doi:10.1051/0004-6361/201118737.

J. Muzerolle, L. E. Allen, S. T. Megeath, J. Hernández, and R. A. Gutermuth.
A Spitzer Census of Transitional Protoplanetary Disks with AU-scale Inner Holes.
The Astrophysical Journal, 708:1107–1118, January 2010.
doi:10.1088/0004-637X/708/2/1107.

A. F. Nelson.
Planet Formation is Unlikely in Equal-Mass Binary Systems with A ˜ 50 AU.
The Astrophysical Journal, 537:L65–L68, July 2000.
doi:10.1086/312752.

S.-J. Paardekooper, P. Thébault, and G. Mellema.
Planetesimal and gas dynamics in binaries.
Monthly Notices of the Royal Astronomical Society, 386:973–988, May 2008.
doi:10.1111/j.1365-2966.2008.13080.x.

G. Picogna and F. Marzari.
Three-dimensional modeling of radiative disks in binaries.
ArXiv e-prints, July 2013.

J. B. Pollack, O. Hubickyj, P. Bodenheimer, J. J. Lissauer, M. Podolak, and Y. Greenzweig.
Formation of the Giant Planets by Concurrent Accretion of Solids and Gas.
Icarus, 124:62–85, November 1996.
doi:10.1006/icar.1996.0190.

D. Queloz, M. Mayor, L. Weber, A. Blécha, M. Burnet, B. Confino, D. Naef, F. Pepe, N. Santos, and S. Udry.

The CORALIE survey for southern extra-solar planets. I. A planet orbiting the star Gliese 86.
Astronomy & Astrophysics, 354:99–102, February 2000.

H. Rein.
A proposal for community driven and decentralized astronomical databases and the Open Exoplanet Catalogue.
ArXiv e-prints, November 2012.
URL http://arxiv.org/abs/1211.7121.

A. Sachs.
Babylonian Observational Astronomy.
Royal Society of London Philosophical Transactions Series A, 276:43–50, May 1974.
doi:10.1098/rsta.1974.0008.

M. E. Schwamb, J. A. Orosz, J. A. Carter, W. F. Welsh, D. A. Fischer, G. Torres, A. W. Howard, J. R. Crepp, W. C. Keel, C. J. Lintott, N. A. Kaib, D. Terrell, R. Gagliano, K. J. Jek, M. Parrish, A. M. Smith, S. Lynn, R. J. Simpson, M. J. Giguere, and K. Schawinski.
Planet Hunters: A Transiting Circumbinary Planet in a Quadruple Star System.
The Astrophysical Journal, 768:127, May 2013.
doi:10.1088/0004-637X/768/2/127.

J. M. Stone and M. L. Norman.
ZEUS-2D: A radiation magnetohydrodynamics code for astrophysical flows in two space dimensions. I - The hydrodynamic algorithms and tests.
Astrophysical Journal Supplement Series, 80:753–790, June 1992.
doi:10.1086/191680.

A. Toomre.
On the gravitational stability of a disk of stars.
The Astrophysical Journal, 139:1217–1238, May 1964.
doi:10.1086/147861.

B. van Leer.
Towards the Ultimate Conservative Difference Scheme. IV. A New Approach to Numerical Convection.
Journal of Computational Physics, 23:276–+, March 1977.
doi:10.1016/0021-9991(77)90095-X.

S. J. Weidenschilling.
Aerodynamics of solid bodies in the solar nebula.
Monthly Notices of the Royal Astronomical Society, 180:57–70, July 1977.

F. L. Whipple.
On certain aerodynamic processes for asteroids and comets.
In A. Elvius, editor, *From Plasma to Planet*, page 211, 1972.

R. Whitehurst.
Numerical simulations of accretion disks. I - Superhumps - A tidal phenomenon of accretion disks.
Monthly Notices of the Royal Astronomical Society, 232:35–51, May 1988.

T. Wilken, G. L. Curto, R. A. Probst, T. Steinmetz, A. Manescau, L. Pasquini, J. I. González Hernández, R. Rebolo, T. W. Hänsch, T. Udem, and R. Holzwarth.
A spectrograph for exoplanet observations calibrated at the centimetre-per-second level.
Nature, 485:611–614, May 2012.
doi:10.1038/nature11092.

A. Wolszczan and D. A. Frail.
A planetary system around the millisecond pulsar PSR1257 + 12.
Nature, 355:145–147, January 1992.
doi:10.1038/355145a0.

Working Group on Extrasolar Planets.
Position statement on the definition of a "planet", February 2003.
URL http://www.dtm.ciw.edu/boss/definition.html.

S. Zucker, T. Mazeh, N. C. Santos, S. Udry, and M. Mayor.
Multi-order TODCOR: Application to observations taken with the CORALIE echelle spectrograph. II. A planet in the system <ASTROBJ>HD 41004</ASTROBJ>.
Astronomy & Astrophysics, 426:695–698, November 2004.
doi:10.1051/0004-6361:20040384.